Operating, Testing and Evaluating Hybridized Silicon P-I-N Arrays

by

Andrew C. Moore

B.S.E.E.
State University of New York at Buffalo
1986

M.S.E.E.
Rochester Institute of Technology
1991

A Dissertation submitted in partial fulfillment of the
requirements for the degree of
Doctor of Philosophy
in the Chester F. Carlson Center for Imaging Science
Rochester Institute of Technology
2005

Signature of the Author _____

Accepted by _____
     Coordinator, Ph.D. Degree Program   Date

CHESTER F. CARLSON CENTER FOR IMAGING SCIENCE

ROCHESTER INSTITUTE OF TECHNOLOGY

ROCHESTER, NEW YORK

<u>CERTIFICATE OF APPROVAL</u>

Ph.D. DEGREE DISSERTATION

The Ph.D. Degree Dissertation of Andrew C. Moore
has been examined and approved by the
dissertation committee as satisfactory for the
dissertation required for the
Ph.D. degree in Imaging Science

Dr. Zoran Ninkov, Ph.D. Advisor

Dr. Ian Gatley

Dr. William J. Forrest

Dr. P. R. Mukund

Date

DISSERTATION RELEASE PERMISSION

ROCHESTER INSTITUTE OF TECHNOLOGY

COLLEGE OF SCIENCE

CHESTER F. CARLSON

CENTER FOR IMAGING SCIENCE

Title of Dissertation:

Operating, Testing and Evaluating

Hybridized Silicon P-I-N Arrays

I, Andrew C. Moore, hereby grant permission to Wallace Memorial Library of R.I.T. to reproduce my thesis in whole or in part. Any reproduction will not be for commercial use or profit.

Signature ——————————————————————————

Date

Operating, Testing and Evaluating
Hybridized Silicon P-I-N Arrays

by

Andrew C. Moore

Submitted to the
Chester F. Carlson Center for Imaging Science
in partial fulfillment of the requirements
for the Doctor of Philosophy Degree
at the Rochester Institute of Technology

Abstract

Use of CCD detector arrays as visible imagers in space telescopes has been problematic. Charge-coupled devices rapidly deteriorate due to damage from the high radiation environment of space. CMOS-based imagers, which do not transfer charge, offer an alternative technology that is more tolerant of a high-radiation environment.

This dissertation evaluates the performance of four "pathfinder" 1K by 1K hybridized silicon P-I-N detector arrays made by Raytheon under subcontract to RIT as candidates for use in a space telescope application. Silicon P-I-N arrays have photon capture properties similar to back-thinned CCD's and should be far more robust than CCD's in the high-radiation environment of space. The first two devices, 180 μm thick prototypes, demonstrate crisp imaging with lateral diffusion of 5 microns at 35 Kelvin. The nodal capacitance is estimated to be 41 fF and the quantum efficiency is remarkably good (typically > 0.75) over a spectral range from 410 to 940 nm. A second pair of devices, fabricated with detectors thinned to 40 μm, exhibits similar performance but with blue-enhanced spectral response from an improved IR coating.

Operating, testing, and evaluating imaging devices similar to the ones tested here is also problematic. Precise, low-noise, flexible control systems are required to operate the devices, and interpretation of the data is not always straightforward. In the process of

evaluating these pathfinder devices, this dissertation surveys and advances systems engineering and analysis (i.e. the application of linear and stochastic system theory) generally useful for operating and evaluating similar hybridized "staring" focal plane arrays. Most significantly, a previously unaccounted for effect causing significant errors in the measurement of quantum efficiency — inter-pixel capacitive coupling — is discovered, described, measured, and compensated for in the P-I-N devices. This coupling is also shown to be measurably present in hybridized indium antimonide arrays. Simulations of interpixel coupling are also performed and predict the coupling actually observed in the P-I-N devices. Additional analysis tools for characterizing these devices are developed. An optimal estimator of signal on a multiply-sampled integrating detector in the presence of both photon and read noise is derived, modeling a pixel as a simple linear system, and is shown to agree with known limiting cases. Theories of charge diffusion in detectors are surveyed and a system model based on the steady state diffusion equation, infinite lifetime, and contiguous pixels is derived and compared to other models. Simulations validate this theory and show the effect of finite mean free path, finite lifetime, and non-contiguous pixels upon it. A simple method for modeling and evaluating MTF from edge spread is developed and used. A model that separately measures system and device noise in multichannel systems is developed, and shown to agree with measurements taken with the same device in both a quiet and a somewhat noisy system. Hardware and software systems that operate these devices are also surveyed, and 'agile' technologies and development methodologies apprpriate for detector research are employed to build a simple and flexible array control system, primarily from open-source components. The system is used to collect much of the experimental data.

Acknowledgements

Thanks first go to Zoran Ninkov for "taking me in" when I was looking for a dissertation topic that could utilize my skills and interests in electronics and system design. He was imaginative enough to envision a research possibility along those lines. His upbeat and easy-going attitude has made the experience enjoyable as well as educational. The expert guidance of University of Rochester Near Infrared Astronomy Lab professors Bill Forrest and Judith Pipher contributed much to my experience, and their support, encouragement, and patience has been overwhelming. I spent many hours in their lab, learning not only about devices and device testing, but also about people and teamwork. NIR Lab engineer Craig McMurtry always provided information and guidance. Rich Sarkis aided with all things computer. Candice Bacon's usage of the system and subsequent enhancement requests greatly improved its usability. Working with Zoran and the NIR Lab connected me intimately with a large astronomical community. Greg Burley and Carnegie Observatories were the originators of the open-source electronics that was built upon here. Greg,

Table of Contents

List of Tables

List of Figures

Preface

Astronomers answer questions about the universe. They hypothesize, design experiments, take data, and examine the data with respect to their theories. Their data often come from sophisticated electronic instruments, each with characteristics of its own. As such, astronomers are often required to obtain a deep understanding of the systems which provide them their data. Focal Plane Arrays and the optics and electronics attached to them are such systems. Systems engineers and software engineers aid the astronomers by providing systems tailored to helping answer the astronomers' questions. These engineers produce better systems if they obtain a deep understanding of the issues concerning the astronomers' questions. Unfortunately, scientists and engineers are sometimes reluctant to obtain this mutual understanding. Scientists often desire a turnkey system that "just works." Engineers often desire a complete "a-priori" description of system requirements. Desirable as these things may be, they often do not reflect the reality that a cutting-edge research instrument is simply not a commodity item. Research by its very nature delves into areas of great uncertainty and the next direction to proceed often depends on information recently acquired and unavailable at the start. The process is iterative and agile — direction is constantly adjusted. This dissertation is written with a belief that the best results come from teams of scientists and engineers who endeavor to understand each other, and targets science and technology in that middle ground where scientists and engineers meet in an astronomical camera system.

This dissertation characterizes silicon P-I-N devices, but much of it develops tools that can be applied to understanding the performance of hybridized detector arrays in general, independent of the particular detector that may be bonded to the multiplexer. Regardless of the wavelength of the incoming radiation, photons are absorbed by the photo-detector and converted to discrete excess minority carriers. Systems theory is applicable in many forms as these photo-carriers make their way through the detector bulk and are trapped in detector nodes, amplified in the multiplexer, amplified again off the multiplexer, digitized, and processed. A solid understanding of this system is needed to answer the questions of system performance: How much information is lost in this process of acquiring an image? What are the mechanisms causing aberrations in the images, and how can they be removed, or at least compensated for in analysis of data that the system produces? How can the next system be improved?

Overview of this dissertation

This dissertation is divided into three parts.

The first part describes the detector arrays that are typically used for astronomical imaging, with a focus on hybridized detector arrays. The general technologies in use (CCD, CID, CMOS, back-thinned/hybridized) are described. An overview of hybridized detector technology follows, with a summary of the advantages of hybridized P-I-N detectors. Hybridized detector arrays consist of a multiplexer, which handles selection and readout, and a detector, which collects incoming photon flux as an electrical signal.[1]

---

[1]When discussing these items separately, the text will refer to them as the "detector" and the "multiplexer." The combination of the two will be referred to as a "detector array" or a "device." The combination device may also casually be referred to as a "detector" in contexts when this meaning is inferable.

The second part reviews and develops the theory of spatial frequency response in both detectors and multiplexers. The overall response of the detector array is broken into several mechanisms, and each one is discussed. One of these mechanisms, inter-pixel capacitance, was discovered and documented as a result of this research.

The P-I-N array testing is covered in the third part. Experiments included both simulations and measurements taken with actual devices, but the simulations are presented in an appendix. Models of the devices are covered, followed by the results of the actual testing.

Appendices are also attached. These include simulations of diffusion and field strength, some relevant stochastic theory, and details about the array controller system. The stochastic theory includes noise in the arrival of the photons and handling of noises introduced from other sources, including the optimal sampling algorithm for multiply sampled images. Summary descriptions of typical tests done to characterize detectors are also included.

Part I

Introduction

Chapter 1

Imaging Arrays in Astronomy

High performance imagers are essential components in many applications, among them astronomical, medical, and remote sensing. Astronomical imagers deal with a special segment of imaging applications. Astronomy requires high precision, low noise detector arrays that can sense very weak signals. Infrared wavelengths are of particular interest to astronomers who desire to detect distant red-shifted objects, and objects embedded in or behind interstellar dust clouds. Space-based astronomy also requires robust detector arrays — ones whose electrical performance does not degrade in the fierce radiation of space and also with mechanically sound construction and a low risk of failure upon mechanical or thermal shock. In many respects, however, astronomical imaging systems are similar to most other imaging systems. Figure 1.1 shows an imaging array in the context of an acquisition system.

Challenges in scientific astronomical detector development are typically ones of improving read noise, spectral response, quantum efficiency, modulation transfer function, and dark current. Development of improved devices is an iterative process. New devices are characterized and the results are compared with expected performance. Based on this new understanding, adjustments are made for the next device. When more can be learned about the proper operation and performance limitations of the state of the art devices, more effective changes are implemented in the next generation. The silicon P-I-N arrays tested
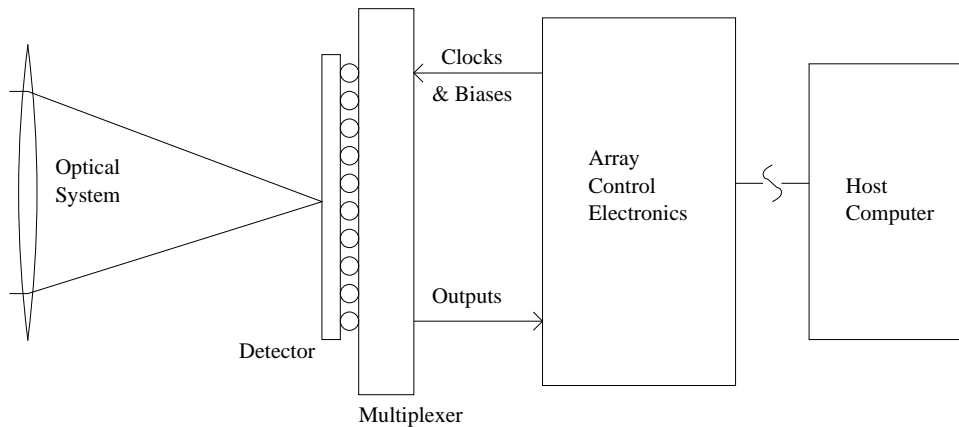
Figure 1.1: A typical electronic imaging system consists of focusing optics, detector array (hybridized shown here,) controller electronics, and host computer.

here are a result of this iterative development cycle and have characteristics that make them especially suited for use in space telescope applications. This chapter surveys the currently available detector technologies. Chapter 2 surveys hybridized CMOS detector arrays, which generally have the advantage in space applications, in more detail.

1.1   Types of Detector Arrays

Electronic imaging devices fall into several overlapping categories: monolithic or hybridized, destructively read or non-destructively read, conventional or back-thinned, etc. Janesick[1, 2] and Magnan[3] both survey the state of the art in this area and provide technical details for some finer distinctions in detector and readout technology beyond what is presented here.

Hybridized detector arrays are built as separate wafers which are then joined together electrically. Typically, hybridized devices separate detection from readout — the detector and the readout are made in separate manufacturing steps. The detector is then typically

8

"flip-chip bonded", or "bump-bonded" to the readout. (Wire-bonding has also been used in some instances.)

This creates the major benefit of hybridized devices: many types of detector and detector material may be used in a hybridized array and the best detectors can be be mated to the best multiplexers. Monolithic detector arrays are imaging devices built on a single semiconductor wafer. The semiconductor material, usually silicon, is processed in various steps involving implantation, deposition of metal or oxide, etching, etc.

Non-destructive readout allows an accumulated image to remain in a detector and be sampled many times and a variety of noise-rejection techniques such as Fowler-sampling [4] to be applied. Back-thinned detectors increase capture efficiency by optimizing the geometry of the detector.

A major distinction in arrays is the type of collection node. CMOS collection nodes have a voltage that can be read directly. These nodes must be reset to a specific reset voltage, which introduces noise. CCD collection nodes have a quantity of charge associated with them and may be reset to zero charge. These nodes may not be read directly, however. Their charge must be transferred into a node that can be read directly, and this charge transfer cannot be undone.

This section considers three readout types — charge-coupled device (CCD) readout, charge injection device (CID) readout and preamp-per-pixel (PPP) complimentary metal-oxide semiconductor (CMOS) readout. Typically, the CMOS multiplexer is the readout mechanism to be found in hybridized devices — CCDs are usually monolithic.

All of these readout mechanisms, however, may be used in hybridized devices. Aspects from CCD and CMOS technologies have been and continue to be combined in various ways. Pipher and Forrest [5, 6] investigated a hybridized InSb CCD in 1983. The "pinned photodiode" described by Janesick[1] is another interesting approach that uses a CMOS readout with a charge-transfer pixel.
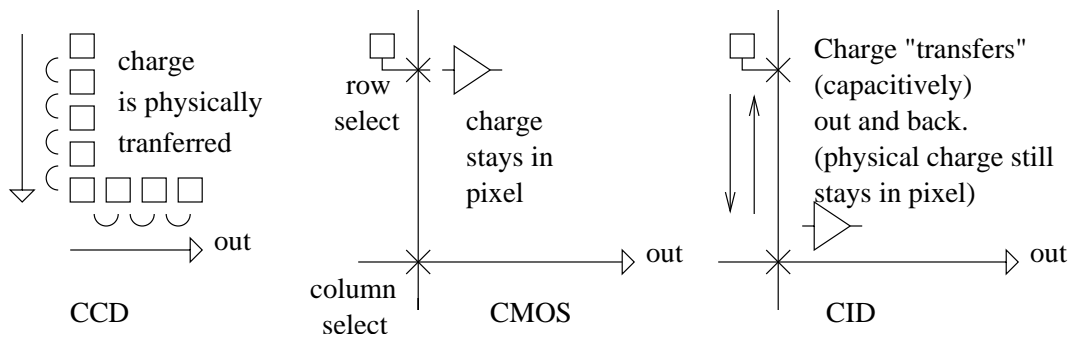
Figure 1.2: CCD readout is destructive — accumulated charge is transferred completely out of the array. CMOS readout can leave the charge in the pixel while reading the array. CID readout capacitively transfers charge onto a shared sensing bus, then pulls it back into the pixel well.

1.2   Monolithic Charge Coupled Devices

Of several types of focal plane array used by the astronomical community, the CCD deserves first mention and is frequently employed in astronomical applications. Indeed, the CCD is and has been very popular in all imaging applications. CCD technology is mature and cost-effective. The CCD readout operates on a "bucket brigade" principle — charge collected in one pixel is repeatedly transferred through neighboring pixels until it reaches the output amplifier for the array. A "three phase" clock is frequently used. This simple design allows for simple implementation, resulting in many benefits. One benefit is manufacturing cost — simple solutions are produced more economically. CCDs have been manufactured in huge volumes for many years, and much is known about how to make them. The CCD is typically manufactured as a monolithic device, and this typically limits the detector to silicon. CCD pixels have no "reset noise" — they can be completely discharged to a state of zero carriers. In many instances, a CCD is the best choice for a scientific application.

10

The CCD's charge transfer process causes it to be "destructively" read — reading the device also resets it. This is not a problem if the readout process is accurate, but the presence of certain kinds of noise can put a destructive read approach at a disadvantage. More significantly, the journey of charge from pixel to output is a treacherous one. Charge transfer efficiency (CTE) must be very good, perhaps as high as 99.9999%[2], each and every step of the way. Space telescopes are subject to fierce radiation — this is the "Achilles' heel" of the CCD in such applications. When high energy radiation strikes a pixel in a CCD, it can damage the charge transfer mechanism and affect many pixels. Even without this damage, these high-energy events can almost completely obscure a long-integration exposure.

Given these weaknesses, there is seldom any advantage to choosing the CCD readout mechanism for a hybridized detector in a space telescope application.

1.3   Monolithic CMOS and Charge Injection Devices

At the time of this writing, devices called "CMOS arrays" are rapidly gaining popularity in both commercial and scientific applications. The term "CMOS" stands for "complimentary metal-oxide semiconductor," and refers to a manufacturing technique[7] which is used widely for digital logic, not just imaging devices. CMOS manufacturing is quite mature now, and the experience of that industry has been successfully applied to making CMOS imagers. In "complimentary" MOS circuits, two kinds of transistor are fabricated that mirror each other's operation from a voltage standpoint. One of the transistors attaches to the upper supply rail and supplies, or "sources" current. The other attaches to the lower rail and receives, or "sinks" current. Logic can be done with only one kind of transistor (NMOS or PMOS) but the complimentary approach is more flexible.

CMOS imaging arrays do not employ the "bucket brigade" readout technique — the charge stays in the pixel during readout. The CMOS devices considered here use a more complicated "preamp per pixel" (PPP) architecture, where the charge present in a detector node is amplified at the pixel location. The amplified voltage, not the charge, is transmitted over switched row and column buses in a selection process known as "multiplexing." Typically, another amplifier buffers the signal again as it leaves the device.

Charge Injection Devices (CIDs)[8] are an interesting combination of CCD and CMOS approaches, similar to the "pinned photodiode" mentioned earlier. The CID "transfers" charge from the pixel to a main output amplifier, much like a CCD. However, the CID does not truly perform this charge transfer. The current is a displacement current onto a global sense bus, and so the sense capacitor is really the parallel combination of the pixel sense capacitor and the capacitance of the sense bus. — thus, the effective capacitance at read time is larger than that of a single pixel, and the CID can never achieve CCD noise performance. This approach, however, allows the charge to be transferred back to the pixel for further integration, yielding non-destructive readout similar to the CMOS device. Preamp-per-pixel CIDs have also been produced[9], but this is not the common practice. The "DEPFET" and "Skipper" approaches[10] appear to be similar. These approaches transfer charge via displacement current to a floating gate. Figure 1.2 illustrates the CCD, CMOS, and CID readouts. Like CCDs, the CID may be reset to zero carriers. CIDs are radiation-hard devices[11] — they are p-channel and do not transfer charge. Some are randomly addressable, and they may[12, 13] be an appropriate choice for space based astronomy.

Like the CCD, CMOS devices and CIDs are typically monolithic and limited to silicon detectors. It is a possible to deposit other detector material on silicon readouts using techniques like molecular beam epitaxy (MBE). Monolithic InSb[14] and InGaAs[15] detector arrays have been fabricated, but their usage is not widespread.

1.4 Hybridized CMOS Detector Arrays

Hybridized photodetector arrays, although not as mature as CCD devices, are often the most sensible choice for space-based astronomical telescopes. On space telescopes, signal-to-noise ratio (SNR) and robustness are prime concerns. Hybridized arrays have no circuitry on the "first" or "back" surface of the detector — the surface which light strikes. Their collection efficiency (signal) is typically very good.

The CCD is generally regarded as superior from the standpoint of raw SNR. Since CMOS imagers may be read in a non-destructive fashion, some SNR improvement is possible using "multiple sampling" techniques, and SNR gain from this technique can help compensate for the increased noise from CMOS readout technology — A CCD only needs one good output amplifier; CMOS devices require one good amplifier on every pixel, and very limited space is available to create this amplifier. CMOS readouts, not manufactured from the purer substrates that CCDs use, are typically noisier to begin with. They are more likely to need the noise reduction techniques unavailable to CCDs. The dominant noise in CMOS amplifiers is related to defect density in semiconductor processes, not immutable laws of physics, so CMOS may yet rival CCD technology as improvements are made.

Multiple sampling is only useful in the lowest signal cases. When the photon noise ($\sqrt{signal}$) rises above the read noise, the photon noise dominates and readout noise is unimportant. Astronomy that peers out into the blackest black of the oldest universe, deep-field infrared astronomy as one example, is a case where signals are particularly low. For such applications, low-noise CMOS multiplexers are being fabricated and operated at very low signal levels with multiple sampling techniques that can reduce read noise and reject cosmic ray events[16, 17].

Figure 1.3 illustrates a cross-section of a typical hybridized array. The pixel implants, manufactured on the "front" side of the detector, capture the photocarriers. The rest of the
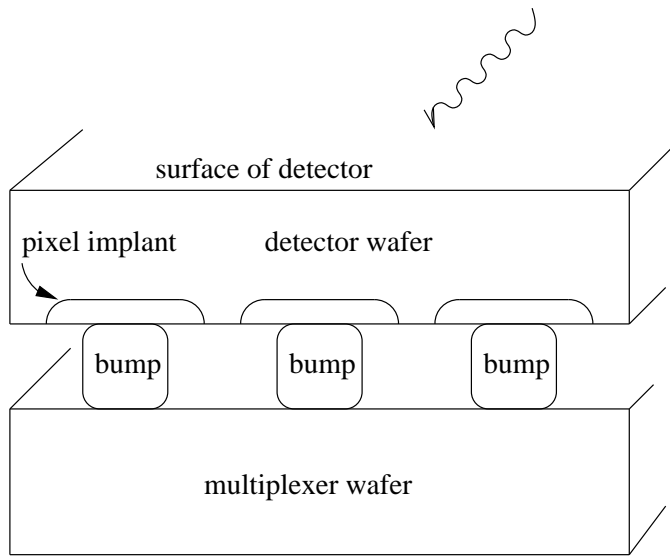
Figure 1.3: Hybidized arrays mate a detector wafer to a multiplexer wafer, typically using bumps
of indium.

detector bulk converts incoming photons to the electrical signal. The detector is flipped
over and "bump-bonded" to the multiplexer's front surface.

Chapter 2

Hybridized Imager Technology

The two parts of a hybridized imager, the multiplexer or "readout" and the detector, are joined together to create the detector array, sometimes called a sensor-chip assembly or "SCA". The detector captures incoming photons, converting them to electrical charges which are trapped in the detector nodes (pixels) for readout by the multiplexer.

The multiplexer selects one pixel or several pixels and amplifies the signal for the acquisition system. Key components of the multiplexer are the unit cell, the selection logic, and the signal path. The unit cell gathers the information. The selection logic determines which pixels are to be read. The signal path connects the unit cell to the output.

The detector is conceptually much simpler. It is typically a large array of photodiodes. Photodiodes employ the photoelectric effect to produce electrical charge that can be swept away and collected by an electric field in a depletion region. This simplicity is deceptive, however. Producing good detectors can be extremely difficult.

2.1 Multiplexers for Hybridized Imagers

Raytheon Vision Systems, (formerly Raytheon Infrared Operations, formerly Santa Barbara Research Center) and Rockwell Scientific are two major manufacturers of CMOS multiplexers for use in hybridized imagers. They are essentially the only manufacturers

of the high performance multiplexers suitable for state of the art astronomical imaging. Multiplexers produced by Rockwell and Raytheon are similar in many ways. This section discusses some general properties of these multiplexers. CMOS circuits are built from field effect transistors (FETs.)

2.1.1 Signal Path

The selected detector element's voltage traverses the signal path to the output of the device, as shown in Figure 2.1. Multiplexers generally have two source followers in the signal path. The row enable FET connects the first (unit cell) source follower to its column bus, and the column select connects the column bus to the second (output) source follower. "Selecting one of many" is indeed the meaning of the word "multiplex". These switches are opened and closed by a pair of shift registers. Pads at the edge of the multiplexer allow access to lines that control these shift registers. Each shift register has a control line (called "sync") that resets the shift register to the start. Two other lines (called phases, or "phis") control the advancing of the shift register.

2.1.2 Unit Cell Variations

The unit cell circuit is repeated once per pixel in the multiplexer, so a simple unit cell is good. A unit cell has three responsibilities: buffer, selection, and reset. Unit cells require a source follower FET to buffer the detector node voltage. They also require an output enable FET to allow several pixels to share a common output bus, so at least two FETs are required per unit cell. The row enable FET can be placed on either the supply or bus side of the source follower. Some method of resetting detectors is also needed. A reset-by-pixel unit cell can be implemented with two transistors in the reset circuitry, one enabled by row, and one by column. In reset-by-row, the column enabled FET is eliminated. Global reset

16
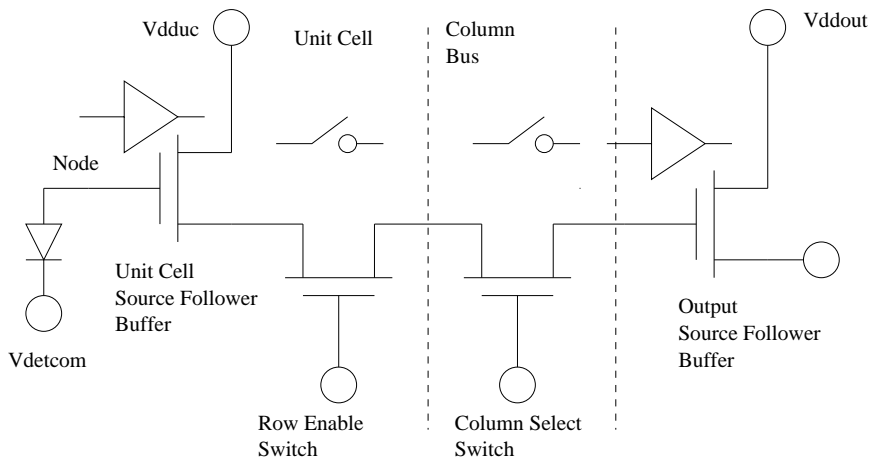
Signal path: 4 FETS

Figure 2.1: Multiplexers use a pair of switches in a signal path to select one of many nodes for presentation at a shared output. The buffered node voltages of one row are placed on the column buses by row enable FETs, and one column bus is selected to drive the output buffer.

is typically implemented in the same fashion as reset-by-row, but all reset transistors share a common drive signal. The three-transistor unit cell is a popular design.

2.1.3   Reset mechanisms

The different reset mechanisms used in multiplexers, reset-by-pixel, reset-by-row, and global reset, all have advantages and disadvantages. There is generally a trade-off between flexibility and simplicity. The most flexible mode, reset-by-pixel, is shown in Figure 2.2. It allows a sampling mode called "correlated triple sampling" (or CTS) to be employed. This mode samples the pixel during reset as well as immediately after reset. Reset-by-pixel allows brightly illuminated pixels to be reset more frequently than darker pixels. This ability can yield impressive dynamic range, but it makes the multiplexer, the clocking, and data acquisition more complicated.

Reset−by−Pixel: 4 FETS
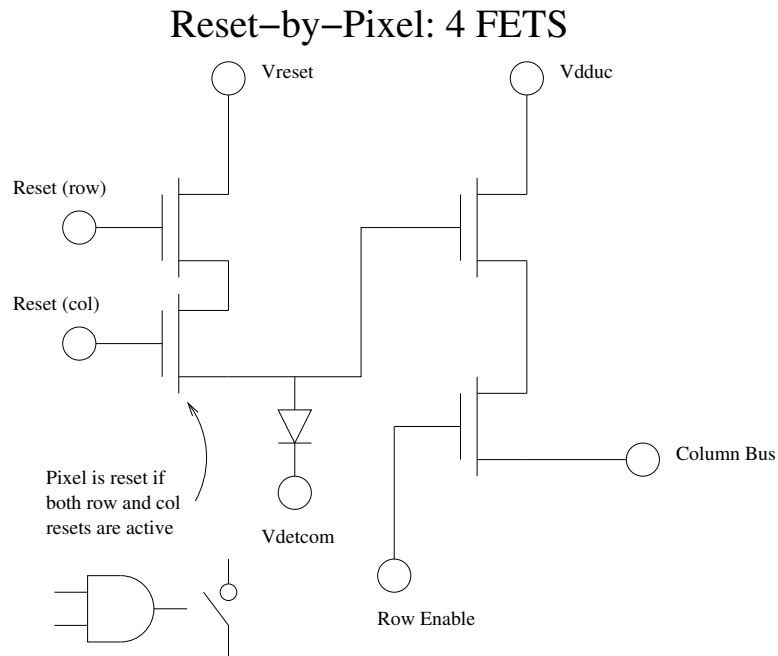
Figure 2.2: The reset-by-pixel mechanism also uses two switches in series. It resets a single pixel when both switches are closed.

In global reset, shown in Figure 2.3, all of the pixels in the array are reset simultaneously. The process is simple, but inflexible. The reset level of an individual pixel cannot be sampled immediately prior to integration, and the individual bright areas cannot be reset more frequently. A different type of correlated triple sampling can be done with global reset however, and since CTS rejects low frequency noise (on the order of the integration time) this method is practically just as effective.

Global reset has a practical disadvantage due to the possibility of shorted pixels. If a detector has shorted pixels, the reset operation draws a continuous current through all of the shorts. For very large arrays and significant resistances in the wires connecting the electronics to the array, the global reset operation has the potential to cause a significant sag in the applied biases. This can also cause a power dissipation problem, since global reset is frequently applied for a relatively long period of time.

18

may be tied together

Vreset · - - - - - - - - - - - - - · Vdduc

Reset (row)

Vdetcom

Row Enable

Column Bus
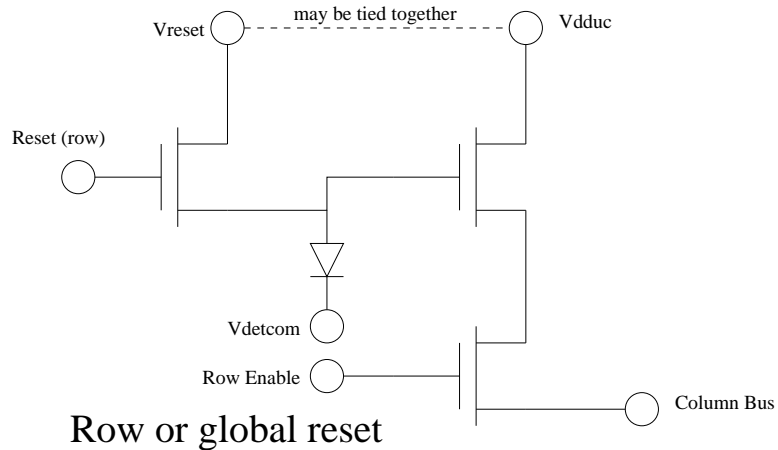
Row or global reset

Figure 2.3: The three-transistor unit cell has only one reset switch.

Reset-by-row uses the same unit cell circuit as global reset. It constrains the current draw from defective pixels, and is favored for large arrays. If a row is sufficiently defective, such that the reset operation causes a problem such as excessive heat generation, reset by row allows a row to be skipped entirely.

2.1.4   Pixel selection mechanisms

Multiplexers have various "bus lines" that cross each other in the row and column directions. Each unit cell's output enable switch connects the pixel to an output bus line. The output enable bus (a logic signal) drives the gate of the switch. The enable line runs orthogonally to the output bus (an analog signal) connected to the switch output. In keeping with the horizontal scan convention of most cameras, the output enable switch is the "row enable" and output bus is the "column bus." A single row remains selected while all of its pixels are read out in sequence. Row enable logic enables a single row of pixels onto the output bus, and column select logic selects one of the output buses to drive its multiplexer output.
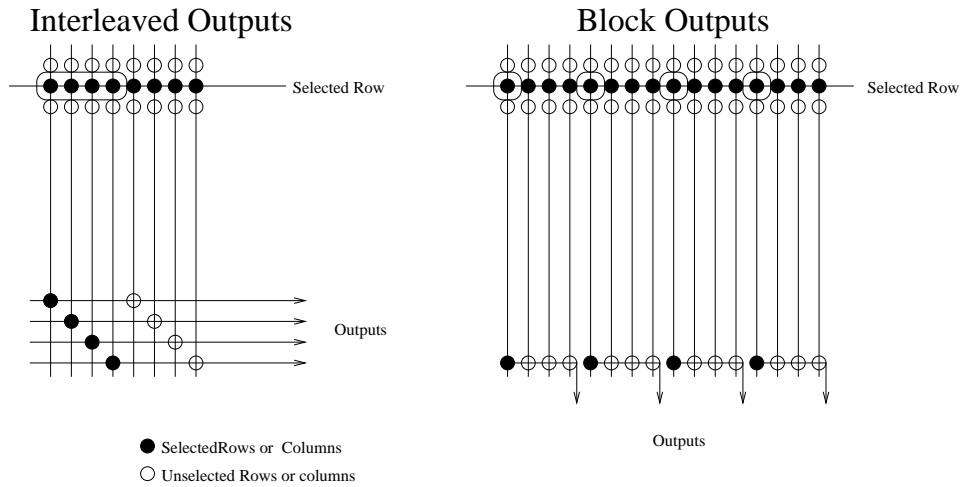
Figure 2.4: Interleaved readout allows multi-output readout most similar to standard readout. Block output is more similar to a mosaic of arrays.

Randomly addressable multiplexers accept bit codes for row and column selection. This mode of operation is not done frequently however. A large number of clocks is involved, and operating the array in random access mode poses many complicated issues from the readout circuitry through the acquisition, data storage, and data analysis. More typically, a shift register mechanism is used, and the pixels are read out in a standard sequence, similar to that of a CCD. Frequently, these imagers are employed in a "mosaic" where a large number of arrays share the focal plane of a large optical system. This creates a need for "buttability" in the multiplexer design — the need to butt several arrays in close proximity to each other, effectively creating a larger array. It is desirable that all of the connections come off of one side of the chip, (three side buttable) and that the shift register circuitry is as thin as possible. Since the shift registers must occupy two sides of the multiplexer, one of them will be on a buttable side, so simple shift register circuity enhances the buttability of a device.
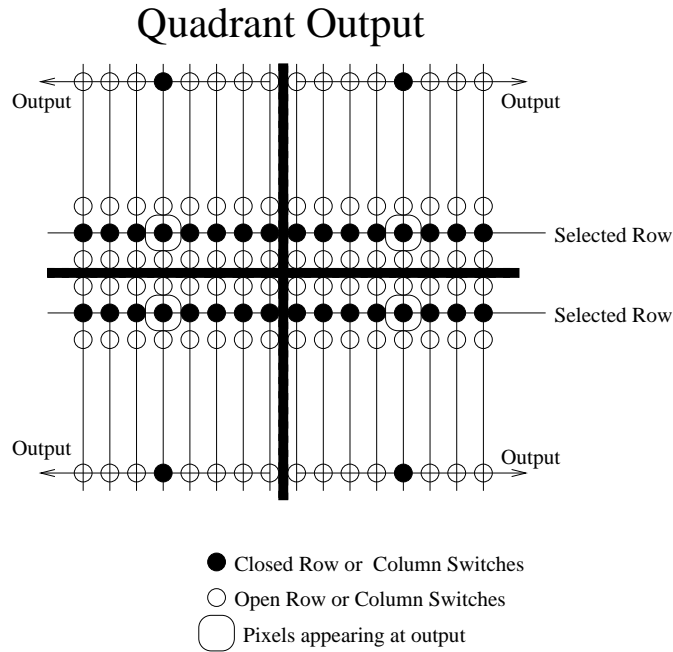
Quadrant Output

Figure 2.5: Quadrant output can be achieved by mirroring an array vertically and horizontally.

2.1.5 Multiple outputs

The settle time (time it takes for a newly selected pixel to change from its previous pixel's voltage) on high performance imagers is generally long, typically 10 microseconds. Since the most basic noise rejection strategy requires that the detector is read twice — a "pedestal" before integration and a "signal" after integration — a 1K by 1K imager with a single output and 10 microsecond settle would take 20 seconds to read out a complete image. This readout time can be reduced if more than one pixel is read out simultaneously. Figure 2.4 shows two typical approaches to increasing the number of outputs. In "interleaved" output, the pixels selected for output are next to each other. This is convenient for receiving pixels serially in a single data-stream. Interleaving complicates multiplexer layout, especially in an array that has a large number of outputs. It is simpler to place all of the columns for each output next to each other in "block" output. In this case, the data stream from the converters

21

may arrive in a non-standard sequence, and software must interleave the data at a later step to form the image. The Raytheon SB284 multiplexer, which has 32 outputs, is an example. A variation of block outputs, shown in Figure 2.5, is quadrant outputs. Here, each corner of the multiplexer has its own video output. Rockwell's NICMOS3 is a quadrant-output multiplexer.

2.1.6   Read Noise

The source follower FET of the unit cell is a critical component in the signal path. This transistor buffers the detector node voltage to the column bus and is the first and most important amplifier in the signal chain. To have the most sensitivity, it is desirable that the gate of this FET have a low capacitance. However, it is also desirable that this FET operate with as low noise as possible. The theoretically achievable thermally limited voltage noise for a FET is "white", and can be shown to be[7]:

$$ e_n^2 = \frac{8kT(1+\eta)}{3g_m}(\frac{V^2}{Hz}). \tag{2-1} $$

The transconductance g_m increases with the square root of drain current, indicating that FET devices should be operated at a high drain current to achieve low noise. The value η is a geometrical correction term that is typically close to zero. However, running high currents in an infrared detector at cryogenic temperatures can cause undesirable side effects such as heating and glow. (This is less of an issue with visible detectors)

MOS-FETs are becoming lower noise every year, but rarely approach the performance of Equation 2-1. They typically exhibit some sort of flicker noise ("low frequency" or "$\frac{1}{f}$" noise) which is unaffected by higher drain current[7]. Janesick [18, 2] attributes this noise to traps in the channels of the transistors, and presents one model of flicker noise that includes terms for the time between samples τ_s and the dominant system time constant τ_D:

$$e_n^2 = \frac{1}{S_v^2 A_{sf}^2 \left(1 - e^{-\tau_s/\tau_D}\right)^2} \int_0^\infty W^2 (1 + \frac{f_c}{f}) + \frac{2 + 2\cos\left(2\pi f \tau_s\right)}{1 + \left(2\pi f \tau_D\right)^2} \mathrm{d}f. \qquad (2\text{-}2)$$

The term $W^2(1 + \frac{f_c}{f})$ is characteristic of flicker noise. W^2 is the base white noise power density of Equation 2-1. At frequencies f above the corner frequency f_c, the noise density is constant, but below the corner frequency noise density increases as frequency decreases. It is desirable that this corner frequency is low. The other terms are just scaling and shaping terms. S_v is the nodal sensitivity and A_{sf} is the source follower gain.

2.2   Detectors for Hybridized Imagers

The detectors considered in this thesis are conceptually very simple — they are reverse biased diodes. Diodes are electrical devices that only allow electrical current to flow one way. The exact mechanism by which they do this is somewhat complicated, and will not be covered here in great detail. Streetman [19] is a good introduction. Sze [20] is a somewhat more advanced book. Rieke [21] is a good photodetector-specific reference.

Diodes work by virtue of having a depletion region, in which there is a strong electric field. Stray mobile carriers (electrons or holes) don't remain in the depletion region for very long. They are immediately swept out of the region in a direction that depends upon their charge. Incoming photons generate electron-hole pairs, and the depletion region's field will sweep one polarity of the pair into a node where it is trapped.

Detectors absorb photons and generate small amounts of charge as a result. The small charges are integrated in small capacitances and the voltage across the capacitance is the signal of a single pixel. Maximizing the voltage that appears on the detector means minimizing the capacitance, so it is important to analyze and understand the capacitance of the detector node.

Q, E field is the same in each capacitor

$$V = \int E \cdot dS$$

V is bigger if plates spaced apart more

$$C = \frac{Q}{V}$$

So, C is smaller if plates spaced apart more
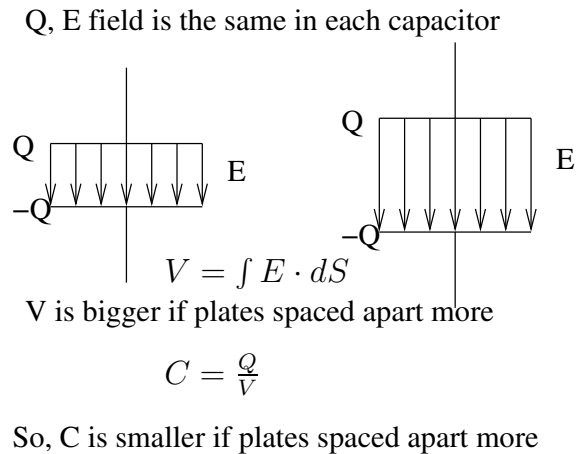
Figure 2.6: Large capacitors are built by placing parallel plates close together.

2.2.1 Capacitance

Capacitors store electrical charge, and the voltage observable across them indicates the amount of charge they are holding. The ratio of charge to voltage is the capacitance:

$$C = \frac{Q}{V}. \tag{2-3}$$

Capacitors are frequently constructed from parallel plates. Equal and opposite charges accumulate on the plates, and a uniform electric field exists almost exclusively between the plates. One counterintuitive aspect of capacitance is that as the plates are moved apart, the capacitor gets physically bigger but its capacitance gets smaller. This is illustrated in Figure 2.6. If you had two charged plates like these and increased their separation, the voltage difference would increase. Since the plates are oppositely charged, and opposite charges attract, it would take some energy to achieve the increased separation. For illustrative purposes, the distance between the plates is exaggerated. Most parallel plate capacitors have a plate separation much smaller than the width of the plate itself.

In a photodiode, the situation is somewhat more complicated. A diode is the junction of P and N doped semiconductor material. In the neighborhood of this junction, these regions become depleted of their normal carriers, and the field increases linearly from zero at the edges of this depletion region. At the junction, the field strength hits a maximum. More heavily doped semiconductor material will have an internal field that ramps more quickly.

2.2.2 Per-pixel depleted detectors

Many detectors are "per-pixel depleted" — each pixel's diode junction has its own thin private depletion region around it. Figure 2.7 shows per-pixel depletion. The edges of the depletion region act as plates in a capacitor, and the thin depletion region creates two effects. The first effect is that the closer plates create a larger capacitance, and the same amount of charge will produce less change in voltage. For a constant voltage noise introduced elsewhere, this means a less sensitive detector. The second effect is that the capacitance changes as the plate separation changes. This creates a non-linear pixel response. For uniformly doped junctions, the linear change in field causes a square-law relationship between distance and voltage.

Since the capacitance changes with voltage, it is often beneficial to model this aspect more accurately. One might find it convenient to consider the "small signal" capacitance — the ratio of change in voltage to change in charge, at a particular depletion of interest:

$$C_{ss} = \frac{\partial Q}{\partial V}.$$
(2-4)

This small-signal capacitance is (roughly) inversely proportional to the square root of the bias voltage. The specific relationship depends on the doping profile of the junction.

When a detector is biased prior to image collection, a voltage is applied to remove more charge from the depletion region. Biasing (resetting) the detector increases the size of this region. As carriers are swept into the detector node, the depletion region shrinks.

Resetting the detector with more bias increases well depth, but at some point no more bias voltage can be practically applied — the dark current rises unacceptably. This point is not precisely defined — it depends upon the application's dark current requirements. The charge associated with this maximum bias is the well depth.

In per-pixel depleted detectors, the bulk of the detector is conductive, and carriers released in the bulk wander in a random walk until they happen upon a depletion region or recombine. The undepleted gap between pixels is an interesting area for study — optimizing dark current and latent image performance often involves this gap. The depletion boundary may meet the detector's mux-side (front) surface at a varying location depending upon other potentials in this area, leaving a wider or narrower gap. Carriers may accumulate in this inter-pixel gap, and manufacturing defects may create traps here that generate latent images or dark current. Sometimes a metal grid is fabricated near the gap to control its behavior.

2.2.3 Thinned detectors

Back-thinning is a manufacturing technique employable on detectors arrays. Monolithic detector arrays are manufactured by layering circuitry on top of a semiconductor wafer. If the substrate is also the detector, this circuitry impedes the capture of incoming photons. For many applications, this loss of capture efficiency is not a grave concern. In astronomy, maximizing detection of available signal is a priority. Hybridized devices may also require thinning. The "bump-bonding" process in a hybridized device puts considerable stress on the detector, and it is helpful if the detector is hundreds of microns thick at this point in
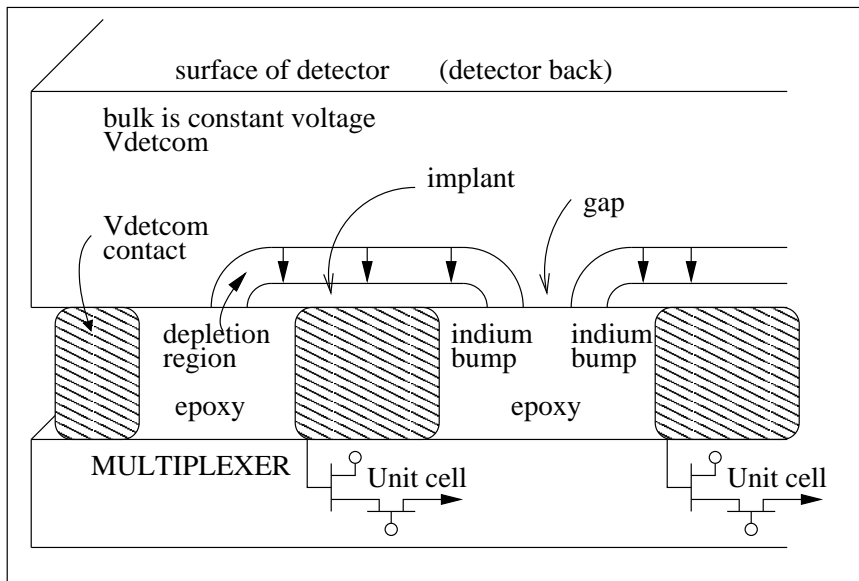
Figure 2.7: The small depletion region in per-pixel depleted detectors yields a larger capacitance. The detector wafer must be quite thin to achieve crisp imaging.

manufacturing. A thick detector in an operating hybridized device is usually not desired, however — detector thickness may affect the capture of carriers in two ways. First, carriers may recombine before being collected for readout. Second, carriers may diffuse laterally and be collected some distance away from their origin. Both of these mechanisms degrade the capture efficiency and image quality of the device.

Back-thinning restores capture efficiency. In monolithic devices, thinning is accomplished by flipping the device over and precisely removing semiconductor material. Then, light entering the back side of the wafer may be captured more efficiently than light entering the front side of the wafer. (The device is operated in the flipped orientation.) Hybridized devices are thinned in a similar fashion. This thinning process is delicate and expensive. Both mechanical and chemical methods of thinning are possible. When it does not destroy the device being thinned, however, it can yield greatly improved collection efficiencies.

27

Thinned detectors may, paradoxically, be more robust mechanically — more tolerant to thermal cycling and some other types of mechanical stress.

2.2.4 Deeply depleted detectors

Very pure detectors (where the balance between stray electrons and holes is very precise) can tolerate biasing to the point that the depletion regions of individual pixels material merge with the neighboring pixels without the bias being excessive. In a fully depleted detector, depletion goes all the way to the back side. Deeply or fully depleted detector arrays have low percentage of nodal capacitance from the detector and have a more linear response. In these detectors, the biased bulk of the detector does not allow carriers to wander for very long. They are quickly swept into a pixel, improving both efficiency and image clarity. Figure 2.8 shows full depletion.

The P-I-N detectors evaluated in this dissertation are typically operated in a fully-depleted mode. Since the detector may be made very thick, P-I-N detectors are more mechanically robust and can have very good response even at wavelengths where the photon penetration depth is relatively long. For example, the penetration depth in room temperature silicon at 940 nm is roughly 50 microns, and penetration depth at 1100 nm is close to 1000 microns.[20]

P-I-N and many other detectors may also be operated in a partially-depleted mode where the depletion regions of the detectors merge and close the gaps, but some of the bulk is still unbiased. Some detectors, however, experience an unacceptable increase in dark current at the point of full depletion due to defects at the back surface. Pixels in monolithic CCDs tend to be made from purer substrate and more amenable to deep depletion that P-I-N devices take advantage of. Monolithic CMOS imagers tend to be made
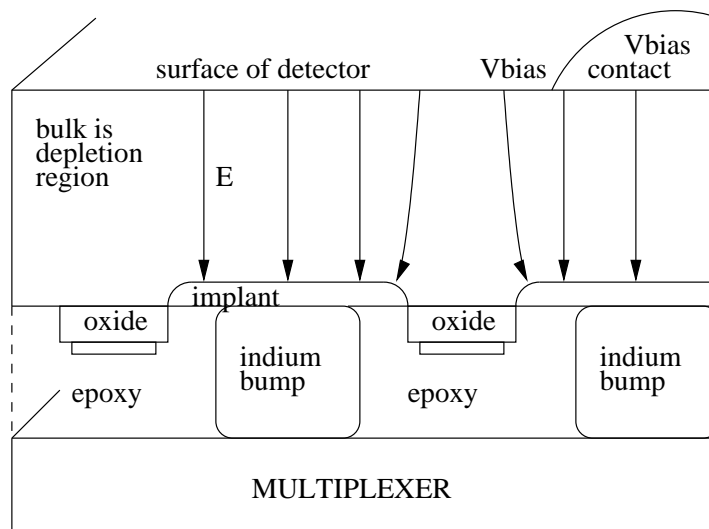
Figure 2.8: Fully depleted detectors have lower nodal capacitance since the depletion region is wide. The electric field maintains sharp imaging even in a thick detector. The thickness improves response at wavelengths near detector cutoff. The term "Vbias" is usually used to express the voltage across the photodiode. In the P-I-N detectors, the back bias voltage was so large that the term "Vbias" seemed more appropriate than "vdetcom" (detector common) for the back potential.

from a more heavily doped substrate, and thus towards shallower depletion and larger dark currents.[1]

2.3 Advantages of Hybridized Silicon P-I-N Arrays

The hybridized silicon P-I-N arrays tested here were expected to have several key properties. First and foremost, the strong field in the depletion region was expected to provide crisp imaging despite the substantial detector thickness. Additionally, the thickness enabled the expected spectral sensitivity to be quite good over the entire visible range and into the near infrared. These detectors have relatively simple anti-reflective coatings, but the blue

response, poor in many detectors, was expected to be quite good. The nodal capacitance was expected to be low as well, since the thickness of the detector resulted in a parallel plate model of negligible detector contribution. The research activity in this thesis work was planned to test these qualities.

Silicon P-I-N arrays should be able to withstand relatively large amounts of radiation. No plans to test this quality of the devices were made. The detector thickness should also make them more mechanically robust; plans were not made to test this quality of the devices either. The thick prototypes were each thermally cycled many times (estimated between 10 and 20 cycles) without any noticeable change in performance. One of the devices, accidentally dropped several feet from the optical bench to the floor, survived this ordeal without any observed harm.

Part II

Theory

Linear and Stochastic Theory Overview

A large body of linear and stochastic systems theory lends itself to the analysis and understanding of imaging systems. The Fourier transform [22, 23] is a central mathematical tool for understanding and analyzing linear systems. Many texts [24, 25, 26, 27] apply the Fourier transform to linear systems. Propagation of light through an optical system also lends itself to linear systems analysis and Fourier transform techniques. This topic is not addressed here — some excellent optics textbooks[28, 29] are suggested. Discrete and continuous digital signal processing [30] is another closely related topic. The Fourier transform is easily discretized and extended to two dimensions [31, 32] for imaging applications. Extension to N-dimensional problems [33] has also been addressed. Treatment of stochastic signals [34, 35] is also fundamental in the study of signals and systems. The flow of information in a system [36] and the signal-to-noise ratio of a communication channel has been studied in depth. A broad theory of estimation [37] has been developed. The semiconductor used in the detector array is quite central to the performance as well. Many texts [20, 21] are available that address the semiconductor physics of photo-detectors.

Successful extraction of all available information from imaging devices is the primary concern of both scientist and engineer. This thesis evaluates and compares the expected and actual images produced by the silicon P-I-N arrays — investigating how well they gather the optical information available to them — tracking the signal as it flows through the signal chain of the imaging array.

First, of course, an object being observed generates a signal. An optical system then focuses this signal upon the detector array. This part's analysis starts after the optical system; ideal optics, producing the ideal test signal — a point source — are assumed. The point spread function of an imaging device is described from a linear systems viewpoint. Inherent in this point spread is a stochastic aspect with a linear expression — charge diffusion. This pre-collection spread due to stochastic carrier migration can also be described by the linear steady state diffusion equation, and will be covered in Chapters 4 and 5. The collection of photocarriers into a single pixel also affects spatial frequency response, and this conversion of shape to spatial frequency, being more fundamental and applicable to diffusion results, is discussed first in Chapter 3. Point spread has an additional purely linear aspect — a deterministic post-collection spread, due to inter-pixel capacitive coupling, covered in Chapter 6. All of these mechanisms lay the foundation for the device modeling in Chapter 7, and for understanding the results of image transfer tests performed on the P-I-N devices later in Chapters 8 and 9.

Additional linear and stochastic theory appropriate for operation and evaluation of these devices was also developed or reviewed; some of this theory is covered in the Appendices. Noise produced from stochastic amplification in the detector is briefly discussed in Appendix D. This is where a single photon may produce more than one photocarrier. The optimal sampling problem is discussed in Appendix E. That problem, in a nutshell: When an image taken with multiple samples contains noise due to both the arrival of photons and the extra noise of the system, what is the optimal estimator for photon arrival rate? Another aspect of system noise, cross-channel correlation of noise in a multi-channel system, is considered in that appendix as well.

Chapter 3

Basics of Spatial Frequency Response

Detector arrays extract information from an optical signal presented to them. The scientist is mostly concerned with "spatial domain" aspects — how much signal was received in a particular pixel. The systems engineer, however, finds the Fourier domain to be far more convenient for many aspects of systems analysis. The discrete two-dimensional Fourier transform conveniently expresses many aspects of this information extraction process. The Fourier transform of an image, generally incomprehensible upon visual inspection, is beneficial in the powerful analysis that may be done with it. Topics which are complicated in the spatial domain (image blurring, information content, etcetera) become simple multiplications in the frequency domain. However, aspects of detector performance such as crosstalk are purely spatial domain, and frequency domain analysis often does not provide much useful information to answer such problems. Accurately relating frequency domain models to performance in the tails of the corresponding spatial-domain function is extremely problematic. The tails of the spatial domain solution flatten out and have very little energy. They are not well-represented in the frequency domain. Slight modeling errors in one domain can cause large errors in the other.

P-I-N devices may be operated in partial or full depletion — much of the promise of these devices is due to their sharp imaging in full depletion. To this end, the theoretical differences between full and partial depletion are elaborated upon in some detail. (Most of
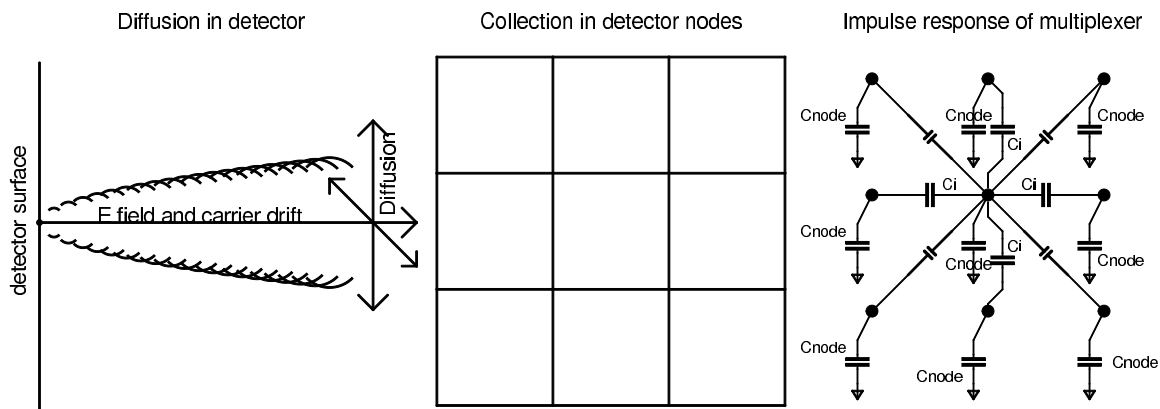
Figure 3.1: Point spread in the array, separated into three components — Diffusion of carriers before collection, averaging by the collection area, and capacitive coupling to adjacent nodes. Each of these components has a physical shape and corresponding frequency domain representation.

the interesting math involves partial depletion case, however.) Later in this dissertation, the modulation transfer function, or MTF, of the P-I-N arrays will be measured. Astronomy is often concerned with the imaging of point-like objects, so the point-spread function, or PSF, is the ultimate concern. Related to this concern is that of corruption of images by cosmic ray events. The PSF need not be measured directly. Edge spread analysis is often preferred since it provides more data. This section develops the underlying theory of MTF, point spread and edge spread.

3.1 Components of Detector Point Spread

Three essentially independent processes, shown in Figure 3.1, contribute to the spatial frequency response and point spread in hybridized arrays.

Lateral diffusion is the first process. When photons are converted to electrical signal, the photo-generated carriers of interest may diffuse before being collected. Diffusion will

be investigated in some detail here — it creates uncertainty about the exact origin of a collected carrier and reduces spatial frequency response.

The second process, sampling, collects the photocarriers in detector nodes. This spatial (not temporal) sampling process turns a continuous image into a discretely sampled array of charges. It collects photocarriers over an area and reports them as effectively originating from the same location. This "blurring" of the exact origination point of the charge also reduces the spatial frequency response.

The final process is inter-pixel capacitance. Inter-pixel capacitance's effect upon device characterization is becoming more widely understood and anticipated, partly as a result of the research in this dissertation, so it will be elaborated upon in some detail here.

It should be noted that these processes are only independent when the pixels can be assumed contiguous at their depletion boundaries. When the gaps in between pixels are significant, the shape of the diffusion profile is influenced by the proximity of the gaps — it is not "shift invariant". If carrier lifetime is long and all carriers get collected with the same probability, overall collection efficiency is still shift-invariant and this shift variance from diffusion may be lumped into the pixel collection (which is also shift variant.) When carrier lifetime is short or surface recombination in the gaps is significant, carriers released over gaps are less likely to be collected, and the model presented here fails. In most astronomical detectors, the gaps between pixels are small or nonexistent, and carrier lifetime is long enough to assure collection by some pixel, so diffusion and collection may be treated independently in many practical cases. In fully depleted detectors such as the P-I-N detectors characterized here, there is no undepleted gap between pixels — carriers actively drift towards collection nodes and only have a finite time to diffuse laterally. (The P-I-N transit time is estimated to be only a few nanoseconds.) In some detectors, sub-pixel sensitivity variations are observable — the total collected charge from a point source varies depending upon the position of the source relative the pixel grid centers. It seems unlikely that

inter-pixel gaps would cause any significant sub-pixel variations in collection efficiency in fully-depleted detectors.

Sub-pixel sensitivity variation is more typically a concern with front-illuminated detectors. Such devices are known to have significant sub-pixel sensitivity variations. [38, 39, 40, 41] In these devices, shift-variant responsive quantum efficiency can come from two sources. First, incoming light must pass through the interfering circuitry and may be attenuated or reflected non-uniformly before the photons are absorbed in the detector. This is pre-diffusion (and pre-detection) shift variance. After photocarriers are generated, they may be collected by some circuitry other than a pixel. This is post-diffusion shift variance, and only this mechanism may be properly treated as occurring at the sampling phase. Back-thinned hybridized devices are typically much more uniform and are less likely to exhibit (but are not immune to) significant sub-pixel sensitivity variations.

Ultimately, a combination of all processes, the pixel response function, results. This function may be obtained by scanning a tiny point of charge generation over a pixel (both inside and outside the area over the pixel) and observing how much of this signal winds up being collected by that pixel. The transform of the pixel response function results in a common specification for detector sharpness, the Modulation Transfer Function, or MTF.[42] In detectors which strive to collect every photon, the ideal pixel collects every photocarrier released in the area within it and none of the photocarriers released elsewhere.

Diffusion in detectors blurs an image. This reduces MTF at high spatial frequencies. Due to the quantum and stochastic nature of the diffusion process, this reduction is an information-losing process. It is impossible to say with certainty which pixel a given quanta "should have" been collected by, so inverse filtering cannot restore the original signal and the quantum noise floor is raised by this diffusion. Inter-pixel coupling also results in a reduction of MTF at high spatial frequencies. However, the reduction from inter-pixel

coupling is deterministic (not stochastic) and in typical "shot noise limited" or "background noise limited" images there is little reduction in the information content.

For space-borne applications, point spread from cosmic ray hits is an often-cited concern [43] because of the destructive effect upon the image during typical long integrations due to these events. If the point spread from a cosmic ray event is small, (and it will only be as small as the detector point spread) the degradation of the image is similarly contained, and fewer pixels are lost to these events in long integration images. ("Up-the-ramp" methods to reject cosmic ray events appear promising[17], and these techniques, if successful, can also greatly reduce that concern.)

3.2 Aperture Shapes and the Frequency Domain

Shapes of elements in the imaging system may be represented in the (spatial) frequency domain by using the Fourier transform. Diffusion profiles, circular apertures in the optical system, square pixels, capacitive coupling — all of these aspects of the system have physical shapes and equivalent frequency domain representations. This section reviews and develops functions and transforms that will be used later in the edge spread analysis of the P-I-N devices.

If the pixels are square, the collection process is typically approximated by the rect function. A 2D pixel is the product of a rect in x and a rect in y. The rect, as defined by Bracewell[44] and Gaskill[26], is:

$$\mathrm{rect}(x) = \begin{cases} 0, |x| > \frac{1}{2} \\ \frac{1}{2}, |x| = \frac{1}{2} \\ 1, |x| < \frac{1}{2} \end{cases} \tag{3-1}$$

This spatial averaging over a square area results in a sinc shaped frequency response, shown in Figure 3.2. The sinc has a gain of 0.64 at the Nyquist frequency of one cycle in
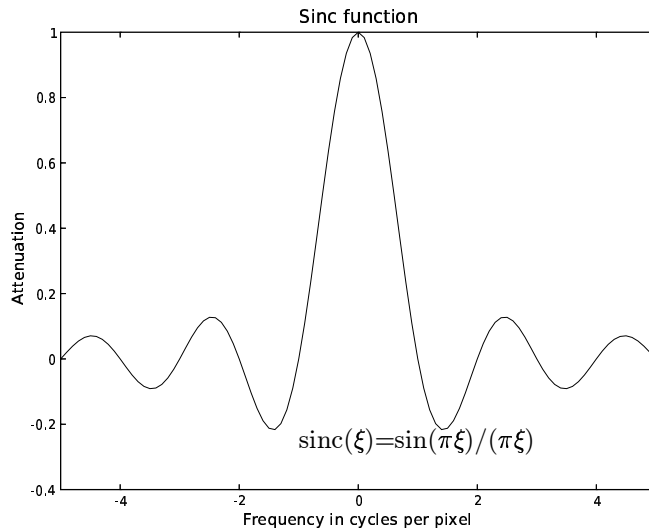
Figure 3.2: Averaging uniformly over a fixed window results in a "sinc" shaped frequency response that may be negative at very high frequencies. (A square pixel is the spatial product of two orthogonal fixed windows.) In a sampled system, response above 0.5 cycles per pixel is "aliased" to lower frequencies.

two pixels. (The Nyquist frequency is the most rapid frequency that a sampling system can reproduce accurately.) The two-dimensional frequency response is product of a sinc in ξ (the x frequency) and a sinc in η (the y frequency). The gain of 0.64 at Nyquist is optimal from a signal-to noise standpoint — efforts to increase this gain by reducing a pixel's active area (fill factor) would reduce RQE — and introduce sub-pixel sensitivity variations as well. In addition, gain *at* Nyquist is rarely of practical concern. Only perfectly aligned sine waves at the Nyquist can be detected with a gain of 0.64 — shift the perfectly aligned wave by a quarter cycle and no response is obtained.

Optical systems limit the spatial frequency content of the signal presented to the detector. The cutoff frequency is typically chosen to be at or below the Nyquist sampling frequency of the detector — no signal at or above the Nyquist is presented optically on the

Jinc function

$$\text{jinc}(x) = 2 J_1(\pi x)/(\pi x)$$

normalized intensity

radial distance
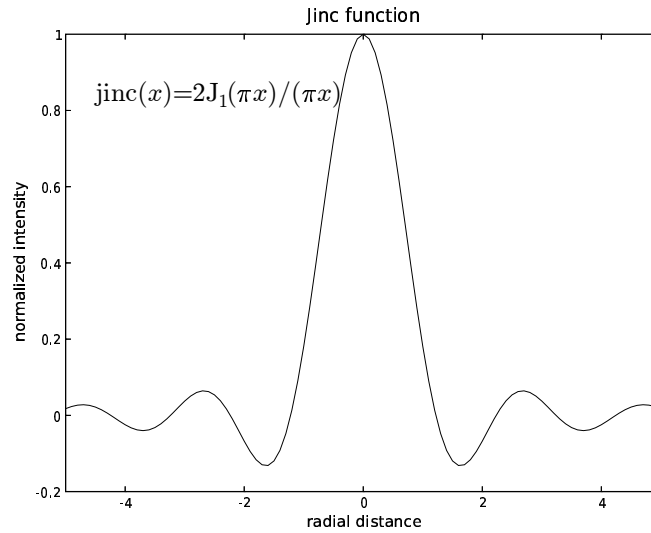
Figure 3.3: Averaging uniformly over a fixed circular window results in a "jinc" shaped frequency response that may also be negative at higher frequencies. In an optical system, the aperture diameter performs circular bandwidth limiting, and the resulting spatial amplitude response is "jinc" shaped.

detector array. This process "matches" the optical system to the array. Unlike electronic filters, a "brick wall" cutoff is easily obtainable optically, simply by varying an aperture diameter. To a good approximation, point spread at the focal plane is the Fourier transform of the aperture. A circular aperture may be treated as a `rect` function with rotational symmetry, also called a cylinder function. Figure 3.3 shows the `jinc` function, which is the spatial response of a circular aperture. Squaring this yields the observed intensity, shown in Figure 3.4.

41
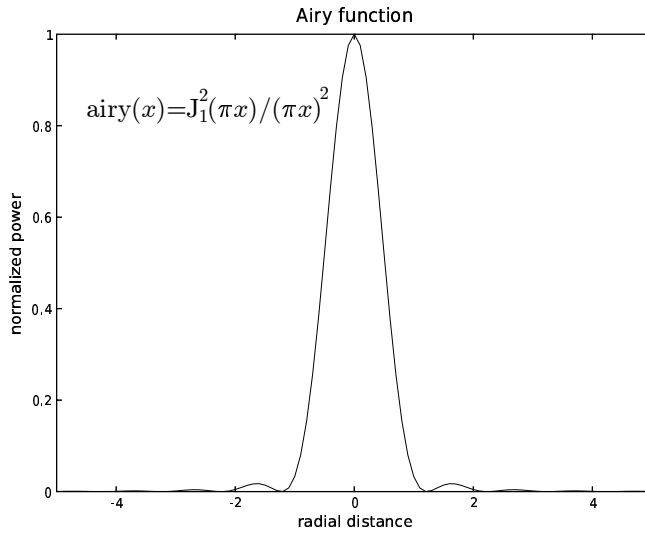
Figure 3.4: Circular apertures can produce an "Airy" point spread which has small ripples in the tails of the spatial response. This shape has no energy at high spatial frequencies and if matched to the detector will not produce aliased output.

3.3 Projections of a square pixel

Pixels are not circularly symmetrical and pixel centers are most commonly centered on a square or rectangular grid. The projection and resulting edge spread function vary with angle. Edge spread of the P-I-N arrays was evaluated with edges placed at various angles. In order to model the expected edge spread, the projection of the pixel response at various angles should be considered.

Here, the variable u represents distance in the projection. At arbitrary angles, the projection of the square pixel can be represented as the convolution of a pair of rect functions, each of unit area but with a width proportional the cosine or sine of the angle.

$$\text{pixel}\left(u\right) = \frac{\text{rect}\left(u\sin(\theta)\right)}{\sin(\theta)} * \frac{\text{rect}\left(u\cos(\theta)\right)}{\cos(\theta)}. \tag{3-2}$$
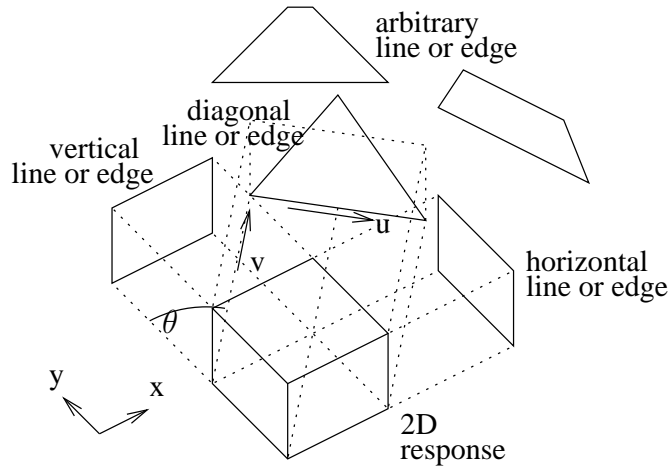
Figure 3.5: For vertical and horizontal edges, a square pixel appears to be *rect* shaped. A 45 degree edge yields a triangular projection. At other angles, a square pixel has a trapezoidal projection.

At zero and 90 degrees, one of the rect functions has zero width — it is a "delta" or "impulse" function. At 45 degrees the rect functions are identical and a triangle shaped function results. Figure 3.5 illustrates this.

In inter-pixel capacitive coupling, to be described in detail later, signal in the central pixel is deterministically "lost" to its four nearest neighbors. This results in an inter-pixel projection of:

$$\text{ipcap}(u) = \alpha[\delta(u + \sin(\theta)) + \delta(u - \sin(\theta))$$
$$+ \delta(u + \cos(\theta)) + \delta(u - \cos(\theta))] + (1 - 4\alpha)\delta(u). \qquad \text{(3-3)}$$

where δ is the "impulse", or "delta" function. Figure 3.6 shows this projection.

The expected edge spread is the convolution of these two functions with the diffused edge — a perfect optical edge blurred only from diffusion in the detector. So, overall
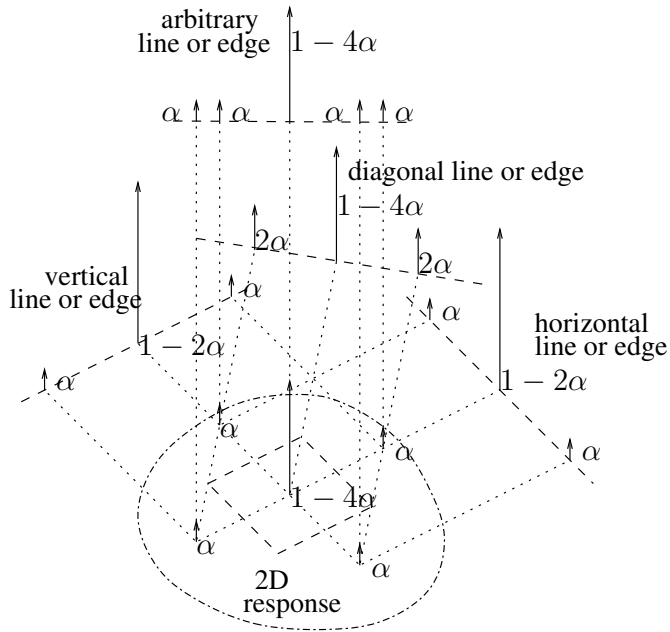
Figure 3.6: The center pixel and four nearest neighbors in the inter-pixel response appear at different relative positions as a function of angle, but their intensities do not change. At zero, 45 and 90 degrees, some pixels coincide and their responses add together.

expected edge spread at the output of the device, expressed in terms of these two projections and the detector's line spread from diffusion (LSF), is given by:

$$\text{ESF}(u) = \text{pixel}(u) * \text{ipcap}(u) * \int_{-\infty}^{u} \text{LSF}(v)\,dv. \tag{3-4}$$

Edge spread, the last term in this equation, is the integral of line spread, and line spread is the response that would be obtained from diffusion of a perfect line impulse — charge on an infinitely thin line, expressed with a density in carriers per unit length. The variable v is a dummy variable for integration.

Figure 3.7 shows the shapes of these functions, and is worth comparing to Figure 3.1. This model will be employed later in Chapter 8, when actual P-I-N edge spread is evaluated.
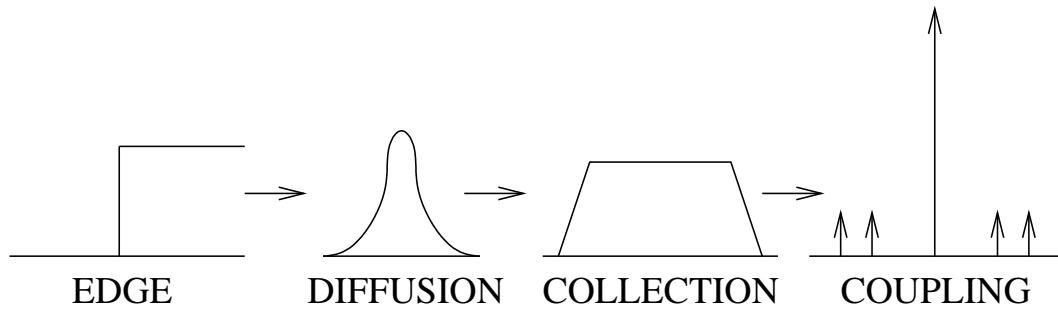
Figure 3.7: Edge spread is modeled as the convolution of four functions — the edge itself, followed by diffusion in the detector, then the pixel projection, and finally the interpixel coupling projection.

The next chapter will investigate the mechanisms that produce the LSF (diffusion) term in Equation 3-4.

Chapter 4

Lateral Diffusion in Detectors

Carriers released in a detector typically diffuse (walk randomly) before they are collected by some nearby pixel. If a carrier originating above one pixel has a probability of being captured by some other pixel instead, the sharpness of the resulting image will suffer. Since photon arrival is a Poisson process, there is noise associated with the incoming signal. Lateral diffusion reduces the signal strength at high spatial frequencies, but does not reduce the noise. As a consequence, lateral diffusion is an information-losing process. In this chapter, the effect of diffusion on image quality is considered. Recombination (the fact that carriers may disappear before being collected) will be neglected for now. Only the case of negligible penetration depth in a back-illuminated detector, i.e. photons absorbed very close to the surface of the detector material, is considered initially. For back-illuminated devices, deeper penetration only improves frequency response. In P-I-N devices, which are fully depleted and have a different diffusion model than per-pixel depleted detectors, the detector thickness is large, and penetration depth does not significantly change the expected diffusion profile.

4.1 Approaches to diffusion analysis

Many approaches to analysis of detector diffusion have been taken. Crowell and Labuda [45] is a seminal and often cited analysis. Holloway's analyses [46, 47] are of similar importance.

Crowell and Labuda modeled charge collection in a diffusion mode detector by solving the steady-state diffusion equation. Their solution is powerful and elegant. It includes many effects: penetration depth, bulk recombination, surface recombination. It solves the problem directly in the frequency domain.

Holloway's analysis is also quite elegant and is implemented in the spatial domain. It is somewhat confusing in that all results are normalized to diffusion length. Holloway's analysis is difficult to interpret when the diffusion length is set to infinity. Being a spatial domain solution, it offers answers to the practical question of expected crosstalk.

Many other parties have also pursued alternate approaches to modeling this problem. Raytheon [48, 49] and Rockwell [50] for example, have approached diffusion analysis in various ways. Rockwell performed a theoretical analysis based on Crowell and Labuda but switched to a Gaussian model for crosstalk analysis. Peter Love and Alan Hoffman of Raytheon also used the Crowell-Labuda model to analyse the theoretical performance of InSb detectors proposed for the JWST, but Joe Rossbeck (also of Raytheon) directly simulated diffusion. Davis *et al.* [51] modeled diffusion in InSb detectors using an exponential decay crosstalk model. Their exponential model is based on the one-dimensional solution of the diffusion equation with no boundary conditions. (This section will show that the exponential decay model is indeed valid, but only in the "far field." Diffusion profiles near the source do not initially decay exponentially.) Forrest and Ninkov [52] modeled point spread using a simpler "straight-line" diffusion model, with some agreement to measured data. This model considered pixels on a 30 micron pitch with an 8 micron undepleted gap

between pixels scanned by a 12 micron spot source. Forrest and Ninkov did not publish this diffusion model. It is of particular interest in this dissertation given their close involvement, and also because it is a natural simplification to attempt. Blynskii *et al.* [53] refer to Holloway's analysis, and then proceed to explain and apply a straight-line diffusion model with an additional term for diffusion length. (Many papers refer to Holloway's analysis, but it appears to be difficult to apply.)

A simpler spatial domain solution (that can be transformed into the frequency domain) for the case of contiguous pixels and negligible surface recombination, is developed here. It is most similar to, and is effectively a simplified version of, Holloway's analysis. It is hoped to be found more usable by those reluctant to apply a more nearly complete model. The case of infinite carrier lifetime will be considered primarily. The infinite lifetime case is a practical one to consider, since it is desirable that diffusion length be large to maximize quantum efficiency. (In high purity silicon such as the P-I-N devices, even at room temperature, the diffusion length is approximately 500 microns and carrier lifetime is hundreds of microseconds.) It also presents a worst-case crosstalk scenario, as longer diffusion lengths increase crosstalk.

4.2   Steady-State Diffusion

The steady-state diffusion equation solves for carrier density ρ in a bounded large volume by balancing the charges entering and leaving small differential volumes due to two mechanisms: diffusion current and recombination.

The carrier density itself is not of concern. The goal is to find the diffusion current **J**, which is the diffusion coefficient D times the negative gradient of the carrier density.

$$\mathbf{J} = -D\nabla\rho. \tag{4-1}$$

In the steady state, diffusion current and recombination balance each other. Consider these mechanisms in isolation first. If the current density is divergent, there is a net diffusion of charge into or out of the differential volume:

$$\nabla \cdot \mathbf{J} = -\frac{\partial \rho}{\partial t}. \tag{4-2}$$

If there is no net diffusion of charge into or out of the volume and only recombination occurs, the charge density will decay exponentially with the recombination time τ setting the rate of decay.

$$\frac{\partial \rho}{\partial t} = -\frac{\rho}{\tau}. \tag{4-3}$$

Setting both mechanisms equal and opposite by combining Equations 4-2 and 4-3 yields

$$\nabla \cdot \mathbf{J} = -\frac{\rho}{\tau}. \tag{4-4}$$

If $\nabla \cdot \mathbf{J}$ is positive, charge is diffusing out of the volume. If $\nabla \cdot \mathbf{J}$ is negative and balances the recombination rate inside the volume (ρ/τ), charge is diffusing into the volume to balance the loss to recombination.

Substituting Equation 4-1 to express everything in carrier density yields:

$$D\nabla \cdot \nabla \rho = D\nabla^2 \rho = \frac{\rho}{\tau}. \tag{4-5}$$

The Laplacian ∇^2 of excess carrier density ρ multiplied by the diffusion coefficient D is the net diffusion current into the differential volume. Equation 4-5 is the "Steady-State Diffusion Equation." When the recombination term is zero, it reduces to "Laplace's Equation." The terms D and τ both change the shape of Equation 4-5 in the same manner, and are often combined in a common parameter — $L = \sqrt{D\tau}$ — the "diffusion length."

$$\nabla^2 \rho = \frac{\rho}{L^2}. \tag{4-6}$$

Symmetry arguments allow a much simpler approach than actually solving the diffusion equation, however. For more complex problems, closed-form solutions do not exist, and simulations must be performed. (This is the case in many similar problems.) Taking Equation 4-4 and setting carrier lifetime to infinite results in

$$\nabla^2 \rho = \nabla \cdot \mathbf{J} = 0. \tag{4-7}$$

This is true everywhere except at sources of excess carriers. For a surface integral enclosing a source generating excess minority carriers at rate I_o, Gauss' divergence theorem can be applied, yielding the more intuitive:

$$I_0 = \oiint \mathbf{J} \cdot d\mathbf{A}. \tag{4-8}$$

Now, consider this point source surrounded in all directions by a uniform substrate. Assuming infinite carrier lifetime, the steady state diffusion current $\mathbf{J}$ around this point is known from symmetry and conservation of charge. The solution, using $r = |\mathbf{r}|$

$$\mathbf{J}(\mathbf{r}) = \frac{\mathbf{r}}{4\pi r^3} I_o. \tag{4-9}$$

is easily obtained. The carrier generation rate is equal to the product of the current density at r and the surface area of an enclosing sphere centered on this point. That current density is normal to the surface of the sphere.

Shen and Kong describe an "image method" [54] (employed more simply in [55]) which is useful in geometries where an "infinite plane" can be assumed. Crowell and Labuda and Holloway made this assumption when they assumed contiguous pixels. As already stated, this assumption will be made here as well. First, however, the straight line diffusion (Blynskii-Forrest-Ninkov) model which does not make these assumptions is investigated.

4.3 Straight Line Diffusion Model

The "straight line diffusion" model starts with Equation 4-9. The reasoning that follows is quite natural and intuitive: since diffusion current takes this form, the depletion boundary will collect this diffusion current scaled with appropriate consideration of its angle to the direction of the diffusion current. If the source is at (0,0,t) above the origin on the depletion boundary, then a small differential area $dA = dxdy$ at location (x,y,0) on the depletion boundary will collect $\mathbf{J} \cdot d\mathbf{A} = JdA\cos(\theta)$, where θ is the angle between the depletion boundary normal and diffusion current. Charge diffusing upwards "reflects" off the detector surface; basically this means the result for the bottom surface is doubled for a charge source at the surface. The distance from the source to the collection point is $r = \sqrt{x^2 + y^2 + t^2}$ and the cosine of the angle is t/r. Putting this all together results in:

$$J_{FN}(x,y) = I_o \frac{t}{2\pi \left(x^2 + y^2 + t^2\right)^{\frac{3}{2}}}. \tag{4-10}$$

This model is flawed, neglecting the stochastic mechanisms that underlie the diffusion process. Consider the boundary condition at the edge of the depletion zone. Carrier density at the depletion boundary, by Equation 4-1, must be zero. Diffusion current, proportional to the gradient of carrier density, must be normal to the depletion edge. Thus, the diffusion current must follow a curved path from a point source to the depletion boundary.

4.4 Modeling Diffusion using the Image Method

The "image method" described in Shen and Kong [54] or Plonus [55] is utilized to correct this error. These sources present the "image method" in the context of solving for electric fields. Mathematically, however the diffusion equation is the same, and the "image method"

was applied by Holloway [46] to this same problem. What follows is a alternate version to Holloway's more general equations.

The "image method" involves setting up mirror charges to satisfy the boundary conditions. When the boundary conditions are satisfied, the uniqueness theorem assures that the solution is the one and only correct one. An example from electrostatics is illuminating here. Given a single infinite conducting plane and a point charge, the boundary condition is that the conductor is at the same potential at all places, thus the tangential component of the E field at the surface of the conductor must be zero. A "mirror charge" of opposite polarity placed on the opposite side of the plane satisfies this boundary condition by symmetry. Thus, the field strength of a charge next to a conducting plane is equal to that of a dipole.

The analogous boundary condition in the detector is that the diffusion current is normal to the edge of the depletion region. This boundary condition can be satisfied in the same way by placing a "mirror source" of opposite polarity on the exact opposite location of the depletion boundary.

The addition of the mirror source causes the tangential components of current density to cancel exactly, leaving only a normal component and satisfying the boundary condition. The direction vectors of this solution (the well-known dipole field) are shown in Figure 4.1

The direction vectors at the plane midway between the sources are all normal to the plane, thus this satisfies the boundary condition. It has the shape of the straight-line diffusion model as well. The straight line diffusion model's shape is correct for a point source some distance away from a depletion boundary, but otherwise surrounded by uniform detector bulk infinitely in all directions. However, the scaling is off by a factor of two. Actually, *all* carriers released by the source eventually cross the boundary and are collected — not half, as straight-line diffusion would predict. This is the stochastic nature of the diffusion process. Even though half of the steradians available to the carrier are in a direction

Dipole Direction Vectors
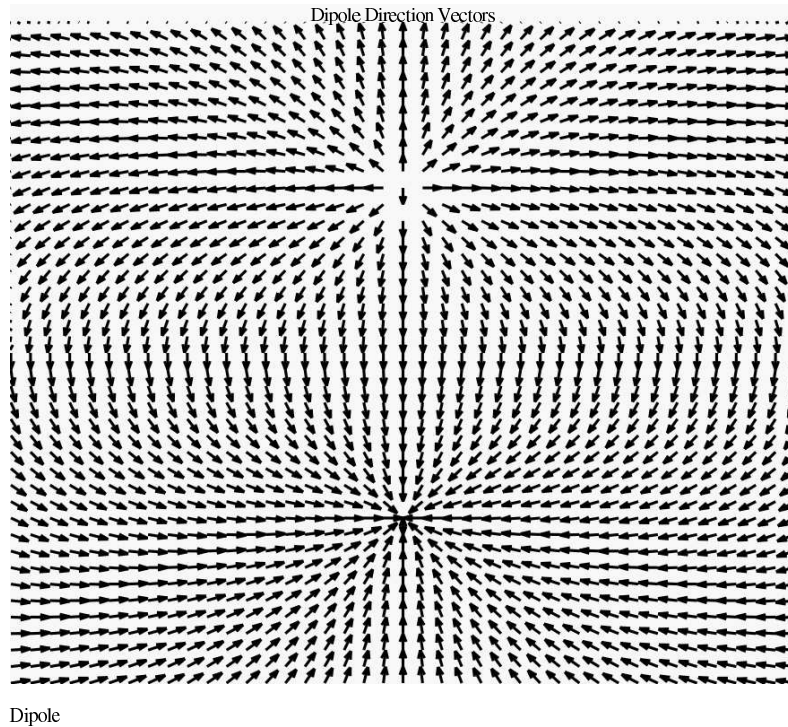
Dipole

Figure 4.1: The dipole solution is the result of a point source some distance away from a collection boundary. There is no back surface here, the diffusion volume extends infinitely upward. Straight line diffusion predicts that half of the carriers diffuse up and are never collected. The steady state diffusion equation predicts that all carriers cross the boundary eventually.

that will not collect it, there is zero probability that the carrier will not cross the boundary eventually given infinite lifetime.

A real detector has two planes of interest; the other plane is the "back" surface of the detector. Neglecting surface recombination, the back surface boundary condition is that no diffusion current is normal to the detector surface. As can be seen in Figure 4.1, the direction vectors at the plane through the source (assumed to be at the surface) are not all tangential to the surface; extra diffusion current is actually *coming in* through this plane in the model.

If the detector "back" were the only surface and the source were some distance away from this surface, this boundary condition could be satisfied with a mirror source of the same polarity on the opposite side of the surface. Exactly the opposite case from the dipole, now the normal components cancel and the tangential components remain. Moving the two sources together so that they are coincident results in a doubled source; half the flux going up and half going down. (Treating the detector surface as a mirror and doubling the one-sided result, which Forrest and Ninkov's model did, is very much the same thing.)

A second mirror source placed on the opposite side of the original source creates symmetry condition around the detector surface and satisfies the detector surface boundary condition. Unfortunately, the symmetry around the depletion boundary is destroyed. The second mirror source must be re-mirrored— the new source above the detector surface must also be mirrored below the depletion zone surface again. For every new source added, a need for another new source appears in a mirror. This quickly turns into a "fun house" situation where the original pair of surfaces mirror each other ad infinitum. Symmetry around both surfaces is created with an infinite line of alternating point sources. Splitting each point source allows modeling a point source below the detector surface. This is shown in Figure 4.2. Pushing the sources in Figure 4.2 back together makes single sources of $2I_o$, and shifting the origin to one of these sources yields the solution for current density at all points $\mathbf{r}$. This is a summation of alternating shifted versions of Equation 4-9,

$$\mathbf{J}\left(\mathbf{r}\right) = \sum_{n=-\infty}^{\infty} -1^n I_o \frac{\mathbf{r}+n\mathbf{d}}{2\pi|\mathbf{r}+n\mathbf{d}|^3}. \tag{4-11}$$

where $\mathbf{d}$ is the cycle distance equal to two detector thicknesses. In this geometry, the nearest point on the depletion boundary is $\mathbf{d}/2$.

Since this summation satisfies both boundary conditions, it must (by the uniqueness theorem) be the unique solution to the diffusion equation.
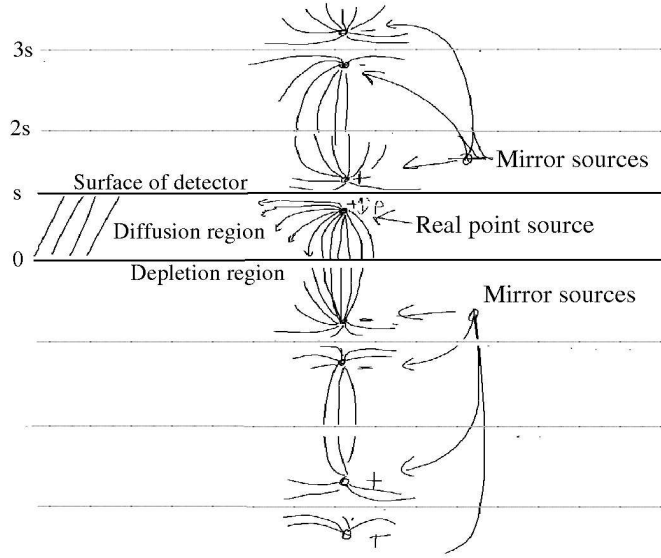
Figure 4.2: The image method satisfies the boundary conditions at both surfaces of the detector by alternating positive and negative sources of excess carriers.

Substitution of Cartesian coordinates for $\mathbf{r}$ and $\mathbf{d}$, using

$$\mathbf{r} = x\hat{\mathbf{x}} + y\hat{\mathbf{y}} + z\hat{\mathbf{z}}. \tag{4-12}$$

and

$$\mathbf{d} = d\hat{\mathbf{z}}. \tag{4-13}$$

results in the expression:

$$\mathbf{J}\left(x,y,z\right) = \frac{I_o}{2\pi} \sum_{n=-\infty}^{\infty} -1^n \frac{x\hat{\mathbf{x}} + y\hat{\mathbf{y}} + \left(z + nd\right)\hat{\mathbf{z}}}{\left(x^2 + y^2 + \left(z + nd\right)^2\right)^{\frac{3}{2}}}. \tag{4-14}$$

Vector field plots in Figure 4.3 and Figure 4.4 graphically show the profile of the diffusion current in the detector as expressed by Equation 4-14. Figure 4.3 confirms that both boundary conditions are satisfied. Diffusion at the top of Figure 4.3 is tangential to the detector surface and diffusion at the bottom is normal to the depletion boundary. Figure 4.4 shows that the diffusion current is not spherically symmetric. Diffusion towards the detector is
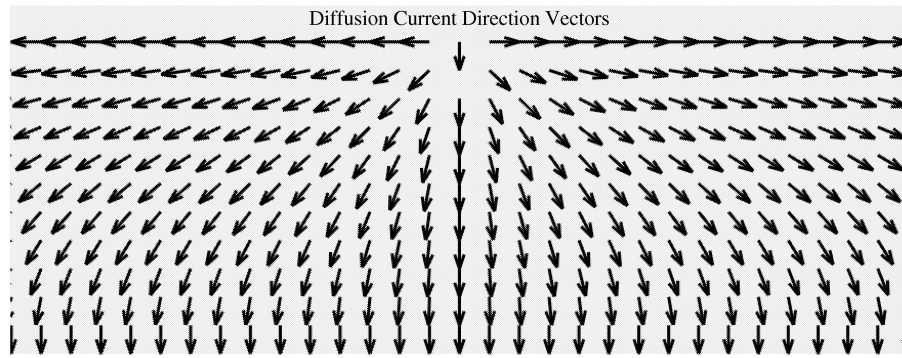
Figure 4.3: Diffusion current direction vector field plot for point source, showing diffusion tangential to the top surface and diffusion normal to the bottom surface.
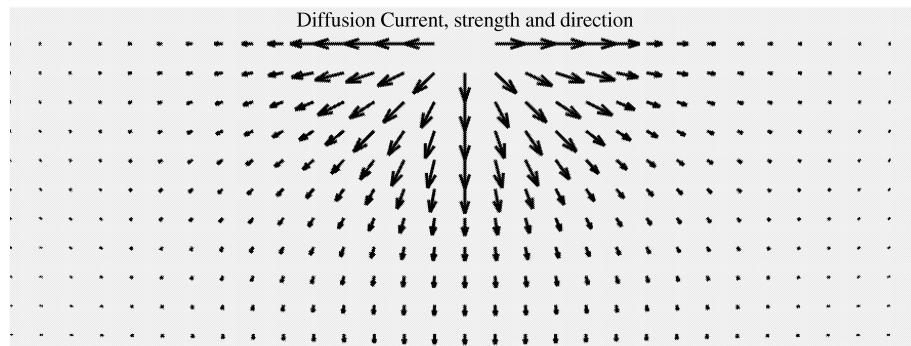
Figure 4.4: A slice through the same 3D vector field, but with arrow length proportional to diffusion current strength. Diffusion towards the bottom is notably stronger than diffusion in any other direction.

much stronger. This is an apparent paradox: How do the carriers "know" to diffuse in that direction? The carriers do not "know" to diffuse that way; they simply do anyway, on average.

This point spread is two-dimensional and rotationally symmetric, so polar coordinates, with r *redefined* as $r^2 = x^2 + y^2$ will now be used. (The symbol ρ was already used to represent charge density.)

Equation 4-9 evaluated at $z = d/2$ yields diffusion current across the depletion boundary at location x, y (the point spread function.)

$$J(r) = \frac{I_o}{2\pi} \sum_{n=-\infty}^{\infty} -1^n \frac{(d/2 + nd)}{\left(r^2 + (d/2 + nd)^2\right)^{\frac{3}{2}}}. \tag{4-15}$$

Dropping the source intensity term and normalizing to detector thickness by setting $d = 2$ yields:

$$PSF(r) = \frac{1}{2\pi} \sum_{n=-\infty}^{\infty} -1^n \frac{(2n+1)}{\left(r^2 + (2n+1)^2\right)^{\frac{3}{2}}}. \tag{4-16}$$

The summation is symmetrical since $-1^n(2n+1)$ is equal to $-1^{-(n+1)}(-2(n+1)+1)$, so a one-sided summation is equivalent:

$$PSF(r) = \frac{1}{\pi} \sum_{n=0}^{\infty} -1^n \frac{(2n+1)}{\left(r^2 + (2n+1)^2\right)^{\frac{3}{2}}}. \tag{4-17}$$

Plots of this point spread function, straight-line point spread, and a unit Gaussian spread (σ = one detector thickness) are shown in Figures 4.5 and 4.6. These profiles are slices through the center of the radially symmetric point spread functions. The logarithmic plot in Figure 4.6 shows an apparently exponential decay in the diffusion equation solution, with the Gaussian and straight-line models differing by orders of magnitude. Actually, since the radius of the diffusion front from a point source changes with distance, there is a slight curvature to this falloff; the decay is slightly faster closer to the point source due to the higher curvature of the diffusion front. Between one and two thicknesses from the center, this function is approximated by an exponential decay of $e^{-1.81|r|}$. From two to three it falls as $e^{-1.76|r|}$, and from three to four, it falls off as $e^{-1.7|r|}$. As radius increases, this decay approaches that of the line spread function covered in the next section.
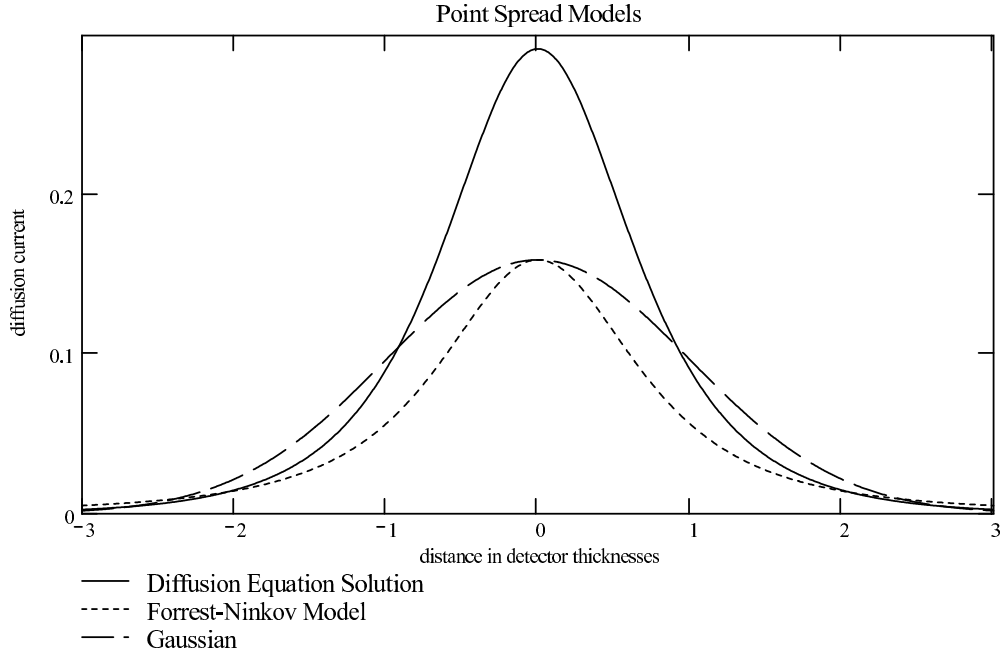
Figure 4.5: A comparison of point spread for straight-line (Forrest-Ninkov), Gaussian, and diffusion equation models. The areas under the curves are unequal, but their volume integrals over a 2D area are equal.

The PSF is a probability distribution. The mean diffusion radius is expressed by

$$E\left[r\right] = \int\limits_{\theta=0}^{2\pi} \int\limits_{r=0}^{\infty} rPSF\left(r\right) r dr d\theta. \tag{4-18}$$

This expression does not evaluate properly for the individual terms used to create the PSF summation, but performing the integration numerically yields a mean diffusion radius (in units of the detector thickness) of

$$E\left[r\right] = 1.166. \tag{4-19}$$

The variance of the PSF can be computed by taking the expectation on the diffusion radius r,

$$E\left[r^2\right] = \int\limits_{\theta=0}^{2\pi} \int\limits_{r=0}^{\infty} r^2 PSF\left(r\right) r dr d\theta. \qquad (4\text{-}20)$$

Performing this integration numerically yields a diffusion variance of

$$E\left[r^2\right] = E\left[x^2 + y^2\right] = 2. \qquad (4\text{-}21)$$

so the RMS diffusion radius from a point source is equal to $\sqrt{2}$ times the detector thickness. Since variances add when the sources are uncorrelated,

$$E\left[x^2 + y^2\right] = E\left[x^2\right] + E\left[y^2\right]. \qquad (4\text{-}22)$$

and the x and y standard deviations are both equal to 1 detector thickness — making the unit Gaussian a relevant comparison.

4.5 Line Spread Function

An analytical expression for the line spread function (LSF) can be derived from the PSF in Equation 4-15. The LSF is the Abel[56] transform of the PSF. This is simply Equation 4-15 integrated along the y axis:

$$LSF\left(x\right) = \int\limits_{-\infty}^{\infty} \frac{1}{\pi} \sum_{n=0}^{\infty} -1^n \frac{(2n+1)}{\left(x^2 + y^2 + (2n+1)^2\right)^{\frac{3}{2}}} dy. \qquad (4\text{-}23)$$

Exchanging the summation and integration results in

$$LSF\left(x\right) = \frac{1}{\pi} \sum_{n=0}^{\infty} \left(-1^n \int\limits_{-\infty}^{\infty} \frac{(2n+1)}{\left(x^2 + y^2 + (2n+1)^2\right)^{\frac{3}{2}}} dy\right). \qquad (4\text{-}24)$$

and performing the integration yields

$$LSF\left(x\right) = \frac{2}{\pi} \sum_{n=0}^{\infty} -1^n \frac{(2n+1)}{x^2 + (2n+1)^2}. \qquad (4\text{-}25)$$
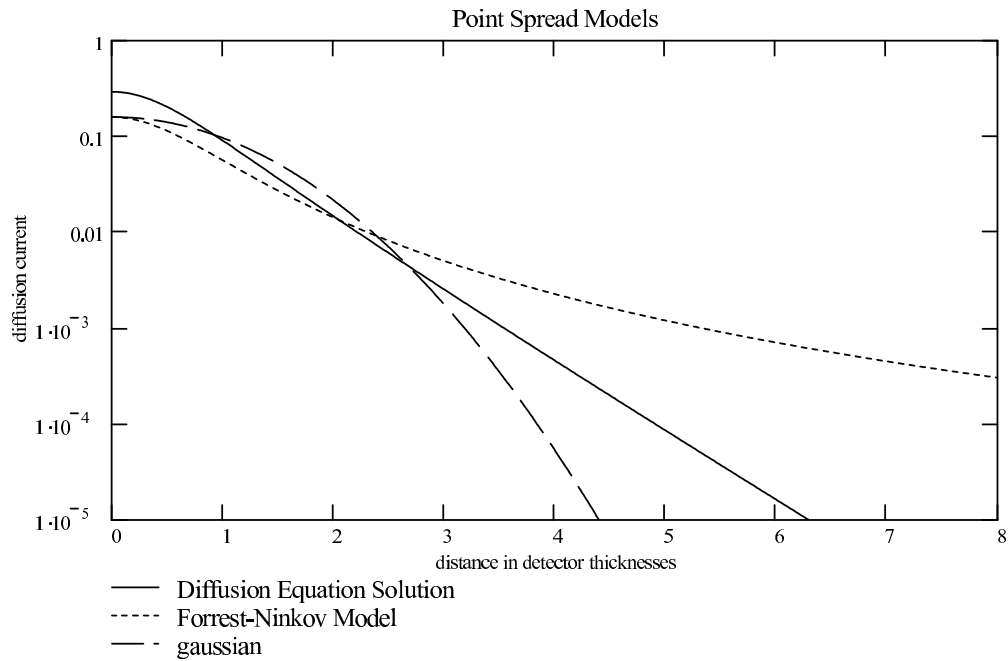
Figure 4.6: Viewing the point spread models with a logarithmic vertical scale reveals exponential decay in the tails of the diffusion equation model. The Gaussian and "straight line" (Forrest-Ninkov) models diverge from this model — in opposite directions.

This expression, simpler than the point spread expression, can be arrived at more directly as an infinite summation of line sources. Figures 4.7 and 4.8 compare this function with Gaussian LSF and straight-line LSF. Differences in the tails of this distribution are much more apparent.

The LSF peaks with a central value of 0.5. For lateral diffusion distances greater than one or two thicknesses, the exponential decay of the line spread function is well approximated by the expression

$$LSF(x) = \exp\left(-\frac{\pi}{2}|x|\right). \tag{4-26}$$
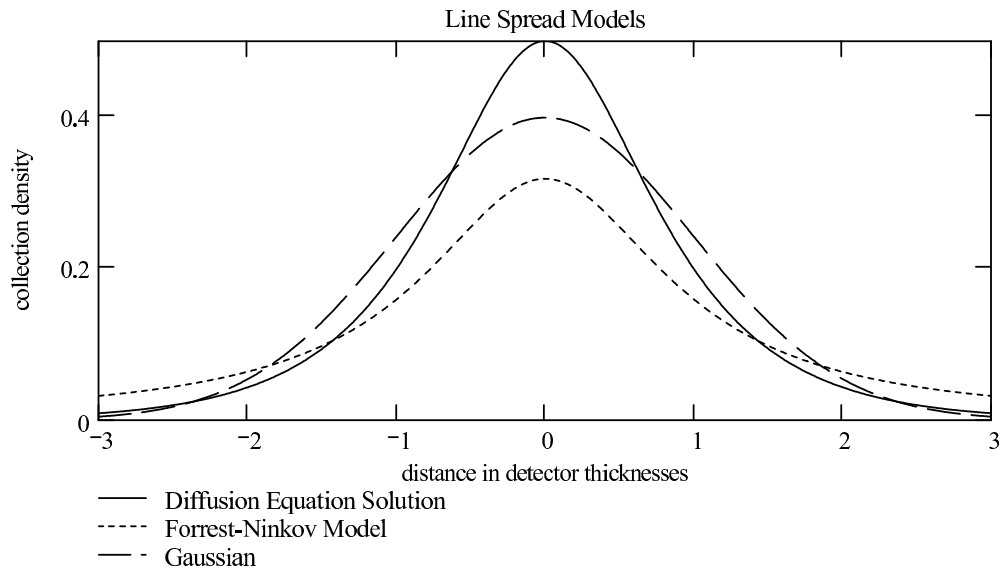
Line Spread Models

Figure 4.7: The line spread produced by the diffusion models is the "Abel" transform of the point spreads. The areas under these curves are all equal.

which is the exact expression in the "far field." Taking the variance of the line spread function numerically yields

$$E\left[x^2\right] = \int\limits_{x=-\infty}^{\infty} x^2 LSF\left(x\right) = 1. \tag{4-27}$$

which agrees with Equation 4-22.

Thus, the RMS line spread is one detector thickness, an interesting result.

At this point, it is also interesting to note that the x and y locations of collection by diffusion are uncorrelated but they are not statistically independent. (They are in a Gaussian spread.) The point spread function would need to be separable in x and y for the x and y coordinates to be statistically independent.

62

Line Spread Models

— Diffusion Equation Solution
---- Forrest-Ninkov Model
— - Gaussian
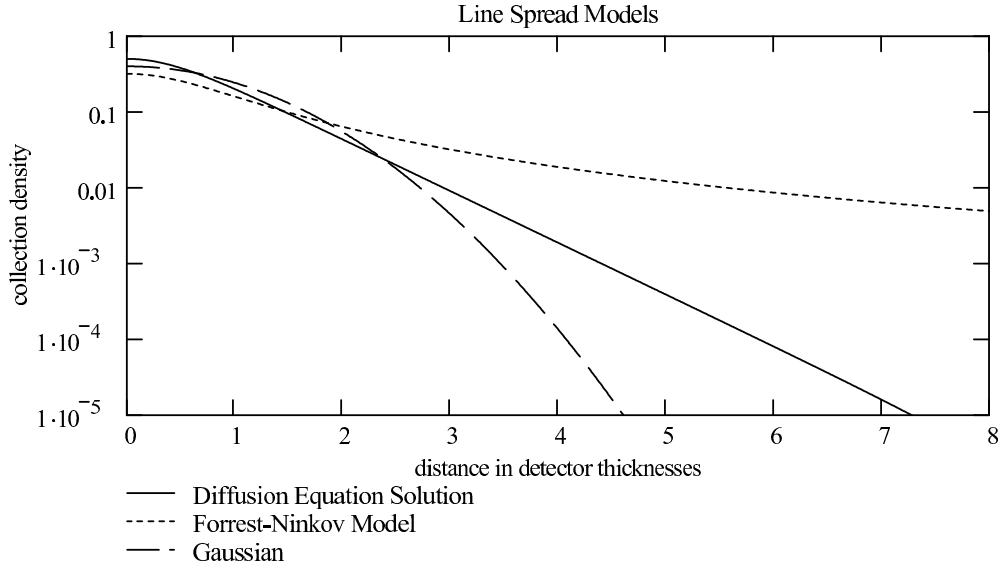
Figure 4.8: Line spread, viewed on a logarithmic vertical scale, reveals exponential decay in the diffusion equation model, and divergence from this in opposite directions in the other two models.

4.6   Far-field LSF Decay

A thickness or two away from the line source collection density decays purely exponentially. In this "far field," the carrier density is a separable function of x and z given by

$$\rho\left(x, z\right) = \exp\left(-\frac{\pi}{2}x\right)\cos\left(\frac{\pi}{2}z\right). \qquad (4\text{-}28)$$

where x is distance across the detector and z is vertical distance in the detector thickness. The z coordinate is zero at the back surface of the detector and one at the depletion edge.

This result can be obtained by assuming carrier density is separable in x and z:

$$\rho\left(x, z\right) = \rho_o f_x\left(x\right) f_z\left(z\right). \qquad (4\text{-}29)$$

Assuming Equation 4-26 for the x dependency and neglecting ρ_o yields

$$\rho\left(x, z\right) = \exp\left(-\frac{\pi}{2}x\right) f_z\left(z\right). \qquad (4\text{-}30)$$

setting the Laplacian of this equal to zero gives

$$f_z(z) \frac{\partial^2}{\partial x^2} \exp\left(-\frac{\pi}{2}x\right) + \exp\left(-\frac{\pi}{2}x\right) \frac{\partial^2}{\partial z^2} f_z(z) = 0. \tag{4-31}$$

which results in

$$f_z(z) \frac{\pi^2}{4} \exp\left(-\frac{\pi}{2}x\right) + \exp\left(-\frac{\pi}{2}x\right) \frac{d^2}{dz^2} f_z(z) = 0. \tag{4-32}$$

and simplifies to

$$f_z(z) \frac{\pi^2}{4} + \frac{d^2}{dz^2} f_z(z) = 0. \tag{4-33}$$

The solution to this equation that satisfies a zero density at $z = 1$ is

$$f_z(z) = \cos\left(\frac{\pi}{2}z\right). \tag{4-34}$$

so the overall solution, Equation 4-28, is obtained. Taking the negative gradient of Equation 4-28 results in a current density of

$$-\nabla \rho(x, z) = \mathbf{J}(x, z) = \rho_o \frac{\pi}{2} \exp\left(-\frac{\pi}{2}x\right) \left(\cos\left(\frac{\pi}{2}z\right) \hat{\mathbf{x}} + \sin\left(\frac{\pi}{2}z\right) \hat{\mathbf{z}}\right). \tag{4-35}$$

which says that the current density is somewhat separable as well. The strength is a function of x only and the direction is a function of z only. The direction rotates linearly with depth, from parallel at the detector surface to normal at the depletion boundary. The direction vectors are plotted in Figure 4.9.

4.7 Edge Spread Function

Edge spread is a common MTF analysis technique. Sharp edges are common optical artifacts, with more optical energy than point or line sources. It is very useful to have an expected edge spread to compare with an observed edge spread. The edge spread function

Diffusion Current Direction Vectors, Far Field
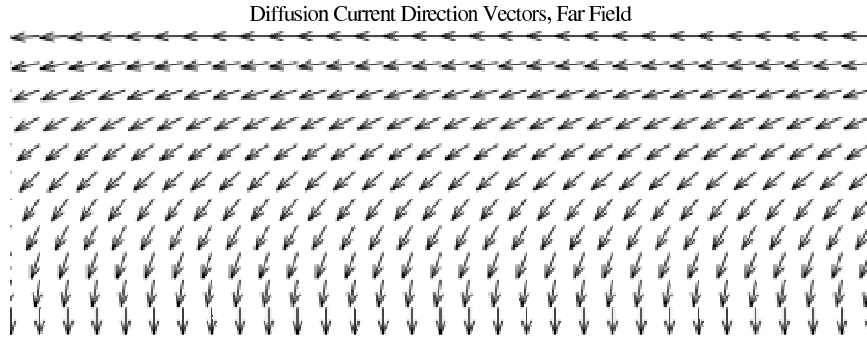
Figure 4.9: In the "tails", or "far-field" (exponential decay region) of the diffusion equation model, diffusion strength decays exponentially in the lateral direction, and diffusion direction is a "complex exponential" (rotates linearly with depth.)

(ESF) is the integral of the line spread. Integrating Equation 4-25 with respect to x results in

$$ESF\left(x\right) = \int_{-\infty}^{x} \frac{2}{\pi} \sum_{n=0}^{\infty} -1^{n} \frac{(2n+1)}{\xi^{2} + (2n+1)^{2}} d\xi.$$ (4-36)

which, after moving the integration inside —

$$ESF\left(x\right) = \frac{2}{\pi} \sum_{n=0}^{\infty} -1^{n} \int_{-\infty}^{x} \frac{(2n+1)}{\xi^{2} + (2n+1)^{2}} d\xi.$$ (4-37)

and evaluating —

$$ESF\left(x\right) = \frac{1}{2} + \frac{2}{\pi} \sum_{n=0}^{\infty} -1^{n} tan^{-1} \left(\frac{x}{(2n+1)} \right).$$ (4-38)

yields an expression of edge spread which increases monotonically from 0 to 1.

This new expression is yet simpler and the differences with "straight line" predicted edge spread are even more apparent. A plot of both edge spread models is shown in Figure 4.10, along with edge spread of a unit Gaussian PSF.

65
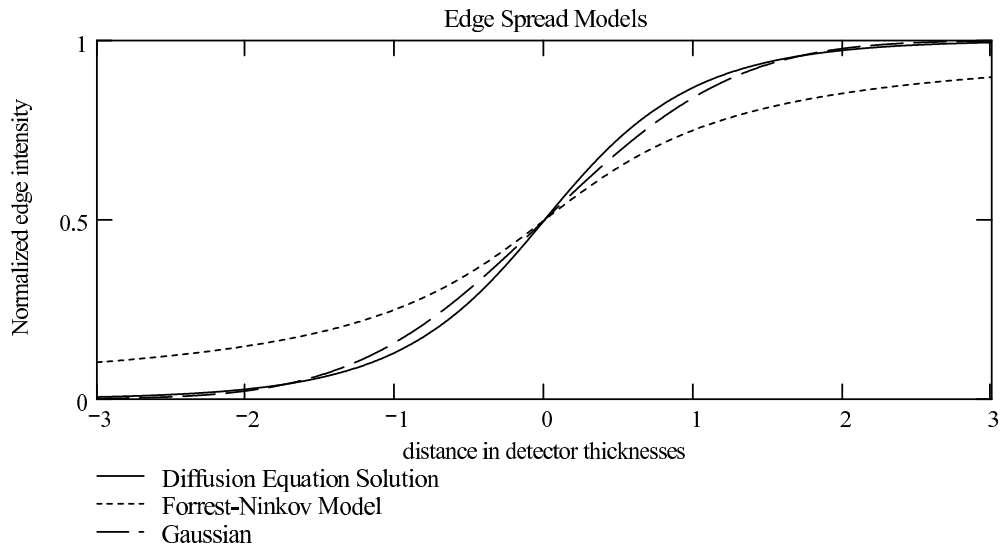
Figure 4.10: Edge spread predicted by the three models. Diffusion theory predicts a much sharper edge than the "straight line"(Forrest-Ninkov) diffusion model.

4.8 Theoretical MTF

The methods used by Crowell and Labuda[45] or Holloway[46] may be used to obtain the MTF, but since the MTF is the normalized magnitude of the Fourier transform of the point spread function, direct term by term transformation is possible. Since the detector point spread is rotationally symmetric, its Fourier transform is also rotationally symmetric. The Hankel transform of the point spread function (expressed as a one dimensional function of radius) yields the Fourier transform of the point spread (*i.e.* MTF, also as a function of radius.) As an alternative to the Hankel transform, the Abel transform of the PSF (the line spread) may be taken, followed by the Fourier Transform. This section takes both approaches to the same conclusion. Taking the Fourier Transform of Equation 4-25, while making use of the transform pair

$$\frac{2}{1 + (2\pi x)^2} \quad \underset{\mathcal{F}}{\Leftrightarrow} \quad e^{-|\xi|} \tag{4-39}$$

and the scaling property of the Fourier transform, yields the transform pair

$$\frac{2}{\pi} \sum_{n=0}^{\infty} -1^n \frac{(1 + 2n)}{x^2 + (1 + 2n)^2} \quad \underset{\mathcal{F}}{\Leftrightarrow} \quad 2 \sum_{n=0}^{\infty} (-1)^n \, e^{-|2\pi(2n+1)\xi|}. \tag{4-40}$$

The same result can be obtained from the Hankel transform of the point spread function of Equation 4-15, using the relationship

$$\frac{1}{(1 + r^2)^{\frac{3}{2}}} \quad \underset{\mathcal{H}}{\Leftrightarrow} \quad 2\pi e^{-2\pi\xi} \tag{4-41}$$

and the Hankel scaling property, to obtain

$$\frac{1}{\pi} \sum_{n=0}^{\infty} -1^n \frac{(2n + 1)}{\left(r^2 + (2n + 1)^2\right)^{\frac{3}{2}}} \quad \underset{\mathcal{H}}{\Leftrightarrow} \quad 2 \sum_{n=0}^{\infty} (-1)^n \, e^{-2\pi(2n+1)\xi} \tag{4-42}$$

This summation does not converge at $\xi = 0$, but MTF at zero frequency is unity by definition.

Further simplification of this expression can be accomplished,

$$2 \sum_{n=0}^{\infty} (-1)^n \, e^{-2\pi(2n+1)\xi} = 2e^{-2\pi\xi} \sum_{n=0}^{\infty} \left(-e^{-4\pi\xi}\right)^n. \tag{4-43}$$

and since

$$\sum_{n=0}^{\infty} \alpha^n = \frac{1}{1 - \alpha}. \tag{4-44}$$

the summation evaluates to the expression

$$MTF(\xi) = \frac{2e^{-2\pi\xi}}{1 + e^{-4\pi\xi}}. \tag{4-45}$$

4.9 Gaussian and Diffusion Equation Comparison

Fully depleted detectors such as P-I-N arrays approximate Gaussian point spread from diffusion. P-I-N detectors have biased bulk, so photocarriers actively drift towards the
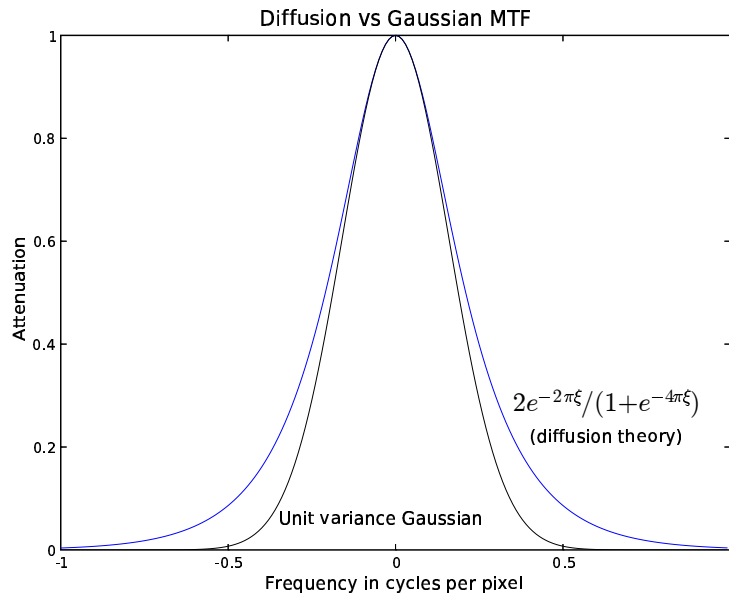
Figure 4.11: At high spatial frequencies, Gaussian diffusion predicts MTF that is significantly poorer than the diffusion equation model. For MTF higher than about 0.8, however, the models are very much in agreement.

detector nodes immediately after generation. The carrier lifetime is consequently fixed, and typically very short — on the order of a few nanoseconds. (This will be shown in Chapter 7.) The mean free time between collisions is on the order of picoseconds so photocarriers make several hundred random collisions while being swept towards the detector node. In the fixed drift lifetime these several hundred random collisions result in a lateral diffusion profile that is (by the law of large numbers) effectively Gaussian.

For the same RMS diffusion radius, which profile is better? The answer is, "it depends." If MTF is the primary concern, the diffusion equation solution has the superior MTF — MTF from diffusion is larger than MTF from Gaussian blur, for the same lateral diffusion variance. This is hinted at in the line spread plots of Figure 4.7. Diffusion has the higher central peak. Putting both into the frequency domain for comparison in Figure 4.11, it can

be sees that diffusion MTF is significantly higher than Gaussian MTF at and around this detector's Nyquist frequency (0.5).

If crosstalk, covered next in more detail, is the primary concern, the Gaussian solution is superior. Gaussian diffusion, seen in fully depleted detectors like the P-I-N, has a significant crosstalk advantage over per-pixel depleted detectors. Given the more rapid decay shown for Gaussian diffusion in many of the figures in this section, is should be apparent it is extremely unlikely that carriers from a cosmic ray event will diffuse laterally far enough to affect many nearby pixels in P-I-N devices.

The question of which profile is "best" is likely academic — it's not a choice; a detector will give one profile or the other. The result is only practical from its enlightenment. Here is a pair of point spreads that occur in real detectors. For equal charge spreading (same RMS lateral diffusion) one exhibits substantially better MTF and the other possesses superior suppression of crosstalk.

Chapter 5

Crosstalk

Crosstalk of a pixel to its neighbor is a common consideration. Brouk *et al.* [57] studied crosstalk in CMOS photodiodes, attributing it to two physical mechanisms, optical and electrical. In their terminology, reflection of photons off surfaces within the detector before absorption is "optical crosstalk" and diffusion of carriers in the substrate before collection is "electrical crosstalk". Shcherback *et al.*[58] measured crosstalk using the spot scanning technique[38, 39, 40, 41]. Crosstalk is often defined (as in Cheung [50] and Holloway [46]) as the ratio of signal in an adjacent detector to signal in the central detector, given a point source in the center of a pixel. In this chapter, this definition is more specifically called "near crosstalk" and will be considered first. This chapter continues with the results of Chapter 4, still assuming infinite carrier lifetime — which gives more crosstalk than finite lifetime.

5.1   Collection within Round and Square Boundaries

Integration of the volume under the PSF of Equation 4-15 outside of a radius r results in the fraction of carriers that successfully diffuse outside of a circular collection area, C_{lost}. The area of each differential ring of radius r is $2\pi r dr$, and $r^2 = x^2 + y^2$. Making these
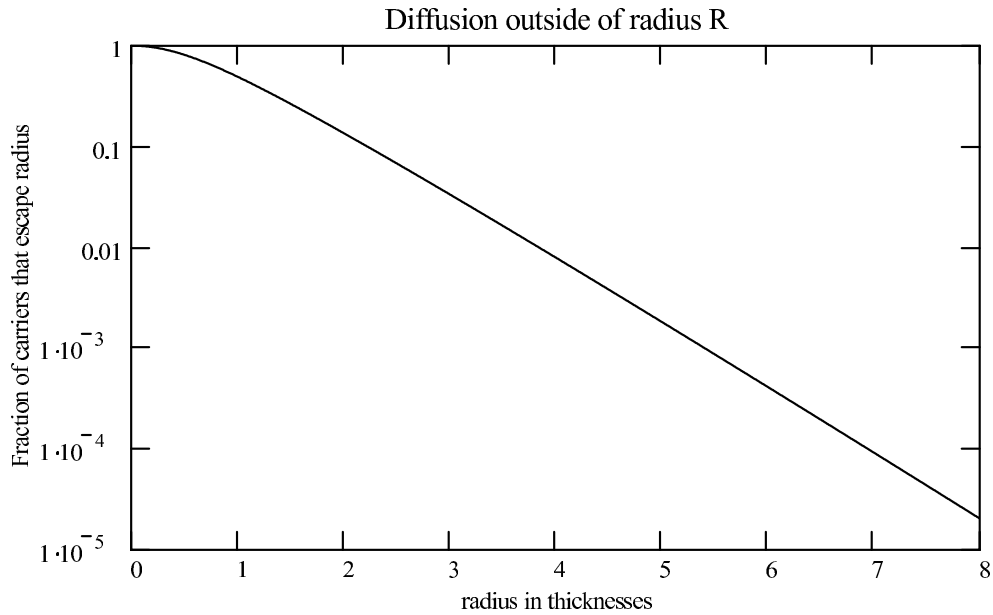
Figure 5.1: Calculating the percentage of carriers that escape a circular boundary shows about 10 percent capture loss from a radius of two thicknesses and less than one percent loss for a radius of four thicknesses. Note that this function is curved at the center but well-approximated by a straight line (exponential decay) approximately one thickness away from the source.

substitutions results in

$$C_{lost}(r) = \frac{1}{\pi} \sum_{n=0}^{\infty} -1^n \int_{\rho=r}^{\infty} \frac{(2n+1)}{\left(\rho^2 + (2n+1)^2\right)^{\frac{3}{2}}} 2\pi \rho \, d\rho. \tag{5-1}$$

and evaluating results in

$$C_{lost}(r) = 2 \sum_{n=0}^{\infty} -1^n \frac{(2n+1)}{\sqrt{r^2 + (2n+1)^2}}. \tag{5-2}$$

Figure 5.1 shows the plot of this expression for lost carriers — the fraction of charge that escapes collection from a point source in the center of a circular area as a function of radius.
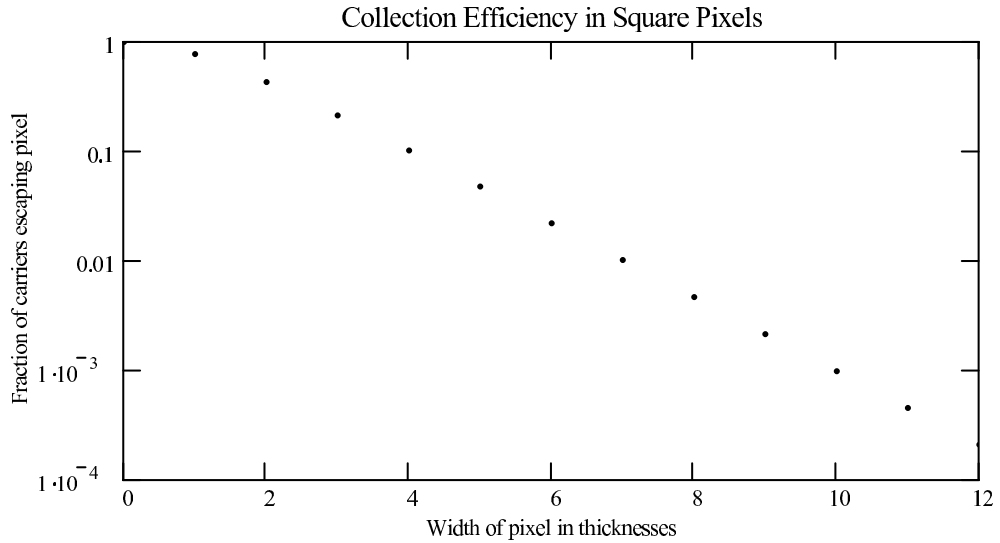
Figure 5.2: Calculating the percentage of carriers that escape a square boundary shows about 10 percent capture loss from a pixel four thicknesses wide and approximately half a percent loss from a pixel eight thicknesses wide.

Pixels are square, however — integrating the PSF of Equation 4-15 over a square area and subtracting it from the original unit charge source yields:

$$C_{lost}(s) = 1 - \frac{1}{\pi} \sum_{n=0}^{\infty} -1^n \int\limits_{x=-w/2}^{w/2} \int\limits_{y=-w/2}^{w/2} \frac{(2n+1)}{\left(x^2 + y^2 + (2n+1)^2\right)^{\frac{3}{2}}} dy dx. \qquad (5\text{-}3)$$

Figure 5.2 shows the plot of Equation 5-3 — the fraction of charge from a point source in the center of a square pixel that escapes collection by that pixel.

5.2 Crosstalk and MTF

The exponential decay characteristic of Equation 4-26 and Equation 4-28 that becomes apparent more than one thickness away from the source (evident in Figures 4.8 and 5.1) is plotted in Figure 5.3 as "far crosstalk", and compared to "near crosstalk" for the same

73
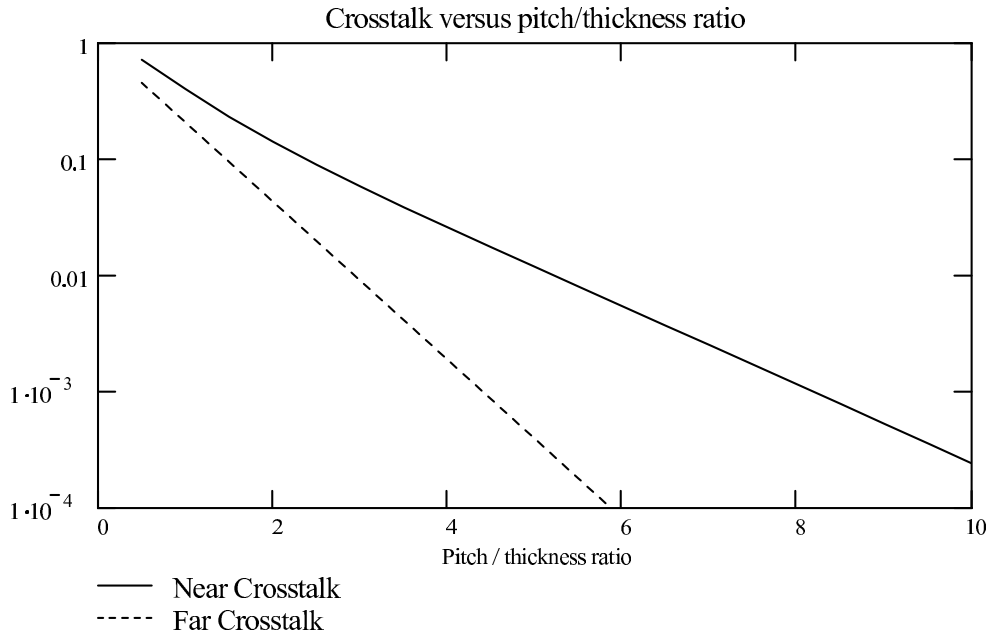
Figure 5.3: "Near crosstalk" (from a point source in the center of an adjacent pixel) and "far crosstalk" (the per-pixel exponential decay rate for a source more than one pixel away) plotted versus the pitch/thickness ratio of the detector.

normalized detector geometry. A comparison of this plot to Figure 5.2 shows that the crosstalk is roughly $\frac{1}{4}$ of the charge lost from a square pixel for reasonably large pixels — most of the charge lost by the center pixel is collected by the four immediate neighbors. At a pitch/thickness ratio of four, crosstalk is a between 2 and 3 percent. This corresponds well with losing 10 percent from a square pixel — roughly 2.5 percent loss to each of four neighbors.

Equation 4-45 plotted in Figure 4.11, is shown in an alternate view in Figure 5.4, plotting MTF at the Nyquist frequency of 1 cycle every two pixels versus the ratio of pixel pitch to detector thickness. This figure shows that thinner detectors (higher pitch to thick-
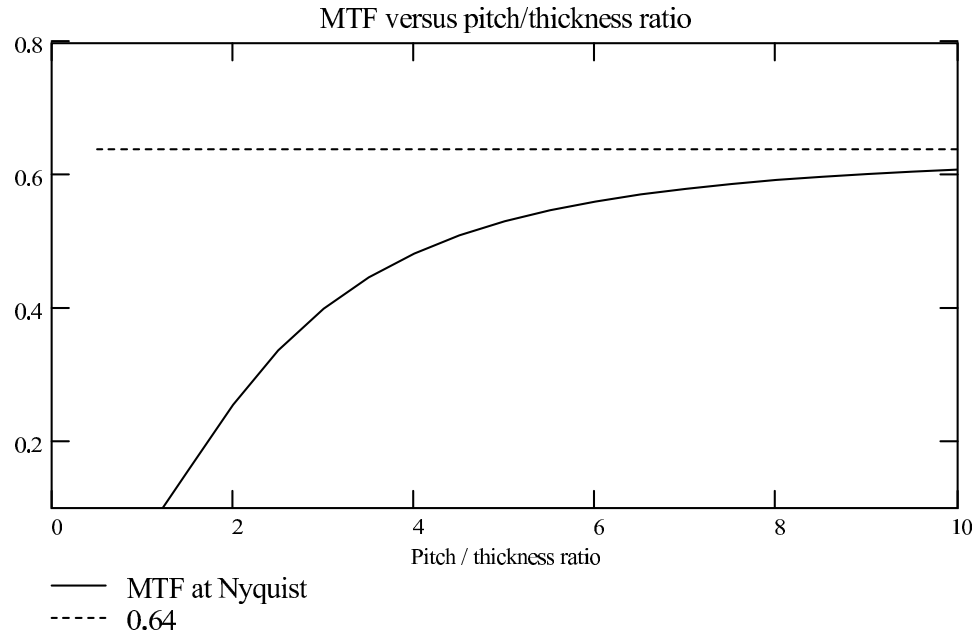
Figure 5.4: MTF at Nyquist versus pitch/thickness ratio. A square pixel yields best-case MTF of
0.64. Diffusion yields the same reduction in MTF as the pixel when the overall MTF is
$0.64^2 = 0.41$ — at a pitch/thickness ratio of approximately 3.

ness ratios) have better MTF at Nyquist. The limiting attenuation of 0.64 associated with a
square pixel and 100% fill factor is included in this plot.

Figure 5.5 relates the MTF in Figure 5.4 to the near and far crosstalk of Figure 5.3. An
expected relationship between crosstalk and MTF at Nyquist, as published in Rauscher's
recommendations for MTF [43] on the James Webb Space Telescope (JWST) and stated in
the JWST MTF specification [59], is included in this plot. The diffusion model's associa-
tion of crosstalk as a function of MTF is one or two orders of magnitude higher than the
JWST relationship, depending upon if near or far crosstalk is chosen for comparison. (The
pure exponential decay model used by Rauscher is arguably "far crosstalk".) This higher
value may stem from misapplication of Fourier analysis. Crosstalk is a spatial domain

quantity of very low energy. If the problem is put in the frequency domain and *any* approximations are made, large errors may result after transforming back to the spatial domain. Rauscher's analysis modeled detector response as exponential decay, but the exponential approximation (accurate in the "far field") is very poor near the central peak of the point spread function — where most of the energy is. (The uniformity at the peak comes into play here. If a hypothetical detector substrate diffused a point source uniformly with a pixel-shaped point spread function, MTF at Nyquist would be $0.64^2 = 0.41$, but there would still be zero "near" crosstalk.)

Cheung's crosstalk analysis[50] bears a similar error. However, Cheung's paper approximates a Gaussian (not an exponential) to the Crowell-Labuda frequency domain model, then (since the fit appears quite convincing) mistakenly concludes that the spatial domain response is similarly Gaussian, rather than the decidedly non-Gaussian actual profile shown in Figure 4.6.

5.3   Neglected effects in the diffusion model

This model has neglected several effects. Surface recombination velocity, carrier lifetime due to bulk recombination, gaps between pixels, and photon penetration depth have all been neglected. Simulations performed in Appendix B address some of these issues. Some observations about these factors are appropriate here. Surface recombination will, in the tails of the diffusion, act very much like the depletion region; its net effect here will be to capture carriers as they diffuse laterally. This should increase the decay of carriers — having the same effect as making the detector "thinner". Gaps between the pixels will have the opposite effect. If no surface recombination occurs between pixels, the gaps decrease the likelihood of capture by the nearest pixel, and make the detector effectively "thicker". Deep implants with a channel between pixels will reduce this "thickening" effect some-
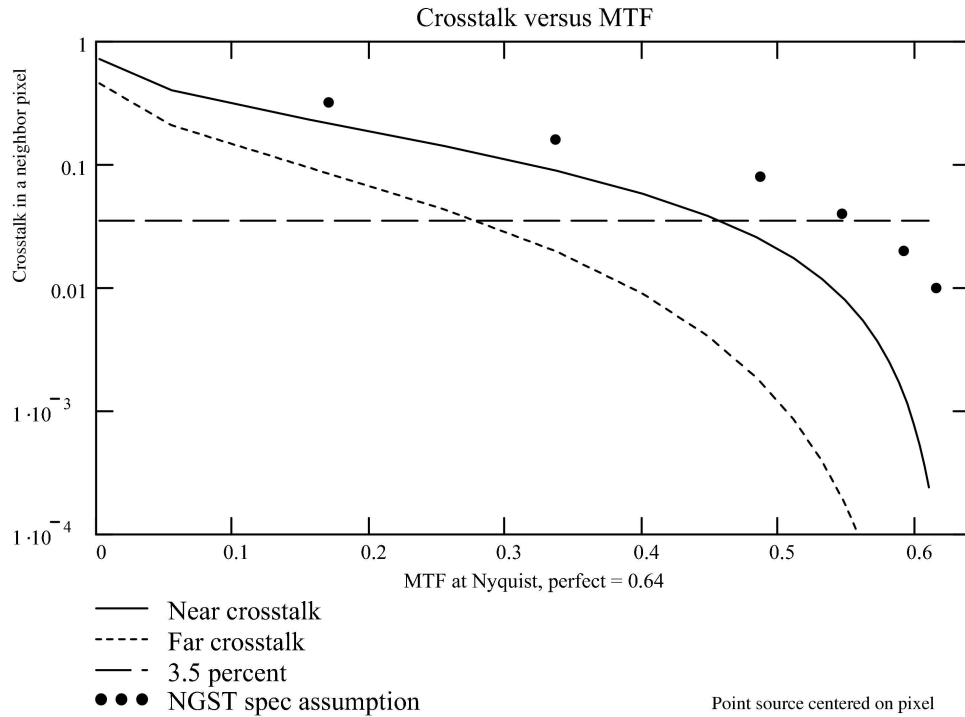
Figure 5.5: Relation between crosstalk and MTF — For a given MTF, the diffusion equation model predicts much less crosstalk than the JWST specification predicts. This error becomes more significant at higher MTF.

what. Extending the result of Equation 4-28 to deep gaps is straightforward. It indicates that a gap as deep as it is wide is, from this point of view, "infinitely deep." Carrier density in a channel that collects on both sides decays exponentially by $e^{-\pi}$, or to about 4.3 percent of its original value, for a distance down the channel equal to the channel width.

If bulk recombination[60] causes the carriers to attenuate with a coefficient $\alpha = 1/L$ where L is the diffusion length, the solution without any boundary conditions is[47]:

$$\mathbf{J}\left(\mathbf{r}\right) = \left(\alpha r + 1\right) e^{-\alpha r} \frac{\mathbf{r}}{4\pi r^3} I_o. \tag{5-4}$$

(This expression is not arrived at as easily as Equation 4-9, as the Laplacian in spherical coordinates is a complicated expression.)

Bulk recombination can be accounted for analytically by replacing the expression in Equation 4-9 and all subsequently derived expressions with the known solution of point source diffusion with recombination, Equation 5-4. All of the subsequently derived expressions will still hold from the symmetry arguments. Simulations performed later show this causes the tails to attenuate more rapidly than they already do. The shape of the central region is largely unaffected, but is similarly attenuated as well.

For backside illuminated detectors, deeper penetration of photons simply increases the relative likelihood of capture in the center of the distribution. Eventually, deep penetration decreases quantum efficiency — photons become likely to pass through the entire detector without being absorbed. An integration of the generalized case pictured in Figure 4.2, will result in an expression that accounts for penetration depth. See Holloway, Cheung, and Crowell and Labuda for more elaborate diffusion models that include these effects.

Chapter 6

Inter-pixel Capacitance

Pixels in CMOS detector arrays (both hybridized and monolithic) may couple capacitively to their neighboring pixels while they are being read. In measurements in the literature to date, this phenomenon has been largely ignored. Inter-pixel capacitance can significantly distort the characterization of conversion efficiency in non-destructively read devices. Fortunately, accounting for inter-pixel capacitance is straightforward. The measurement of Poisson noise, traditionally done by finding the mean square difference in a pair of images, simply needs to include the mean square correlation of the differences with their neighboring pixels.

This effect may be observable in CMOS devices, even monolithic CMOS, since the detector node voltages are read directly and non-destructively. Devices that transfer charge and perform a "short time scale" differential read (such as the CCD and CID arrays described in Chapter I) are not likely to exhibit the effect — the coupling, even if present, is likely to affect both parts of the differential read equally.

This chapter treats the imaging array as a discrete linear shift invariant system. In reality, each pixel in an array is slightly different, and many scientific detectors have individual calibrations for each pixel to reflect this. If both coupling and pixel-to-pixel variations are large, per-pixel calibration of the coupling effect may be required. Many of the results of

this chapter simply require a linear system, and application to shift-variant arrays should be straightforward.

6.1   Inter-pixel Capacitance Overview

Small amounts of stray capacitance can couple detector nodes to their neighboring pixels. This capacitance is enhanced by the dielectric epoxy injected between the indium bumps of hybridized detectors by the manufacturer. In fully-depleted detectors (i.e. P-I-N arrays), additional capacitive coupling exists in the detector substrate itself. Inter-pixel capacitance can be very prominent in fully depleted detectors, partly due to the higher dielectric constant of the detector substrate and partly due to the low detector capacitance that comes with full depletion.

Inter-pixel capacitance creates two effects. The first and most obvious is crosstalk is generated. A strong signal in one pixel will create a weak signal in neighboring pixels. This observed crosstalk may easily be mistaken for diffusion. A second effect is that the signal appearing in neighboring pixels is signal that "would have" appeared in the originating pixel had there been no inter-pixel capacitance. The signal in the originating node is attenuated. This attenuation may also be mistaken for attenuation resulting from diffusion.

Crosstalk from the diffusion process and crosstalk resulting from the capacitive coupling are from different mechanisms, and have different properties. Crosstalk from diffusion is a "pre-sampling" phenomenon, and Poisson noise from diffusion crosstalk is completely uncorrelated in neighboring pixels. Crosstalk from inter-pixel capacitance is a "post-sampling" phenomenon, and Poisson noise from inter-pixel capacitive crosstalk in neighboring pixels is correlated.

The presence of inter-pixel capacitance in detector arrays was anticipated in simulations performed by Kavadias *et al.* circa 1993.[61] Caccia *et al.*[62, 63] measured inter-pixel

coupling in a hybrid "Vertex" detector for a particle collider in 2000. Moore *et al.* [64] first suggested that inter-pixel capacitance can create significant errors in the "noise squared versus signal" method of estimating nodal capacitance[65], and presented data supporting this suggestion. The effects of inter-pixel capacitance and the mechanisms which cause them were investigated in more detail in a second paper[66]. Inter-pixel capacitance causes Poisson noise in a device to appear lower than it actually is. As a result, the responsive quantum efficiency (RQE) is *overestimated* — the detector array appears to be collecting more photons than it actually is. For scientific detector arrays in low-signal applications such as space telescopes, the RQE of the array is the "bottom line" of its information-gathering ability. [1]Arrays with poor RQE take longer to accumulate the same information, and are proportionally that much more "expensive" to operate in order to make the same scientific discoveries. Crosstalk of 1% or more to neighboring pixels, observable in either hot pixels or cosmic events, may be a warning sign that actual RQE is *significantly poorer* than reported RQE determined from noise squared versus signal methods — A crosstalk of 1% from inter-pixel coupling results in an 8% error in RQE measurement.[2]

Inter-pixel capacitance is expected to become more significant with modern arrays. Photo-detector array designers strive for many simultaneous qualities in their devices. High pixel density requires small distances between pixel centers. High quantum efficiency and low latent images suggests 100% fill factor and thus small gaps between pixel implants. High sensitivity requires low capacitance multiplexer nodes. As designs move towards these goals, the stray capacitance to neighboring pixels will be more pronounced. Stray capacitance to a detector node results from the presence of conductors adjacent to the detector

---

[1]Good RQE is necessary — but not sufficient — for good performance. "DQE" (detective quantum efficiency, covered later) is a truer measure — but DQE can never be better than RQE.

[2]Some measures of DQE can be affected by the noise attenuation caused by coupling and exhibit similar overestimation.
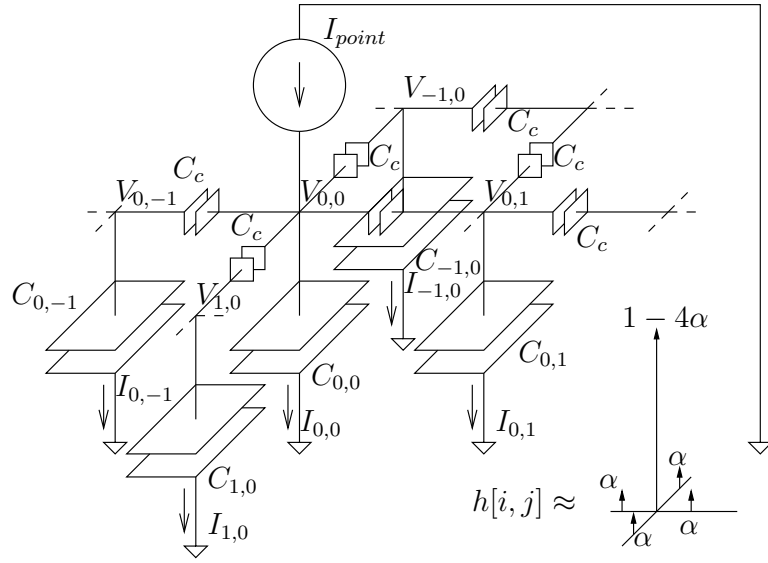
Figure 6.1: Photocurrent physically entering a detector node may leave the node as displacement current through small coupling capacitors (labeled C_c) and appear on adjacent nodes instead. Even if all quanta are captured by the central pixel with node capacitance C_{00}, signal still appears on neighboring nodes that have captured no quanta.

node. Detector nodes *must* be conductive to accumulate charge. Thus, the nearest conductors adjacent to the pixels in the lowest capacitance detector arrays will be the neighboring pixels.

6.2   Basic mechanism

A photo-detector array is modeled here as an array of capacitors $C[i,j]$, each receiving a signal $Q[i,j]$, the accumulated photo-current *entering* node i,j over some integration time t. Considering input signals that do not change over the integration time,

$$Q[i,j] = \int_{t}^{t+\Delta t} I[i,j](\tau)\, d\tau \approx I[i,j]\, \Delta t. \tag{6-1}$$

All capacitors $C[i,j]$ are assumed equal by fabrication so $C[i,j] = C_{node}$. The array is modeled as a discrete linear shift-invariant [31] (LSI) system, outputting an array of voltages:

$$V[i,j] = \sum_{m=-\infty}^{\infty} \sum_{n=-\infty}^{\infty} Q[i,j] h_c[i-m, j-n]. \qquad (6\text{-}2)$$

or, more simply:

$$V[i,j] = Q[i,j] * h_c[i,j]. \qquad (6\text{-}3)$$

where $*$ is the 2D convolution operator and $h_c[i,j]$ is the impulse response of the collection array.

Ideally,

$$h_c[i,j] = \frac{\delta[i,j]}{C_{node}}. \qquad (6\text{-}4)$$

where $\delta[i,j]$ is the discrete 2D "unit impulse" or "delta function". The ideal output of the array is simply a voltage $V[i,j]$ such that

$$V[i,j] = \frac{Q[i,j]}{C_{node}}. \qquad (6\text{-}5)$$

Equation 6-5, although very simple, has been the nodal electrical model to date. Inter-pixel capacitance models a new "electrical crosstalk" mechanism.

Upon introducing small coupling capacitors C_c between detector nodes, as shown in Figure 6.1, photo-current into a single detector node returns via multiple paths. From Kirchoff's current law, the total charge entering the node (equivalent to the photo-current at the top of Figure 6.1) is equal to the total charge appearing electrically on that node and its neighbors:

$$Q_{point} = I_{point}\Delta t = \sum_{i,j} I_{i,j}\Delta t = \sum_{i,j} A[i,j]. \qquad (6\text{-}6)$$

where $I_{i,j}$ is the current through $C[i,j]$ and $A[i,j]$ is the *apparent* charge appearing electrically on that node.

Thus,

$$\sum_{i,j} V[i,j] = \sum_{i,j} \frac{A[i,j]}{C_{node}} = \frac{Q_{point}}{C_{node}}. \tag{6-7}$$

and the photo-carriers collected in a single node appear upon readout to be distributed into several nodes, but only the nodal capacitance C_{node} appears in the "DC" output of the detector array. The impulse response of the detector nodes is

$$h_c[i,j] = \frac{A[i,j]}{Q_{point}C_{node}}. \tag{6-8}$$

At this point, it is convenient to normalize by the nodal capacitance C_{node} and express the impulse response as a deviation from ideal response — the ratio of apparent charge A to actual collected charge Q. Thus,

$$h[i,j] = h_c[i,j]\,C_{node} = \frac{A[i,j]}{Q_{point}}. \tag{6-9}$$

and

$$\sum_{i,j} h[i,j] = 1. \tag{6-10}$$

Since inter-pixel capacitance pulls the voltages of neighboring nodes in the same direction,

$$h[i,j] \geq 0. \tag{6-11}$$

Also, the circuit is passive and cannot create an output greater than its input. Thus:

$$h[i,j] \leq 1. \tag{6-12}$$

Symmetry is a direct consequence of the array of identical pixels. [3]

$$h[i,j] = h[-i,-j]. \tag{6-13}$$

---

[3]If this approximation is not valid, a per-pixel calibration may be performed.

Photo-current arrives in detector nodes quantized by the charge of an electron. Photon arrival and diffusion in the detector are both stochastic processes, and without correlation mechanisms in photon arrival, carrier generation and diffusion, the individual collection events are statistically independent and obey Poisson statistics. Thus, charge collected by detector nodes may be expressed as a mean signal component $M[i, j]$ plus a "white" noise image $N[i, j]$

$$Q[i, j] = M[i, j] + N[i, j].$$ (6-14)

The white noise image has a uniform spatial power spectral density S_N—

$$
\begin{aligned}
S_N(\xi, \eta) &= \lim_{T \to \infty} \frac{E\left\{|\mathcal{F}\{N[i, j]\}|^2\right\}}{2T} \\
&= \lim_{T \to \infty} \frac{E\left\{|F_N(\xi, \eta)|^2\right\}}{2T} \\
&= \sigma_N^2.
\end{aligned}
$$ (6-15)

where $E\{\}$ is the expectation operator, $\mathcal{F}\{\}$ is the Fourier transform operator resulting in $F_N(\xi, \eta)$, and ξ and η are spatial frequency (in x and y) expressed in cycles per pixel. The inter-pixel capacitive impulse response $h[i, j]$ causes apparent charge to be a spatially filtered version of the actual charge. The observed output is:

$$A[i, j] = (M[i, j] + N[i, j]) * h[i, j].$$ (6-16)

In the absence of an internal gain mechanism in the detector itself, i.e., assuming one electron per photon, the variance of the noise image is equal (in quanta) to the mean signal M:

$$\sigma_M^2[i, j] = M[i, j].$$ (6-17)

The difference $D[i, j]$ of a pair of otherwise identically acquired images A_1 and A_2 cancels out the signal component and leaves a noise image that is twice the variance of the

original images' noise components.

$$D\left[i,j\right] = A_1\left[i,j\right] - A_2\left[i,j\right] = \left(N_1\left[i,j\right] - N_2\left[i,j\right]\right) * h\left[i,j\right]. \qquad (6\text{-}18)$$

The noise energy in this difference image is typically compared to the mean of the images to obtain an estimate of the conversion factor (e^-/Volt). Uniform illumination $M\left[i,j\right] = M$ is typically used but is not required and has not been assumed. Assuming the noise difference image is stationary, (this covers random spatial variations in illumination and detector efficiency) the power spectral density of the noise image in Equation 6-18 is

$$S_D\left(\xi,\eta\right) \;=\; 2\sigma_N^2 |H\left(\xi,\eta\right)|^2 = 2\sigma_N^2 H\left(\xi,\eta\right) H^*\left(\xi,\eta\right). \qquad (6\text{-}19)$$

Thus, the power spectral density of the observed difference image yields significant information about the inter-pixel capacitive effect. Since the input signal (the noise on the charge collected by the nodes) is white (a constant) the output power spectrum is proportional to the squared magnitude of the Fourier transform of the impulse response.

Direct measurement of the power spectra[67] of random processes by averaging spectra from samples is generally discouraged; autocorrelation techniques are preferred. The Weiner-Khinchine relation in two dimensions

$$S\left(\xi,\eta\right) = \sum_{x,y} R\left[x,y\right] e^{-j2\pi\xi x} e^{-j2\pi\eta y} = \mathcal{F}\left\{R\left[x,y\right]\right\}. \qquad (6\text{-}20)$$

expresses the power spectral density of a 2D random process in terms of its autocorrelation function. The power spectral density of a 2D stationary random process $S\left(\xi,\eta\right)$ is obtained by measuring its autocorrelation function $R\left[x,y\right]$, then taking the Fourier transform of that.

Combining Equations 6-19 and 6-20 results in:

$$\mathcal{F}\left\{R_D\left[x,y\right]\right\} = 2\sigma_N^2 H\left(\xi,\eta\right) H^*\left(\xi,\eta\right). \qquad (6\text{-}21)$$

or, equivalently:

$$\mathcal{F}\left\{R_D\left[x,y\right]\right\} = 2\sigma_N^2 \mathcal{F}\left\{h\left[x,y\right] * h\left[-x,-y\right]\right\}. \tag{6-22}$$

Taking the inverse Fourier transform of Equation 6-22 yields

$$R_D\left[x,y\right] = 2\sigma_N^2 h\left[x,y\right] * h\left[-x,-y\right]. \tag{6-23}$$

and the normalized autocorrelation is equal to the convolution of the impulse response with itself.

Since the impulse response $h\left[x,y\right]$ has unit area, its convolution with itself does also, and the summation of Equation 6-23 results in:

$$\sum_{x,y} R_D\left[x,y\right] = 2\sigma_N^2. \tag{6-24}$$

Equation 6-24 is the key result, and should be used to estimate "noise squared" in lieu of the traditionally applied variance estimator

$$\widehat{R}_D\left[0,0\right] = \widehat{2\sigma_N^2} = \widehat{D^2} = \frac{\sum\limits_{i,j} D^2\left[i,j\right]}{N-1}. \tag{6-25}$$

which does not account for inter-pixel coupling.

Since (Equations 6-11 and 6-13) $h\left[x,y\right]$ is non-negative and even, no phase information is present and Equation 6-21 or Equation 6-22 can be expressed as

$$\mathcal{F}\left\{R_D\left[x,y\right]\right\} = 2\sigma_N^2 \left(\mathcal{F}\left\{h\left[x,y\right]\right\}\right)^2. \tag{6-26}$$

Taking the square root of Equation 6-26 (this can also be done here since $h\left[x,y\right]$ and $H\left(\xi,\eta\right)$ are both non-negative and even) and then taking the inverse Fourier transform results in

$$\mathcal{F}^{-1}\left\{\mathcal{F}\left\{R_D\left[x,y\right]\right\}^{\frac{1}{2}}\right\} = \sqrt{2}\sigma_N h\left[x,y\right]. \tag{6-27}$$

This is a direct expression which may be used to obtain the impulse response of inter-pixel capacitance from the autocorrelation of the shot noise in a difference image.

The total power of the output power spectral density in Equation 6-19 is the mean square output, and by Parseval's relation, is:

$$
\begin{aligned}
\overline{D^2} &= R_D\,[0,0] \\
&= 2\sigma_N^2 \sum_{\xi,\eta} \left[H\,(\xi,\eta)\,H^*\,(\xi,\eta) \right] \\
&= 2\sigma_N^2 \sum_{x,y} h^2\,[x,y].
\end{aligned}
\tag{6-28}
$$

Thus, the sum of the squares of the impulse response is the attenuation of the white input noise caused by inter-pixel capacitance. From Equations 6-10, 6-11, and 6-12, this is indeed attenuation — always less than one if there is any coupling.

6.3 Measurement of correlation

Lifting the correlation out of the noise images takes a lot of averaging. For a uniform strength of μ quanta, the variance of the incoming Poisson noise is μ quanta squared. It is assumed here that μ is large enough that a Gaussian approximation is appropriate. A difference image will have a variance 2μ quanta squared of noise, but zero mean. The variance of the product of any uncorrelated pair x, y of these noise values is equal to:

$$
\begin{aligned}
\mathrm{E}\left[(xy)^2 \right] &= \mathrm{E}\left[x^2 y^2 \right] \\
&= \mathrm{E}\left[x^2 \right] \mathrm{E}\left[y^2 \right] \\
&= 4\mu^2.
\end{aligned}
\tag{6-29}
$$

which is a variance (in quanta to the fourth power) that is the square of the mean variance in the difference image itself.

If the pair x, y is completely correlated, this variance is doubled. In addition, the mean is non-zero and the distribution is not Gaussian.

$$\begin{aligned} E\left[(x^2)^2\right] - E^2\left[x^2\right] = & \ E\left[x^4\right] - 4\mu^2 \\ = & \ 3E^2\left[x^2\right] - 4\mu^2 \\ = & \ 8\mu^2. \end{aligned} \qquad (6\text{-}30)$$

If accurately measured cross-correlation of some fraction α of the photon noise is desired, N averages are required such that the standard deviation of the cross-correlation estimator is less than some small fraction of the mean square pixel noise in a difference image:

$$\frac{2\mu}{\sqrt{N}} \ll \alpha 2\mu. \qquad (6\text{-}31)$$

Dropping the dependency on the signal strength and rearranging yields:

$$N \gg \frac{1}{\alpha^2}. \qquad (6\text{-}32)$$

So, bringing a one percent correlation signal up to the noise level requires averaging 10000 samples. Raising it a factor of ten above the noise requires a million samples.

6.3.1 Approximations

Practically speaking, only correlations to the nearest neighbors need to be considered in most cases. It should be apparent from inspection of the autocorrelation if more (or fewer) terms are required. (Perhaps Equation 6-25 is accurate enough.) For significant but small amounts of inter-pixel coupling, the "second neighbor" coupling is effectively zero. In two dimensions, neglecting "second neighbor" and "diagonal neighbor" coupling, the center node loses 4α of its charge — α to each of its four nearest neighbors. The resulting convolution is shown in Figure 6.2.

The center term of the convolution, $R(0,0)/2\sigma_N^2 = \overline{h^2} \approx (1 - 4\alpha)^2 \approx 1 - 8\alpha$, also expressed in Equation 6-28, is the relative mean square output of the noise compared to what would be measured without any inter-pixel coupling — the factor by which conversion gain is in error when inter-pixel capacitance is significant. The approximation $1 - 8\alpha$ holds for small amounts of coupling, and illustrates the magnitude of error this effect can cause. 1.25% coupling to a neighbor can cause a 10% error in estimated conversion factor. Modern arrays vary widely. Silicon P-I-N arrays tested in this dissertation showed $\alpha \approx 0.0375$ for an error of 30%, but similarly manufactured InSb arrays showed $\alpha \approx 0.005$ for an error of only 4%. Details of these tests are in Chapter 8.

6.4 Inter-pixel Capacitance and DQE

The true measure of a detector array's performance is its detective quantum efficiency, or DQE. DQE, the squared SNR at the output of the array compared to the squared SNR incident at the surface of the array, is a power ratio. It tells how much power is necessary in an imperfect detector to attain the SNR that a perfect detector would get. Zero-frequency DQE may depend upon other conditions, such as signal and background levels and exposure time. Background levels are neglected here — this section just considers the additional DQE loss that occurs at high spatial frequencies, as pioneered by Doerner[68], and built upon by Shaw[69], Van Metter, Rabbani[70, 71], Yao and Cunningham[72], and others. Doerner generalized the definition of DQE for imaging application to include a spatial frequency dependence. Figure 6.3 shows a stochastically generated two dimensional sine wave that may help visualize the signal and noise at high spatial frequencies. Stochastic scattering from diffusion reduces DQE at high spatial frequencies, and in an otherwise perfect detector, DQE is reduced by the square of $T(\xi)$, the scattering MTF[70, 71]:

$$
\begin{array}{c}
\alpha^2 \\
2\alpha^2 \qquad 2\alpha(1-4\alpha) \qquad 2\alpha^2 \\
\alpha^2 \quad 2\alpha(1-4\alpha) \quad (1-4\alpha)^2 + 4\alpha^2 \quad 2\alpha(1-4\alpha) \quad \alpha^2 \\
2\alpha^2 \qquad 2\alpha(1-4\alpha) \qquad 2\alpha^2 \\
\alpha^2
\end{array}
$$

Figure 6.2: The autocorrelation of the 2d impulse response is equal to the expected correlation coefficients R. Neglecting the tiny α^2 terms results in nearest-neighbor correlation coefficients of 2α, leaving $1 - 8\alpha$ in the center.

$$
DQE\left(\xi\right) = \left|T\left(2\pi\xi\right)\right|^2. \tag{6-33}
$$

In fully depleted arrays such as the Si P-I-N device shown in Figure 6.4, stochastic scattering leads to a Gaussian scattering MTF. In detectors with "per-pixel" depletion regions as shown in Figure 6.5, such as the InSb devices treated later, the MTF (from Equation 4-45) is approximately:

$$
T\left(\xi\right) = \frac{2e^{-2\pi\xi}}{1 + e^{-4\pi\xi}}. \tag{6-34}
$$

where ξ is the spatial frequency in cycles per thickness of the detector. (Thinner detectors have better MTF.)

Inter-pixel capacitance, like scattering, also reduces MTF, with a transfer function of approximately

$$
T\left(\xi, \eta\right) = \left(\left(1 - 2\alpha\right) + 2\alpha\cos\left(2\pi\xi\right)\right)\left(\left(1 - 2\alpha\right) + 2\alpha\cos\left(2\pi\eta\right)\right). \tag{6-35}
$$
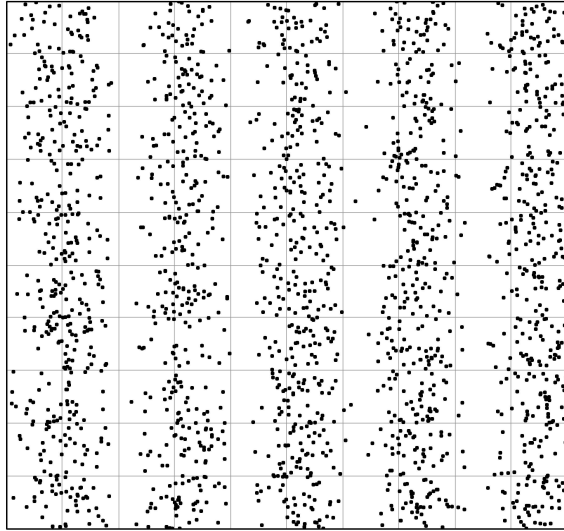
Figure 6.3: A stochastically generated sine wave illustrates the signal and noise at high spatial frequencies associated with low photon fluxes.

for small α. In Equation 6-35, ξ and η are spatial frequency in cycles per pixel — the minimum MTF is at the Nyquist frequency of one cycle per two pixels.

It is very easy to mistakenly attribute the effects of inter-pixel capacitive coupling to diffusion. Inter-pixel capacitance is a deterministic scattering mechanism however, and **attenuates photon noise and signal identically at all spatial frequencies.** Diffusion would cause some of the carriers shown in Figure 6.3 to wander to neighboring pixels, and information about their origin would become more uncertain. Inter-pixel coupling does not cause such a loss of information. Thus, inter-pixel capacitance has no effect upon *device* DQE, and its effect should be distinguished from diffusion MTF for the purpose of accurately evaluating $DQE(2\pi\xi)$ for an array. The inter-pixel capacitive effect *can* cause errors in the *measurement* of DQE, as it reduces the observed Poisson noise and causes DQE to be overestimated the same way RQE is overestimated.

6.5 Mechanisms of inter-pixel capacitive coupling

Moore *et al.*[64] initially suggested that the primary inter-pixel coupling mechanism was between the indium bumps. This hypothesis appeared incorrect. It is far more likely[66] that coupling exists mainly through fringing fields between the edges of the pixel implants. As an illustration of this, two very different types of detector are considered here, which couple pixel-to-pixel with two different field paths. The first is a hybridized silicon P-I-N array for visible imaging, a detector with fully depleted bulk. The second is a hybridized indium antimonide array for infrared imaging, a "per-pixel" depleted detector.

The P-I-N array shown in Figure 6.4 is somewhat unusual — it operates with the detector bulk fully depleted, so electric fields exist throughout the bulk. A metal grid, deposited on thick oxide between the pixels, controls the electrical state of the silicon gap between the pixel implants. This voltage is biased to keep the gap out of both inversion and accumulation. The presence of this grid also prevents significant inter-pixel coupling in the space between the indium bumps — it heavily influences the potential in this region where significant coupling otherwise would occur. It must do this, unfortunately, by increasing the nodal capacitance, and thus reducing sensitivity. Arsenic-doped silicon IBC detectors[73] (for 5-30 micron infrared) are similar to the silicon P-I-N arrays in that they are operated with partially or fully depleted bulk.

Simulations of the electric field in the P-I-N devices tested in this dissertation were performed. The simulation and results (which agree with observations) are explained in Appendix B.

The indium antimonide array depicted in Figure 6.5 is a typical detector for the near infrared. The bulk is doped opposite that of the implants and each pixel maintains a separate depletion region close to the pixel implant. The bulk of the detector is not depleted, however. No electric field (and therefore no inter-pixel capacitive coupling) exists in the
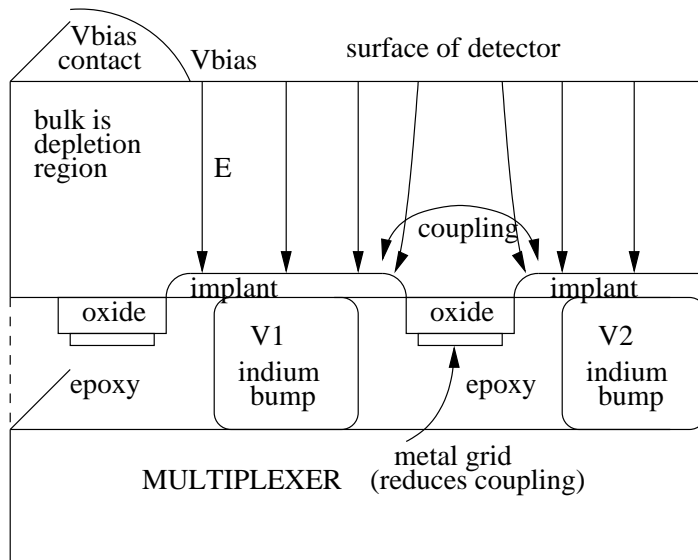
Figure 6.4: Most coupling in fully or deeply depleted detectors occurs in the detector bulk. In silicon, this is enhanced by its relatively high dielectric constant. The metal grid in the P-I-N detector tested inadvertently inhibited additional coupling underneath the detector.

detector bulk. There is no metal grid controlling the surface state in the gaps between pixels in the illustration however, (although some per-pixel depleted arrays do have field control grids) and inter-pixel coupling can exist there.

6.5.1 Assumptions and Simplifications used here

This analysis has used several simplifications, but none that seem significant. First, pixels are frequently non-linear — the capacitance changes with voltage. This non-linearity may be ignored since the stochastic signal considered (the Poisson noise) is small compared to the well depth of the pixel. Pixel non-linearity can also cause significant error in measurement of conversion factor if conversion factor is not measured in the low-signal (linear) region.[74]
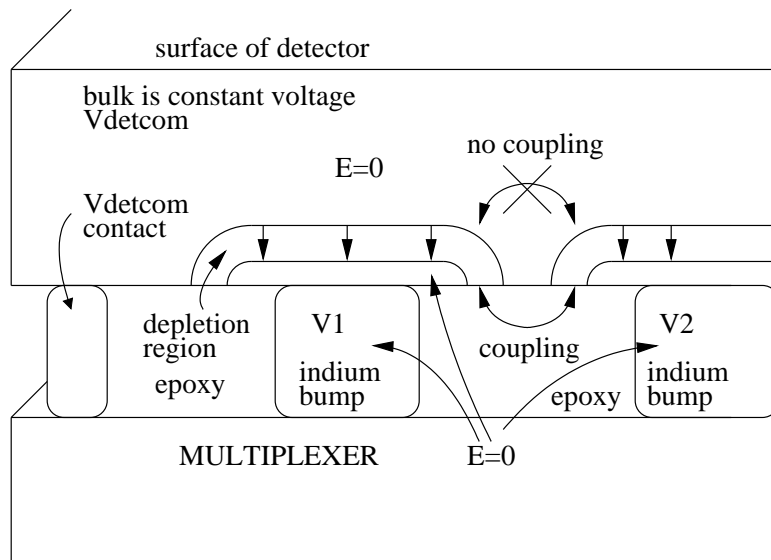
Figure 6.5: Coupling in a more typical "per-pixel depleted" detector array occurs in the space between the readout and the detector. Fully-biased shallow depletion detectors have a smaller gap between depletion regions, and should exhibit non-linear interpixel coupling that decreases as the pixels accumulate charge and the inter-pixel gap widens.

There are also slight variations in nodal capacitance that were ignored here. There is strong evidence that inter-pixel capacitive coupling is not symmetrical around defective ("hot") pixels in InSb arrays. Normal pixels are likely to have slight variations as well — but the average coupling must be symmetrical. Should a complete map of pixel capacitance, including coupling, be desired, it should be obtainable from a large number of noise images.

It has also been assumed that photon arrival and carrier diffusion and capture are uncorrelated. Known correlation mechanisms in photon arrival (such as Bose-Einstein or Hanbury-Brown-Twiss) and diffusion (such as carrier-carrier interaction) seem unlikely to be significant here at visible or near infrared wavelengths, although Bose-Einstein correlation at longer wavelengths may be measurable. If any stochastic gain is present in the detector however, the carriers produced by a single photon will create correlation in

neighboring pixels when they diffuse to different pixels. Carrier-carrier interaction may be significant here.

Part III

Application

Chapter 7

P-I-N Array Expected Performance

Silicon P-I-N arrays are a promising detector technology. The term "P-I-N", referring to the three layer structure (P doping, Intrinsic, N doping) employed in the detector diode, contains an "I" — a wide intrinsic region that greatly reduces detector capacitance. They also offer low dark current, very sharp imaging with low diffusion crosstalk, and efficient response in both the blue and near-IR spectral regions. Blue response is enhanced since surface recombination is less of an issue. Near IR response is enhanced since the detector can be made quite thick without loss of MTF to diffusion. Multiplexed CMOS arrays like these P-I-N arrays are radiation-hard, a critical consideration for space applications and one which plagues CCDs in space. Their non-destructive readout allows algorithmic rejection of cosmic ray events unavailable to data produced by CCDs.

7.1   Silicon P-I-N Array / SB226 Multiplexer

The P-I-N arrays were the main devices among several visible and infrared imaging devices tested. Their nodal capacitance, stray nodal coupling, inter-pixel coupling, noise performance, quantum efficiency, and MTF were characterized at the Rochester Institute of Technology. Additional measurements of inter-pixel coupling and MTF in indium antimonide (InSb) infrared detectors were taken at the University of Rochester. This section

describes the P-I-N devices with mathematical modeling of some of the relevant characteristics.

Zoran Ninkov proposed the NASA-funded SB226/P-I-N research initiative. A team led by Dr. Paul Hickson at the University of British Columbia, after hearing of Zoran Ninkov's planned Si P-I-N array prototypes, proposed the use of silicon P-I-N arrays similar to the ones tested here as visible imagers on the James Webb Space Telescope (JWST, previously NGST). The University of British Columbia and the Canadian Space Agency supported this concept[75, 76, 77, 78]. Four devices have been produced by Raytheon Vision Systems under subcontract to RIT, one pair of thick hybridized silicon P-I-N arrays, followed by another pair of thinned detectors.

Testing of these P-I-N arrays was primarily done at 35K to see how such an imager might perform at the planned JWST focal plane temperature. The P-I-N arrays tested here may be the very first visible imagers to operate below pumped liquid nitrogen temperatures. Unfortunately, the P-I-N array concept is not included in the current plans for JWST.

7.1.1 Raytheon SB226 Multiplexer

The multiplexer, a Raytheon SB226 (with global reset only) 1024 by 1024 cryogenic CMOS multiplexer, supports pixels on a 27 micron pitch. This three-transistor unit cell, four output interleaved multiplexer has been extensively characterized by the Near Infrared Astronomy (NIR) laboratory at the University of Rochester. [79, 80] It has been used with InSb and IBC detectors[81, 73]. On the NIR lab's recommendation, multiplexers believed to be the finest (lowest noise) of their lot were selected for bonding to the silicon P-I-N detectors.

The shift registers in the SB226 each have three control lines. One line resets the register. The other two advance the shift register along. Reset is controlled by one more

line, a logic line that actually does the reset. Each pixel in the multiplexer is connected through its own switch to the reset voltage, and the SB226 shares the reset and unit cell supply voltages as shown in Figure 2.3. Reset by row and reset by pixel are not supported in the 226.

7.1.2   P-I-N detector

P-I-N arrays have a wide biased intrinsic region, unlike the thinner depletion region of a typical p-n junction. This has two advantages. First, released photocarriers are actively swept into detector nodes. MTF degradation due to diffusion is substantially reduced. Second, the capacitance of the detector junction is a negligible part of the total detector node capacitance of a hybridized device. This is due to the large distance between the p and n regions. A small node capacitance is important in an imager since it results in increased detector sensitivity.

The "thick" detectors tested here measure 185 microns thick. Wafers of high purity silicon had P doped pixels implanted on the bonding side. The thinned detectors were thinned to $\approx$ 40 microns.

Susceptibility to cosmic rays is a concern for astronomical imaging. Generally, thick detectors have poor MTF and are highly susceptible to image degradation from cosmic events. The P-I-N detector, however, has theoretically excellent MTF, and additionally has Gaussian lateral diffusion which rolls off stronger than the exponential crosstalk characteristic of undepleted detectors. Its only disadvantage is cosmic events entering the detector at shallow angles — these events leave long streaks. A project to reduce this cosmic ray susceptibility yielded the two thinned P-I-N arrays.

In between the pixels is a metal grid, illustrated in Figure 7.1, separated physically and electrically from the detector by an oxide layer. This field control grid is held at approxi-
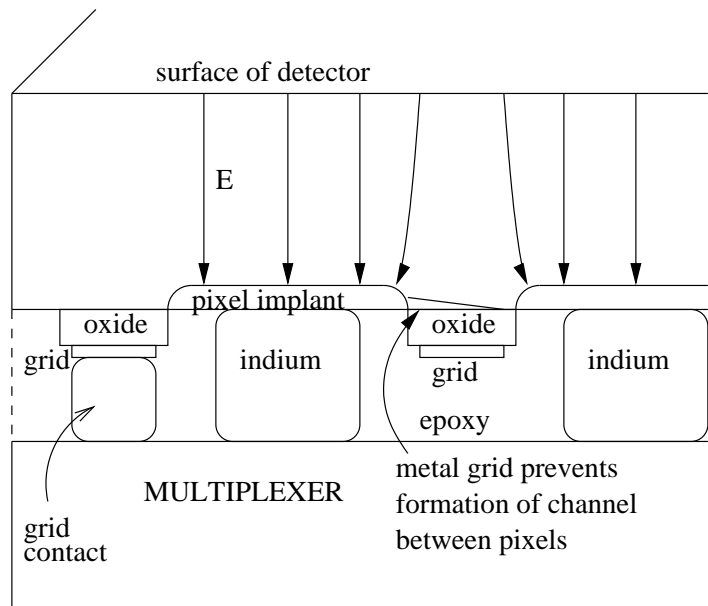
Figure 7.1: An aluminum grid in the P-I-N devices controls the potential near the gap between pixels. This allows inter-pixel channel formation to be inhibited.

mately the same voltage as the detector nodes, and keeps the areas between the pixels from accumulating or inverting. If the grid voltage is pulled too negative, the intrinsic region between pixels becomes "inverted" at the surface, and a channel forms between pixels, allowing current to flow from one pixel to its neighbor. If the grid voltage is too positive, the area between pixels accumulates electrons.

When pixels integrate, their voltages rise higher than the grid voltage. This can also cause a channel to form in between the pixels, resulting in charge spillage from pixel to pixel. A pixel will continue to integrate to this spillage point unless some mechanism is available to bleed off the charge. The reset FET can be biased to do this as a secondary purpose. As the node voltage goes higher, the reset FET's gate-source voltage approaches the threshold voltage, at which point the reset FET turns on and clamps the integrating node. This clamping does not allow integration to progress any further. If the node voltage

102

Vreset

Node voltage turns
on reset fet
when pixel saturates

Reset

Goes negative
to turn on FET

Clamping prevents
channel formation
and image bleed

BackBias = ++++
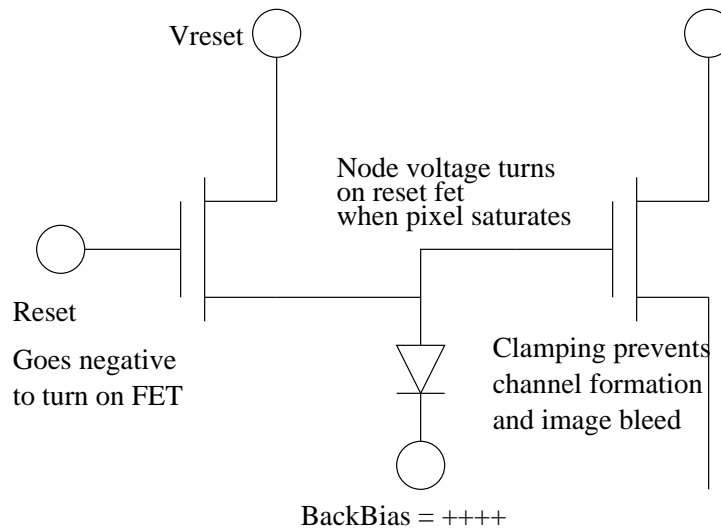
Figure 7.2: Optical signal causes P-I-N detector nodes to move towards the bias potential. When the reset FET was turned off hard, the node voltage rose high enough to create an interpixel channel, an charge spilled into neighboring pixels. Adjusting the off rail allowed the reset FET to turn on and bleed excess charge instead.

at which this happens is below the voltage at which a channel forms between the pixels, charge spillage will not occur.

7.2 Nodal Capacitance

The P-I-N detector's contribution to node capacitance of arrays is theoretically

$$C_{pix} = \epsilon_r \epsilon_o A/d. \tag{7-1}$$

which, with a pixel area of 22 microns squared, a thickness of 185 microns and silicon's relative dielectric constant of 11.8 yields 0.273 fF. This is quite small compared to the multiplexer capacitance of about 30 fF. (In per-pixel depleted detectors, the distance d may only be one or two microns. The resulting C is typically tens of femto-Farads in such devices.)

7.3 P-I-N Intrinsic Field

The intrinsic region of the Si P-I-N is not of high enough purity to neglect.

It is lightly doped with arsenic, and must be depleted fully before the entire intrinsic region has an electric field in it to sweep carriers across.

This electric field can be calculated quite simply. Gauss's law (and the assumption of a unidirectional field) dictates that the electric field increase linearly with distance through the depletion region, so

$$E\left(x\right) = \frac{xN_dq}{\epsilon}. \tag{7-2}$$

Integrating the electric field yields the potential:

$$V\left(x\right) = \frac{1}{2}x^2N_d\frac{q}{\epsilon}. \tag{7-3}$$

Substituting the actual doping density, the thickness of the intrinsic region, and the other physical constants yields a requirement for 22.5 volts of back bias to fully deplete the intrinsic region.

Additional bias increases the field strength above the profile given by Equation 7-2.

A calculation that takes into account the increasing field strength could be done for the theoretical lateral diffusion, but since little data was available to justify that complication and the detector was operated a a substantial over-bias, a simplified approach was taken.

7.4 Theoretical P-I-N MTF

As shown in Figure 3.1, three components create the overall point spread function of the P-I-N device: transverse diffusion in the detector bulk, capture by square pixels, and inter-pixel capacitive effects between the detector nodes.

When a photon is absorbed in the intrinsic region of the P-I-N device and an electron-hole pair is generated, the pair splits up in the applied bias field. One carrier is swept to the
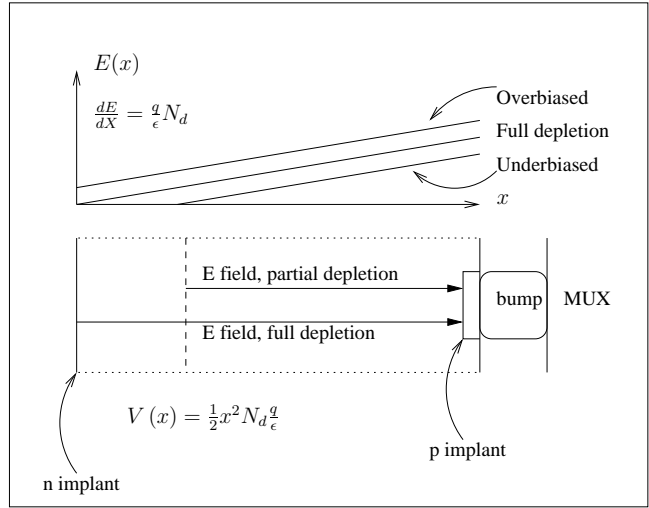
Figure 7.3: The "intrinsic" region of the P-I-N device, extremely pure by most standards, in actuality is still slightly n-doped. This creates a ramped E field which is stronger near the pixels. The potential required to deplete the region varies with the square of the detector width.

back bias contact, and the other is swept towards the detector nodes. In these devices, the back bias is a positive voltage; holes are detected. Along the way to the detector nodes, the hole is subject to thermal diffusion, so there is some probability that the hole will diffuse to a different pixel than the one immediately beneath its point of origin. Predicting the MTF of the detection process is basically a comparison of these two mechanisms. The applied bias sweeps the hole at its drift velocity from its origination point to the detector node. This takes a certain amount of time. In this time, thermal diffusion is acting upon the hole. Given the sweep time, what is the diffusion length? The sweep time can be determined from the hole mobility, the field strength, and the distance the hole must travel. At 30K, the hole mobility is approximately [82]:

$$\mu_p = 5 \times 10^4 \frac{\text{cm}^2}{\text{Vs}}. \tag{7-4}$$

The field strength used was 33.6 V over 185 microns, an average of $1.8 \times 10^3 \text{V/cm}$.

The drift velocity is the product of the hole mobility μ_p, and the field strength E_b—

$$\mu_p E_b = (1.8 \times 10^3) \cdot (5.0 \times 10^4)\frac{\text{cm}}{\text{s}}. \qquad (7\text{-}5)$$

This calculation indicates a drift velocity on the order of $9 \times 10^7 \text{cm/s}$. The drift velocity, however, is not linear with field strength. The effect becomes significant at $\approx 5 \times 10^6 \text{cm/s}$. Below that speed, the thermal velocity is generally the dominant component of real particle motion, and diffusion and drift are well-behaved and independent. Above that speed, drift velocity becomes limited by increased collision rate. There is an effect on the diffusion as well, because now collisions are at a higher velocity.

At this field, the hole drift velocity in the neighborhood of 40 K is more likely $\approx 6 \times 10^6 \text{cm/s}$[83]. It was assumed that, despite the ramped field, carriers would be swept into pixels at constant velocity.

This allows the hole to diffuse for $(0.0185cm)/(6 \times 10^6 \text{cm/s}) \approx 3$ nanoseconds before it reaches the detector nodes. Einstein's relation yields the diffusion coefficient from the mobility:

$$D_p = \mu_p \frac{kT}{q} = 130 \left(\text{cm}^2/\text{s}\right). \qquad (7\text{-}6)$$

The diffusion length is then

$$L = \sqrt{D_p \tau} = 6\mu m. \qquad (7\text{-}7)$$

Since the particle velocity is now significantly affected by the E field, the effective lateral diffusion coefficient is altered as well.

One might conclude that the increased velocity might increase scattering, but this is not so. Under high fields, the diffusion coefficient D_p splits into two components. $D_{//}$ denotes the "longitudinal" component, (along the field) and $D_\perp$ denotes the "transverse" or lateral

component (at right angles to the field). $D_\perp$ is the component of interest for modeling point spread, but data on $D_{//}$, which is important in high-speed circuitry, seems to be more abundant. Canali [84] has shown that the lateral diffusion coefficient drops in high fields and gives $30\text{cm}^2/\text{s}$ as a more likely value —- citing Persky and Bartelink[85]. Persky and Bartelink measured transverse and longitudinal diffusion coefficients of electrons and holes in high fields. Their data indicate $D_{//} = 20 - 30 \text{ cm}^2/\text{s}$ at $1.8 \times 10^3\text{V/cm}$ and 77K. This value increases with the increased mobility at lower temperatures. Transverse diffusion of holes $D_\perp$ in silicon appears to be equal to $D_{//}$ at moderately high fields, and is higher than $D_{//}$ only under very high fields. $D_\perp = 40 - 60 \text{ cm}^2/\text{s}$ is an estimate for 35K, assuming an inverse relationship with temperature. This model predicts a lateral diffusion of 3.4 - 4.2 microns, with a Gaussian spread.

A thinner detector (such as the thinned 40 micron detectors) will give a slight advantage over this already superb PSF. It is expected to vary proportionally to the square root of thickness.

The Gaussian definition preferred by Gaskill and Bracewell [26, 44] was used in the model:

$$\text{Gaus}\,(x, y; b) = \frac{1}{|b|} \exp\left(-\pi \frac{x^2}{b^2}\right) \frac{1}{|b|} \exp\left(-\pi \frac{y^2}{b^2}\right). \tag{7-8}$$

The scaling parameter b changes the spread of the Gaussian.

7.4.1   Collection by pixels

An ideal square pixel is modeled with the rect function; the 2D pixel is the product of a rect in x and a rect in y. The rect, as defined by Bracewell and Gaskill, is:

$$\text{rect}(x) = \begin{cases} 0, |x| > \frac{1}{2} \\ \frac{1}{2}, |x| = \frac{1}{2} \\ 1, |x| < \frac{1}{2} \end{cases} \quad . \tag{7-9}$$

The model used the pixel spacing as the base dimensional unit, so the rect does not need a scaling parameter. The P-I-N array pixels have a gap between them that was not accounted for in the model — given the powerful field near the implants, there seems to be little justification to include it.

7.5   Theoretical P-I-N ESF

One common MTF analysis uses the Edge Spread Function, or ESF. The ESF is the integral of the line spread function, or LSF. The LSF is the convolution of a line impulse with the point spread function. For circularly symmetrical point spread, the process of deriving LSF from PSF is called the Abel transform [56]. Separability of the Gaus makes the Abel transform trivial here; Gaussian line spread is expected. Section 3.3 discusses this in more detail. (Some of that section's results are repeated here.)

The pixel projection and resulting edge spread function change with angle. Here the variable u is used to represent the distance along the projection. At arbitrary angles, the projection of a square pixel is the convolution of a pair of rect functions, each of unit area but with a width proportional the cosine or sine of the projection angle, as shown in Figure 3.5.

$$\text{pixel}(u) = \frac{\text{rect}(u\ \sin(\theta))}{\sin(\theta)} * \frac{\text{rect}(u\ \cos(\theta))}{\cos(\theta)}. \tag{7-10}$$

The zero and 90 degree cases find one of these rect functions has zero width — it is an impulse instead. At 45 degrees the rect functions are identical and a triangle shaped projection results.

The four nearest neighbor pixels contribute via inter-pixel coupling resulting in an inter-pixel projection of:

$$\text{ipcap}(u) = \alpha[\delta(u + \sin(\theta)) + \delta(u - \sin(\theta))$$
$$+\delta(u + \cos(\theta)) + \delta(u - \cos(\theta))] + (1 - 4\alpha)\delta(u). \qquad (7\text{-}11)$$

$$\text{ESF}(u) = \text{pixel}(u) * \text{ipcap}(u) * \int_{-\infty}^{u} \text{Gaus}(\upsilon; b) \, d\upsilon. \qquad (7\text{-}12)$$

If only vertical or horizontal edges are used, the expected ESF is the convolution of the inter-pixel capacitance's 1D response, the 1D rect, and an integrated Gaussian. The pixel, inter-pixel line response, and resulting ESF are:

$$\text{pixel}(x) = \text{rect}(x). \qquad (7\text{-}13)$$

$$\text{ipcap}(x) = (\alpha\delta(x + 1) + \alpha\delta(x - 1) + (1 - 2\alpha)\delta(x)). \qquad (7\text{-}14)$$

and

$$\text{ESF}(x; b) = \text{pixel}(x) * \text{ipcap}(x) * \int_{-\infty}^{x} \text{Gaus}(\xi; b) \, d\xi. \qquad (7\text{-}15)$$

For per-pixel diffusion detectors this analysis is pretty much the same but the shape of the diffusion is given by Equation 4-25 rather than Gaussian. This model has obviously been based upon the assumption that the diffusion of carriers is independent of the pixel implant geometry. There are cases when this is not a good assumption.

Chapter 8

Device Testing Results

8.1 Basic Test Setup

Figure 8.1 shows the basic P-I-N test setup used for tests in this chapter. A simple mask was used to generate sharp edges. The pinhole was wide enough to blur details of the white paper on the ceiling used as the illumination source. Various filters were placed in a filter wheel attached above the dewar entrance window. Immediately beneath the filter wheel was a precision shutter synchronized with the acquisition timing.

8.1.1 Array Controller

In the course of this P-I-N array research a variety of controllers were investigated and used. An older controller developed at the University of Rochester had software written in FORTH. A newer controller was developed based somewhat upon this system, with interface software written in Python. This control system, shown in Figure 8.2, was built to operate the P-I-N devices with the intention that it would be useful for operating a variety of other devices. More details about this system can be found in Appendix H through Appendix I. At the Rochester Institute of Technology, this first Python-based controller was used to operate thick and thin silicon P-I-N detectors and InSb detectors on SB226 multiplexers. At the University of Rochester, both the older FORTH-based controller and
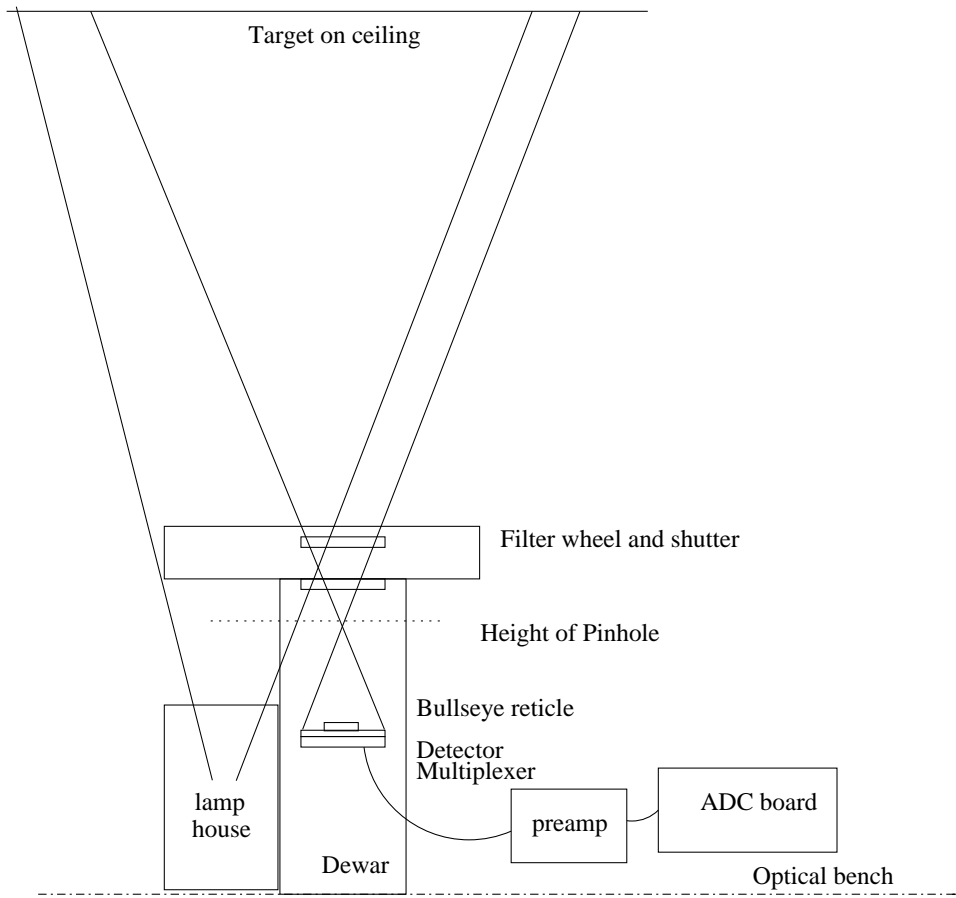
Figure 8.1: Conversion factor testing required stable illumination and edge spread testing required optically sharp edges. A stable illumination source flooded a white piece of paper on the ceiling of the lab. A filter wheel and shutter controlled illumination entering the dewar. A simple pinhole further reduced and controlled incoming light, and a chromed mask target in contact with the array surface provided sharp edges.
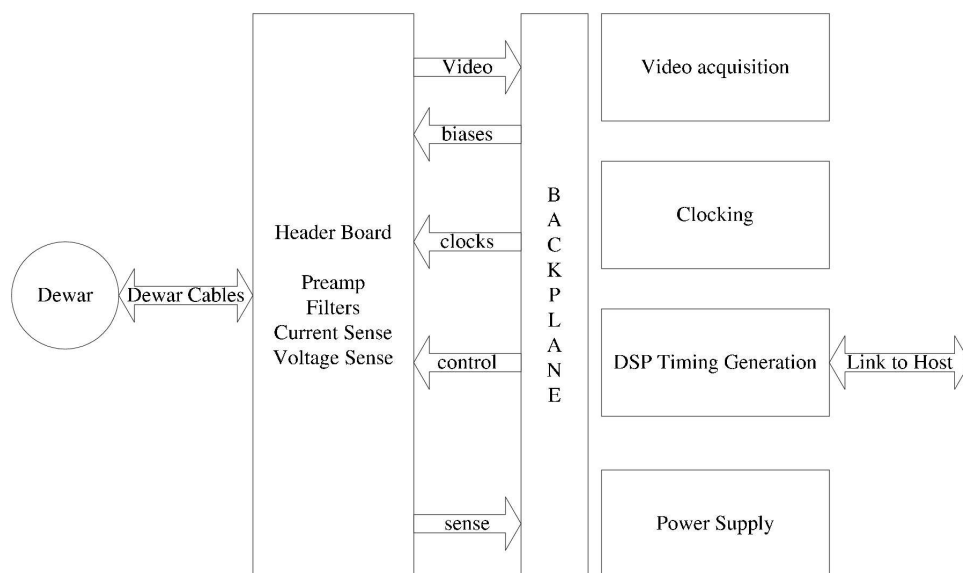
Figure 8.2: The array control system was a modified version of a suite of boards originally designed by OCIW's Greg Burley. A DSP board controlled the operation and acquisition. The clocking board provided programmable voltages to the pins of the device and a video acquisition board digitized the amplified signals returning from the array.

a second generation version of the Python-based controller were used to test InSb devices on SB226, SB291, SB294, and SB304 multiplexers.

The software that operated the DSP was written mostly in C, but included a significant amount of assembly language. This software coordinated the control and timing of the voltages applied to the pins of the device. It also operated the analog-to-digital converters and a precision shutter. Details about the DSP software may be found in Appendix H.

User interface software evolved over the course of the research. Initially, the DSP debugger served as a primitive user interface. Then, a modified version of the University of Rochester's "dspsys" host controller software was used. This software was rewritten in Python. Details about the UI software may also be found in Appendix H.

8.1.2   Equipment used

Various other equipment was needed for the P-I-N testing. The devices needed to be operated in a vacuum, so a vacuum chamber, turbo-pump, closed cycle refrigerator, and temperature controller were employed. Various illumination sources were used as well.

Equipment used at Rochester Institute of Technology:

1   Janis CTS-250 vacuum chamber

1   PicoDry Turbo-molecular Vacuum Pump

1   CTI Cryogenics Model 22 closed-cycle helium refrigerator

1   Water-cooled CTI Cryogenics Model 8200 compressor

1   Lake Shore 321 auto-tuning temperature controller

2   Lake Shore temperature sensing diodes

1   Incandescent source

1   5 watt White-light LED

1   Infrared LED

1   Diffraction-grating type monochromator

Equipment used at University of Rochester:

1   Custom manual-fill Nitrogen/helium dewar

2   Lake Shore temperature sensing diodes

Other equipment used:

1   Integrating sphere

1   Calibrated light meter

8.2   Thick P-I-N Devices, Basic Tests

Two aspects of the P-I-N arrays described in Chapter 7 were considered especially notewor-
thy for being characterized. First, low nodal capacitance was expected. Second, ultra-sharp
imaging was expected. In this section, the nodal capacitance of the thick P-I-N device is
investigated. The next section will look at image sharpness. Spectral sensitivity and dark
current will be discussed after that.

It was (and is still) hoped that these high performance arrays will share a focal plane on
a space telescope with other detector arrays — likely infrared ones that need to operate at
very low temperatures in the range of 10K-77K. On their own, silicon P-I-N arrays require
only a moderate amount of cooling to do long integrations — dark current was expected to
be nearly unmeasurable in these devices at temperatures as high as 200K . With this space
telescope application in mind, these tests focused on P-I-N operation and performance at
what would otherwise be considered very low temperatures for them to operate at.

8.2.1   SB 226 Gain measurement

It was important to know the signal path gain — when a voltage change was observed at the
output of the device, how much was the detector node voltage changing in order to cause the
observation? The source follower gain of the main output FET was measured by turning on
the reset continually and varying the reset voltage while reading out frames. The back bias
was disconnected and left floating so that no reset current would flow. The reset FET gate
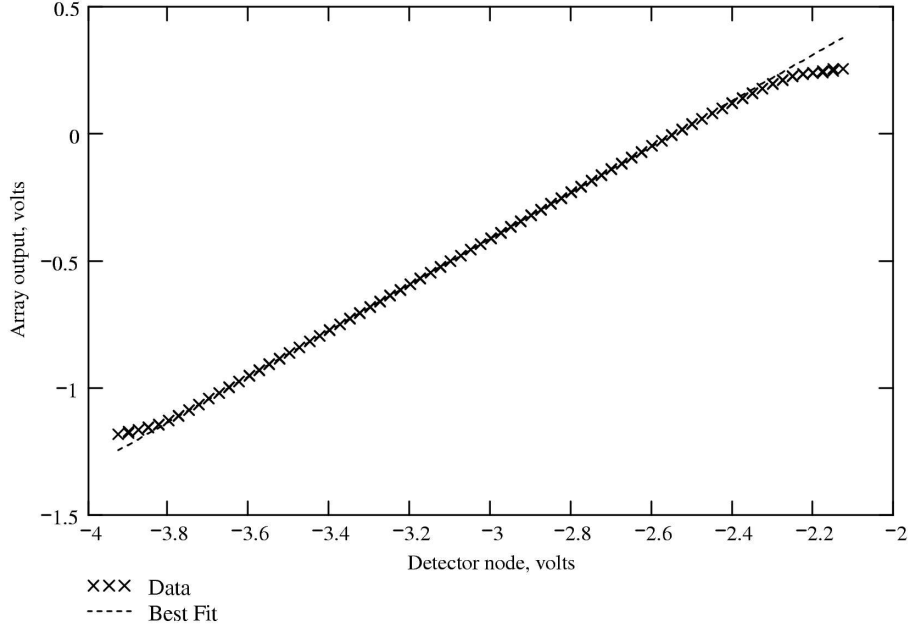
Figure 8.3: The source-follower gain was measured by keeping the device in constant reset and varying the reset voltage. This plot shows the observed output versus applied reset voltage, and indicates a gain of 0.902 with good linearity.

voltage was also kept at a constant 1.8 volts below the reset voltage to maintain a constant state in the reset FET. A succession of images was taken, and the pedestal images were saved. Figure 8.3 shows one resulting measurement, typical of all the devices. It shows a gain of 0.90 as the input is swept from -3.8 volts to -2.4 volts and the output voltage rises from -1.0 volts to 0 volts, with a slight reduction in gain before and after that range.

8.2.2 Charge Dump in SB226 Multiplexer

Since low nodal capacitance was a primary expectation in the P-I-N devices, experiments were performed to determine the coupling of the detector nodes to two of the unit cell
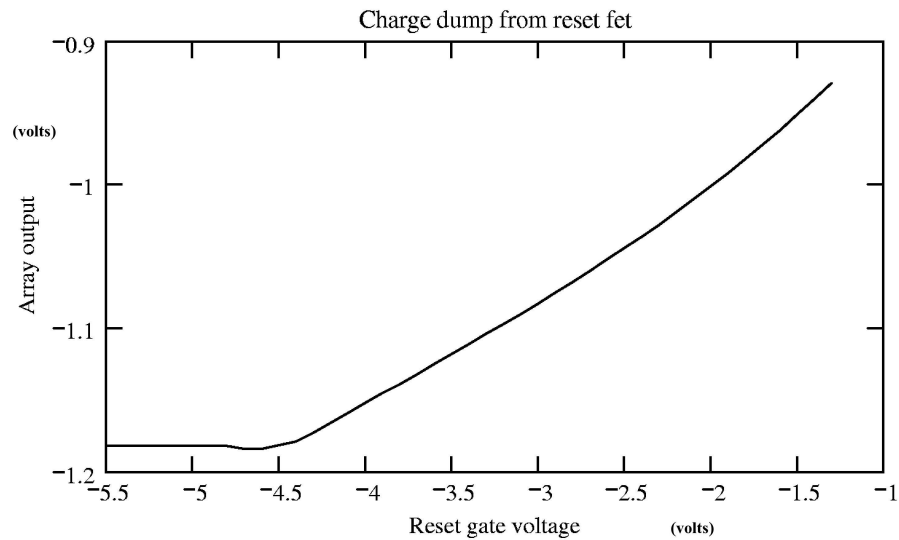
Figure 8.4: Variation of the SB-226 reset FET's gate in the off state allowed investigation of its stray coupling to the detector node. This plot indicates ≈8 % of the bare mux capacitance is to the reset gate.

control lines that were known to "dump" charge into the detector nodes — The reset line, and the unit cell power.

These couplings were determined by resetting the device, and then removing the reset and monitoring the output voltage while varying one of the control lines in question. If the line in question coupled into the detector nodes, a shift in the output voltage proportional to the coupling would be observable. The ultra-low dark current made these measurements relatively easy.

Figure 8.4 shows the measured coupling of the reset FET's gate into the detector node. The reset gate was slowly de-asserted. At roughly -4.5 volts, the reset FET turned off, and the array output started to track the reset gate voltage. For two volts of swing on the reset gate, approximately 0.15 volts of signal shift at the output was observed. Slowly reasserting
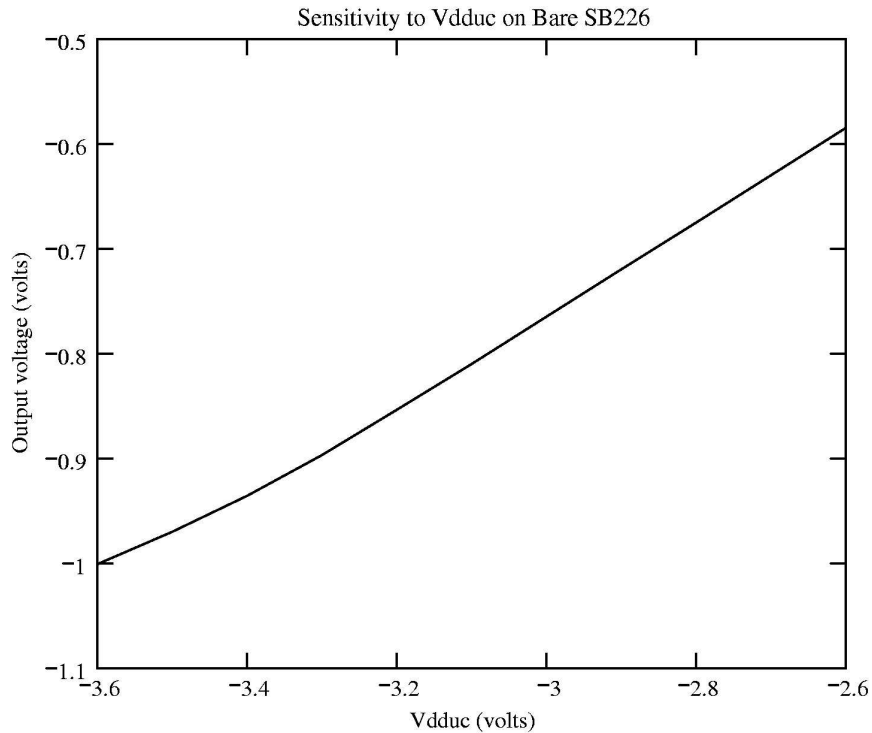
Figure 8.5: Variation of the unit cell supply voltage shows a very strong coupling from the supply into the unit cell. It indicates that roughly half the bare mux capacitance is to the unit cell supply rail.

the voltage showed no hysteresis or dark current. Taking into account the gain of 0.90, this indicates one part in twelve of the bare mux capacitance is to the reset line.

Figure 8.5 shows a similar measurement varying the unit cell power supply instead. Coupling here is quite significant. A shift of 0.40 volts in the power rail yields about 0.20 volts of shift in the output voltage. This indicates that roughly half of the bare multiplexer nodal capacitance is to the unit cell supply rail — most likely via the unit cell output FET.

8.2.3 Initial nodal capacitance measurements

The thick prototype silicon P-I-N detector arrays were expected to exhibit ultra-low nodal capacitance (34 fF), due to the large distance (185 microns) between their "parallel plates".

The thick P-I-N's electron conversion factor was estimated by using the noise variance versus signal method [65]. Pairs of images with uniform illumination were taken using successively longer integration times, and the variance of the difference images was plotted against the mean value of the summed images. Since the noise due to photon quantization obeys Poisson statistics (where the variance is equal to the mean) the slope of this line is the inverse detector conversion factor. This plot, showing $2.4e^-/\text{ADU}$, is the lower trace shown in Figure 8.6.

From the conversion factor, the thick P-I-N nodal capacitance was initially estimated at approximately 57 fF.

$$C = 1.6 \cdot 10^{-19}(\text{coul}/e^-) \cdot 2.4(e^-/\text{ADU}) \cdot (1\text{ADU}/6.1\mu\text{V}) \cdot 0.9 = 57\text{fF}. \qquad (8\text{-}1)$$

This relatively straightforward computation, requiring the measured gain of the system, the signal path, the conversion factor, and a physical constant, yielded an unreasonable result. Only 34 fF was expected — 30 fF from the bare multiplexer, and (according to Raytheon) 4 fF from the indium bumps. The measurement was clearly much larger than the expected value.

8.2.4 Thick P-I-N coupling to grid

Capacitive coupling to the metal field control grid on the thick P-I-N prototype was immediately suspected as a source of additional capacitance. A simple test confirmed that indeed, the grid added more capacitance to the nodes – the device was reset and the grid
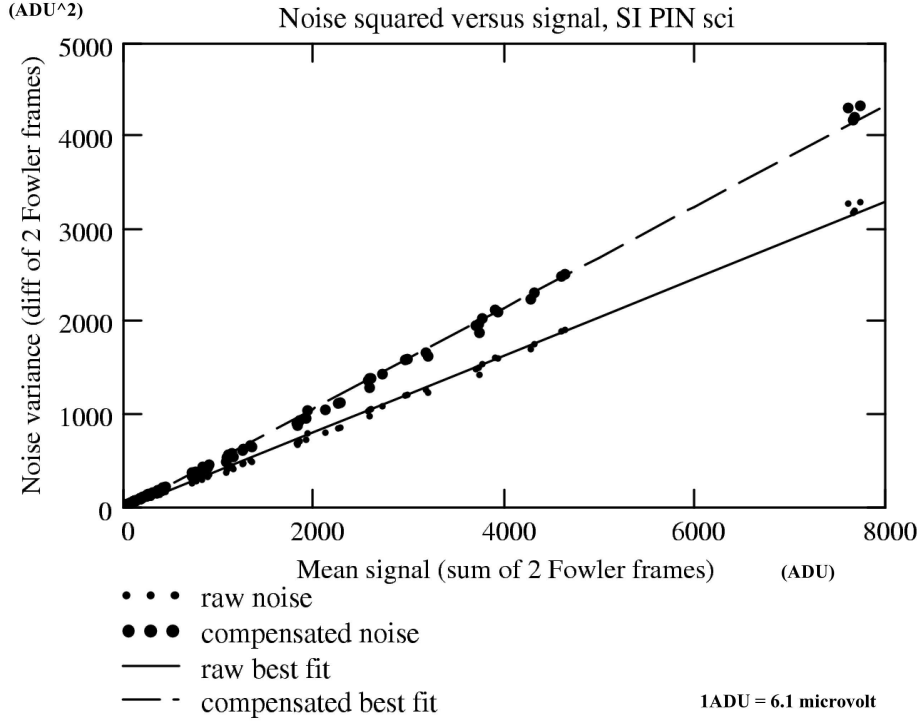
Figure 8.6: Lower trace: Raw noise-squared (in ADU^2) versus signal (in ADU), indicated 2.4 electrons per ADU. Scaling by the system gain indicated an unbelievably large nodal capacitance of 57fF. Upper trace: The corrected measurement made much more sense (43 fF) but initially the correction required was unknown.

voltage was adjusted to observe its effect upon node voltage. The results indicated that 16.5 percent of the grid voltage shift appeared at the output, indicating about 18.3 percent of the total nodal capacitance was to the grid. This did not explain the observation. Reducing the 57 fF by 18.3 percent left 46 fF. Compared to a known bare mux capacitance and expected bump capacitance totaling 34 fF, this was still much higher than expected.

120

8.2.5 Thick P-I-N coupling to back bias

The back bias, connected to the n-doped detector surface on the far left in Figure 3.1, was varied by 5 volts during an integration. This shifted the resulting image by only 30 millivolts, confirming that there is very little additional detector capacitance (0.6 percent of total) added by the P-I-N junction.

Equation 7-1 predicted 0.273 fF coupling the back bias. Relative to a measured 57 fF of detector nodal capacitance, 0.4 percent coupling was expected — so there was an unexplained discrepancy here as well. Relative to the expected lower nodal capacitance however, the percentage seemed proper — so this was somewhat promising.

8.2.6 Initial edge spread testing

Edge spread testing was initially confusing as well. A simple image mask was used to perform MTF testing. Rather than attempt to project and focus an image into the dewar, a small pinhole aperture was used. This kept light in the room from being a problem as it would have been with a wide entrance aperture, and relatively long integrations could be performed without saturating the sensitive detector. The image was created by a bullseye target reticle, with a surface chrome pattern, in direct contact with the array. The array faced up at the ceiling of the room, and gravity held the bullseye reticle in place. There was some fear of damaging the device with this mechanical contact, but its placement was performed gently, and ultimately no apparent harm came from the procedure.

This small bullseye patterned reticle, placed pattern side down on the detector surface, created nice test images. The center of the pattern is shown in Figure 8.7. Illumination was limited by a 200 micron pinhole approximately 1.8 inches from the array surface. The outer edge of the last (fifth) ring of the bullseye target was used to provide the edge, as it was nearly straight compared to the dimensions of a pixel. Initially, only pixels that were a
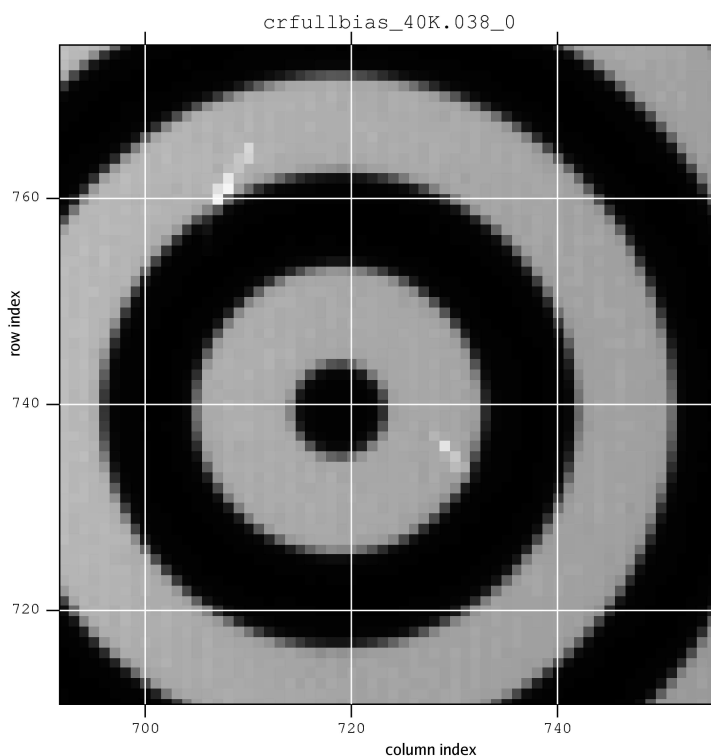
Figure 8.7: Edge spread analysis used a precision "bullseye" reticle in contact with the array detector surface. This easily produced optically sharp edges of various orientations, as shown in this screen capture of a 'fitsview' image. The white streaks are muon hits. The numbers are from fitsview and indicate pixel coordinates in the image.

small angular displacement from horizontal and vertical were used. Each pixel's intensity was normalized to the bright and dark levels of the image, and plotted against its distance from the center of the bullseye, shifted by the radius of the ring.

Two contributors to the edge spread were anticipated — Gaussian diffusion caused by the fixed lifetime of the photocarriers, and the square collection area of the pixels. The strong electric field in the depleted "i" region would rapidly sweep photocarriers into detector nodes (3 nanoseconds) and sharp imaging ($\approx 4\mu m$ diffusion spread) was anticipated.

The overall point spread expected was the convolution of a 2D Gaus and a 2D rect:

$$\text{psf}_{pixel}(x, y; b) = [\text{rect}(x)\,\text{rect}(y)] * \text{Gaus}(x, y; b).\qquad (8\text{-}2)$$

Vibration from the closed-loop refrigeration unit occasionally moved the reticle, so it was necessary to recompute the bullseye center for each image, and even reject images when there was evidence of motion during integration. Many runs of this acquisition were averaged into bins 0.01 pixel in width.

Data collected and processed did not conform to this model. It was suspected that the incoming radiation was possibly dominated by NIR wavelengths, causing an odd diffraction effect from collection deep in the device. A "Bessel V" filter (visible, $\lambda = 550$nm) was added to remove the more deeply penetrating red wavelengths, so that the carriers would be generated near the surface of the detector. This change did not influence the shape of the observed edge at all. The same spread was seen with long wavelength NIR, visible green, and shorter wavelength blue — and *no* choice of Gaussian shape parameter fit the observed edge spread to the model with any satisfaction.

8.2.7   Muon hits provide a clue

While trying to explain the strange edge spread observations, cosmic events were looked at in more detail. Muon hits would strike the array and leave trails, or in some cases, tiny points. A rapid Gaussian decay was expected, and the odd edge spread results at least confirmed that this decay rate was small compare to the pixel pitch. A perpendicularly incident muon hit in the center of a pixel should only crosstalk to its neighbors by less than 1 percent. A muon hit on a gap between pixels, or at a four corner intersection could never significantly diffuse across a full pixel into the next neighbor. Such muon hits were searched for in the data, but no examples were found. The minimum crosstalk observed in any neighbor of a pixel hit by a muon was always greater than 3 percent, and this exact

minimum ratio appeared in observed data more often than not. It became apparent that pixels struck by a muon were electrically pulling all their neighbors along with them when they got a jolt of charge from the muon. The inter-pixel coupling model detailed in Chapter 6 began to take shape, and an interesting method of confirming the model validity was devised.

8.2.8   Thick P-I-N inter-pixel coupling

A statistical approach was used to prove that the crosstalk was arising from capacitive coupling and not carrier diffusion. New data was taken — long runs of uniformly illuminated images, multiply-sampled so that read noise was extremely low. The thick P-I-N inter-pixel coupling was measured from this data by performing spatial autocorrelation of the Poisson noise in many (1800) multiply-sampled difference patches 50 by 50 pixels in size. The first estimates of inter-pixel coupling were performed in a roundabout way — the 2D Fourier Transform of the autocorrelation was taken, then each term in the transform was replaced by its square root. Taking the inverse transform yielded an estimate of the multiplexer impulse response. See Chapter 6 for the theory behind Equation 6-27, which was used for these initial estimates. The more direct approaches described there were refined later. The raw correlation result is shown in Table 8.1.

From these correlation data, the central value of the impulse response was estimated at 0.871, the four nearest neighbors at 0.027, and the four diagonal neighbors at 0.00525. The inter-pixel correlation here is remarkably strong, and even second-neighbor coupling is measurable, both vertically and horizontally.

As an aside — in these and the other autocorrelation data there is an "almost symmetric" profile observable. The autocorrelation only needs to compute half of the coefficients off

234	-5141	3731	-5354	-3304	3869	-3886	-5010	-661
295	2974	590	-6231	-1335	3484	117	-4145	4097
-1434	-4694	-574	16196	23060	5123	521	-1549	3556
-6783	-10180	9578	63021	253064	61183	12483	4232	-513
7065	-569	30770	258440	4044351	259273	30120	1392	7085
-1271	3493	12989	59031	252469	64626	11585	-10714	-9797
3915	-8	-83	5127	21765	16001	468	-6371	-5731
950	-3846	-671	6788	-3679	-8255	-80	-125	782
-1674	-2180	-4439	3440	-5133	-3676	1106	-4557	-105

Table 8.1: These autocorrelation data from P-I-N noise images indicate interpixel coupling of approximately 3 % of the nodal capacitance — to each of the four immediate neighboring pixels. Diagonal, and even second-neighbor coupling is observable. This created an error of 31 percent in the initial measurement of conversion factor.

the origin. The other half can be obtained by mirroring. The lack of perfect symmetry in these results is an artifact of the simpler computer program used.

8.2.9 Thick P-I-N conversion factor, adjusted

It was now apparent why the capacitance measurements were indicating such a large nodal capacitance. The inter-pixel coupling impulse response, being deterministic and post-capture, caused the noise-squared measurements to be attenuated. The data shown in the lower trace of Figure 8.6 were low by a factor of $0.871^2 + 4(0.027^2 + 0.00525^2) = 0.762$. Compensation resulted in the upper trace. In Table 8.1, this is the ratio of energy in the center cell (the simple sum of the squares) to the total energy in the entire autocorrelation — but since that is an infinite summation, insignificant correlation terms should be treated as zeros. This method of properly estimating the incoming shot noise is also expressed in
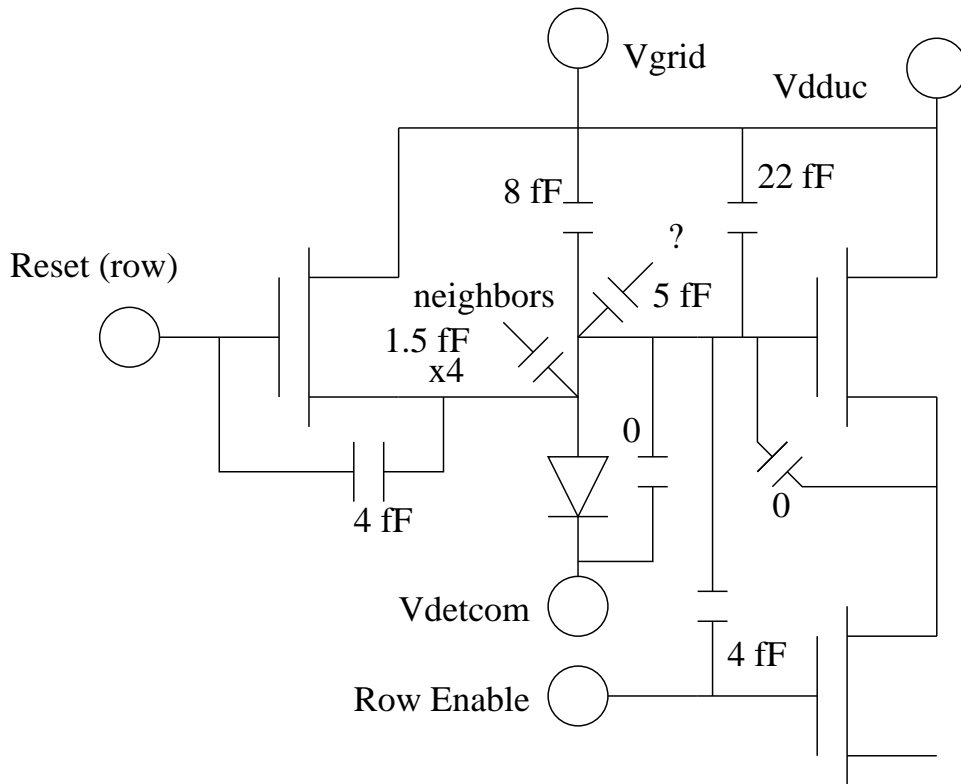
Figure 8.8: Breakdown of P-I-N nodal capacitance into known components — 22 fF to the unit cell supply, 8 fF to the grid, 4 fF to the row enable gate, 4 fF to the reset gate, and the remaining stray 5 fF to unspecified sources. In addition there is 1.5 fF to each of 4 neigboring pixels. The source-follower output FET's gate-source coupling is effectively zero due to the unity gain of the follower, and the detector capacitance is negligble.

Equation 6-24. Correcting the slope for this effect resulted in an estimate of 1.83 electrons per ADU.

8.2.10 Thick P-I-N nodal capacitance, adjusted

From this new conversion factor, the thick P-I-N nodal capacitance was estimated at approximately 43fF.

$$C = 1.6 \cdot 10^{-19}(\text{coul}/e^-) \cdot 1.83(e^-/\text{ADU}) \cdot (1\text{ADU}/6.1\mu\text{V}) \cdot 0.9 = 43\text{fF}. \qquad \text{(8-3)}$$

The result now seemed more reasonable — 30 fF from the bare multiplexer, 8 fF additional capacitance from the grid, and another 4 fF from the indium bumps. This breakdown is shown in Figure 8.8. Note that the inter-pixel coupling capacitors do not contribute to well capacity, and are not included here.

8.3 Thick P-I-N MTF, adjusted

The expected edge spread now had a new component. This new edge spread model, given generally by Equation 3-4, had a value for α set to 0.0375 from the autocorrelation measurement of inter-pixel coupling. The exact Gaussian diffusion coefficient was still treated as an unknown parameter — expected to be in the neighborhood of four microns (see Chapter 7) but with relatively high uncertainty, given the lack of available tabulated data.

Figure 8.9 shows the best fit model plotted against the normalized and averaged data. Figure 8.10 shows this same plot with expanded detail. The best fit curve for the simpler model in Equation 8-2 suggested almost twice as much diffusion, but did not follow the curve well at all. When the effect of inter-pixel coupling was introduced, the model (solid line) fit the shape of the data much more closely.

The Gaussian shape parameter was varied in the model to find the best fit. The mean square error between the model and the binned edge data was tallied. The shape parameter that provided the lowest mean square error, $b = 0.475$, was used as the estimate of spreading.

A shape parameter of $b = 0.475$ corresponds to a σ of $0.475/\sqrt{2\pi} = 0.19$ pixels, or roughly 5.1 micron spread in the detector. Thus, this detector delivers on the promise of extremely low crosstalk from lateral diffusion — at a temperature of 30K, anyway. 98.4
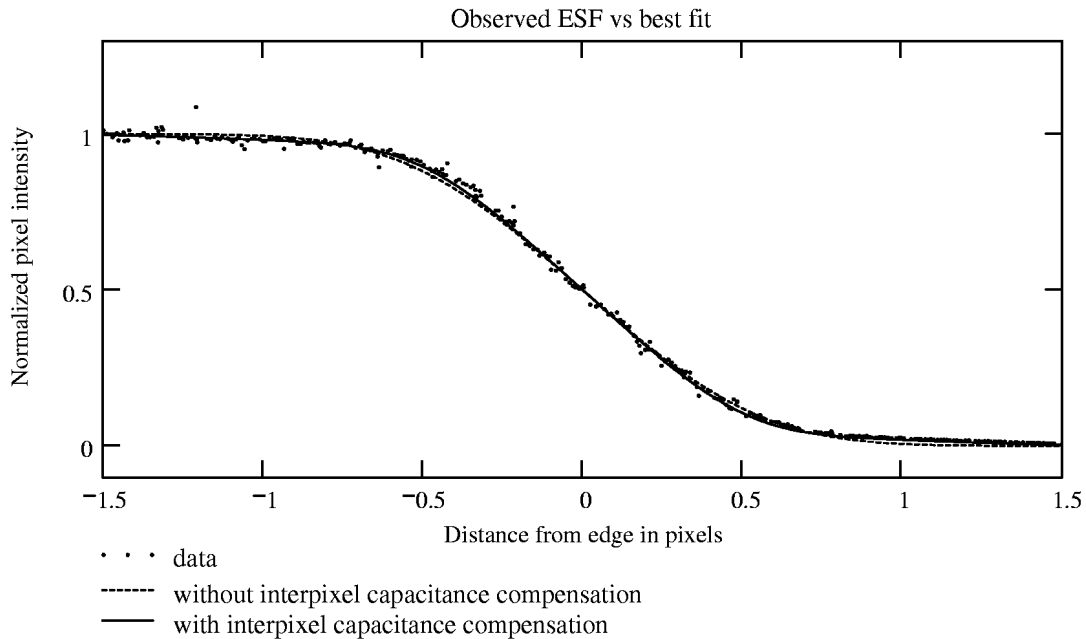
Figure 8.9: P-I-N edge spread did not fit the model well — until the model took inter-pixel coupling into account. Then the agreement was remarkable. At this scale, the disagreement is not readily apparent. Figure 8.10 show a small section of this plot in more detail.

percent of the carriers produced by a point source centered on a pixel should remain in that pixel's detection node; each immediate neighbor node should only get 0.4 percent.

The edge spread was modeled at all angles by developing Equation 3-4. The initial model, Equation 7-15, was one-dimensional. If an edge is not perfectly vertical or horizontal, the more general edge spread function of Equation 3-4 had to be used. Plugging the observed inter-pixel coupling and diffusion spread derived from the vertical and horizontal data into Equation 3-4 allowed the expected 45 degree edge response plotted in Figure 8.11 to be calculated. A vertical deviation of approximately 0.02 can be seen in the toe and shoulder of these theoretical edge spreads. The observed edge spreads, averaged in the
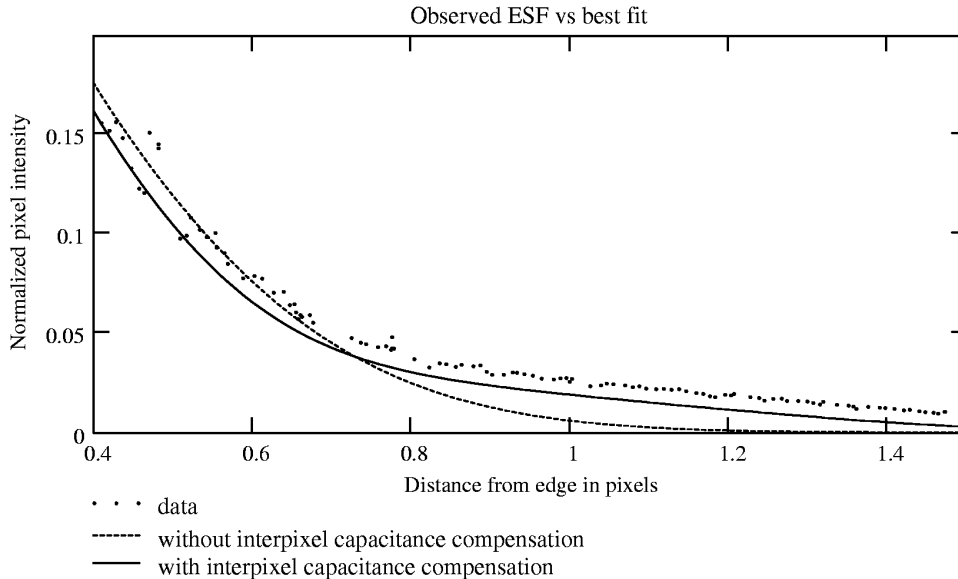
Figure 8.10: This expanded plot of the observed and expected P-I-N edge spread shows the "toe" of the edge — where the interpixel coupling had the most influence. The coupling created a slight "echo" of the main edge, shifted one pixel over, as seen in the ramp from 0.8 and higher. The Gaussian-diffusion-only model did not predict this ramping.

45 ± 22.5 degree range, and in the 0 ± 22.5 degree range, are plotted in Figure 8.12. This averaging over a full 45 degree range naturally reduces the separation somewhat. A vertical deviation of approximately 0.01, half of the theoretical, is observable in the plot. Given that the data was averaged over the widest non-overlapping ranges of angles, the compression by a factor of two seems sensible.

It has been suggested that many edge profiles could be processed to yield a sub-pixel sensitivity map such as the maps produced by spot-scanning and in principle this is true. However, the assumed pixel response function fits the observed data so nicely for this device, so it is arguable that little insight would be gained from this more complex analysis.
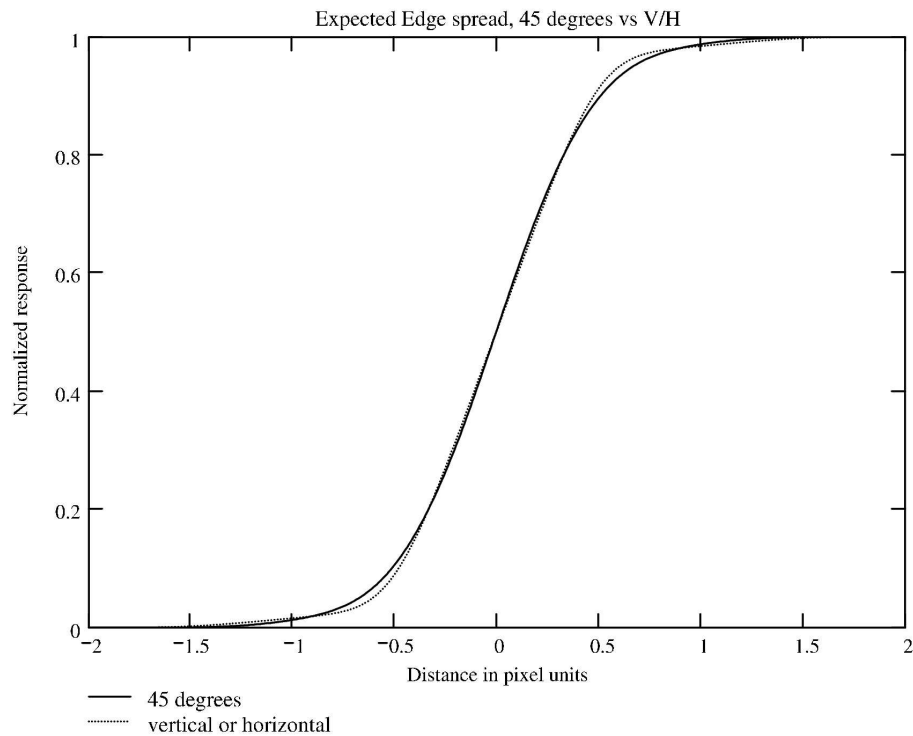
Figure 8.11: The model predicted a slightly softer edge spread for diagonal edges, visible mostly in the toe and shoulder of the edge.

In the frequency domain, these results are expressed by MTF curves shown in Figure 8.13. The detector diffusion component at the top shows the most faithful spatial reproduction of the three components (despite its incredible thickness). The square pixel (27 micron pitch) is the worst component. In a newer device, this is easily remedied by a finer pixel pitch. Somewhere in the middle is the loss in MTF due to inter-pixel coupling. At lower frequencies, it is almost identical as the square pixel. (The frequency axis is logarithmic, from 0.1 Nyquist to 1.0 Nyquist)

This loss in MTF from inter-pixel coupling is not as serious a problem. Since the coupling attenuates shot noise and high spatial frequency signal alike, there is no loss of
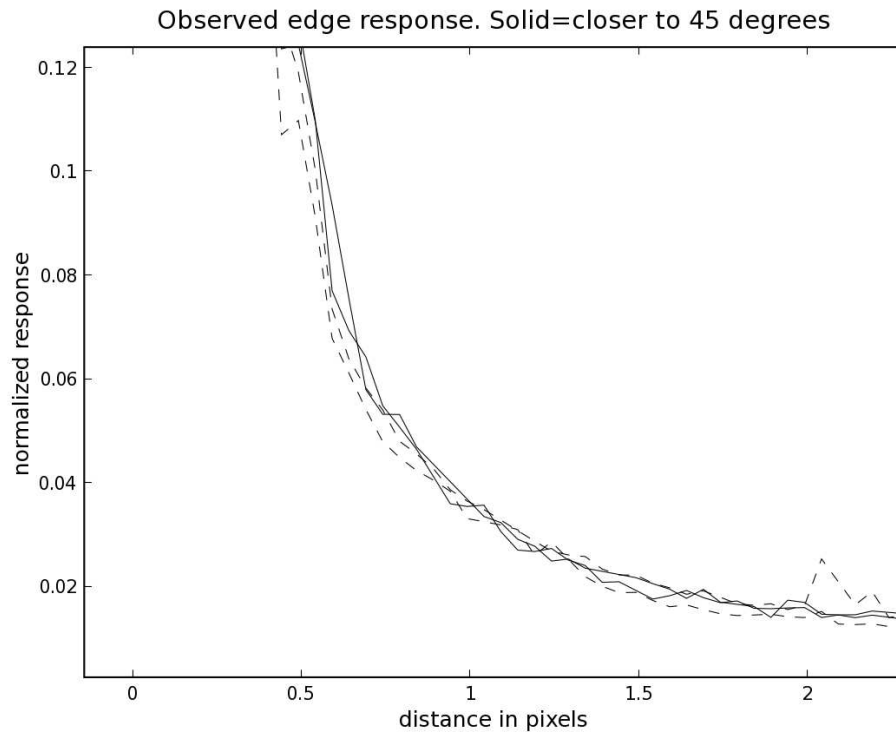
Figure 8.12: The actual ±45 degree edge data traces (solid lines) showed a slightly softer edge compared to vertical and horizontal traces(dashed lines). Edges were averaged over a ±22.5 degree range — this averaging blurred the distinction somewhat.

information. If read noise is sufficiently small, inverse filtering may be successfully applied.

8.4 Thick P-I-N grid voltage effect

The grid voltage is believed to be optimally set as positive as possible, without accumulating carriers on the back surface and causing image degradation. Raytheon suggested simply setting it at Vdduc, so this was the default setting. Curious what such degradation might

MTF in Si Pin Array
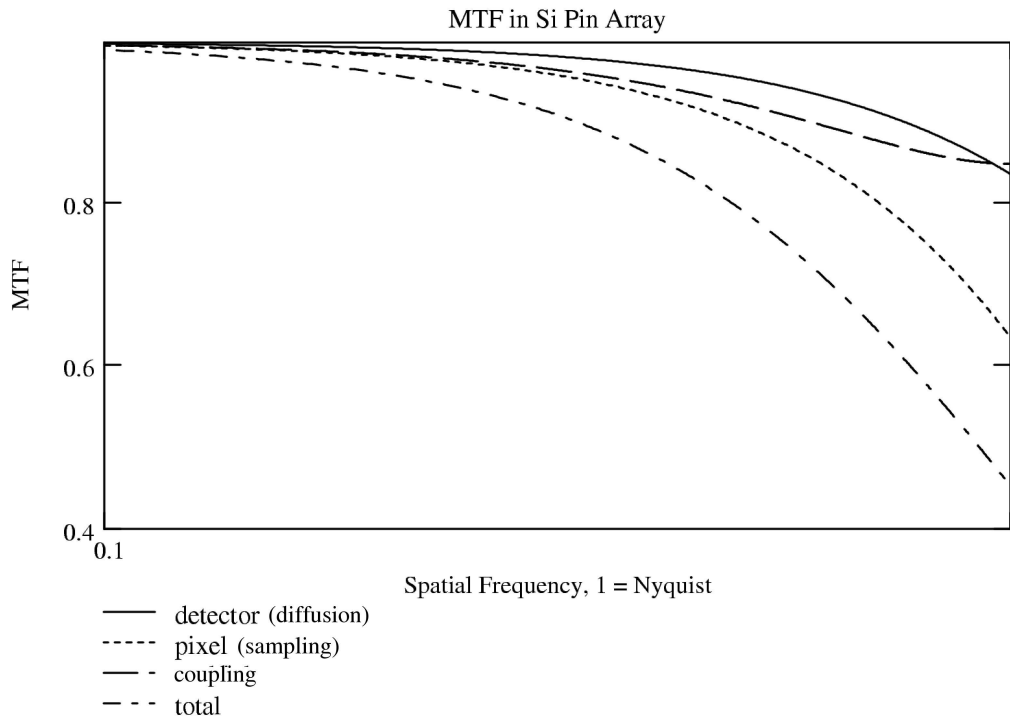
Figure 8.13: P-I-N Modulation transfer function was a result of three components — diffusion in the detector, averaging by the square pixel, and interpixel capacitance. The inter-pixel component is cosine shaped, but the frequency axis above is logarithmic.

look like, images were taken with the grid at varying voltages. Strange things happened when the grid was set at more negative voltages, as shown in Figure 8.14.

Bringing the grid voltage more positive restored image quality. Figure 8.15 was taken with the grid one volt more negative than its recommended value, but the image seems to be quite good compared to Figure 8.14. Since the detector nodes go more positive as they integrate, the recommended value probably allows another volt of signal swing before the effect seen in Figure 8.14 returns.
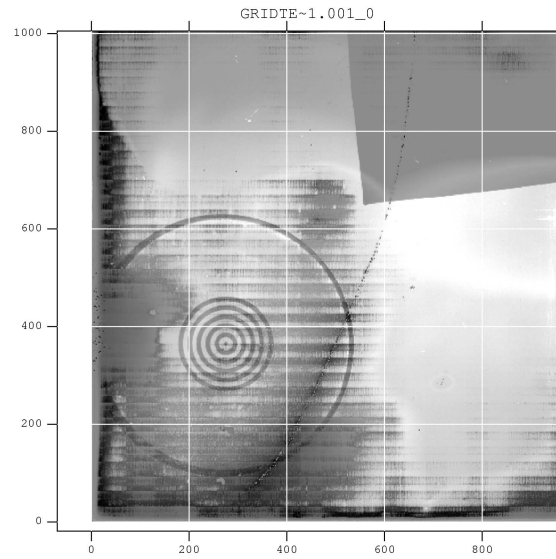
Figure 8.14: When the P-I-N grid voltage was improperly set at -5.0 volts, sections of the resulting image appeared to be washed out.
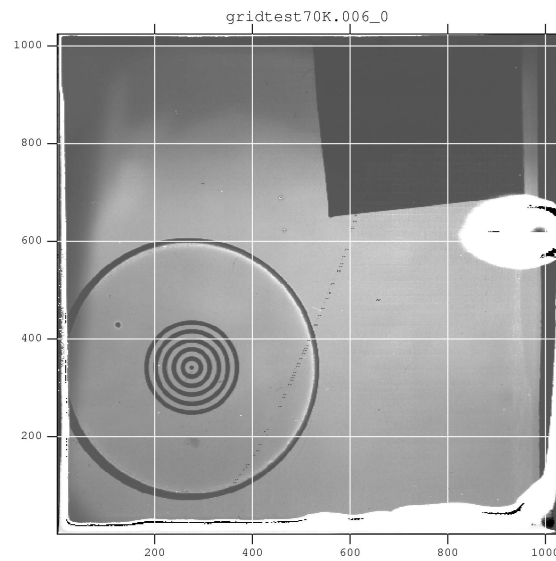
Figure 8.15: Adjusting the grid voltage to be slightly more positive (-4.6 V) greatly improved the image quality.

8.4.1 Estimated P-I-N well depth

Images were obtained that used the full range of the converters, (0.4 volts, or 65535 ADU) so the well depth is at least $1.83e^-/\text{ADU} * 65535 = 120,000e^-$. Since the detector is a current source, the DC well depth is arguably limited only by the multiplexer; thus $300,000e^-$ appears possible given the 1 volt swing measured in the gain test. Practically, DC and AC well depth (pixel bright to pixel dark) are also influenced by the grid voltage. Well depth headroom should increase as this grid voltage goes more positive. The consequences of raising the grid voltage above its suggested value were not investigated.

8.4.2 Thick P-I-N Read Noise (35K)

The read noise of the P-I-N array was measured in RMS electrons with two experiments. In one experiment, a pair of short integration time CDS (Fowler-1) images were subtracted from each other, and the noise in the difference image was analyzed. The RMS noise in Analog to Digital Units (ADU) was observed to be 6 ADU RMS. Dividing by the square root of two yielded 4.24 ADU in a single image. Combining the results of these experiments yields a read noise of $7.77e^-$ at 35K.

8.4.3 Thin P-I-N inter-pixel coupling

Two additional P-I-N arrays, these ones thinned and blue-enhanced, were also delivered to RIT as part of the NASA/Raytheon fabrication contract. Less extensive testing was done with these devices. These devices had the back bias contact implanted after thinning. One was implanted with 15KeV ions and the other with 10KeV ions, otherwise they were identical.

Given the thinner detector, it seemed possible that the inter-pixel coupling could have been reduced very slightly by the closer proximity of the pixels to the back bias. No

-95	-1361	-1024	3007	-2412	-5751	3696	-4630	1099
2808	3155	3620	365	2755	1347	4449	1121	3095
2459	3751	4329	5676	12601	10844	570	1120	-3153
1138	4612	6108	28680	128334	36731	4428	936	-2773
2496	4732	16602	126258	2027889	126122	14990	3135	4766
-2261	563	5687	37702	128195	29233	5965	3582	3094
-1387	2371	2126	11513	12335	6426	5351	5569	5207
3324	1863	3541	-51	1640	247	2940	5237	4230
-477	-5663	3618	-3366	-3703	3240	-1552	-91	-1471

Table 8.2: The thinned P-I-N devices also exhibited a large amount of interpixel coupling. These correlation data are from the 15KeV implanted detector.

significant reduction in coupling was observed. Table 8.2 shows sample autocorrelation results for that device. The ratio of central energy to total energy is 0.76 for the 15KeV detector and 0.78 for the 10KeV detector — a slight reduction in coupling, if any.

The 10KeV thinned P-I-N array results shown in Table 8.3 exhibits stronger correlations a decent distance from the center. This seemed odd. Further investigation of the data revealed some instability in the liquid crystal tunable filter that explains the observation. The tunable filter requires occasional "exercise" to improve stability — the thick detectors were characterized using a fixed glass filter.

8.4.4   Thin P-I-N Conversion Factor

The 15KeV thinned P-I-N device, at a signal of 16840 ADU, yielded noise of 85.1 ADU. This is an uncompensated estimate of 2.32 electrons per ADU, or a compensated estimate of 1.837 electrons per ADU. Compensation factor for the 15KeV device was measured at 0.76.

-13464	-2236	-9115	1705	-15288	-13212	-4609	2285	-10064
-12501	-15599	-23297	-16160	-21311	-11027	-4501	-9418	-12611
-5156	-6603	-7495	4299	1536	-366	194	-7783	-7670
-9481	2617	-10106	30337	191212	38960	-2623	5664	2640
44733	-2693	1267	211068	3412237	212055	-1861	-7419	50768
351	11003	453	41765	188103	28899	-6917	5678	-10610
-4875	-8157	4943	2075	-5822	4989	-8144	-7794	-2555
-10464	-11498	-1411	-14840	-30647	-18028	-19887	-12925	-6067
-9823	-1784	-6805	-18590	-30503	-3075	-12170	3055	-11577

Table 8.3: Correlation observed in 10KeV thinned P-I-N array was similar to the 15KeV data. The background noise in these data seems unusually high, indicating that non-Poisson events have slipped through the cosmic event rejection filter.

$$C = 1.6 \cdot 10^{-19}(\text{coul}/e^-) \cdot 1.837(e^-/\text{ADU}) \cdot (1\text{ADU}/6.1\mu\text{V}) \cdot 0.9 = 43.4\text{fF}. \quad (8\text{-}4)$$

For the 10KeV thinned P-I-N device, a signal of 14128 ADU yielded noise of 74.52 ADU — an uncompensated estimate of 2.54 electrons per ADU. The compensation factor for the 10KeV device was measured at 0.78, resulting in a compensated estimate of 1.98 electrons per ADU. Using a signal path gain of 0.9 and conversion constant of 6.1 microvolts per ADU in the controller electronics, the nodal capacitance is thus estimated as:

$$C = 1.6 \cdot 10^{-19}(\text{coul}/e^-) \cdot 1.98(e^-/\text{ADU}) \cdot (1\text{ADU}/6.1\mu\text{V}) \cdot 0.9 = 46.7\text{fF}. \quad (8\text{-}5)$$

The gain of 0.9 was assumed, not actually measured, for these devices.

8.4.5   Thick P-I-N Dark current

It was expected that the dark current would be immeasurable below 150K, and this proved to be the case. Thermal fluctuations of tenths of a degree Kelvin from finite temperature controller resolution caused DC shifts in the output that made direct measurement of dark current impossible. Measuring the noise due to dark current was more feasible, and in 1000 second integrations, this noise did not rise significantly until 160K. Above 200K, an increase in noise became noticeable at longer integrations. Dark current was not uniform, and "hot pixels" became apparent.

At lower temperatures, dark current was estimated by looking at the noise in the difference of two long integrations with no illumination. The sigma, in ADU, was converted to a sigma in electrons by the conversion factor. Squaring this value gave a variance in electrons squared which, assuming Poisson statistics for the dark current, should be equal to the mean accumulated dark current in electrons. Inter-pixel capacitance compensation is required for this measurement. Dividing by the effective integration time (twice the integration time of each frame) yielded a dark current estimate in electrons per second. Figure 8.16 shows an Arrhenius plot of these noise-derived dark currents.

When the DC signal was significant enough in the images, direct measurement of dark current was done instead. The measurements below 200K were on the "engineering" array, and the measurements 200K and above were on the "science" array.

An Arrhenius plot of these data, in Figure 8.17, shows sensible linear behavior 200K and above (1000/T $<=$ 5 in the plot,) where an actual shift of image DC level was observable. The measurements made below 200K show more dark current than would be expected, and probably reflect some other source of noise than actual dark current (which should be nonexistent at those temperatures)
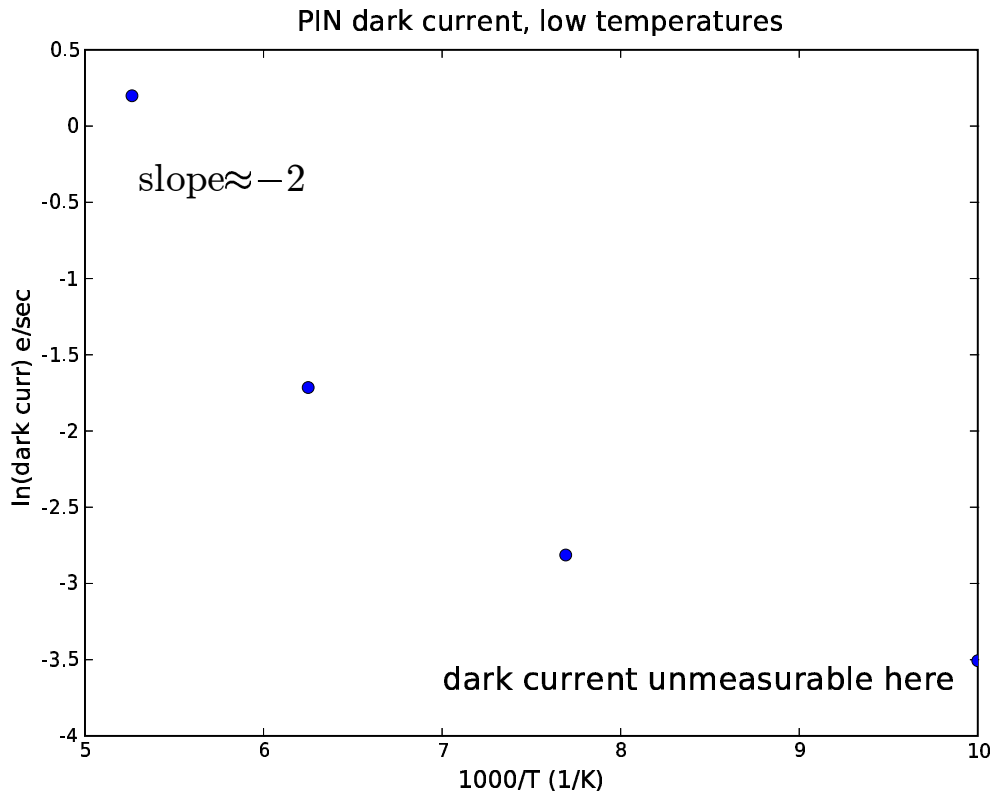
Figure 8.16: At very low temperatures, dark current was not measurable directly. This Arrhenius plot shows estimated equivalent dark current based on observed noise as a function of temperature.

8.4.6 Bare SB226 inter-pixel capacitance

After discovering inter-pixel capacitance, the question of where else it was to be found (and what other effects it might cause) was considered. Bare SB226 multiplexers still act as imagers, just not very efficient ones — made from silicon, they can generate and trap photocarriers. A bare 226 multiplexer was illuminated uniformly and many images were taken to collect the Poisson noise data needed to look for evidence of inter-pixel coupling, and some of these data are shown in Table 8.4. Only slight evidence of significant inter-
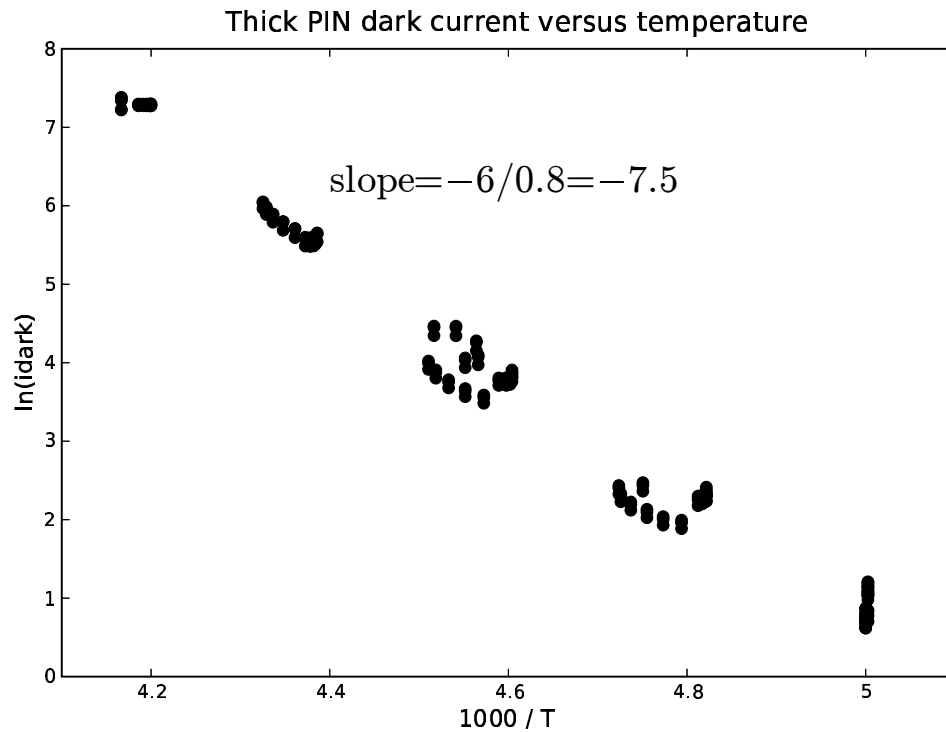
Figure 8.17: At higher temperatures, dark current was more easily measurable. The variation in the colder data is believed to be a result of temperature changes during integration. Slight variations in device temperature during the longer integrations required for the lower dark current measurements caused the estimated current to fluctuate.

pixel coupling was found in the bare multiplexer data, however. For a raw center correlation value of approximately 3×10^6, the nearest neighbor correlation was on the order of 2×10^4, two parts in three hundred, and barely above the noise in the correlation response (several thousand counts). This indicates an inter-pixel coupling of one part in three hundred — roughly 0.33 percent maximum, but given the possibility of other mechanisms to create this correlation (covered later in the InSb correlation) the result is not trustworthy, merely interesting. It does indicate reliably that inter-pixel coupling is not significantly present in the bare 226 multiplexer. This particular multiplexer did not have indium bumps or epoxy

6567	10801	-10158	-3960	-4049
-4788	8639	22304	5101	1482
12625	31178	3021758	31509	10734
578	4209	19363	8320	-2377
-4549	-3203	-11861	13122	1818

Table 8.4: A small amount of correlation was observed in Poisson noise data taken in a bare SB226 multiplexer. A small amount of correlation appears to be present, but it is not significantly above the coefficient noise level.

deposited on it. It is suspected that simply adding bumps and epoxy may create a slight but measurable increase in interpixel coupling.

Given the relatively strong coupling observed to the reset and supply rails, a tiny result makes sense. Buses like these act as Faraday cages between the pixels, and reduce their inter-pixel coupling. An increased nodal capacitance is an unfortunate side effect of this Faraday shielding.

The noise correlation data and known system gains yielded enough information to estimate the bare mux capacitance — an estimate of 30 fF. The capacitance of the same multiplexer had been estimated at 28 fF by the NIR lab at the University of Rochester, a similar figure.

8.4.7 InSb inter-pixel coupling

An experiment was performed to determine if the effect was to be found in the per-pixel depleted indium antimonide detector arrays being tested at the University of Rochester's NIR lab. It was common to measure quantum efficiency greater than 100 percent at wavelengths where this was known to be impossible. Similarly, DQE measurements of 100 percent at wavelengths where stochastic gain was apparently present[86] and stable DQE

-2613	987	611	-638	-1	1175	514	1640	656
-559	-850	-580	-1537	-614	-228	-129	372	-111
-392	608	296	-441	-927	-1170	-242	536	-1336
1304	-252	-1186	1499	14341	2357	-482	513	-856
5773	-519	-187	15236	476374	15200	145	-319	6460
-645	682	-140	2609	14502	1173	-1015	-191	1426
-997	908	-191	-1373	-1295	-296	734	500	462
-664	-83	-600	-196	-1100	-1627	-274	-1190	-838
960	1335	257	1128	-430	-1311	687	678	-2203

Table 8.5: Correlation tests on an indium antimonide detector array indicated a small amount of coupling — but more coupling than hot pixel tests suggested. Extra correlation may have come from photoconductive gain.

with increasing gain from bias[73] (both imply gain without noise) have been published. Inter-pixel coupling may offer an explanation for these observations.[1]

Autocorrelation tests on data collected on representative indium antimonide arrays indicated smaller, but measurable and significant inter-pixel coupling. Table 8.5 shows one the observed correlations.

This degree of coupling (1.5 percent) appeared to be too large. It implied over a ten percent error in many measurements that seem otherwise reasonable. Hot (defective) pixels seemed to indicate that the coupling was more on the order of half a percent. Simulations

---

[1]The IBC detectors referred to in [73] were assumed to be fully depleted at a 1 volt bias, but this threshold was determined by an apparent divergence of gain and noise at this voltage. If the devices are indeed fully depleted at this voltage, than interpixel coupling should not change with any increase in bias. It is the author's opinion that at 1 volt of bias, the devices were merely sufficiently depleted such that interpixel coupling started to become significant — and that photoconductive gain did not occur until a much higher bias, perhaps 2 or 3 volts. This disagreement indicates an area where further research is needed.

of the coupling also indicated a smaller value, on the order of half a percent, was more likely.

8.4.8 Stochastic gain and inter-pixel correlation measurement

Since these indium antimonide detectors are infrared and have a much smaller band gap, stochastic gain in the detection process is more likely. The presence of any stochastic gain will occasionally produce two (or more) carriers for an incoming photon. Occasionally, one of those carriers will wind up in a neighboring pixel from its sibling particle, and this will create correlation of noise in neighboring pixels. J-band illumination was used for these measurements, and some stochastic gain is present in the detector at this energy. The experiment should be repeated with longer wavelength illumination.

Thus, one caveat to keep in mind while attempting to measure the correlation — the wavelength must be filtered to ensure that stochastic gain is not present in any significant degree. (This should be done anyway — such gain will also interfere with the expected Poisson statistics and produce errors in measurement of conversion factor. It will introduce additional noise, rather than reduce the observed noise as inter-pixel coupling does.)

The difference images in Figures 8.18 and 8.19 show single particle events (muon hits) observed in the silicon P-I-N detectors over the 2000 second total integration time. Such events created huge artificial correlations in the silicon correlation tests, and frames containing these events were actively detected and removed from consideration. Significantly smaller events of stochastic gain would not be detectable, however, and must be prevented if possible.

38minus37.fts_0
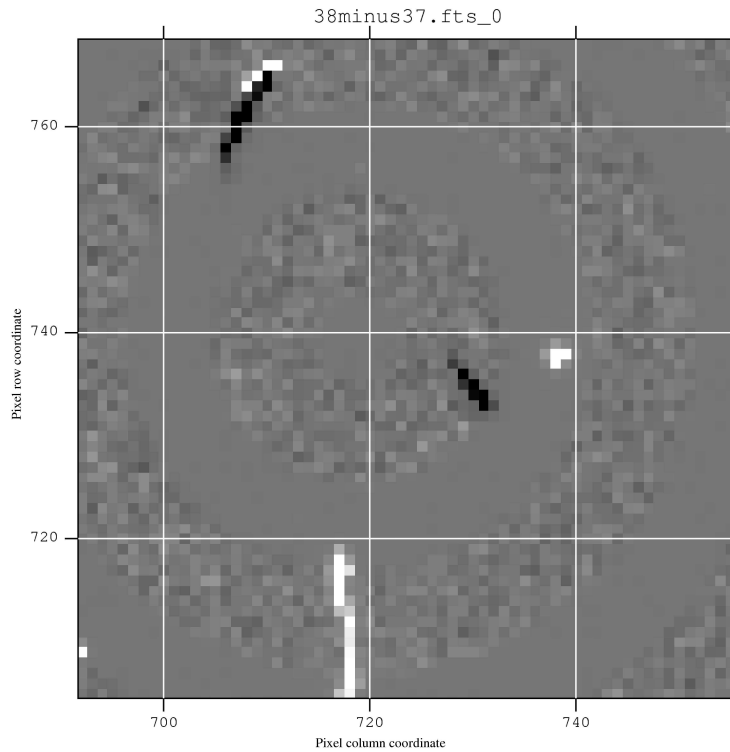
Figure 8.18: This difference image of a pair of 1000 second integrations shows several things. The differences of black rings show no photon noise. The illuminated ring differences show observable near-white noise. The dark and light streaks are higher energy events that released many carriers and created correlation in adjacent pixels. Note the sudden jump between columns in the lower white streak.

8.4.9   Nonlinear inter-pixel coupling

Another possible explanation for the InSb discrepancy is that the inter-pixel coupling is expected to vary significantly with bias in per-pixel depleted detectors. When the detector nodes are fully reset, the depletion region is wider, the pixels are electrically closer together, and the inter-pixel coupling should be stronger. As the nodes discharge during integration, the depletion regions shrink and the inter-pixel coupling reduces as the nodal capacitance increases.
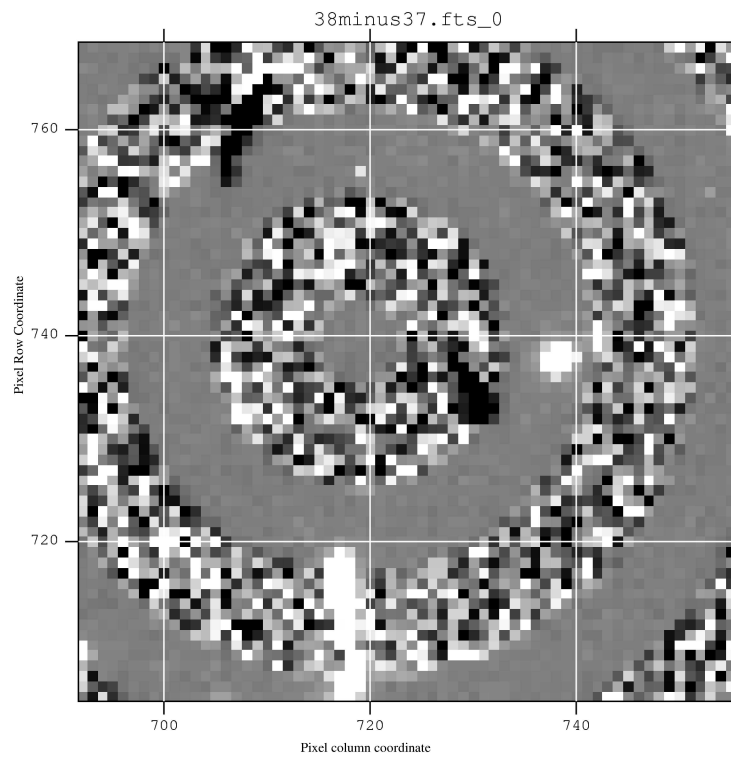
Figure 8.19: An enhanced-contrast version of the previous image shows the noise in the white rings in greater detail.

Chapter 9

P-I-N Quantum Efficiency

The spectral sensitivity of both thick (prototype) and thinned P-I-N devices was measured.

An Ealing stabilized power supply, catalog number 27-3540 S/N 0807 was used for supplying the illumination source. This supply was tested for stability and proved stable enough for use. It drove a variety of illuminators, including several 12V type 7023 lamps, a five watt white-light LED and a narrow-band infrared LED.

For the broadband sources, a Varispec liquid crystal tunable filter, model VIS2-10 S/N 50234 controlled the wavelength up to 720 nm, and a diffraction grating type manually tunable filter selected wavelengths up to 820 nm. An LED infrared emitter was used for 940 nm, and a narrow-band 1094 nm filter was used to measure QE near the cutoff wavelength.

A Graseby 370 / UDT type 621 meter served as the calibrated detector. This NIST-traceable 1 cm photodiode / calibrated pico-ammeter combination was calibrated as a unit over narrow bands in the spectral range that the quantum efficiency was measured in.

A simple optical system was set up to illuminate the array in a small area. This basic setup is shown in Figure 9.1.
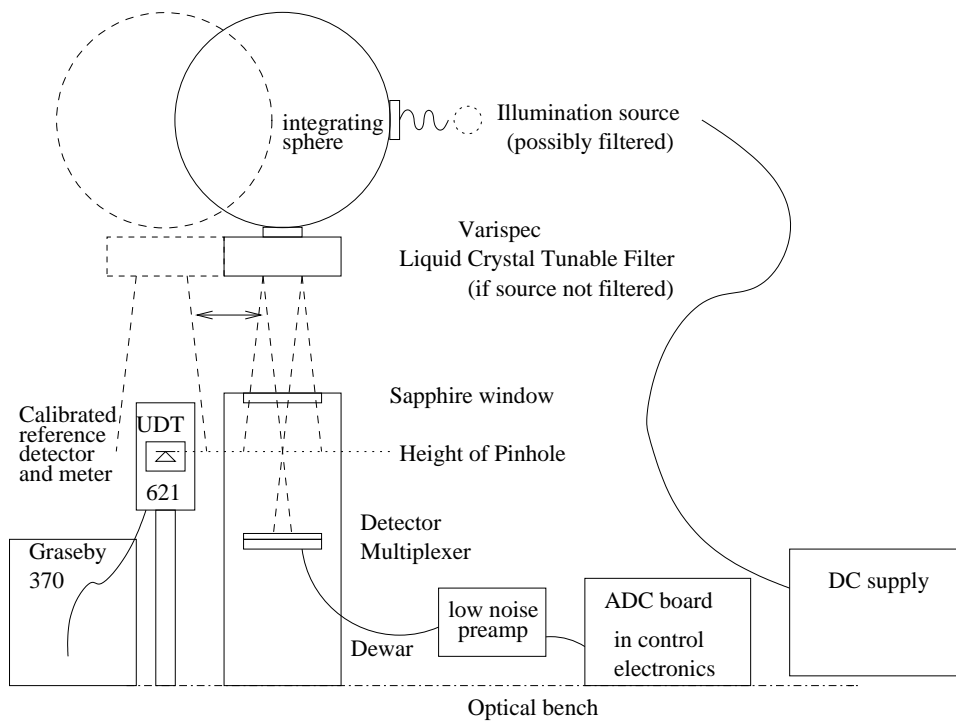
Figure 9.1: Quantum efficiency testing required stable calibrated illumination. A UDT calibrated light meter measured optical power density at the same height as the pinhole in the dewar. The figure is not to scale — a relatively large distance separated the integrating sphere and the dewar to reduce the effect of path length errors.

9.1 Visible Quantum Efficiency

Quantum efficiency was measured in the visible range with a stable illumination source (12 Volt DC power supply and high-power white LED) an integrating sphere, and the Varispec liquid crystal tunable filter supplying the controlled illumination. A pinhole of known diameter (200 μm) and at a known height over the optical bench allowed a controlled amount of illumination through from the source to the array. Using a calibrated meter (UDT 247, SN31686), the illumination at the height of the pinhole was measured over all liquid crystal frequencies. The optical sensor's position was varied horizontally to check the
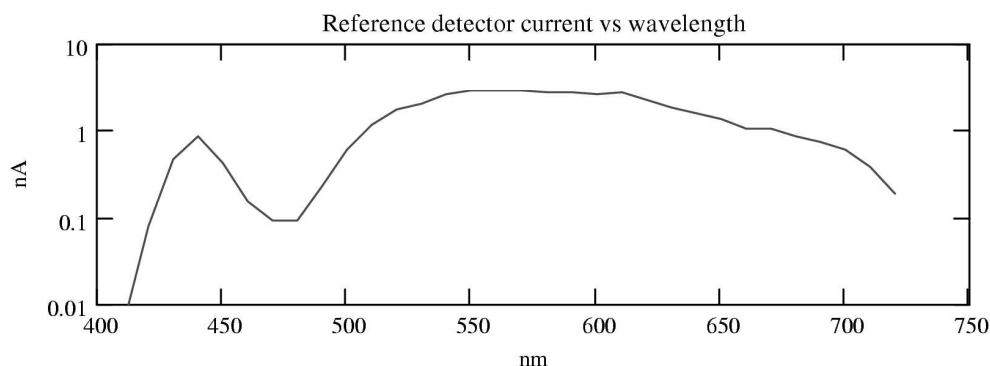
Figure 9.2: A white light LED was used as an illumination source. These LEDs have a blue monochromatic source that excites phosphors which re-emit at longer wavelengths.

uniformity of illumination at this position under the sphere. Then the illuminator assembly was slid into position over the dewar, and images were taken over varying wavelengths and temperatures.

Concern that the illumination source might drift during the data collection (which took several days) prompted a re-check at the end of collection. The illuminator was rotated back over the calibrated detector, and the source intensity measurements were repeated. This verified that drift had not occurred — the before and after measurements were well within one percent of each other.

The measured white light LED intensity versus wavelength is plotted in Figure 9.2. The transmittance of the sapphire window is shown in Figure 9.3. It is a constant 0.85 over the wavelengths used here.

The images collected were analyzed with respect to the measured pixel capacitance, yielding the actual number of electrons captured. The actual number of photons striking the array was computed for comparison, using the calibrated illumination profile, the transmittance of the sapphire window, and the pinhole diameter. The photons struck a circular area of the array. The diameter of this circle was approximately 120 pixels. Responsive

147
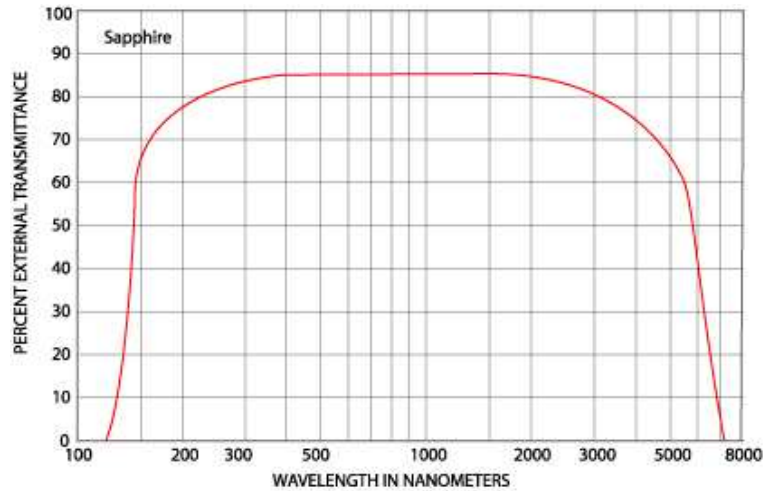
Figure 9.3: The sapphire window transmittance is mainly limited by surface reflections — and remarkably flat over a wide spectral range. This data, from Melles-Griot, shows a transmittance of 0.85 at the wavlengths used in this thesis.

quantum efficiency, the ratio of detected electrons to incoming photons, is shown plotted in Figures 9.5, which compares three devices, and 9.6, which shows just the thick engineering P-I-N device in detail as a function of temperature as well. The pair of thinned P-I-N arrays (40 um thickness) were only tested using the visible liquid crystal tunable filter setup.

Both thick and devices were manufactured with blue-enhancing A-R coatings. The coating on the thick devices was a simple one. The thinned devices show improved blue-enhancement.

9.1.1 Very Near IR Quantum efficiency

The liquid crystal tunable filter allowed automatic control of the wavelength of light, but the device's working range only extended to 720 nm. The white light LED also performed poorly in this wavelength range. To obtain QE measurements at longer wavelengths, the

148
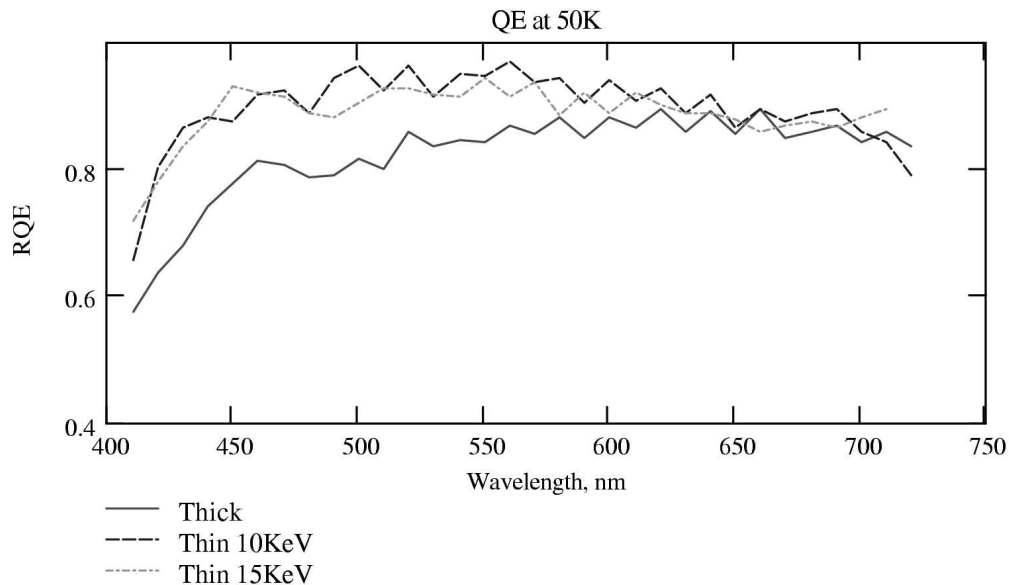
Figure 9.4: Visible QE (uncertainty≈4%) of Silicon P-I-N, 50K.

Figure 9.5: Visible RQE of three P-I-N devices is shown here. The thinned devices exhibited improved performance in the blue relative to the prototype, with a value of approximately 0.9 for most wavelengths. Uncertainty is ≈ 4 percent except at 410 nm where the source illumination was low. Uncertainty for this reading is ≈ 10 percent.

source was changed to an incandescent bulb, and a diffraction-grating type manually tunable filter was used instead.

Images were taken at 760 nm, 820 nm, and 870 nm using the diffraction grating setup. These results, for the thick engineering P-I-N, are shown in Appendix A in Table A.1. These numbers agree nicely with the liquid crystal tunable filter measurements.

9.1.2   Cutoff-wavelength measurements

A 940 nm infrared LED served as a source for a "spot" measurement shortward of the cutoff wavelength, and a fixed 1094 nm narrow-band filter was used with the incandescent
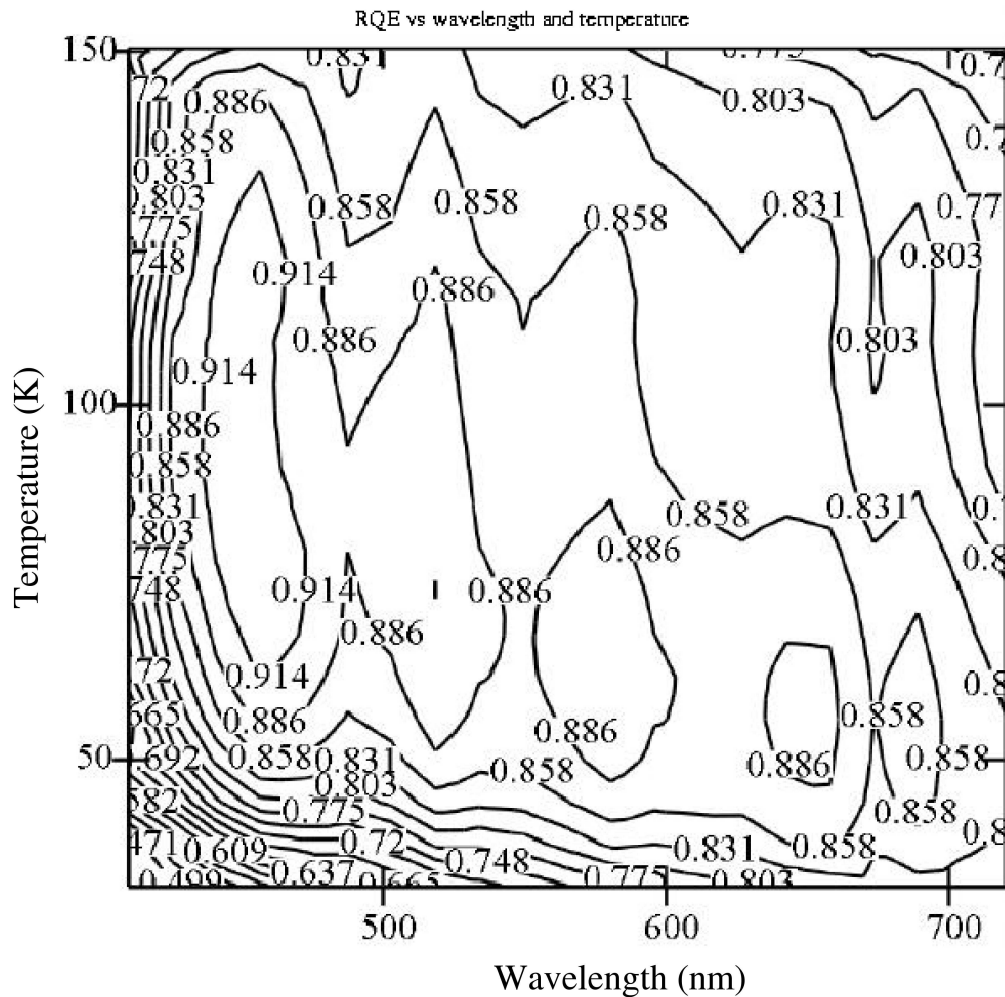
Figure 9.6: This plot shows the thick P-I-N quantum efficiency at visible wavelengths and various temperatures. The lower left corner shows that blue response deteriorates at lower temperatures. The lower right corner and far right edge indicate improvement in red response at lower temperatures.

source to measure QE just outside the cutoff frequency. QE at 940 nm was measured at 0.57 at temperatures below 100K, rising slightly to 0.58 at 150K. QE at 1094 nm was poor, as expected: 0.007 at low temperatures (30K ad 78K) and 0.02 at 154K. The 940nm LED and 1094nm filter QE measurements are reported in Appendix A at the bottom of Table A.1. The low QE at 940 nm (where silicon is usually quite efficient) is not entirely unexpected — these prototype arrays were fabricated with a blue-enhancing A-R coating. It is somewhat unexpected that the 940 nm efficiency did not drop more noticeably at low temperature, however. Penetration depth, tens of microns at 940 nm and 300K, increases as the temperature drops. Apparently the detector is thick enough that even at 30K the detector is one or more penetration depths thick. It also appears, as shown on the right side of Figure 9.6 that the A-R coating gets better at longer wavelengths as temperature drops.

9.2   Error analysis for quantum efficiency measurements:

The system can be described this way: A luminance, known at the height of the pinhole, impinging on this pinhole after passing through a sapphire-windowed dewar in the optical path, provides photons striking the surface of the array. These photons cause the nodal capacitance to charge over time. The exposure time is controlled electronically with a shutter. The voltage on the capacitance drives the multiplexer signal path (which has a certain gain) and then the preamplifier. This voltage is measured by an analog-to-digital converter in ADU (Analog / Digital converter Units). These ADU measurements are converted to a measurement of quanta by knowing the conversion factor of the system — which involves measuring the capacitance.

The total ADU converter counts observed (summed over all illuminated pixels) is:

$$ADU_{observed} = \frac{E_v T_{sapphire} A_{pinhole} \tau_{int} \eta_\lambda \lambda g_{mux} g_{preamp} k_{aduc} q_e}{C_{node} hc}. \tag{9-1}$$

where:

E_v is the measured optical flux (per unit area) at pinhole height with no sapphire window present.

$T_{sapphire}$ is the transmissivity of the sapphire window.

$A_{pinhole}$ is the area of the pinhole.

τ_{int} is the integration time.

λ is the wavelength of the incoming radiation.

g_{mux} is the gain of the multiplexer signal path.

g_{preamp} is the gain of the preamplifier board.

k_{adc} is the conversion constant for the analog to digital converter boards in ADU per volt.

C_{node} is the nodal capacitance.

The rest are constants:

q_e is the charge on an electron in Coulombs.

h is Planck's constant.

c is the speed of light.

η_λ is the real quantum efficiency as a function of wavelength (assuming no photoconductive gain)

Some of these items are correlated. C_{node} was measured with the same system, so it also depends on the gains g_{mux}, g_{preamp}, and k_{adc}.

Also, the reference meter is a silicon detector. Uncertainties in λ affect the measured flux E_v. This correlation will not be addressed. Since the meter fundamentally operates as a photon counting device, it will see the same error and the effect should cancel to some degree if the detectors have similar responses. They are both silicon, but they do have different coatings.

Uncertainty of the power at pinhole is from both the meter and uncertainty in height and position matching. Uncertainty from positioning is estimated at 2 percent. The pinhole diameter is specified by the manufacturer as 200 microns ± 6 microns. Assuming a uniform distribution, this corresponds to a diameter uncertainty of roughly 1.7 percent. This puts its area as uncertain to 3.4 percent, as it goes with the square of the diameter. The integration time is very tightly controlled and its uncertainty can be ignored. The reference meter is good to 0.7 percent, except at the lowest signal strengths where it may go up to 5-10 percent. The transmittance of sapphire window is assumed known within 1 percent. The filter center frequency is good to 1 percent. The gain test did not technically measure the unit cell output FET gain, since both the unit cell drain and gate were swept simultaneously but the device is not operated in this mode. Previous tests indicated it was safe to assume a unit cell signal gain of unity. The output FET gain measurement is assumed accurate to 1 percent. The preamp gain uncertainty is estimated at 1 percent. The converter board gain is known to 0.005 percent. The uncertainty in measuring QE nodal capacitance, however, is a little more complex. Nodal capacitance was measured on the *same* system, using the noise squared versus signal method.[65] Since it was, any errors in its measurement are correlated with the ADU measurement and it cannot be treated as an independent error source.

Given a signal in ADU and a noise level in ADU squared, noise-squared versus signal results in a conversion constant K_{node} quanta per ADU that matches the observation. A repeatability error of 1 percent is assumed for the K_{node} observations. The estimate of nodal capacitance is a function of the system gain — knowledge of how many ADU are produced at the converter per volt at the node capacitance is needed in order to estimate the nodal capacitance.

$$C_{node} = \frac{coul}{volt} = \frac{quanta}{ADU}\frac{coul}{quanta}\frac{ADU}{volt}. \tag{9-2}$$

So the nodal capacitance, expressed in these other quantities, is actually

$$C_{node} = K_{node}q_e g_{mux} g_{preamp} k_{adc}. \tag{9-3}$$

and the model of observation (in quanta) is now:

$$Q = quanta_{observed} = \frac{E_v T_{sapphire} A_{pinhole} \tau_{int} \lambda}{K_{node} hc}. \tag{9-4}$$

In other words, errors in the system gain are not a factor in the measurement of quantum efficiency. This result, perhaps unexpected, is sensible. Poisson statistics allow measurement of the K_{node} conversion constant (quanta per ADU) directly, independent of any system conversion constants.

Neglecting any other correlation of errors yields

$$\begin{aligned}
\sigma_Q^2 &= \sigma_E^2 (\frac{\partial Q}{\partial E})^2 + \sigma_T^2 (\frac{\partial Q}{\partial T})^2 + \sigma_A^2 (\frac{\partial Q}{\partial A})^2 + \\
&\quad \sigma_\tau^2 (\frac{\partial Q}{\partial \tau})^2 + \sigma_{knode}^2 (\frac{\partial Q}{\partial k_{node}})^2 + \sigma_\lambda^2 (\frac{\partial Q}{\partial \lambda})^2.
\end{aligned} \tag{9-5}$$

or

$$\begin{aligned}
(\frac{\sigma_Q}{Q})^2 &= (\frac{\sigma_E}{E})^2 + (\frac{\sigma_T^2}{T})^2 + (\frac{\sigma_A}{A})^2 + \\
&\quad (\frac{\sigma_\tau}{\tau})^2 + (\frac{\sigma_{knode}}{k_{node}})^2 + (\frac{\sigma_\lambda}{\lambda})^2.
\end{aligned} \tag{9-6}$$

Plugging in the numbers above yields an overall uncertainty of about 4 percent (0.0375) for quantum efficiency measurement given the original assumptions. Much of this error is due to uncertainty in the pinhole area.

The uncertainty in measuring capacitance is dependent only upon the signal path gain, and is:

$$\sigma_C^2 \;=\; \sigma_{gmux}^2 \Big(\frac{\partial Q}{\partial g_{mux}}\Big)^2 + \sigma_{gpre}^2 \Big(\frac{\partial Q}{\partial g_{preamp}}\Big)^2 + \sigma_{kadc}^2 \Big(\frac{\partial Q}{\partial k_{adc}}\Big)^2 + \sigma_{knode}^2 \Big(\frac{\partial Q}{\partial k_{node}}\Big)^2 \tag{9-7}$$

or

$$\Big(\frac{\sigma_C}{C}\Big)^2 \;=\; \Big(\frac{\sigma_{gmux}}{g_{mux}}\Big)^2 + \Big(\frac{\sigma_{gpre}}{g_{preamp}}\Big)^2 + \Big(\frac{\sigma_{kadc}}{k_{adc}}\Big)^2 + \Big(\frac{\sigma_{knode}}{k_{node}}\Big)^2. \tag{9-8}$$

This results in roughly a 2 percent error (0.0018).

9.3 Nodal capacitance, corrected again.

The two percent error budget for nodal capacitance at this point was now raising a concern. The same bare multiplexer nodal capacitance was measured at both the University of Rochester and RIT, and these measurements were 28 and 30 fF respectively. This discrepancy, felt to be small (6.6 %, within the error budget of U/R's measurement) was still suspicious.

A check of the signal path in the RIT system revealed an attenuation that had not been accounted for. An RC filter on the converter card and a relatively low input impedance of the analog-to-digital converter module introduced an attenuation of 0.946. This attenuation was measured with high precision (<0.001). Adjusting the system constant k_{adc} (and the nodal capacitance measurements) by this value resulted in a pair of capacitance measurements of the same device on two systems that agreed within the error budget. Table 9.1 summarizes these results, with the nodal capacitance estimates corrected for the RC attenuation. It should be noted that the multiplexer gain was measured with the same system,

Characteristic	Value	Notes
Pixel Pitch	27 microns	SB226 mux
Thick detector	185 microns thick	prototype, unthinned
Thin detector	40 microns thick	thinned after bonding
C_{node}(thick)	41 fF	$\sigma \approx 2\%$
C_{node}(thin, 10KeV)	41 fF	$\sigma \approx 5\%$
C_{node}(thin, 15KeV)	43 fF	$\sigma \approx 5\%$
QE (thick, 50K)	>0.75, typ.	$\sigma \approx 4\%$
QE (thin 10KeV, 50K)	>0.85, typ.	$\sigma \approx 4\%$
QE (thin 15KeV, 50K)	>0.85, typ.	$\sigma \approx 4\%$
Read noise, thick	7.77 e^-	Fowler-1
Well depth, thick	$3 \times 10^5 e^-$	1 volt p-p output swing
Dark current, thick	$<2e^-$/s below 200K	
Diffusion, thick	$\sigma = 6$ microns at 35K	Gaussian profile
inter-pixel α	≈ 3.25	diag. & 2nd nbr.

Table 9.1: Silicon P-I-N Summary.

but the offset was adjusted as data was taken to keep the signal near zero, and this converter
gain error did not influence that gain measurement significantly.

9.4   Conclusions, and Future Directions

In this dissertation, a system was constructed and used to operate, test, and characterize
hybridized silicon P-I-N detector arrays. These devices are the culmination of many years
and many iterations of both low-noise cryogenic CMOS multiplexer design and high qual-
ity silicon photodetector research and development. CMOS multiplexers are more radiation
hard than charge-coupled readout strategies because CMOS multiplexers buffer the signal

at the pixel, rather than employ the charge transfer mechanism that is easily compromised by radiation. CMOS detectors, however, tend to have higher dark currents than CCDs.

The P-I-N detector wafers used in these devices were fabricated from high-purity silicon — more characteristic of the high resistivity silicon used in CCDs. This combination of qualities makes the hybridized silicon P-I-N array a very attractive device to use for a visible imager on a space telescope, where low noise, low dark current, and high tolerance to radiation are all important characteristics.

The P-I-N arrays also promised high sensitivity, sharp imaging and good spectral response over the entire visible range. The expected sharpness of image was calculated and data was taken that confirmed these expectations were indeed being met. No model of expected spectral sensitivity was constructed, but spectral sensitivity was measured and found to be commendable — between 0.75 and 1.0 over a wide range of wavelengths and temperatures.

The silicon P-I-N arrays do live up to their promise of sharp imaging and low nodal capacitance, and it was concluded they are fine quality imagers. It is expected that they will become more popular. The nodal capacitance was measured to be 41 femtofarads, and the Gaussian point spread from carrier diffusion was only 5 microns. However, initial results indicated 57 femtofarads and a wider, non-Gaussian diffusion profile. These unexpected initial results were explained by the revelation that small electric fields in detectors like these can couple adjacent pixels together and taint the measurement of Poisson noise, a component in the measurement of conversion factor that is a cornerstone of detector array characterization. This unanticipated coupling was found to be the culprit behind both odd observations, since it explained the strange observed diffusion profile as well. It appears that this coupling explains similarly odd observations in other devices, and casts some uncertainty on characterizations of other such devices. Previously reported quantum efficiencies may be overestimated. Previously reported crosstalk may not be from diffusion,

and real image signal to noise at high frequencies may actually be better. This indicates a need for re-evaluation of previous data on other devices.

Interpixel coupling attenuates signal and photon noise equally, so information is not lost. The process should be reversible in software. Answering the questions of exactly how to perform this inverse filtering and how well it performs on various algorithms and devices is an area for further research.

The P-I-N devices themselves are not yet fully characterized or appreciated. These devices may indeed make good imagers for small X-ray machines or X-ray telescopes. Only a small amount of data was taken at warmer temperatures, and the fine details of sensitivity very near the cutoff wavelength was not observed either, so these areas are suggested. Verification of the radiation hardness is also encouraged — perhaps using the engineering prototype that has a scratch on it. P-I-N detectors made from other semiconductor materials may be a possibility, so research in this area is encouraged.

It was suspected that an "electronic shuttering" technique on the P-I-N devices might have been possible. The basic idea behind electronic shuttering was that photons released near the surface of the detector would be more likely to recombine if the detector was not fully depleted. This idea was experimented with, but significant QE reduction with underbias was not observed. The low temperatures may have prevented significant recombination, however, and perhaps above 200K there may be a noticeable effect. For the next fabricated devices, adjustments to the field control grid may further reduce nodal capacitance and make these devices more sensitive.

The simple edge spread testing approach also proved effective, and multi-angle processing of these edges to extract a detailed pixel response function that agrees with spot-scanning results on the same device may be an attractive research area. Tomographic data processing similar to that used in CAT scanners and MRI machines would be required. Spot-scanning is more of a "brute-force" method — direct, but tedious to physically ac-

complish. The less complex physical setup of the edge spread testing performed in this thesis may be beneficial if the data processing can be shown to be robust. Front-illuminated devices and back-illuminated CCDs are the devices that would seem best be suited to this approach, however, as they have known fill-factor issues.

Subarray scanning (quickly reading out only a small area of the array) was one particular research area that was found interesting, but not pursued in great detail. Sampling-up-the-ramp (and cosmic ray rejection) was a related area that was also considered interesting. Appendix E presents foundational theory for optimal treatment of photon and read noise that may be of interest to a researcher in this area. Latent images are another concern for astronomers, and the relationship between latent images, cosmic ray events, and sample-up-the-ramp algorithms may be an interesting practical challenge for scientists interested in extracting information from telescopes currently or soon to be in operation.

Part IV

Appendices

Appendix A

P-I-N Visible Quantum Efficiency Tables

These tables summarize the measured responsive quantum efficiency in three hybridized silicon P-I-N arrays. Table A.1 shows near-cutoff QE measurements on a thick prototype device. It can be seen that the 760 nm response improves slightly at low temperatures.

Manual control of the diffraction grating monochromator was required, thus Table A.1 did not benefit from the automated temperature and illumination control that was able to produce the volumes of information in Tables A.2 to A.14. Each column in Tables A.2 to A.14 is a measured RQE at single temperature, over a range from 420 nm to 720 nm. The thinned arrays are remarkably good, with RQE measurements above 0.75 at nearly all wavelengths and temperatures. The thicker device shows even better blue response than the thinned at higher temperatures, but blue efficiency drops at low temperatures. It is unlikely that the differences in RQE have much to do with the differing thicknesses of

nm\K	150	76	30
760	0.715	0.787	0.775
820	0.698	0.770	0.775
870	0.676	0.739	0.750
940	0.581	0.570	0.570
1094	0.019	0.005	0.007

Table A.1: Thick (Prototype) P-I-N NIR QE

these detectors. More likely this is because the thick detector arrays were fabricated with different anti-reflective coatings. It is possible that the thickness of the back side implant has an influence in the blue, however. The 15 KeV back-side implants are thicker, and photons absorbed within the implant are perhaps more likely to recombine rather than be collected.

nm\K	165	160	155	150	145	140	135	130	125	120
420	0.749	0.746	0.754	0.761	0.768	0.775	0.781	0.789	0.793	0.799
430	0.791	0.793	0.801	0.809	0.816	0.823	0.830	0.835	0.840	0.844
440	0.797	0.798	0.807	0.814	0.821	0.828	0.833	0.838	0.843	0.848
450	0.781	0.783	0.792	0.801	0.807	0.813	0.817	0.822	0.827	0.832
460	0.817	0.817	0.828	0.836	0.844	0.850	0.854	0.859	0.864	0.871
470	0.817	0.820	0.831	0.834	0.845	0.852	0.858	0.863	0.865	0.873
480	0.786	0.790	0.795	0.805	0.815	0.819	0.820	0.829	0.835	0.838
490	0.832	0.837	0.846	0.854	0.861	0.869	0.872	0.879	0.885	0.891
500	0.849	0.856	0.864	0.872	0.879	0.885	0.892	0.897	0.902	0.908
510	0.815	0.822	0.829	0.836	0.842	0.848	0.853	0.859	0.863	0.868
520	0.851	0.857	0.864	0.872	0.877	0.883	0.888	0.893	0.898	0.903
530	0.805	0.812	0.819	0.825	0.831	0.836	0.840	0.845	0.850	0.854
540	0.843	0.849	0.856	0.862	0.867	0.873	0.877	0.882	0.887	0.891
550	0.837	0.844	0.851	0.857	0.862	0.867	0.872	0.876	0.881	0.886
560	0.857	0.865	0.871	0.878	0.883	0.888	0.892	0.897	0.902	0.906
570	0.825	0.833	0.839	0.845	0.850	0.855	0.860	0.864	0.869	0.873
580	0.829	0.837	0.844	0.850	0.855	0.860	0.864	0.869	0.874	0.878
590	0.794	0.802	0.808	0.814	0.819	0.824	0.828	0.832	0.837	0.841
600	0.824	0.831	0.839	0.845	0.850	0.855	0.859	0.863	0.868	0.872
610	0.795	0.803	0.810	0.816	0.821	0.825	0.830	0.833	0.838	0.842
620	0.809	0.818	0.825	0.831	0.836	0.840	0.845	0.849	0.853	0.858
630	0.775	0.783	0.790	0.796	0.800	0.805	0.809	0.814	0.818	0.822
640	0.799	0.808	0.815	0.821	0.826	0.831	0.835	0.839	0.844	0.849
650	0.752	0.760	0.768	0.773	0.778	0.783	0.787	0.791	0.796	0.800
660	0.777	0.785	0.793	0.799	0.804	0.809	0.813	0.817	0.822	0.826
670	0.760	0.768	0.775	0.781	0.786	0.791	0.795	0.799	0.804	0.809
680	0.771	0.779	0.786	0.792	0.797	0.802	0.807	0.811	0.815	0.820
690	0.778	0.786	0.793	0.800	0.805	0.809	0.814	0.818	0.823	0.828
700	0.748	0.756	0.764	0.770	0.774	0.779	0.784	0.788	0.792	0.796
710	0.738	0.747	0.754	0.759	0.764	0.768	0.771	0.773	0.778	0.783
720	0.699	0.708	0.713	0.718	0.722	0.724	0.728	0.728	0.732	0.736

Table A.2: 10KeV Thin P-I-N, Visible QE 165K-120K

nm\K	115	110	105	100	95	90	85	80	75	70
420	0.798	0.800	0.801	0.803	0.804	0.811	0.809	0.810	0.814	0.814
430	0.846	0.849	0.852	0.854	0.856	0.858	0.862	0.865	0.867	0.867
440	0.851	0.856	0.860	0.864	0.868	0.871	0.874	0.877	0.879	0.880
450	0.838	0.845	0.851	0.856	0.861	0.864	0.867	0.870	0.871	0.873
460	0.876	0.886	0.891	0.896	0.903	0.907	0.909	0.911	0.914	0.913
470	0.875	0.888	0.890	0.895	0.903	0.907	0.903	0.913	0.913	0.925
480	0.844	0.850	0.855	0.861	0.868	0.865	0.872	0.871	0.880	0.883
490	0.895	0.900	0.904	0.908	0.912	0.915	0.920	0.923	0.927	0.932
500	0.913	0.916	0.920	0.926	0.929	0.933	0.937	0.941	0.945	0.948
510	0.872	0.876	0.881	0.885	0.889	0.893	0.897	0.901	0.905	0.908
520	0.908	0.913	0.918	0.923	0.927	0.932	0.936	0.940	0.943	0.946
530	0.859	0.865	0.869	0.874	0.879	0.883	0.887	0.891	0.894	0.897
540	0.896	0.901	0.906	0.910	0.915	0.919	0.923	0.927	0.931	0.934
550	0.891	0.896	0.901	0.905	0.910	0.914	0.918	0.922	0.926	0.929
560	0.912	0.917	0.922	0.927	0.932	0.937	0.941	0.945	0.948	0.952
570	0.879	0.884	0.889	0.893	0.898	0.903	0.907	0.911	0.914	0.918
580	0.883	0.889	0.894	0.899	0.904	0.908	0.912	0.916	0.920	0.924
590	0.846	0.852	0.857	0.861	0.866	0.871	0.875	0.878	0.882	0.885
600	0.878	0.884	0.890	0.895	0.900	0.905	0.909	0.913	0.916	0.920
610	0.848	0.854	0.859	0.865	0.870	0.874	0.878	0.882	0.886	0.889
620	0.864	0.871	0.876	0.881	0.887	0.891	0.896	0.900	0.903	0.906
630	0.828	0.834	0.840	0.845	0.850	0.854	0.859	0.862	0.866	0.869
640	0.856	0.862	0.868	0.873	0.878	0.883	0.887	0.891	0.894	0.898
650	0.807	0.813	0.819	0.824	0.829	0.834	0.838	0.841	0.844	0.847
660	0.834	0.841	0.846	0.852	0.857	0.861	0.865	0.869	0.873	0.876
670	0.815	0.822	0.827	0.832	0.837	0.842	0.846	0.849	0.853	0.855
680	0.827	0.833	0.839	0.844	0.849	0.854	0.857	0.861	0.864	0.868
690	0.834	0.840	0.845	0.850	0.856	0.860	0.864	0.868	0.871	0.874
700	0.803	0.808	0.814	0.819	0.823	0.828	0.831	0.835	0.838	0.841
710	0.790	0.796	0.802	0.806	0.810	0.814	0.817	0.820	0.823	0.827
720	0.745	0.750	0.755	0.759	0.766	0.768	0.772	0.773	0.776	0.779

Table A.3: 10KeV Thin P-I-N, Visible QE 115K-70K

166

nm\K	65	60	55	50	45	40	35	30	25	20
420	0.813	0.810	0.818	0.808	0.809	0.802	0.802	0.803	0.802	0.770
430	0.868	0.869	0.869	0.869	0.867	0.866	0.863	0.862	0.861	0.868
440	0.881	0.881	0.882	0.881	0.881	0.880	0.879	0.876	0.877	0.875
450	0.873	0.874	0.874	0.874	0.875	0.874	0.872	0.873	0.871	0.875
460	0.917	0.914	0.914	0.918	0.916	0.916	0.918	0.916	0.918	0.920
470	0.917	0.918	0.920	0.928	0.924	0.922	0.922	0.918	0.927	0.928
480	0.871	0.883	0.841	0.887	0.890	0.887	0.890	0.888	0.902	0.903
490	0.933	0.936	0.926	0.941	0.942	0.943	0.943	0.948	0.951	0.960
500	0.951	0.954	0.957	0.960	0.962	0.963	0.965	0.967	0.970	0.975
510	0.911	0.914	0.916	0.919	0.921	0.924	0.925	0.927	0.928	0.931
520	0.949	0.952	0.955	0.958	0.960	0.963	0.965	0.966	0.968	0.969
530	0.900	0.902	0.906	0.908	0.911	0.913	0.915	0.917	0.919	0.919
540	0.937	0.940	0.943	0.946	0.949	0.951	0.953	0.956	0.958	0.956
550	0.932	0.935	0.939	0.941	0.944	0.947	0.949	0.951	0.953	0.945
560	0.955	0.958	0.961	0.964	0.968	0.970	0.972	0.975	0.977	0.964
570	0.921	0.924	0.927	0.930	0.933	0.936	0.938	0.941	0.943	0.936
580	0.927	0.930	0.933	0.936	0.940	0.943	0.945	0.947	0.950	0.944
590	0.889	0.892	0.896	0.898	0.901	0.904	0.906	0.908	0.911	0.908
600	0.923	0.927	0.929	0.933	0.936	0.939	0.942	0.944	0.947	0.944
610	0.892	0.895	0.898	0.901	0.905	0.908	0.910	0.912	0.915	0.907
620	0.909	0.913	0.916	0.919	0.922	0.925	0.928	0.930	0.932	0.933
630	0.872	0.875	0.879	0.881	0.885	0.887	0.890	0.892	0.895	0.896
640	0.901	0.905	0.908	0.911	0.915	0.917	0.920	0.923	0.925	0.927
650	0.850	0.854	0.856	0.859	0.863	0.866	0.868	0.870	0.873	0.876
660	0.878	0.882	0.885	0.888	0.892	0.895	0.897	0.900	0.902	0.907
670	0.859	0.862	0.865	0.868	0.872	0.874	0.877	0.879	0.882	0.886
680	0.870	0.874	0.877	0.879	0.883	0.886	0.888	0.891	0.895	0.900
690	0.878	0.880	0.884	0.886	0.890	0.893	0.896	0.899	0.902	0.908
700	0.843	0.847	0.849	0.852	0.855	0.858	0.860	0.863	0.867	0.874
710	0.829	0.831	0.834	0.837	0.838	0.842	0.844	0.845	0.849	0.857
720	0.780	0.783	0.785	0.786	0.790	0.791	0.796	0.797	0.798	0.809

Table A.4: 10KeV Thin P-I-N, Visible QE 65K-20K

nm\K	148	146	144	142	140	138	136	134	132	130
420	0.659	0.659	0.662	0.666	0.663	0.666	0.668	0.662	0.646	0.637
430	0.714	0.714	0.717	0.718	0.720	0.721	0.720	0.715	0.700	0.695
440	0.768	0.768	0.769	0.770	0.772	0.774	0.775	0.770	0.756	0.749
450	0.808	0.809	0.808	0.811	0.812	0.815	0.817	0.813	0.801	0.793
460	0.855	0.852	0.853	0.854	0.858	0.857	0.861	0.859	0.849	0.840
470	0.830	0.831	0.836	0.835	0.823	0.840	0.843	0.839	0.834	0.829
480	0.817	0.817	0.816	0.820	0.819	0.822	0.830	0.821	0.819	0.817
490	0.787	0.789	0.789	0.789	0.791	0.794	0.794	0.796	0.794	0.794
500	0.786	0.785	0.785	0.786	0.787	0.788	0.791	0.792	0.792	0.793
510	0.813	0.813	0.813	0.814	0.816	0.817	0.819	0.820	0.821	0.821
520	0.838	0.838	0.838	0.839	0.840	0.842	0.843	0.845	0.847	0.848
530	0.844	0.844	0.844	0.846	0.847	0.849	0.850	0.852	0.855	0.856
540	0.837	0.837	0.837	0.839	0.840	0.842	0.843	0.845	0.849	0.851
550	0.836	0.837	0.838	0.839	0.841	0.842	0.843	0.846	0.850	0.852
560	0.867	0.868	0.869	0.870	0.872	0.874	0.875	0.878	0.882	0.885
570	0.841	0.843	0.844	0.846	0.847	0.849	0.850	0.853	0.858	0.860
580	0.864	0.866	0.868	0.870	0.871	0.873	0.875	0.877	0.882	0.886
590	0.820	0.822	0.824	0.826	0.828	0.830	0.832	0.834	0.839	0.842
600	0.853	0.856	0.859	0.861	0.863	0.865	0.867	0.869	0.875	0.878
610	0.827	0.830	0.833	0.835	0.838	0.840	0.842	0.844	0.849	0.852
620	0.857	0.861	0.864	0.867	0.870	0.872	0.874	0.876	0.881	0.884
630	0.841	0.845	0.848	0.851	0.854	0.856	0.859	0.861	0.866	0.869
640	0.828	0.832	0.836	0.840	0.842	0.845	0.847	0.849	0.854	0.858
650	0.828	0.833	0.838	0.841	0.844	0.846	0.849	0.851	0.856	0.859
660	0.822	0.828	0.832	0.836	0.839	0.842	0.844	0.847	0.851	0.854
670	0.801	0.807	0.812	0.815	0.818	0.821	0.824	0.826	0.830	0.833
680	0.810	0.816	0.821	0.825	0.828	0.831	0.834	0.837	0.840	0.844
690	0.817	0.823	0.829	0.833	0.837	0.839	0.842	0.845	0.848	0.852
700	0.811	0.818	0.823	0.827	0.830	0.833	0.836	0.839	0.842	0.845
710	0.834	0.841	0.847	0.850	0.854	0.857	0.861	0.863	0.866	0.870
720	0.853	0.865	0.870	0.874	0.877	0.879	0.885	0.885	0.890	0.893

Table A.5: 15KeV Thin P-I-N, Visible QE 148K-130K

nm\K	128	126	124	122	120	118	116	114	112	110
420	0.647	0.648	0.655	0.667	0.675	0.677	0.681	0.685	0.686	0.687
430	0.696	0.706	0.713	0.721	0.729	0.733	0.738	0.741	0.744	0.748
440	0.750	0.757	0.761	0.765	0.766	0.776	0.780	0.782	0.786	0.789
450	0.791	0.795	0.798	0.799	0.802	0.805	0.809	0.813	0.816	0.819
460	0.835	0.842	0.846	0.846	0.848	0.851	0.856	0.861	0.865	0.866
470	0.826	0.833	0.834	0.836	0.835	0.841	0.845	0.847	0.852	0.854
480	0.827	0.825	0.829	0.835	0.840	0.844	0.846	0.851	0.850	0.855
490	0.801	0.805	0.811	0.815	0.822	0.824	0.830	0.832	0.835	0.837
500	0.796	0.804	0.809	0.814	0.819	0.824	0.826	0.830	0.832	0.835
510	0.825	0.832	0.836	0.840	0.845	0.848	0.851	0.854	0.857	0.859
520	0.850	0.856	0.860	0.863	0.865	0.869	0.872	0.874	0.877	0.879
530	0.858	0.863	0.856	0.867	0.869	0.872	0.875	0.877	0.879	0.882
540	0.854	0.859	0.861	0.863	0.865	0.868	0.870	0.872	0.874	0.876
550	0.855	0.859	0.860	0.862	0.863	0.865	0.868	0.870	0.871	0.873
560	0.887	0.891	0.891	0.892	0.893	0.895	0.897	0.899	0.901	0.903
570	0.863	0.866	0.866	0.866	0.867	0.869	0.870	0.872	0.874	0.875
580	0.888	0.891	0.889	0.889	0.889	0.891	0.892	0.893	0.895	0.897
590	0.844	0.846	0.844	0.843	0.842	0.843	0.845	0.846	0.847	0.849
600	0.880	0.882	0.878	0.877	0.875	0.876	0.877	0.878	0.880	0.881
610	0.853	0.855	0.851	0.849	0.847	0.848	0.848	0.850	0.851	0.852
620	0.886	0.888	0.882	0.880	0.877	0.877	0.878	0.880	0.880	0.882
630	0.871	0.872	0.867	0.864	0.862	0.862	0.863	0.864	0.865	0.866
640	0.859	0.860	0.854	0.851	0.848	0.848	0.848	0.849	0.850	0.851
650	0.860	0.861	0.854	0.850	0.847	0.846	0.847	0.848	0.849	0.850
660	0.855	0.856	0.848	0.844	0.840	0.840	0.840	0.841	0.842	0.843
670	0.835	0.836	0.828	0.825	0.821	0.820	0.821	0.822	0.822	0.823
680	0.845	0.847	0.838	0.835	0.832	0.831	0.831	0.832	0.833	0.834
690	0.853	0.856	0.849	0.845	0.843	0.842	0.842	0.843	0.844	0.844
700	0.848	0.848	0.841	0.838	0.835	0.833	0.834	0.833	0.834	0.835
710	0.869	0.869	0.861	0.856	0.851	0.849	0.849	0.849	0.850	0.850
720	0.892	0.888	0.880	0.874	0.864	0.863	0.860	0.863	0.861	0.863

Table A.6: 15KeV Thin P-I-N, Visible QE, 128K-110K

nm\K	108	106	104	102	100	98	96	94	92	90
420	0.692	0.694	0.694	0.699	0.701	0.701	0.702	0.708	0.704	0.705
430	0.750	0.752	0.755	0.758	0.760	0.762	0.765	0.765	0.765	0.767
440	0.792	0.794	0.797	0.799	0.803	0.805	0.809	0.812	0.814	0.816
450	0.822	0.824	0.826	0.828	0.833	0.836	0.841	0.847	0.851	0.853
460	0.869	0.871	0.874	0.876	0.879	0.885	0.889	0.895	0.889	0.901
470	0.858	0.862	0.866	0.866	0.871	0.872	0.877	0.880	0.892	0.887
480	0.854	0.861	0.862	0.864	0.868	0.876	0.877	0.876	0.883	0.886
490	0.840	0.843	0.846	0.848	0.850	0.854	0.854	0.856	0.860	0.860
500	0.837	0.840	0.842	0.844	0.847	0.849	0.851	0.853	0.854	0.856
510	0.862	0.864	0.866	0.868	0.871	0.873	0.875	0.878	0.879	0.881
520	0.881	0.883	0.885	0.887	0.890	0.892	0.895	0.897	0.899	0.901
530	0.884	0.886	0.887	0.890	0.892	0.894	0.897	0.900	0.902	0.904
540	0.878	0.880	0.882	0.884	0.886	0.887	0.890	0.892	0.894	0.896
550	0.875	0.877	0.878	0.880	0.882	0.884	0.886	0.889	0.891	0.892
560	0.905	0.906	0.908	0.909	0.911	0.913	0.915	0.918	0.921	0.922
570	0.877	0.878	0.880	0.882	0.883	0.885	0.887	0.890	0.892	0.893
580	0.898	0.900	0.901	0.903	0.905	0.906	0.908	0.911	0.914	0.914
590	0.850	0.851	0.853	0.854	0.856	0.857	0.859	0.862	0.865	0.866
600	0.883	0.884	0.885	0.887	0.888	0.890	0.892	0.895	0.898	0.899
610	0.853	0.854	0.856	0.857	0.858	0.860	0.862	0.865	0.868	0.869
620	0.883	0.884	0.885	0.887	0.888	0.890	0.892	0.895	0.899	0.899
630	0.868	0.869	0.870	0.871	0.872	0.874	0.876	0.879	0.882	0.883
640	0.852	0.854	0.854	0.856	0.857	0.859	0.860	0.864	0.867	0.868
650	0.851	0.852	0.853	0.854	0.855	0.857	0.859	0.862	0.866	0.867
660	0.844	0.845	0.846	0.847	0.848	0.850	0.852	0.855	0.859	0.860
670	0.824	0.825	0.826	0.827	0.829	0.830	0.831	0.834	0.838	0.839
680	0.835	0.836	0.837	0.838	0.839	0.840	0.841	0.844	0.847	0.849
690	0.846	0.847	0.847	0.848	0.849	0.850	0.852	0.854	0.857	0.858
700	0.835	0.837	0.838	0.839	0.840	0.841	0.842	0.844	0.848	0.849
710	0.851	0.851	0.851	0.852	0.854	0.854	0.854	0.858	0.863	0.864
720	0.861	0.862	0.862	0.863	0.862	0.861	0.865	0.868	0.875	0.876

Table A.7: 15KeV Thin P-I-N, Visible QE, 108K-90K

nm\K	88	86	84	82	80	78	76	74	72	70
420	0.710	0.711	0.713	0.714	0.715	0.710	0.714	0.714	0.714	0.721
430	0.770	0.772	0.773	0.774	0.775	0.776	0.776	0.777	0.779	0.782
440	0.818	0.821	0.823	0.825	0.826	0.828	0.829	0.829	0.833	0.836
450	0.856	0.858	0.861	0.862	0.865	0.866	0.868	0.869	0.873	0.877
460	0.906	0.911	0.914	0.914	0.916	0.918	0.918	0.922	0.926	0.930
470	0.892	0.894	0.898	0.903	0.899	0.904	0.903	0.911	0.910	0.915
480	0.886	0.889	0.892	0.895	0.897	0.899	0.898	0.902	0.905	0.904
490	0.863	0.866	0.868	0.871	0.871	0.873	0.873	0.876	0.878	0.880
500	0.859	0.861	0.863	0.865	0.865	0.867	0.868	0.869	0.872	0.873
510	0.883	0.885	0.887	0.889	0.890	0.892	0.893	0.894	0.896	0.897
520	0.903	0.905	0.907	0.910	0.911	0.912	0.914	0.915	0.917	0.919
530	0.906	0.907	0.909	0.912	0.913	0.915	0.916	0.917	0.919	0.920
540	0.897	0.899	0.901	0.903	0.905	0.906	0.907	0.908	0.910	0.911
550	0.894	0.895	0.897	0.899	0.901	0.902	0.903	0.905	0.906	0.907
560	0.923	0.925	0.927	0.929	0.930	0.932	0.933	0.934	0.936	0.937
570	0.894	0.896	0.898	0.900	0.901	0.902	0.904	0.905	0.906	0.907
580	0.916	0.918	0.919	0.921	0.923	0.924	0.925	0.927	0.928	0.929
590	0.867	0.868	0.870	0.872	0.873	0.874	0.875	0.877	0.878	0.878
600	0.900	0.902	0.903	0.905	0.906	0.908	0.909	0.911	0.912	0.913
610	0.870	0.871	0.873	0.875	0.876	0.877	0.879	0.880	0.881	0.882
620	0.900	0.902	0.903	0.905	0.907	0.908	0.910	0.911	0.913	0.913
630	0.884	0.885	0.887	0.888	0.890	0.891	0.892	0.894	0.895	0.896
640	0.869	0.870	0.872	0.874	0.875	0.876	0.878	0.879	0.881	0.881
650	0.868	0.869	0.871	0.873	0.874	0.875	0.876	0.878	0.880	0.880
660	0.861	0.862	0.864	0.865	0.867	0.868	0.869	0.871	0.873	0.873
670	0.840	0.841	0.842	0.844	0.846	0.846	0.848	0.849	0.851	0.851
680	0.850	0.851	0.852	0.854	0.855	0.857	0.857	0.859	0.861	0.861
690	0.859	0.860	0.861	0.863	0.864	0.864	0.867	0.868	0.870	0.870
700	0.849	0.851	0.852	0.854	0.855	0.856	0.857	0.859	0.860	0.861
710	0.865	0.867	0.868	0.870	0.871	0.873	0.874	0.876	0.879	0.879
720	0.876	0.880	0.881	0.882	0.885	0.886	0.887	0.889	0.894	0.891

Table A.8: 15KeV Thin P-I-N, Visible QE, 88K-70K

nm\K	68	66	64	62	60	58	56	54	52	50
420	0.724	0.721	0.723	0.718	0.721	0.719	0.716	0.721	0.717	0.719
430	0.783	0.784	0.784	0.783	0.782	0.783	0.781	0.780	0.780	0.780
440	0.838	0.838	0.839	0.839	0.838	0.838	0.837	0.835	0.835	0.833
450	0.879	0.881	0.881	0.882	0.882	0.882	0.880	0.878	0.876	0.873
460	0.933	0.934	0.939	0.935	0.936	0.938	0.933	0.933	0.931	0.927
470	0.916	0.922	0.925	0.918	0.920	0.925	0.919	0.921	0.919	0.918
480	0.909	0.911	0.912	0.910	0.915	0.912	0.913	0.912	0.913	0.912
490	0.882	0.883	0.885	0.884	0.886	0.888	0.886	0.886	0.888	0.888
500	0.875	0.876	0.877	0.878	0.878	0.879	0.880	0.880	0.881	0.883
510	0.899	0.900	0.900	0.901	0.902	0.903	0.904	0.904	0.905	0.905
520	0.920	0.921	0.922	0.923	0.924	0.924	0.925	0.926	0.926	0.926
530	0.921	0.923	0.924	0.925	0.926	0.926	0.926	0.927	0.926	0.928
540	0.912	0.913	0.914	0.915	0.916	0.916	0.917	0.918	0.918	0.919
550	0.908	0.909	0.910	0.911	0.912	0.913	0.914	0.914	0.915	0.915
560	0.938	0.939	0.940	0.941	0.942	0.943	0.943	0.944	0.944	0.944
570	0.908	0.908	0.909	0.911	0.912	0.912	0.913	0.913	0.914	0.914
580	0.929	0.930	0.931	0.932	0.933	0.934	0.935	0.935	0.936	0.936
590	0.879	0.880	0.880	0.882	0.883	0.883	0.884	0.884	0.885	0.885
600	0.913	0.914	0.915	0.916	0.917	0.918	0.918	0.919	0.919	0.919
610	0.882	0.883	0.884	0.885	0.886	0.887	0.887	0.888	0.888	0.888
620	0.913	0.914	0.915	0.916	0.918	0.918	0.919	0.919	0.919	0.919
630	0.896	0.897	0.898	0.899	0.900	0.900	0.901	0.902	0.902	0.902
640	0.881	0.882	0.883	0.884	0.886	0.886	0.887	0.887	0.888	0.887
650	0.881	0.881	0.882	0.883	0.885	0.885	0.886	0.886	0.886	0.886
660	0.874	0.874	0.875	0.876	0.877	0.878	0.878	0.879	0.879	0.879
670	0.852	0.852	0.853	0.854	0.855	0.856	0.856	0.857	0.857	0.857
680	0.861	0.861	0.862	0.864	0.865	0.865	0.866	0.866	0.867	0.867
690	0.871	0.871	0.871	0.873	0.874	0.874	0.875	0.876	0.876	0.877
700	0.861	0.862	0.862	0.863	0.864	0.865	0.866	0.866	0.866	0.866
710	0.879	0.879	0.879	0.880	0.881	0.882	0.882	0.883	0.882	0.882
720	0.893	0.892	0.894	0.895	0.896	0.896	0.897	0.897	0.895	0.894

Table A.9: 15KeV Thin P-I-N, Visible QE, 68K-50K

172

nm\K	48	46	44	42	40	38	36	34	32	30
420	0.719	0.720	0.716	0.714	0.717	0.706	0.700	0.710	0.707	0.714
430	0.781	0.783	0.781	0.780	0.778	0.775	0.774	0.775	0.777	0.775
440	0.832	0.832	0.831	0.830	0.829	0.829	0.829	0.827	0.832	0.832
450	0.870	0.868	0.867	0.866	0.867	0.868	0.867	0.867	0.871	0.874
460	0.924	0.922	0.920	0.919	0.921	0.923	0.923	0.926	0.928	0.929
470	0.914	0.912	0.911	0.908	0.916	0.911	0.914	0.915	0.922	0.923
480	0.910	0.914	0.914	0.913	0.914	0.913	0.912	0.914	0.917	0.918
490	0.890	0.891	0.890	0.891	0.892	0.892	0.892	0.892	0.900	0.898
500	0.883	0.885	0.885	0.885	0.886	0.886	0.887	0.887	0.893	0.894
510	0.906	0.908	0.908	0.909	0.909	0.909	0.910	0.911	0.916	0.917
520	0.926	0.927	0.928	0.929	0.930	0.930	0.931	0.932	0.938	0.939
530	0.927	0.928	0.928	0.929	0.931	0.931	0.933	0.934	0.940	0.941
540	0.919	0.919	0.920	0.921	0.922	0.923	0.924	0.925	0.931	0.932
550	0.914	0.915	0.916	0.917	0.918	0.919	0.921	0.922	0.928	0.929
560	0.944	0.944	0.945	0.946	0.947	0.949	0.950	0.952	0.958	0.959
570	0.914	0.914	0.915	0.916	0.917	0.919	0.920	0.921	0.927	0.928
580	0.935	0.935	0.936	0.937	0.939	0.940	0.942	0.943	0.949	0.951
590	0.884	0.883	0.884	0.885	0.887	0.889	0.890	0.891	0.897	0.899
600	0.918	0.917	0.918	0.920	0.922	0.923	0.925	0.927	0.933	0.934
610	0.886	0.885	0.887	0.888	0.890	0.891	0.893	0.895	0.901	0.902
620	0.917	0.916	0.917	0.919	0.921	0.923	0.925	0.926	0.932	0.934
630	0.901	0.899	0.901	0.901	0.904	0.906	0.907	0.909	0.915	0.917
640	0.886	0.884	0.886	0.887	0.889	0.891	0.893	0.894	0.901	0.902
650	0.884	0.882	0.884	0.885	0.887	0.889	0.891	0.893	0.900	0.901
660	0.877	0.875	0.876	0.878	0.879	0.882	0.883	0.885	0.891	0.894
670	0.856	0.854	0.855	0.856	0.858	0.860	0.862	0.864	0.870	0.871
680	0.866	0.864	0.865	0.866	0.868	0.870	0.872	0.874	0.880	0.881
690	0.876	0.875	0.876	0.877	0.879	0.880	0.882	0.884	0.887	0.892
700	0.866	0.864	0.866	0.866	0.868	0.870	0.871	0.874	0.876	0.881
710	0.881	0.877	0.877	0.878	0.880	0.881	0.885	0.887	0.889	0.895
720	0.893	0.887	0.886	0.887	0.887	0.891	0.891	0.895	0.899	0.905

Table A.10: 15KeV Thin P-I-N, Visible QE, 48K-30K

nm\K	150	147	144	141	138	135	132	129	126	123
420	0.835	0.826	0.825	0.826	0.829	0.832	0.832	0.835	0.838	0.839
430	0.855	0.848	0.848	0.849	0.851	0.854	0.857	0.859	0.862	0.865
440	0.873	0.874	0.881	0.886	0.891	0.895	0.899	0.902	0.905	0.908
450	0.857	0.867	0.881	0.890	0.896	0.902	0.907	0.912	0.916	0.921
460	0.863	0.876	0.889	0.901	0.908	0.913	0.920	0.924	0.928	0.933
470	0.843	0.857	0.869	0.876	0.882	0.887	0.894	0.901	0.901	0.906
480	0.822	0.829	0.836	0.843	0.846	0.855	0.856	0.870	0.864	0.868
490	0.823	0.823	0.828	0.833	0.837	0.840	0.844	0.848	0.850	0.854
500	0.841	0.842	0.846	0.850	0.853	0.857	0.861	0.864	0.868	0.871
510	0.811	0.813	0.818	0.823	0.826	0.829	0.833	0.836	0.839	0.842
520	0.852	0.857	0.863	0.869	0.873	0.877	0.880	0.883	0.887	0.890
530	0.816	0.823	0.830	0.836	0.840	0.844	0.848	0.851	0.855	0.858
540	0.824	0.829	0.835	0.840	0.843	0.846	0.849	0.852	0.855	0.859
550	0.812	0.819	0.825	0.830	0.834	0.837	0.840	0.843	0.846	0.849
560	0.827	0.834	0.841	0.846	0.850	0.853	0.857	0.860	0.863	0.866
570	0.807	0.815	0.821	0.827	0.830	0.834	0.837	0.840	0.844	0.847
580	0.823	0.832	0.839	0.845	0.849	0.853	0.856	0.859	0.863	0.866
590	0.786	0.795	0.802	0.808	0.813	0.816	0.820	0.823	0.827	0.830
600	0.808	0.818	0.826	0.831	0.837	0.841	0.844	0.848	0.851	0.854
610	0.787	0.797	0.806	0.812	0.817	0.821	0.825	0.828	0.832	0.835
620	0.806	0.818	0.826	0.833	0.838	0.842	0.846	0.850	0.854	0.857
630	0.770	0.781	0.789	0.796	0.800	0.805	0.809	0.812	0.816	0.817
640	0.795	0.807	0.815	0.822	0.827	0.832	0.836	0.840	0.844	0.847
650	0.755	0.766	0.775	0.782	0.787	0.792	0.796	0.800	0.804	0.807
660	0.786	0.797	0.807	0.814	0.819	0.825	0.829	0.833	0.837	0.841
670	0.748	0.758	0.766	0.773	0.778	0.782	0.786	0.791	0.794	0.798
680	0.754	0.764	0.771	0.778	0.783	0.787	0.792	0.796	0.800	0.803
690	0.763	0.771	0.779	0.784	0.790	0.795	0.799	0.803	0.807	0.810
700	0.733	0.742	0.750	0.756	0.761	0.766	0.770	0.774	0.778	0.781
710	0.736	0.747	0.756	0.764	0.769	0.774	0.779	0.783	0.787	0.790
720	0.705	0.716	0.727	0.735	0.741	0.747	0.752	0.755	0.759	0.762

Table A.11: Thick (prototype) P-I-N, Visible QE, 150K-123K

nm\K	120	117	114	111	108	105	102	99	96	93
420	0.843	0.845	0.859	0.868	0.873	0.879	0.878	0.877	0.881	0.878
430	0.867	0.872	0.887	0.894	0.899	0.902	0.903	0.903	0.903	0.903
440	0.911	0.915	0.921	0.921	0.922	0.923	0.923	0.924	0.924	0.924
450	0.923	0.925	0.921	0.916	0.915	0.913	0.913	0.914	0.915	0.915
460	0.937	0.937	0.931	0.924	0.926	0.923	0.923	0.923	0.925	0.925
470	0.911	0.908	0.905	0.902	0.902	0.905	0.905	0.904	0.905	0.907
480	0.872	0.872	0.876	0.876	0.877	0.879	0.882	0.883	0.885	0.886
490	0.859	0.862	0.867	0.873	0.876	0.881	0.884	0.882	0.886	0.886
500	0.874	0.879	0.886	0.892	0.895	0.897	0.900	0.902	0.904	0.906
510	0.845	0.851	0.857	0.860	0.863	0.864	0.866	0.868	0.871	0.872
520	0.893	0.899	0.901	0.903	0.905	0.906	0.908	0.910	0.912	0.914
530	0.861	0.866	0.867	0.867	0.868	0.869	0.871	0.873	0.875	0.876
540	0.861	0.866	0.868	0.869	0.871	0.872	0.874	0.876	0.878	0.880
550	0.852	0.856	0.857	0.857	0.859	0.860	0.862	0.864	0.866	0.868
560	0.869	0.873	0.873	0.873	0.875	0.875	0.877	0.879	0.882	0.884
570	0.849	0.854	0.853	0.853	0.855	0.856	0.858	0.860	0.862	0.864
580	0.869	0.873	0.872	0.871	0.872	0.873	0.875	0.878	0.880	0.882
590	0.833	0.837	0.834	0.833	0.834	0.835	0.837	0.839	0.841	0.844
600	0.858	0.861	0.858	0.856	0.857	0.858	0.859	0.862	0.865	0.867
610	0.838	0.840	0.836	0.835	0.835	0.836	0.837	0.840	0.842	0.845
620	0.860	0.862	0.858	0.856	0.856	0.857	0.858	0.861	0.864	0.867
630	0.822	0.825	0.821	0.819	0.820	0.821	0.822	0.825	0.828	0.831
640	0.851	0.852	0.848	0.846	0.846	0.847	0.849	0.851	0.855	0.858
650	0.811	0.812	0.807	0.804	0.804	0.805	0.807	0.810	0.813	0.816
660	0.845	0.845	0.840	0.837	0.838	0.838	0.840	0.843	0.847	0.850
670	0.801	0.802	0.798	0.796	0.797	0.798	0.800	0.803	0.806	0.809
680	0.807	0.808	0.804	0.803	0.803	0.804	0.806	0.810	0.813	0.815
690	0.814	0.814	0.812	0.812	0.813	0.815	0.817	0.820	0.823	0.826
700	0.785	0.785	0.782	0.783	0.783	0.784	0.786	0.789	0.792	0.794
710	0.794	0.791	0.786	0.785	0.786	0.786	0.787	0.790	0.792	0.795
720	0.765	0.762	0.753	0.752	0.752	0.751	0.751	0.753	0.755	0.758

Table A.12: Thick (Prototype) P-I-N, Visible QE, 120K-93K

nm\K	90	87	84	81	78	75	72	45	66	63
420	0.876	0.870	0.868	0.857	0.850	0.834	0.830	0.827	0.701	0.791
430	0.903	0.900	0.895	0.886	0.876	0.868	0.859	0.859	0.748	0.827
440	0.924	0.924	0.919	0.916	0.914	0.909	0.905	0.904	0.807	0.880
450	0.915	0.915	0.915	0.919	0.922	0.922	0.921	0.921	0.841	0.904
460	0.928	0.928	0.930	0.936	0.939	0.940	0.941	0.940	0.873	0.928
470	0.912	0.910	0.919	0.919	0.919	0.920	0.922	0.918	0.865	0.908
480	0.888	0.888	0.893	0.890	0.890	0.890	0.890	0.884	0.848	0.878
490	0.889	0.889	0.889	0.886	0.884	0.882	0.880	0.878	0.845	0.871
500	0.907	0.908	0.907	0.905	0.904	0.902	0.901	0.896	0.871	0.891
510	0.874	0.875	0.874	0.874	0.874	0.872	0.872	0.868	0.849	0.865
520	0.915	0.917	0.917	0.919	0.920	0.921	0.921	0.918	0.903	0.917
530	0.878	0.880	0.881	0.884	0.886	0.888	0.889	0.886	0.876	0.887
540	0.882	0.884	0.886	0.888	0.889	0.890	0.891	0.889	0.881	0.890
550	0.870	0.872	0.874	0.877	0.879	0.881	0.882	0.881	0.876	0.883
560	0.886	0.889	0.891	0.894	0.897	0.900	0.901	0.900	0.898	0.903
570	0.867	0.869	0.871	0.875	0.878	0.881	0.883	0.882	0.881	0.885
580	0.885	0.888	0.890	0.895	0.898	0.901	0.904	0.904	0.904	0.907
590	0.844	0.849	0.852	0.857	0.861	0.865	0.867	0.868	0.869	0.872
600	0.870	0.873	0.876	0.882	0.887	0.891	0.894	0.897	0.897	0.899
610	0.848	0.851	0.854	0.861	0.866	0.870	0.873	0.876	0.878	0.880
620	0.870	0.873	0.877	0.884	0.890	0.895	0.898	0.902	0.904	0.906
630	0.834	0.837	0.841	0.847	0.852	0.857	0.861	0.865	0.866	0.868
640	0.861	0.864	0.868	0.876	0.882	0.887	0.891	0.897	0.898	0.899
650	0.819	0.822	0.827	0.834	0.840	0.846	0.850	0.856	0.857	0.859
660	0.853	0.856	0.862	0.870	0.876	0.882	0.887	0.894	0.894	0.896
670	0.811	0.815	0.820	0.828	0.833	0.838	0.842	0.850	0.849	0.851
680	0.818	0.821	0.827	0.834	0.840	0.845	0.849	0.857	0.856	0.858
690	0.829	0.832	0.838	0.844	0.849	0.854	0.858	0.866	0.864	0.867
700	0.798	0.801	0.808	0.814	0.819	0.824	0.828	0.837	0.835	0.837
710	0.799	0.803	0.814	0.822	0.827	0.833	0.838	0.848	0.846	0.849
720	0.763	0.768	0.779	0.790	0.797	0.804	0.808	0.832	0.818	0.822

Table A.13: Thick (Prototype) P-I-N, Visible QE, 90K-63K

nm\K	59	56	53	50	47	44	41	38	35	32
420	0.782	0.763	0.743	0.714	0.693	0.635	0.592	0.533	0.481	0.441
430	0.817	0.801	0.782	0.754	0.736	0.680	0.635	0.575	0.520	0.486
440	0.872	0.856	0.839	0.815	0.800	0.740	0.697	0.635	0.580	0.544
450	0.898	0.885	0.871	0.848	0.835	0.777	0.736	0.676	0.631	0.597
460	0.923	0.912	0.899	0.878	0.867	0.812	0.774	0.715	0.673	0.639
470	0.905	0.896	0.886	0.864	0.854	0.805	0.772	0.719	0.679	0.630
480	0.876	0.867	0.856	0.837	0.829	0.785	0.755	0.712	0.678	0.634
490	0.869	0.859	0.852	0.838	0.826	0.790	0.760	0.715	0.685	0.636
500	0.888	0.880	0.874	0.860	0.849	0.817	0.787	0.745	0.721	0.672
510	0.862	0.857	0.851	0.839	0.829	0.801	0.774	0.736	0.715	0.676
520	0.915	0.910	0.905	0.894	0.883	0.857	0.831	0.793	0.771	0.738
530	0.886	0.882	0.878	0.868	0.856	0.836	0.813	0.779	0.761	0.731
540	0.888	0.885	0.882	0.872	0.859	0.844	0.821	0.790	0.770	0.745
550	0.882	0.879	0.876	0.868	0.856	0.842	0.822	0.793	0.774	0.754
560	0.902	0.900	0.897	0.890	0.880	0.867	0.847	0.820	0.803	0.785
570	0.885	0.883	0.881	0.875	0.865	0.854	0.836	0.811	0.799	0.778
580	0.907	0.906	0.904	0.899	0.890	0.880	0.863	0.839	0.829	0.804
590	0.872	0.871	0.870	0.866	0.857	0.849	0.834	0.813	0.806	0.780
600	0.900	0.900	0.898	0.895	0.888	0.880	0.866	0.846	0.840	0.813
610	0.881	0.881	0.880	0.877	0.871	0.864	0.851	0.834	0.828	0.804
620	0.907	0.908	0.907	0.905	0.899	0.893	0.880	0.863	0.855	0.835
630	0.869	0.870	0.869	0.868	0.864	0.858	0.847	0.833	0.825	0.808
640	0.901	0.902	0.902	0.901	0.897	0.892	0.882	0.868	0.863	0.843
650	0.861	0.862	0.862	0.862	0.858	0.854	0.846	0.833	0.831	0.812
660	0.898	0.900	0.901	0.901	0.898	0.894	0.886	0.874	0.875	0.852
670	0.853	0.855	0.855	0.855	0.853	0.850	0.843	0.833	0.833	0.814
680	0.861	0.862	0.863	0.863	0.862	0.859	0.852	0.843	0.843	0.826
690	0.869	0.871	0.872	0.872	0.871	0.868	0.862	0.854	0.854	0.838
700	0.840	0.841	0.843	0.843	0.843	0.841	0.836	0.829	0.828	0.814
710	0.852	0.855	0.857	0.858	0.858	0.857	0.853	0.847	0.841	0.832
720	0.827	0.831	0.833	0.834	0.834	0.834	0.830	0.826	0.821	0.810

Table A.14: Thick (Prototype) P-I-N, Visible QE, 60K-33K

Appendix B

Simulations

Simulations are useful in many cases. Perhaps the real device is not built yet. Perhaps it will not be built until strong evidence of feasibility exists. Perhaps it is built, but there is risk of breaking it. Perhaps a theory requires a double-check. Perhaps something strange that cannot really be explained at all is being observed.

Given the current cost of computing horsepower, simulations are usually inexpensive to run. The thought process to set them up, debug them, and interpret their results is generally the expensive part — the right tests need to be run. A "test first and test often" approach to many research and development activities is also prudent. This Appendix covers some of the simulations performed to double-check some of the results and the theory developed in Chapters 4, 5, and 6.

B.1   Simulation of Detector Diffusion Processes

The expected effect of carrier migration in a detector on image quality was explained by many sources, (see Chapter 4) and most seemed to contradict each other and admit approximation. The diffusion of carriers in semiconductors is both simple and complex. Several simulations of the detector diffusion process were performed to validate the theoretical results expressed in Chapter 4 of this dissertation, and extend those results to areas where

closed form solutions probably do not exist. A purely stochastic simulation with discrete particles and particle motion was performed first. A second, more "linear" simulation was then performed, treating the particle position as a changing probability density over time. These results compared favorably to both each other and the theoretical diffusion profile.

B.1.1 Stochastic Simulation of Diffusion from a Point Source

A Monte-Carlo [87] simulation of diffusion from a point source of carriers at the surface of the detector was performed in Mathcad. The simulation served to experimentally verify the model of diffusion in detectors and investigate the effects of mean free path, which is typically only one order of magnitude smaller than many detector thicknesses. An excellent reference for this simulation technique may be found in Canali *et al.*[84]. Many subtle aspects of simulation of quantum conductive processes in semiconductors are detailed in this reference, and some can be neglected or re-modeled more efficiently depending upon the particular problem being simulated. Virtually all of these known effects except for the existence of a mean free path were neglected in the stochastic simulations performed here.

In this simulation, carriers were released one by one starting at the same point. For each carrier, a random direction was chosen and the carrier was moved a random distance (one mean free path) in this random direction. This process was repeated until the Z component of the carrier exceeded the distance from the surface to the depletion region. At this point, the exact x and y point of carrier collection was computed, and this location was added to a list of points. This was repeated for 5000 carriers. Two collection surfaces were actually used, one above and one below the detector surface. This gave the equivalent of reflecting the diffusion path off the detector surface. Several variations of this simulation were performed.
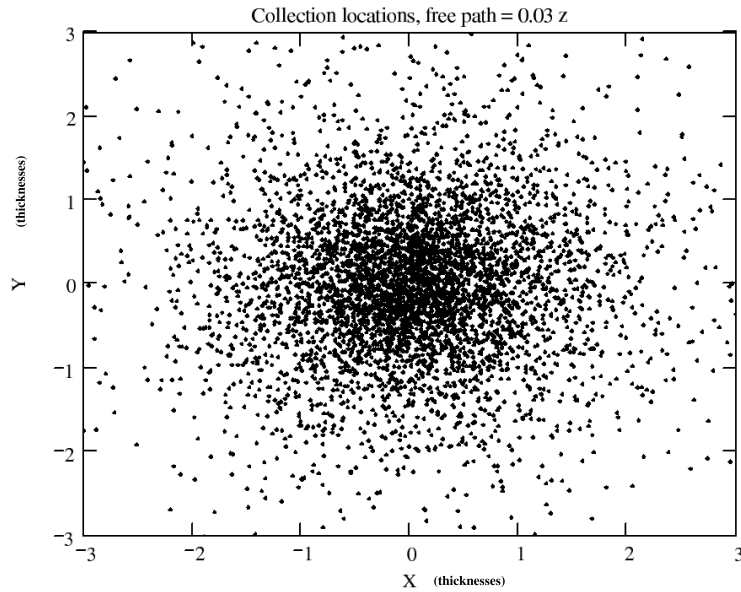
Figure B.1: This scatter plot shows the collection locations of a Monte-Carlo diffusion simulation. The detector was one unit thick, and the mean free path was 0.03 units. Carriers were released at the upper surface and allowed to diffuse until they crossed the lower surface. At collection, the location and collection time was recorded.

The simulation was normalized to a unity detector thickness. The shortest mean free path was 0.03 times the detector thickness. Other simulations were done with a free path of 0.1 and 0.3 times detector thickness.

An increasing circular radius was applied to this collection simulation data, and the percentage of carriers collected within the radius was tallied. This collection efficiency was compared to the theoretical collection efficiency from Chapter 4, and is shown in Figures B.2, B.3 and B.4.

When the mean free path was increased to 0.3 (a sizable chunk of the distance from emission to collection) the modeling became poorer. (An infinite mean free path results in the Forrest-Ninkov model.)
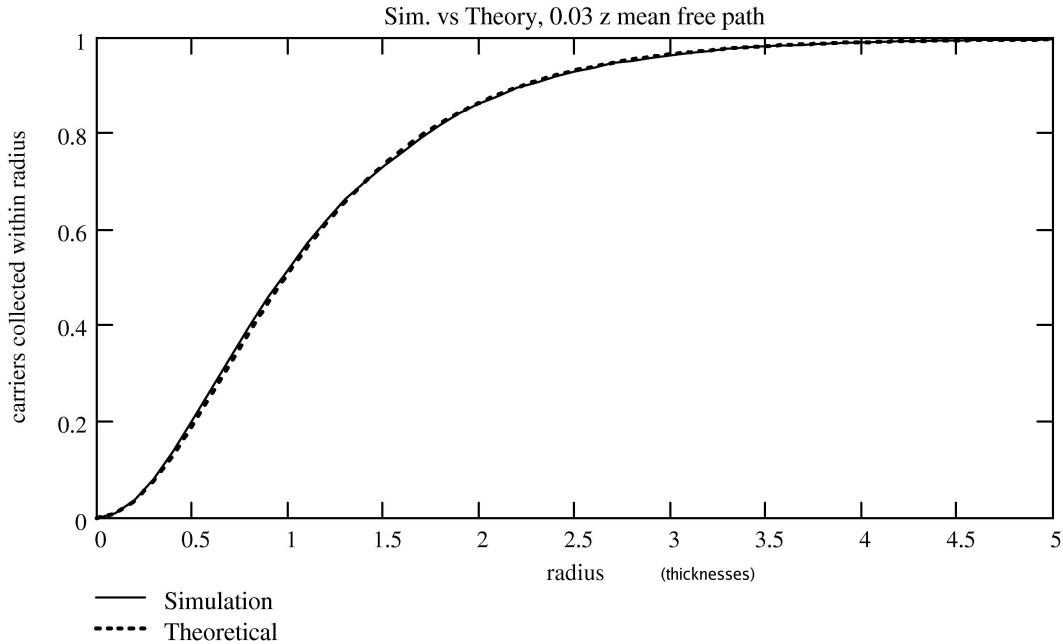
181

Figure B.2: The results of the simulation compared almost identically with diffusion theory for a small (0.03 unit) mean free path.

The simulations show that the diffusion equation model agrees nicely with simulation, especially when the mean free path is small compared to the detector thickness. Mean free path is typically a fraction of a micron, with detector dimensions of several microns to tens of microns.

When line spread was extracted from the shortest mean free path simulation data, it showed similar agreement. This is shown in Figure B.5. Figure B.6 is logarithmic plot of line spread, and shows lateral diffusion from the line decaying exponentially with a lateral diffusion depth of 0.63 times the detector thickness. This experimentally-obtained slope is in good agreement with the slope of the line spread expression in Equation 4-26, namely $2/\pi = 0.637$.

The experimental crosstalk several thicknesses away appears to show a slight increase in crosstalk probability over theory.
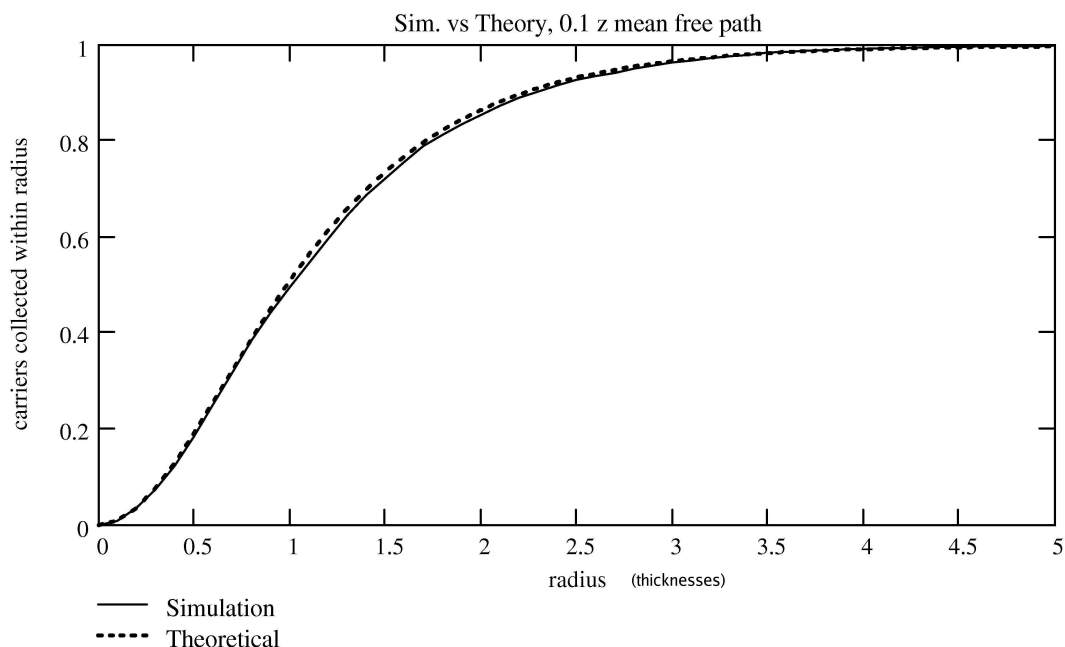
Figure B.3: The results of the simulation compared reasonably well with diffusion theory for a mean free path of 0.1 units, but carriers were more likely to diffuse farther than theory predicted.

B.1.2   Linear Simulation of Diffusion

Stochastic simulation of the diffusion of carriers (by modeling mean free path and random collisions) can certainly provide an accurate method if consideration of quantum effects is required. However, it consumes large amounts of computational horsepower. The previous simulations ran for many hours. If the effects of mean free path can be neglected (and it appears that they can in many cases) a non-stochastic approach yields more useful point spread results somewhat more quickly. This technique, illustrated in Figure B.7, can be applied to simulations with varying detector geometries and varying carrier lifetimes. One set of simulation data yields diffusion profiles at all carrier lifetimes for geometries that can have arbitrary pixel shapes (including gaps) as well as surface recombination effects.
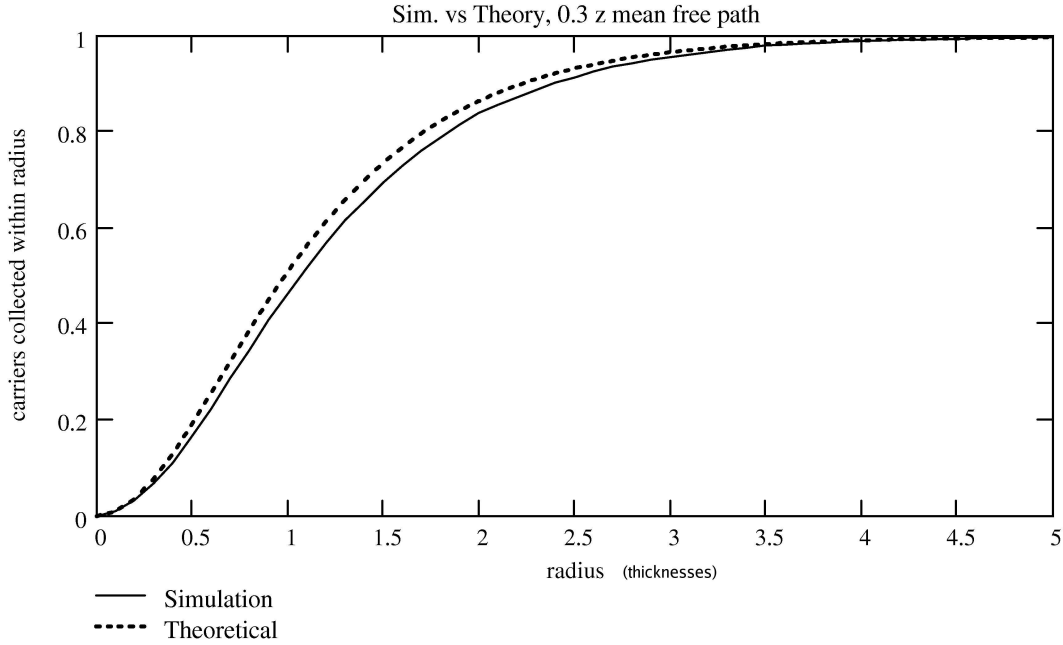
Figure B.4: The results of the simulation visibly diverged with diffusion theory for a mean free path of 0.3 units. Carriers were noticeably more likely to diffuse farther than theory predicted. Note that the discrepancy disappears at longer distances, when the mean number of collisions becomes large again.

In this technique, the simulation begins at $t = 0$ with a point charge in a bounded geometry, either three dimensional:

$$p\left(x, y, z, t\right)|_{t=0} = \delta\left(x, y, z\right).$$ (B-1)

or two dimensional:

$$p\left(x, y, t\right)|_{t=0} = \delta\left(x, y\right).$$ (B-2)

The diffusion process is then simulated over time as a varying probability distribution. At the collection boundaries, assuming immediate collection, there is zero probability of charge crossing back into the simulation once it enters the collection zone — so a zero density boundary condition is maintained. (Surface Recombination may be simulated with a
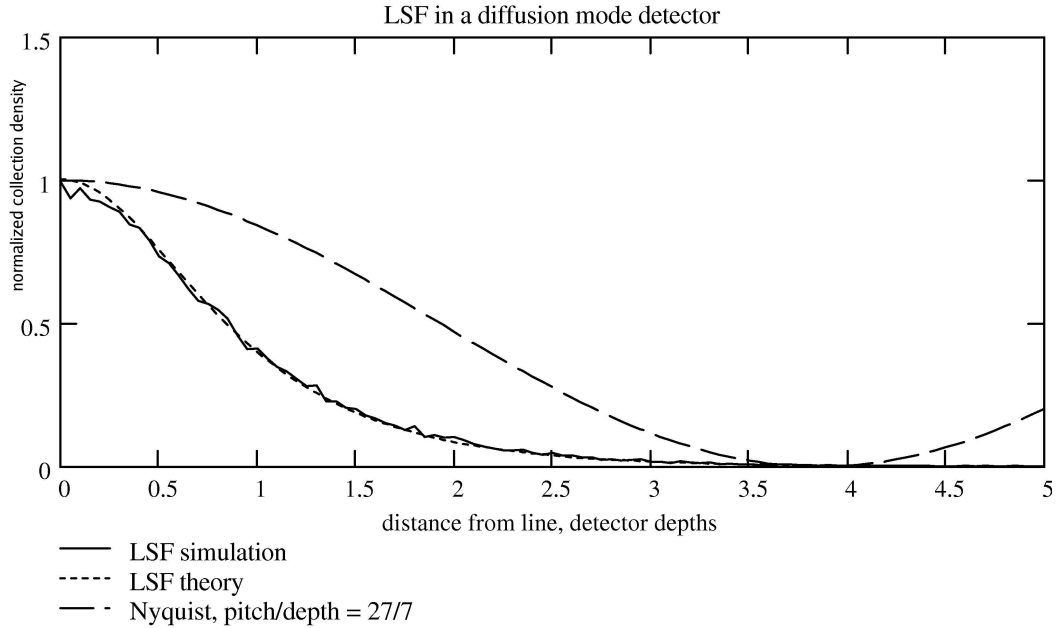
184

Figure B.5: Taking an Abel transform of the diffusion simulation showed similar agreement with diffusion theory when the mean free path was small.

variation of this.) The output data is in the form $p(s, t)$ where s represents a location on the boundary. Since the recombination probability (assumed the same at all positions) is independent of the diffusion process, the effects of recombination may be considered after the diffusion simulation is complete. The total collection density at a boundary location s and carrier lifetime decay constant α can be expressed as a post-processing of the simulation data:

$$p(s) = \int_{t=0}^{t=\infty} p(s, t) e^{-\alpha t} dt. \tag{B-3}$$

B.1.3 Line Spread function with Bulk Recombination

A simulation of the time-dependent diffusion equation was performed starting with a point charge at the surface. Charge was represented as a probability density in small cells in a two dimensional grid: One dimension was the thickness of the detector and the other was the
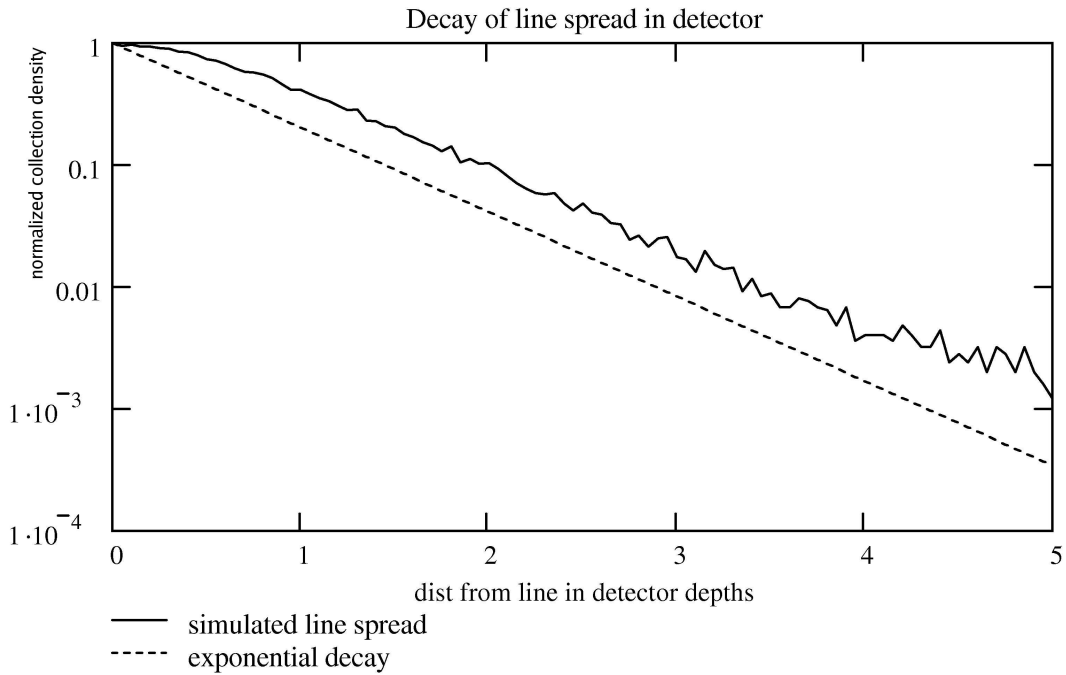
185

Figure B.6: A logarithmic plot of the line spread simulation shows agreement with the theoretical "far-field" decay rate.
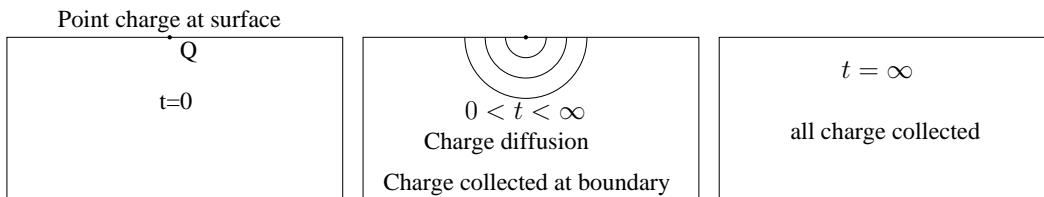

Figure B.7: If mean free path can be neglected, a time-varying probability density function (PDF) can yield results more quickly. The PDF is non-zero in a single voxel at the start of the simulation. As time progresses, charge in a voxel has some probability of moving to a neighboring voxel. Charge crossing a collection boundary is recorded and removed from the simulation.

width of the detector. Simulated diffusion changed the distribution by moving a fraction of the charge in each cell to each neighbor cell. The cells were assumed small enough to approximate the continuous distribution. Charge crossing the collection boundary was not allowed to diffuse back. The probability of collection at the boundary at all locations and times was recorded until 99.998% of the original point charge was collected. Using the resulting simulated data, the effect of bulk recombination upon the line spread function was investigated. The same simulation data set $p(s, t)$ was usable for computing line spread for any assumed carrier lifetime. Several different lifetimes were tried. Mathcad was used to plot the results.

Results from this simulation with varying lifetimes are shown in Figure B.8. It shows the probability density of carrier collection in lateral distance units normalized to detector thickness and the variation in line spread function as the carrier diffusion length is reduced.

A logarithmic plot is shown in Figure B.9. It was suspected that distances past the diffusion length might show a different profile than distances less than the diffusion length, but this is not the case. Collection well within the "diffusion length" shows attenuation as well, and there is no clear change in mode. This is likely due to the stochastic nature of carrier lifetime and diffusion length, which represent mean values and not predictable behavior for carriers. It is expected that Holloway's analysis of diffusion should agree with these simulations.

The simulation was rewritten with gaps between the pixels. These gap areas along the boundary reflected diffusion normal to the boundary back into the sourcing cell. Figure B.10 shows this diffusion profile near one of the gaps. A logarithmic plot in Figure B.11 shows the larger scale behavior of the gap. As diffusion makes its way over the gap, density sees a boost, then rapidly shifts back into exponential decay after an initial transient peak.
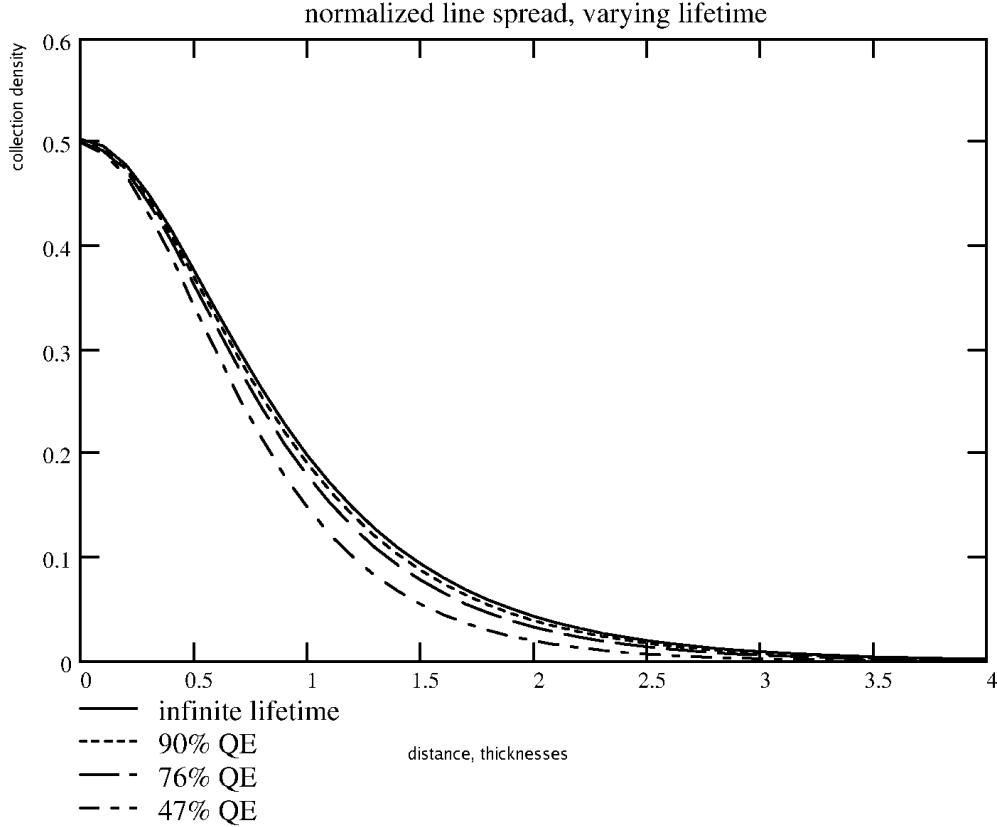
Figure B.8: PDF simulation of diffusion allowed easy experimentation with the effects of carrier lifetime. This simulation shows an increase in sharpness and decrease in quantum efficiency.

B.2 Simulation of intrinsic P-I-N electric field

A simulation of the potential between the pixels and the back bias surface of the P-I-N array was performed using a Python script employing the "numarray" Python module developed by Space Telescope Science Institute. A pixel-to-pixel spacing of 27 microns, detector thickness of 185 microns, and a gap of 5 microns (estimated) were used in the simulation. Detector node voltages were fixed at ground, and the back bias fixed at 30 volts. The intrinsic region was modeled as purely intrinsic. The potential at each point in a rectangular
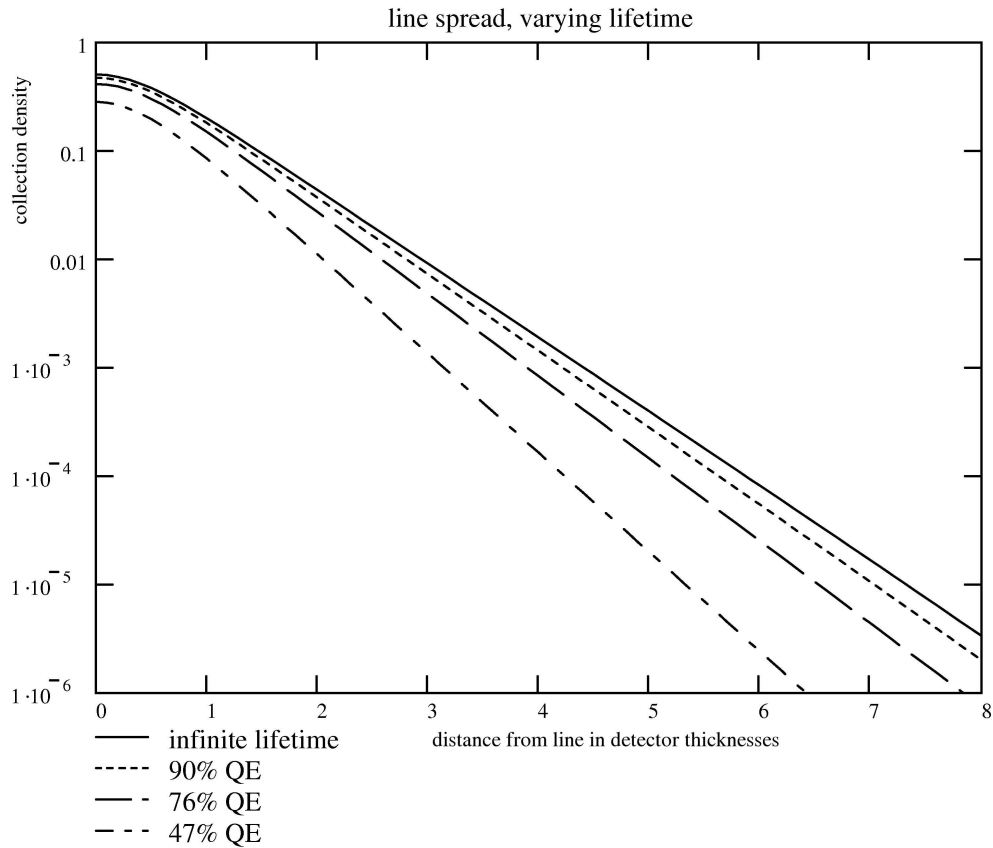
Figure B.9: A shorter diffusion length results in a more rapid "far-field" exponential decay.

grid was iteratively solved for, and the electric field at the edge of the pixel implants was derived from these potentials. The vertical dimension in the grid represented the thickness of the detector, with the top of the grid at the back bias and the bottom of the grid at the pixel implants. The horizontal dimension represented position along a row of the array. Since the simulation was two-dimensional, not volumetric, its results are representative of the line response. A three dimensional simulation could be done as well. The center pixel was varied slightly, the potentials were recomputed iteratively, and fields re-derived. The results are shown in Figure B.12.
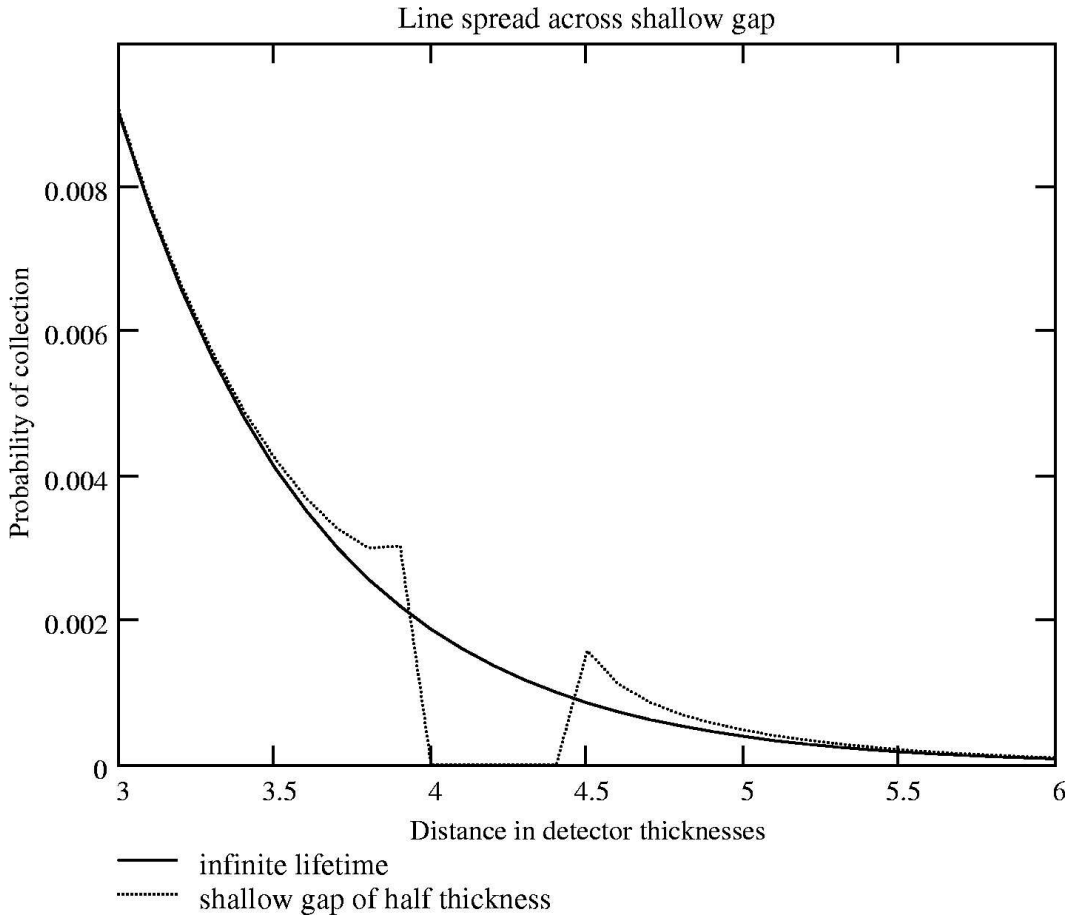
Line spread across shallow gap

Figure B.10: Diffusion simulation can be useful for exploring the effect of gaps between pixels. This simulation shows the effect of an inter-pixel gap half as wide as the detector is thick. Probability of collection on either side of the gap is increased, but is zero in the gap itself.

Figure B.12 shows the vertical electric field strength just above the P-I-N detector implants in this 2-D simulation. The trace with long dashes represents the field with all pixels at ground potential, and the back bias, 185 microns away, at 30 volts. The area underneath this curve, from Gauss' law, is proportional to the charge created by a 30 volt bias. Reducing the bias on the center pixel by only 0.5 V resulted in the trace with short dashes. A change in voltage of one-sixtieth of the back bias has caused the pixel to lose approxi-
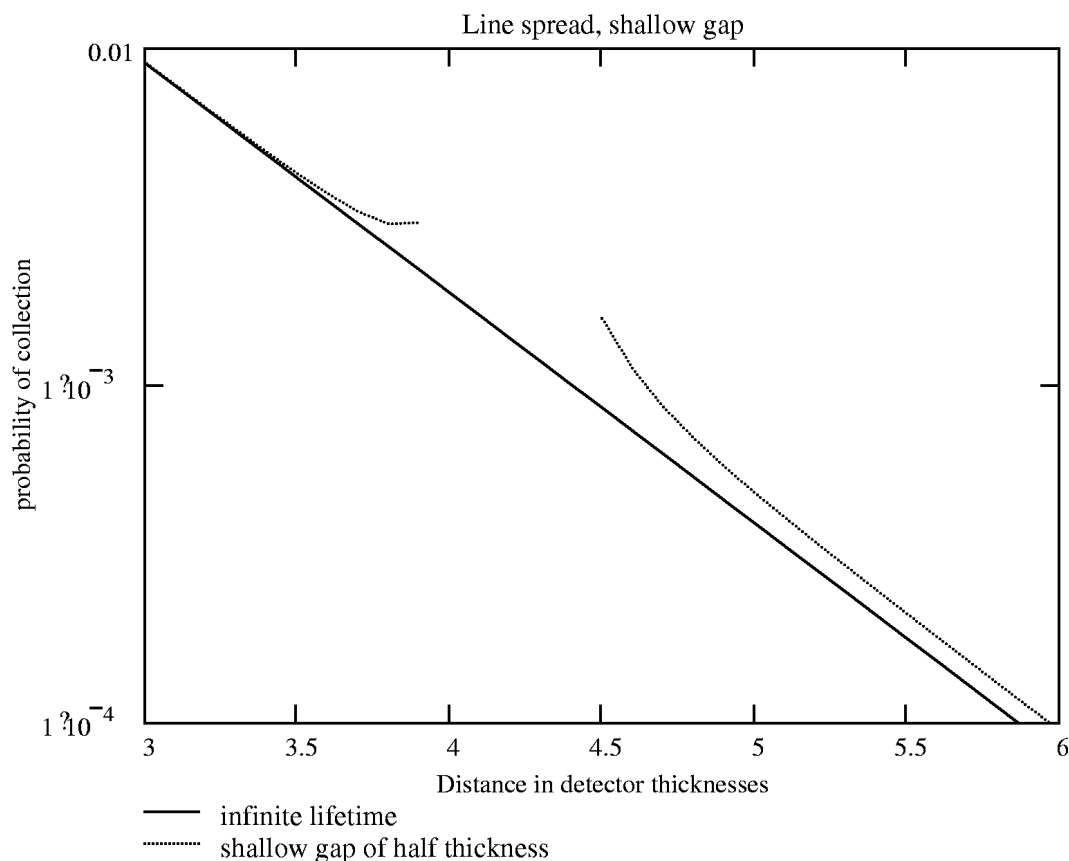
Figure B.11: A logarithmic plot of diffusion over a gap shows the increase in collection probability near the edges of the gap. There is no probability of collection in the gap itself — this cannot be plotted on a log scale.

mately *one-sixth* of its field, and thus, one-sixth of its charge. This lost area is gained by the two neighboring pixels. The increased area indicates a theoretical inter-pixel coupling of approximately *ten times the coupling to the back bias* for this assumed geometry. Doubling this result yields a rough estimate of the coupling in the two-dimensional array, as the pixel is fringed on four edges rather than two.

The solid trace at the bottom shows the difference between the two fields, illustrating the loss of charge from the center pixel and the gain by its two neighbors.
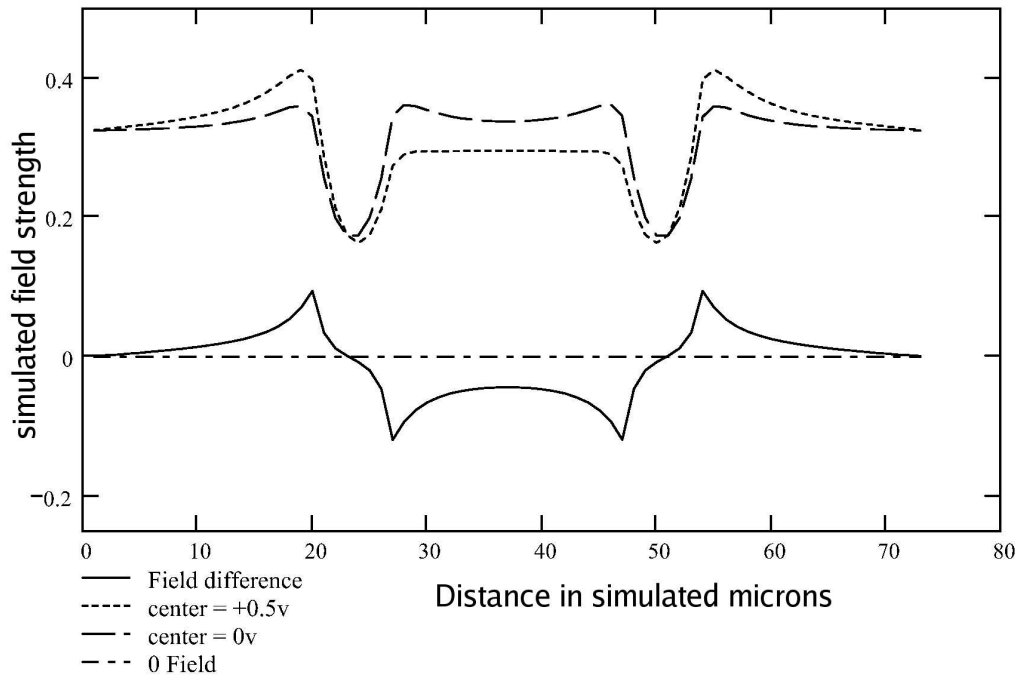
Figure B.12: The electric potential in the P-I-N intrinsic region was simulated by applying Laplace's equation iteratively. The electric field strength was derived from the potentials. Changing the potential of a single pixel by a small fraction of the bias potential resulted in large changes in field strength — in both that pixel and its neighbors. (The magnitude of this field indicated an increase in surface charge density in agreement with observed interpixel coupling.)

Similar simulations of the potentials and fields underneath a pixel implant were also performed. For a similar geometry and epoxy between the indium bumps, additional coupling of a little less than half this amount is possible. Silicon has a dielectric constant of 11, but epoxy's dielectric constant is closer to 5. Isolated conductors between the pixels could increase this coupling by forming an artificial dielectric, but conductors that are connected to definite potentials will serve to stabilize the inter-pixel potentials and reduce coupling even further.

192

Appendix C

System Noise

C.1 Noise in multichannel systems

When a detection system has multiple channels, the noise observed in each channel is ide-ally only produced by independent mechanisms internal to the detectors that feed each channel. If the surrounding system introduces extra noise into each channel, this excess noise adds in to the noise of the channels, resulting in a higher noise than what may ul-timately be achievable. If the noise is a crosstalk or interference, a correlation is often created between the channels. This correlation can be used to extract a power spectrum for the common noise. Cooper and McGillem[88] provide an excellent reference; some of the techniques described there are employed here.

Consider two signals, $x_1(t)$ and $x_2(t)$, which are zero mean random processes.

The autocorrelation of either single signal $x(t)$ is:

$$R_{xx}(\tau) = E\left[x(t)\,x(t-\tau)\right].$$ (C-1)

The cross-correlation of a pair of signals x_1 and x_2 is:

$$R_{12}(\tau) = E\left[x_1(t)\,x_2(t-\tau)\right].$$ (C-2)
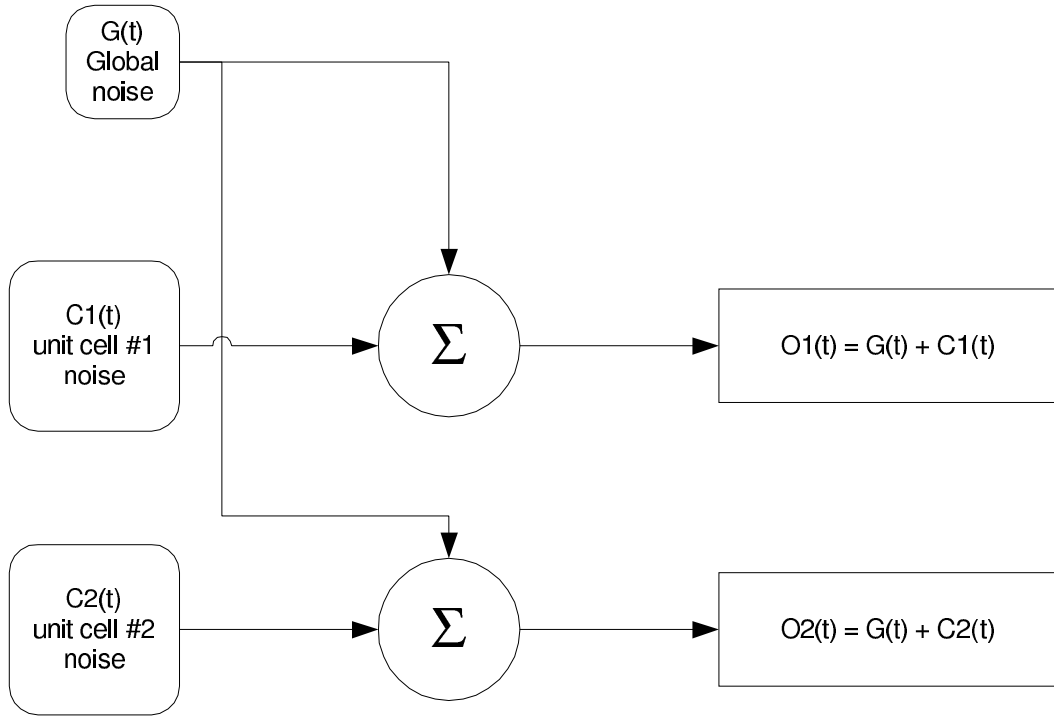
Figure C.1: Multichannel model of noise as global noise added to channel-independent noise.

When the signal is a zero mean, the autocorrelation is also the auto-covariance, and this simplification is assumed here.

Modeling these signals as channel-dependent noise sources $C_i(t)$ (*e.g.* unit cell output FET noise) corrupted by a global noise $G(t)$ that appears on each channel (*e.g* electromagnetic interference, bias or temperature fluctuations, or warm electronics noise) yields:

$$x_1(t) = C_1(t) + G(t). \qquad \text{(C-3)}$$

and

$$x_2(t) = C_2(t) + G(t). \qquad \text{(C-4)}$$

Looking at the autocorrelation of one of the signals:

$$R_{11}(\tau) = E\left[(C_1(t) + G(t))(C_1(t-\tau) + G(t-\tau))\right]. \qquad \text{(C-5)}$$

Since C_i and G are independent, the expected value of their product is zero. Thus, this simplifies to:

$$R_{11}(\tau) = E\left[(C_1(t)C_1(t-\tau)) + (G(t)G(t-\tau))\right]. \qquad \text{(C-6)}$$

and then to:

$$R_{11}(\tau) = R_{C_1C_1}(\tau) + R_{GG}(\tau). \qquad \text{(C-7)}$$

Even more interesting is the cross-correlation:

$$R_{12}(\tau) = E\left[(C_1(t) + G(t))(C_2(t-\tau) + G(t-\tau))\right]. \qquad \text{(C-8)}$$

which expands to

$$E\left[C_1(t)C_2(t-\tau) + C_1(t)G(t-\tau) + G(t)C_2(t-\tau) + G(t)G(t-\tau)\right]. \qquad \text{(C-9)}$$

Since there is no correlation between the channels sources or between either channel source and the global source, this simplifies to

$$R_{12}(\tau) = E\left[G(t)G(t-\tau)\right]. \qquad \text{(C-10)}$$

which is the autocorrelation function of the global noise, $R_{GG}(\tau)$. Subtracting Equation C-10 from Equation C-7 results in the expression

$$R_{11}(\tau) - R_{12}(\tau) = R_{C_1C_1}(\tau). \qquad \text{(C-11)}$$

which says that the autocorrelation of a single channel minus the cross-correlation of adjacent channels can serve as an estimator of the autocorrelation of the device noise only. It is the "residual noise" of a single channel, with the system noise contribution removed.

C.1.1   Power Spectral Density of System and Device noise

The Wiener-Khinchine relation,

$$S_x(\omega) = \int_{-\infty}^{+\infty} R_x(\tau)e^{j\omega\tau}d\tau = \mathcal{F}\{\mathcal{R}_\mathcal{X}(\tau)\}. \qquad \text{(C-12)}$$

expresses the power spectral density of a random process in terms of the Fourier Transform of its autocorrelation function. This expression for the power spectral density is generally considered a far better estimator of power spectral density than squaring the direct Fourier transform of a sample of the random process.

Using the Wiener-Khinchine expression and the expressions in Equations C-7, C-10, and C-11, power spectral densities of the total noise, system noise, and device noise may be estimated. The Fourier Transform of the output autocorrelation is the total power spectral density. The Fourier Transform of the output cross-correlation is the power spectral density of the system noise. The transform of their difference (or the difference of their transforms) is the power spectral density of the residual (device) noise.

Hence, the spectrum of the unit cell noise can be estimated by taking the Fourier transform of the difference between the output autocorrelation and the output cross-correlation.

It was not assumed that unit cell noises have identical spectra to reach this result. This technique can be used to estimate the device noise or the power spectral density of an individual unit cell.

The "system noise" referred to here is more accurately the "correlated" system noise. If the system introduces uncorrelated noise to the channels, this will be indistinguishable from device noise.

C.2   Spatial (fixed pattern) Noise

Correlation can also be spatial. Figure C.2 shows a distinct odd-even row and column effect of unknown origin. Correlation between even and odd rows and columns is visible in this difference of two long fowler integrations at 100K with no illumination. Row, column, and checkerboard noise appears exclusively at the very highest spatial frequencies (the Nyquist) and filtering them out digitally should have no ill effect on images. The imaging optics are
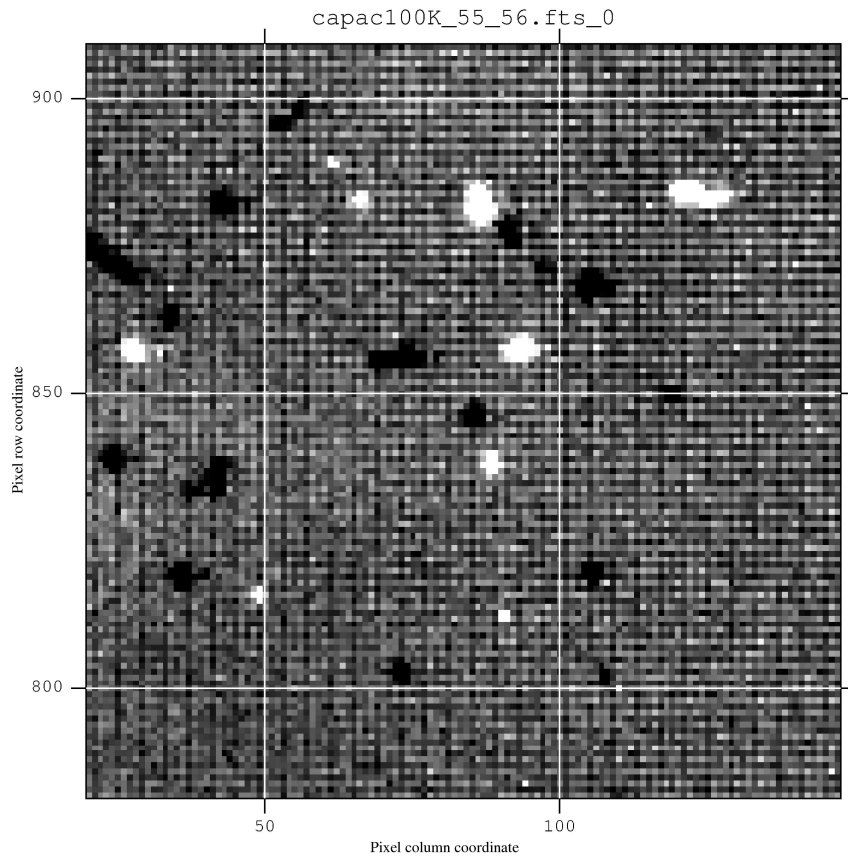
Figure C.2: This difference of two long-integration images shows two different anomalies. The black and white spots are higher energy cosmic ray events. The fixed checkerboard pattern may be from a thermal drift over the long time it took to acquire the original images, and indicate a patterned variation in the multiplexer.

usually designed such that no optical signal is present at the Nyquist; otherwise aliasing can occur. Such noise can cause problems in the estimation of dark current by device noise when the dark current is too low to measure directly.

Appendix D

Noise from Stochastic Amplification

Semiconductor photo-detectors generally cannot detect photons without sufficient energy. Longer wavelength photons are unable to move an electron from the valence band into the conduction band. This transition requires a photon with an amount of energy that exceeds the semiconductor's "band gap." If incoming photons have enough energy, they may actually release more than one electron. A single energetic electron is released and this particle knocks loose one or more additional electrons. This gain is generally a stochastic process — sometimes only one electron is released, sometimes two or more — it introduces additional noise. Since this mechanism in important both in the proper characterization of the conversion factor of a device, it should be considered. (Silicon P-I-N devices do not exhibit stochastic amplification at visible wavelengths.)

D.1   Basic theory

The amplification can be expressed as a discrete probability distribution $p(m)$ where $m >= 0$ and $p(m)$ is the probability that m electrons are released for a single incoming photon. From this distribution, it is easy to compute the mean

$$\overline{m} = \sum_{m=0}^{\infty} mp\left(m\right).\tag{D-1}$$

and variance:

$$\sigma_m^2 = \sum_{m=0}^{\infty} (m - \overline{m})^2 \, p\,(m)\,.$$ (D-2)

The probability that an incoming photon is captured in some way is called η and is simply

$$\eta = 1 - p\,(0)\,.$$ (D-3)

It can be shown [70] that if the input to the amplification process is a random variable with mean $\overline{x}$ and variance σ_x^2, then the output y is a random variable of mean

$$\overline{y} = \overline{mx}.$$ (D-4)

and variance

$$\sigma_y^2 = \sigma_x^2 \overline{m}^2 + \sigma_m^2 \overline{x}.$$ (D-5)

The term $\sigma_x^2 \overline{m}^2$ is expected. After gain, the output variance will be increased by at least the gain squared. Poisson statistics would only increase the variance by the gain, so it should be obvious that Poisson statistics are now lost. However, the additional variance from $\sigma_m^2 \overline{x}$ might not be expected. Since the gain itself is a stochastic process, there is *additional* uncertainty in exactly how many extra carriers were produced. The ratio of the magnitude of the noise including this term to the noise without this term is called β, the noise increase associated with the gain.

$$\beta = \frac{\sigma_x^2 \overline{m}^2 + \sigma_m^2 \overline{x}}{\sigma_x^2 \overline{m}^2}.$$ (D-6)

D.2 A simple example of gain statistics

For an example, consider the case when gain exceeds unity but is less than two. The lowest noise amplification that could possibly be achieved is the case when all input quanta are
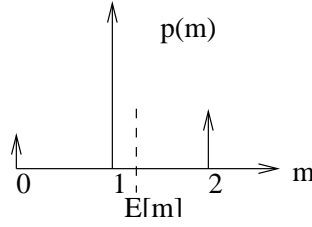
Figure D.1: Detector gain can be represented as a probability density function — given one photon, what it the probability that zero, one, two (or more) electrons are produced?

captured, *i.e.* $\eta = 1$, and either one or two electrons are released. If α of the incoming photons produce an extra electron, and the remainder only produce one electron the gain from Equation D-1 is

$$\overline{m} = 1 \cdot (1 - \alpha) + 2 \cdot \alpha = 1 + \alpha \tag{D-7}$$

The amplification variance in this case, from Equation D-2 is

$$\sigma_m^2 = (\overline{m} - 1)^2(2 - \overline{m}) + (2 - \overline{m})^2(\overline{m} - 1). \tag{D-8}$$

which simplifies to

$$\sigma_m^2 = (\overline{m} - 1)(2 - \overline{m}) \cdot [(2 - \overline{m}) + (\overline{m} - 1)] = (\overline{m} - 1)(2 - \overline{m}). \tag{D-9}$$

and there is definitely an increase in noise. Note that the amplification variance is zero for both $\overline{m} = 1$ and $\overline{m} = 2$. This is expected, as there is no uncertainty at integral gains in the lowest noise case. (It is unlikely that this performance *will* be achieved, however.)

D.3   A simpler example of gain statistics

The expression in Equation D-5 holds even when at most one electron is released per incoming photon. The mean value $\overline{m}$ is the fraction of incoming photons that release one

electron.

$$p(0) = 1 - \overline{m}. \tag{D-10}$$

and

$$p(1) = \overline{m}. \tag{D-11}$$

The variance of this amplification process is thus:

$$\sigma_m^2 = (1 - \overline{m})\,\overline{m}^2 + m\,(1 - \overline{m})^2. \tag{D-12}$$

which expands to

$$\sigma_m^2 = \overline{m}^2 - \overline{m}^3 + \overline{m} - 2\overline{m}^2 + \overline{m}^3. \tag{D-13}$$

and simplifies to

$$\sigma_m^2 = \overline{m} - \overline{m}^2. \tag{D-14}$$

If the incoming mean is $\overline{x}$ then the output mean is

$$\overline{y} = \overline{xm}. \tag{D-15}$$

and the variance of the output is

$$\sigma_y^2 = \sigma_x^2 \overline{m}^2 + \left(\overline{m} - \overline{m}^2\right)\overline{x}. \tag{D-16}$$

Assuming the input process is Poisson distributed, $\sigma_x^2 = \overline{x}$, so

$$\sigma_y^2 = \overline{x}\,\overline{m}^2 + \left(\overline{m} - \overline{m}^2\right)\overline{x}. \tag{D-17}$$

Simplifying this yields

$$\sigma_y^2 = \overline{xm}. \tag{D-18}$$

This is the expected result — $\overline{y} = \overline{xm}$, so $\sigma_y^2 = \overline{y}$. Thus, the process is still Poisson as would be expected with random loss of single collections. In other words, binomial selection preserves Poisson statistics.

Appendix E

Optimal Sampling

In many chapters of this dissertation, sampling was considered in the spatial domain. Non-destructive readouts allow sampling in the time domain as well. This Appendix considers the time domain aspects of sampling an integrating detector. When the device noise and the photon noise are roughly equal, an optimal estimator for photon arrival rate must consider the different natures of these noise sources. This Appendix describes the optimal estimator.

E.1   Theory of Optimal Sampling

Non-destructive readouts allow the possibility of taking intermediate images while integrating. This is called "multiple sampling." Fowler and Gatley [89] proposed multiple sampling as a way to reduce read noise on FPA readouts for astronomy back in 1989. At the time, they described the technique as "one of the simplest imaginable" and said "it may well be that more complex multi-read strategies will result in further noise reduction." At that time, techniques known as "delta reset," "double correlated sampling," and "triple correlated sampling" were in use. The next year, they looked at these various sampling techniques as well as a "line fitting" or "sampling up the ramp" technique. Forrest and Garnett [90] subsequently investigated the theoretical performance of these techniques. They showed that the "multiple correlated sampling" (which they dubbed "Fowler-sampling")

was close to optimal— some improvement could be made, but improvement was small. They showed that the "sampling up the ramp" techniques did perform better than the "correlated double sampling" if the read noise was significant, otherwise correlated double sampling was the best. When read noise was dominant, line fitting was shown to be superior. Otherwise, Fowler sampling was shown to be better. In many practical situations, read noise is significant, but not dominant, and Fowler sampling is employed. When measuring dark current (or the noise that it generates) on arrays with extremely low dark current, read noise is the dominant noise source. In these laboratory situations, and in some real observational situations, there is some improvement to be had in estimation.

E.1.1 Best Linear Unbiased Estimation

The general optimal sampling algorithm presented here is derived from the "Best Linear Unbiased Estimator" or "BLUE"[91]. Offenberg and Fixsen [17] employed the BLUE optimal estimator for white read noise in a simulation of a cosmic ray rejection algorithm for JWST.

Here is a derivation of the algorithm, with some generalizations. The BLUE, besides being unbiased by design, is also the minimum variance estimator. In this sense it is considered "best," and is sometimes called an unbiased minimum variance estimator or UMVE. Best Linear Unbiased Estimation is a special case of Weighted Least Squares Estimation. It is derived from the "linear" model

$$Z = H\Theta + V \tag{E-1}$$

where Z is a k element measurement vector, Θ is a deterministic but unknown parameter vector with n elements, H is a deterministic k by n system matrix, and V is a k element zero mean noise vector with positive known covariance matrix R.

A linear solution of the form

$$\hat{\Theta}_{BLU} = FZ. \tag{E-2}$$

is assumed. Unbiasedness, which is such that

$$E\{\Theta - \hat{\Theta}\} = \vec{0}. \tag{E-3}$$

requires that

$$FH = I. \tag{E-4}$$

where I is an identity matrix. Proof of Equation E-4 is straightforward, and is taken from Mendel[91]. From here:

$$E\{\hat{\Theta}\} = \Theta. \tag{E-5}$$

Substituting Equation E-2:

$$E\{FZ\} = \Theta. \tag{E-6}$$

Substituting Equation E-1:

$$E\{F(H\Theta + V)\} = \Theta. \tag{E-7}$$

Taking the expectation separately:

$$E\{FH\Theta\} + E\{FV\} = \Theta. \tag{E-8}$$

Noise V is zero mean, and everything else is constant, so

$$FH\Theta = \Theta. \tag{E-9}$$

and this promptly yields the result:

$$FH = I. \tag{E-10}$$

Only two assumptions are made to reach this — First, H is assumed deterministic, and so can be moved outside the expectation operator. Second, V is assumed zero mean

noise, thus it has zero expectation. Generally, it is easy to model the noise as zero mean. Assuming a deterministic system is not always as easy.

This result effectively allows each row of the F matrix to be considered independently. Since each row of F is a set of coefficients for estimating a single parameter in the parameter vector Θ, the solution finds the best coefficients for a single parameter Θ_i, and constructs the F matrix out of the individual solutions. The following derivation is also taken from Mendel [91]. The F matrix is partitioned into individual rows, and each row f_i' is considered as the transpose of a column vector.

$$F = \begin{pmatrix} f_1' \\ f_2' \\ \vdots \\ f_n' \end{pmatrix}. \tag{E-11}$$

The elements in the ith row of the matrix are the coefficients that determine the solution for the estimation of the ith parameter of the Θ vector. In other words, each row of the F matrix is an independent estimator that can be applied to the Z vector to estimate one element of the parameter vector Θ.

$$\hat{\Theta}_i = f_i' Z. \tag{E-12}$$

To make the following derivation easier, the unbiasedness constraint is transposed:

$$H'F' = I. \tag{E-13}$$

which is the same as

$$H' \begin{pmatrix} f_1 & f_2 & \cdots & f_n \end{pmatrix} = \begin{pmatrix} e_1 & e_2 & \cdots & e_n. \end{pmatrix} \tag{E-14}$$

$$H'f_i = e_i. \tag{E-15}$$

where e_i is the ith unit vector; all elements are zero except the ith, which is 1.

The derivation of the BLUE follows, expressing the squared estimation error on the ith parameter vector, then minimizing this error.

$$
\begin{aligned}
E\{[\Theta_i - \hat{\Theta}_i]^2\} &= E\{[\Theta_i - f_i'Z]^2\} \\
&= E\{[\Theta_i - Z'f_i]^2\} \\
&= E\{\Theta_i^2 - 2\Theta_i Z'f_i + (Z'f_i)^2\}.
\end{aligned} \tag{E-16}
$$

and substitution of linear system model and $\Theta e_i = \Theta_i$ yields

$$
\begin{aligned}
E\{[\Theta_i - \hat{\Theta}_i]^2\} &= E\{\Theta_i^2 - 2\Theta_i(H\Theta + V)'f_i + ((H\Theta + V)'f_i)^2\} \\
&= E\{\Theta_i^2 - 2\Theta_i\Theta'H'f_i - 2\Theta_i V'f_i + (\Theta'H'f_i + V'f_i)^2\} \\
&= E\{\Theta_i^2 - 2\Theta_i\Theta e_i - 2\Theta_i V'f_i + (\Theta e_i + V'f_i)^2\} \\
&= E\{\Theta_i^2 - 2\Theta_i^2 - 2\Theta_i V'f_i + \Theta_i^2 + 2\Theta_i V'f_i + (V'f_i)^2\} \\
&= E\{(V'f_i)^2\} \\
&= E\{f_i'VV'f_i\} \\
&= f_i'Rf_i.
\end{aligned} \tag{E-17}
$$

where R is the covariance matrix associated with noise V. The method of Lagrange multipliers is employed on the objective function

$$
J_i = f_i Rf_i + \lambda_i'(H'f_i - e_i). \tag{E-18}
$$

to minimize the error. Taking the partial derivative of this function with respect to f_i and setting it equal to zero (a requirement for minimization) yields the relationship

$$
2Rf_i + H\lambda_i = \vec{0}. \tag{E-19}
$$

The solution for this is

$$
f_i = -\frac{1}{2}R^{-1}H\lambda_i. \tag{E-20}
$$

Substituting this expression into the unbiasedness constraint

$$H' f_i = e_i. \tag{E-21}$$

yields

$$H' \left(-\frac{1}{2} R^{-1} H \lambda_i \right) = e_i. \tag{E-22}$$

which is easily solved for:

$$\lambda_i = -2(H' R^{-1} H)^{-1} e_i. \tag{E-23}$$

Substituting this back again yields

$$f_i = R^{-1} H (H' R^{-1} H)^{-1} e_i. \tag{E-24}$$

The matrix $R^{-1} H (H' R^{-1} H)^{-1}$ is effectively the complete solution, and the unit vector e_i simply sifts out the proper column of the solution. After some manipulation

$$F' = \begin{pmatrix} f_1 & f_2 & \cdots & f_{n.} \end{pmatrix} \tag{E-25}$$

$$F' = R^{-1} H (H' R^{-1} H)^{-1} \begin{pmatrix} e_1 & e_2 & \cdots & e_n \end{pmatrix} \tag{E-26}$$

$$F' = R^{-1} H (H' R^{-1} H)^{-1} I. \tag{E-27}$$

which, taking advantage of the symmetry of R, transposes back to

$$F = (H' R^{-1} H)^{-1} H' R^{-1}. \tag{E-28}$$

So, the final solution is

$$\hat{\Theta}_{BLU} = (H' R^{-1} H)^{-1} H' R^{-1} Z. \tag{E-29}$$

208

E.1.2 Linear model of an integrating detector

The pixel is an integrating detector, and assuming constant illumination, the charge on a pixel increases linearly over time proportional to the illumination. Thus, the pixel may be modeled with

$$Z_i = V_0 + St_i + \tilde{Z}_i. \tag{E-30}$$

where V_0 is a (noiseless) initial value. This expression may be rearranged as a linear system:

$$
\begin{bmatrix} Z_n \\ Z_{n-1} \\ \vdots \\ Z_0 \end{bmatrix}
=
\begin{bmatrix} 1 & t_n \\ 1 & t_{n-1} \\ & \vdots \\ 1 & t_0 \end{bmatrix}
\begin{bmatrix} V_0 \\ S \end{bmatrix}
+
\begin{bmatrix} \tilde{Z}_n \\ \tilde{Z}_{n-1} \\ \vdots \\ \tilde{Z}_0 \end{bmatrix}.
\tag{E-31}
$$

Now the system matrix H is

$$
H =
\begin{bmatrix} 1 & t_n \\ 1 & t_{n-1} \\ & \vdots \\ 1 & t_0 \end{bmatrix}.
\tag{E-32}
$$

and the parameter vector is

$$
\Theta =
\begin{bmatrix} V_0 \\ S \end{bmatrix}.
\tag{E-33}
$$

This "direct" approach is somewhat problematic. Read noise is easy to consider — In the absence of any shot noise, white read noise simply results in a diagonal correlation matrix, and non-white noise has a correlation matrix that is symmetric. The problem is that the Poisson arrival (shot) noise of each sample includes the shot noise of every sample before it. Physical measurements of an integrating detector are all correlated in their shot noise contribution, and the magnitude of the noise grows as time increases. Thus, the absolute value of the shot noise of a single reading is not well defined. Forming a covariance matrix for these readings is cumbersome, and the resulting matrix is not unique.

For this reason, it is useful to apply a transformation to the model and consider the signal to be the successive differences of the pixel readings. When this is done, the Poisson noise on individual differences becomes uncorrelated. The contribution of the readout noise to successive differences results in a more complex correlation than the original readings, but not as cumbersome as the original Poisson correlation. For example, four readings from the detector in the physical measurement vector Z, (with the most recent reading in the first row of Z) yields three successive differences in the transformed measurement vector $\dot{Z}$. This is a linear transformation using the 3×4 transformation matrix T

$$\dot{Z} = TZ. \tag{E-34}$$

where

$$T = \begin{bmatrix} 1 & -1 & 0 & 0 & \cdots & 0 & 0 \\ 0 & 1 & -1 & 0 & \cdots & 0 & 0 \\ & & & \ddots & & & \\ 0 & 0 & 0 & 0 & \cdots & 1 & -1 \end{bmatrix} \tag{E-35}$$

The transform T applied to the original model yields a transformed model:

$$\dot{Z} = T \begin{bmatrix} 1 & t_n \\ 1 & t_{n-1} \\ \vdots & \vdots \\ 1 & t_0 \end{bmatrix} \begin{bmatrix} V_0 \\ S \end{bmatrix}. \tag{E-36}$$

and then

$$\dot{Z} = \begin{bmatrix} 0 & t_n - t_{n-1} \\ 0 & t_{n-1} - t_{n-2} \\ \vdots & \vdots \\ 0 & t_1 - t_0 \end{bmatrix} \begin{bmatrix} V_0 \\ S \end{bmatrix}. \tag{E-37}$$

Note that the first column is all zeros. The first element of the parameter vector V_0 is lost. However, this lost information is basically a constant, (the reset noise) which was ignored anyway. This loss is of no practical consequence. The parameter vector Θ is now

210

a single scalar, and the system matrix H is now a single column of times between reads. Each element Z_i in the Z observation vector is a combination of a signal $\bar{Z}$ and a noise term $\tilde{Z}_i$:

$$Z_i = \bar{Z} + \tilde{Z}_i. \tag{E-38}$$

This equation, transformed into successive differences, results in a successive difference signal term and a successive difference noise term

$$
\begin{aligned}
\dot{Z} = TZ &= T\left(\bar{Z} + \tilde{Z}\right) \\
&= T\bar{Z} + T\tilde{Z} \\
&= \dot{\bar{Z}} + \dot{\tilde{Z}}.
\end{aligned}
\tag{E-39}
$$

The covariance matrix of $\dot{Z}$ is

$$
\begin{aligned}
E\left\{\dot{\tilde{Z}}\dot{\tilde{Z}}'\right\} &= E\left\{T\tilde{Z}\left(T\tilde{Z}\right)'\right\} \\
&= E\left\{T\tilde{Z}\tilde{Z}'T'\right\} \\
&= TE\left\{\tilde{Z}\tilde{Z}'\right\}T'.
\end{aligned}
\tag{E-40}
$$

Assuming that the read noise on physical readings is white, zero mean, and has variance σ_r^2, the covariance of Z is the identity matrix scaled by σ_r^2:

$$E\left\{\tilde{Z}\tilde{Z}'\right\} = \sigma_r^2 I. \tag{E-41}$$

This results in the following simple expression for the covariance of the read noise after successive differences:

$$
\begin{aligned}
E\left\{\dot{\tilde{Z}}\dot{\tilde{Z}}'\right\} &= T\sigma_r^2 IT' \\
&= \sigma^2 TT'.
\end{aligned}
\tag{E-42}
$$

For eight samples, the read noise correlation on the seven deltas is:

$$R_{read} = \sigma^2 \begin{bmatrix} 2 & -1 & 0 & 0 & 0 & 0 & 0 \\ -1 & 2 & -1 & 0 & 0 & 0 & 0 \\ 0 & -1 & 2 & -1 & 0 & 0 & 0 \\ 0 & 0 & -1 & 2 & -1 & 0 & 0 \\ 0 & 0 & 0 & -1 & 2 & -1 & 0 \\ 0 & 0 & 0 & 0 & -1 & 2 & -1 \\ 0 & 0 & 0 & 0 & 0 & -1 & 2 \end{bmatrix}. \tag{E-43}$$

For any number of samples, the matrix is tri-diagonal, with the main diagonal elements all 2 and the super-diagonal and sub-diagonal elements all -1. If the read noise is not white, the matrix is not tri-diagonal. (The autocorrelation of the read noise can be determined experimentally and used here instead.) The solution in the read noise dominated case is simple. going back to the original solution

$$\hat{\Theta}_{BLU} = (H'R^{-1}H)^{-1}H'R^{-1}Z \tag{E-44}$$

it is seen that the expression

$$\dot{F} = (H'R^{-1}H)^{-1}H'R^{-1} \tag{E-45}$$

yields the optimal coefficients to apply to the observed differences. Using equal time intervals for sampling, normalized to unity, the H matrix is simply a column of 1s. For 6 samples, or 5 differences, this yields the coefficients:

$$\dot{F} = \begin{pmatrix} 0.143 & 0.2285 & 0.257 & 0.2285 & 0.143 \end{pmatrix} \tag{E-46}$$

or

$$\hat{\Theta}_{BLU} = \dot{F} \begin{bmatrix} 1 & -1 & 0 & 0 & 0 & 0 \\ 0 & 1 & -1 & 0 & 0 & 0 \\ 0 & 0 & 1 & -1 & 0 & 0 \\ 0 & 0 & 0 & 1 & -1 & 0 \\ 0 & 0 & 0 & 0 & 1 & -1 \end{bmatrix} \begin{bmatrix} Z_5 \\ Z_4 \\ Z_3 \\ Z_2 \\ Z_1 \\ Z_0 \end{bmatrix} \tag{E-47}$$

212

The optimal coefficients F for the original samples are found by pre-multiplying the optimal coefficients for the successive differences $\dot{F}$ by the transpose of the transformation matrix T.

$$F = T'\dot{F}. \tag{E-48}$$

E.2 Noise performance of Fowler sampling

Forrest and Garnett[90] suggest that Fowler sampling is very close to ideal. This section evaluates the performance of Fowler sampling, applying the linear systems framework of the previous section.

This expression is useful in experiments which estimate shot noise in Fowler-N images obtained without a shutter. In such images, it is desirable to reduce the read noise with multiple samples. However the Fowler averaging disrupts the Poisson statistics in the averaged image, and the observed shot noise in such images is slightly lower than what would be observed in a Fowler-1 image without any read noise.

The Fowler averaging operation is effectively an average of overlapping single read integrations. For Fowler-n, each single read has $n-1$ incremental reads separated by the frame time t_f and one read that is separated by the integration wait time t_I. The effective integration time, t_{eff} is the sum of these time differences. The total integration time on a single node is $t_I + 2(n-1)t_f$ and the total read time is one more frame time above that.

For example, a linear model for Fowler-4 can be thought of as a vector of four Fowler-1 reads. Fowler averaging sums these overlapping reads and divides by the number of reads. In matrix notation:

$$\hat{s} = AT\left(Hs + V\right). \tag{E-49}$$

The estimate of the signal, $\hat{s}$, is the average A of four overlapping CDS reads. T is a transformation matrix which turns seven incremental reads into four overlapping Fowler-1

reads. It is given by:

$$T = \begin{bmatrix} 1 & 1 & 1 & 1 & 0 & 0 & 0 \\ 0 & 1 & 1 & 1 & 1 & 0 & 0 \\ 0 & 0 & 1 & 1 & 1 & 1 & 0 \\ 0 & 0 & 0 & 1 & 1 & 1 & 1 \end{bmatrix}. \tag{E-50}$$

A is the Fowler averaging operation, which adds the overlapping reads together and divides by the number of reads:

$$A = \begin{bmatrix} 0.25 & 0.25 & 0.25 & 0.25 \end{bmatrix}. \tag{E-51}$$

H is the system matrix, which turns unknown parameter s into seven successive differences

$$H = \begin{bmatrix} t_f & t_f & t_f & t_I & t_f & t_f & t_f \end{bmatrix}'. \tag{E-52}$$

The value s is the real signal strength in electrons per second. The estimation of s is denoted $\hat{s}$. More accurately, it is estimating the total charge collected in t_{eff}, the product of signal strength and effective integration time:

$$E\left[\hat{s}\right] = s t_{eff}. \tag{E-53}$$

The variance of the estimator due to Poisson contribution is:

$$var_{\hat{s}} = E\left[\left(AT\left(Hs + V\right)\right)^2\right] - E^2\left[AT\left(Hs + V\right)\right]. \tag{E-54}$$

All values are deterministic except the V term, which is zero mean, so this can be simplified to:

$$var_{\hat{s}} = E\left[\left(ATV\right)^2\right]. \tag{E-55}$$

Matrices are squared by multiplication with their transpose. This results in

$$var_{\hat{s}} = E\left[ATVV'T'A'\right] = ATRT'A'. \tag{E-56}$$

214

The product AT is a 1 by $2n - 1$ row vector:

$$AT = \frac{1}{n} \begin{bmatrix} 1 & 2 & 3 & \ldots & n & \ldots & 3 & 2 & 1 \end{bmatrix}. \tag{E-57}$$

At this point, consider the correlation matrix R. Since the shot noise and the read noise are uncorrelated, their correlation matrices may be added.

$$R = R_{shot} + R_{read} \tag{E-58}$$

$$var_{\hat{s}} = E\left[AT\left(R_{shot} + R_{read}\right)T'A'\right] = ATR_{shot}T'A' + ATR_{read}T'A'. \tag{E-59}$$

Considering only the shot noise component, the consecutive difference vector V has a noise component with the diagonal covariance matrix:

$$R_{shot} = s \begin{bmatrix} t_f & 0 & 0 & 0 & 0 & 0 & 0 \\ 0 & t_f & 0 & 0 & 0 & 0 & 0 \\ 0 & 0 & t_f & 0 & 0 & 0 & 0 \\ 0 & 0 & 0 & t_I & 0 & 0 & 0 \\ 0 & 0 & 0 & 0 & t_f & 0 & 0 \\ 0 & 0 & 0 & 0 & 0 & t_f & 0 \\ 0 & 0 & 0 & 0 & 0 & 0 & t_f \end{bmatrix}. \tag{E-60}$$

Yielding

$$var_{\hat{s}} = \frac{2t_f s}{n^2} \sum_{i=1}^{n-1} i^2 + t_I s. \tag{E-61}$$

for the case of shot noise only. The covariance matrix for the read noise is given in Equation E-43.

The product of R_{read} and $T'A'$ is zero for every row except the center row, in which case the product is $2/n$. The center coefficient of AT is 1, so the overall read noise contribution in Fowler Sampling is fixed at

$$ATR_{read}T'A' = \frac{2\sigma_r^2}{n}. \tag{E-62}$$

215

There is nothing shocking about this familiar expression, which may be arrived at using a much simpler analysis. Taking the square root leaves $\sqrt{2}$ in the numerator (from the pair of reads) and $\sqrt{n}$ in the denominator (from the averaging of n reads) times the single sample read noise σ_r, the expected result. The total read noise is simply the sum of both terms:

$$var_{\hat{s}} = \frac{2\sigma_r^2}{n} + \frac{2t_f s}{n^2} \sum_{i=1}^{n-1} i^2 + t_I s. \qquad \text{(E-63)}$$

It is easier to use this result expressed in terms of the effective integration time, not the wait time of the central delta. Substituting

$$t_I = t_{eff} - (n-1)t_f. \qquad \text{(E-64)}$$

and using the relationship:

$$\sum_{i=1}^{n-1} i^2 = \frac{2n^3 - 3n^2 + n}{6}. \qquad \text{(E-65)}$$

the expression in Equation E-63 can be simplified to

$$var_{\hat{s}} = \frac{2\sigma_r^2}{n} + t_{eff} s - \frac{\left(n^2 - 1\right) t_f}{3n} s. \qquad \text{(E-66)}$$

Appendix F

291 Additional Bare Mux and InSb Testing

A 291 multiplexer was also tested for capacitive coupling to the reset and supply rails. In addition, this device's coupling to the row enable was measured. Edge spread analysis was also performed on InSb detectors. These results are presented here.

F.1   SB291 Coupling to unit cell buses

Undesired coupling of the detector node voltage to logic lines controlling the unit cell reset and enable switches exists. Tests were performed to measure the magnitude of this coupling. In Figure F.1, the reset gate voltage was varied, and the output voltage was observed. A three volt swing on the gate created a 0.4 volt swing at the output, indicating over 10 percent coupling to this line. The hysteresis observed was caused by the reset being applied and then removed. When the reset was applied, the detector node took on a different amount of charge which was maintained as the reset was removed.

Performing the same test, but varying the unit cell supply voltage resulted in the observation shown in Figure F.2. Nearly half of the voltage shift in vdduc appears at the output, indicating that nearly half of the bare multiplexer's nodal capacitance is to the supply.

The third unit cell control bus of interest is the row enable line. Two separate tests were done to investigate this coupling. First, the row enable was applied successively stronger
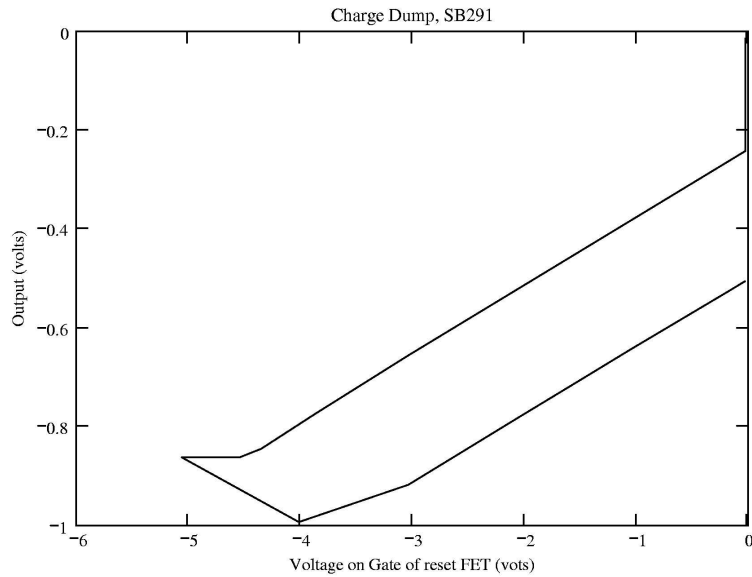
Figure F.1: This plot shows a small coupling from the reset FET gate into the detector node of the SB291. The jump occurred when the reset FET finally opened and the node voltage could change. Removing the reset again repeated the slope seen at appplication.
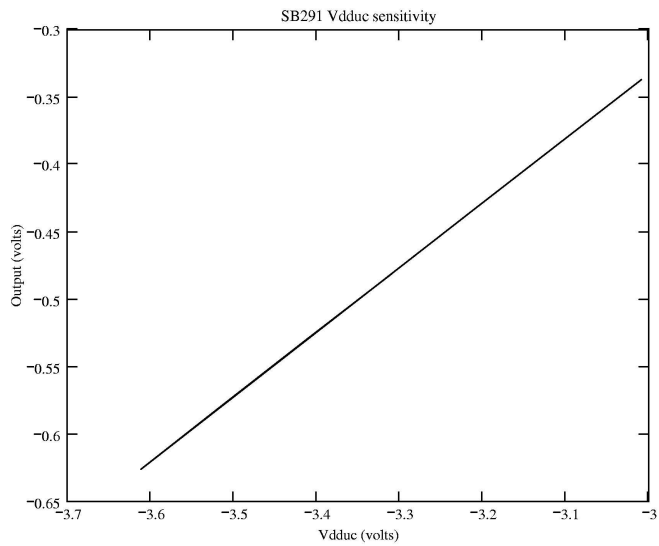

Figure F.2: The SB291 showed strong coupling between the supply voltage and the detector node, very similar to the SB226 coupling.
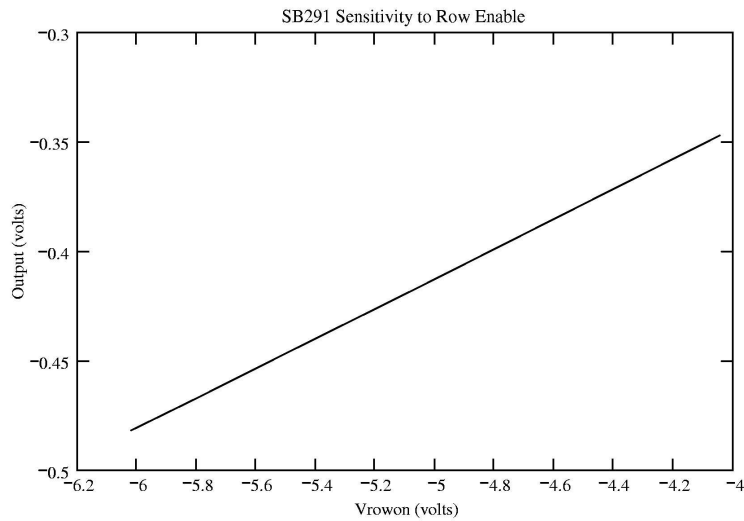
218

Figure F.3: The detector node also showed some sensitivity to the row enable FET, similar to the reset FET coupling.

and stronger. This generated the observation shown in Figure F.3. Two volts of swing on the row enable FET showed just a little more than a tenth of a volt at the output, indicating only a small amount stray coupling here.

Concern that the observation could have been affected by varying drain-source resistance in the row enable FET, rather than coupling of the detector node to the row enable gate prompted a second experiment. In this experiment, the reset FET was held on to fix the node voltage. The row enable was varied again. Any change in output voltage here would have to be from the row enable FET resistance changing.

This experiment showed very little change in output voltage when the row enable was between -4 and -6 volts, indicating that the change in channel resistance was not significant.
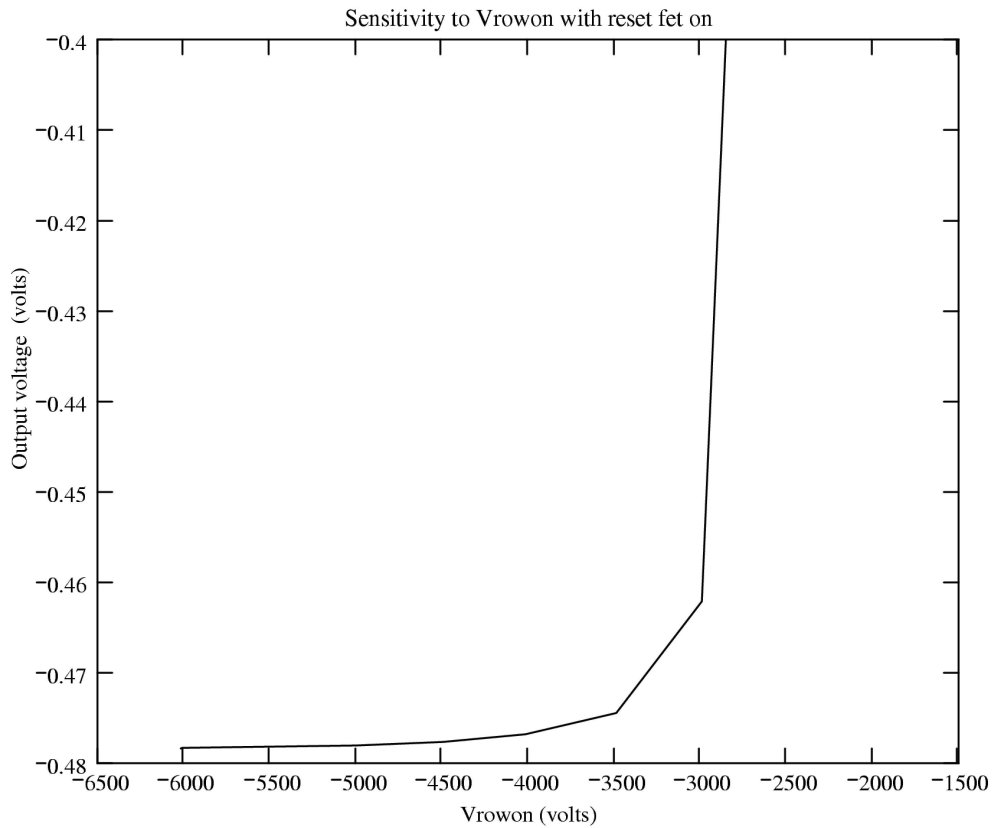
Figure F.4: Sensitivity to the row enable FET voltage could have been an artifact due to varying resistive drop in the row enable FET. Keeping the detector node in reset while varying the row enable verified that this was not occurring in the previous test.

F.2   InSb edge spread analysis

The bullseye reticle used at RIT for the P-I-N edge spread tests produced good results, so a similar experiment was performed at the University of Rochester on an SB226/InSb device. This measurement proved somewhat more difficult. The NIR dewars face the arrays downwards, so gravity could not be used to hold the bullseye reticle against the device. A strip of black plastic was used instead. It was placed in direct contact with the surface of
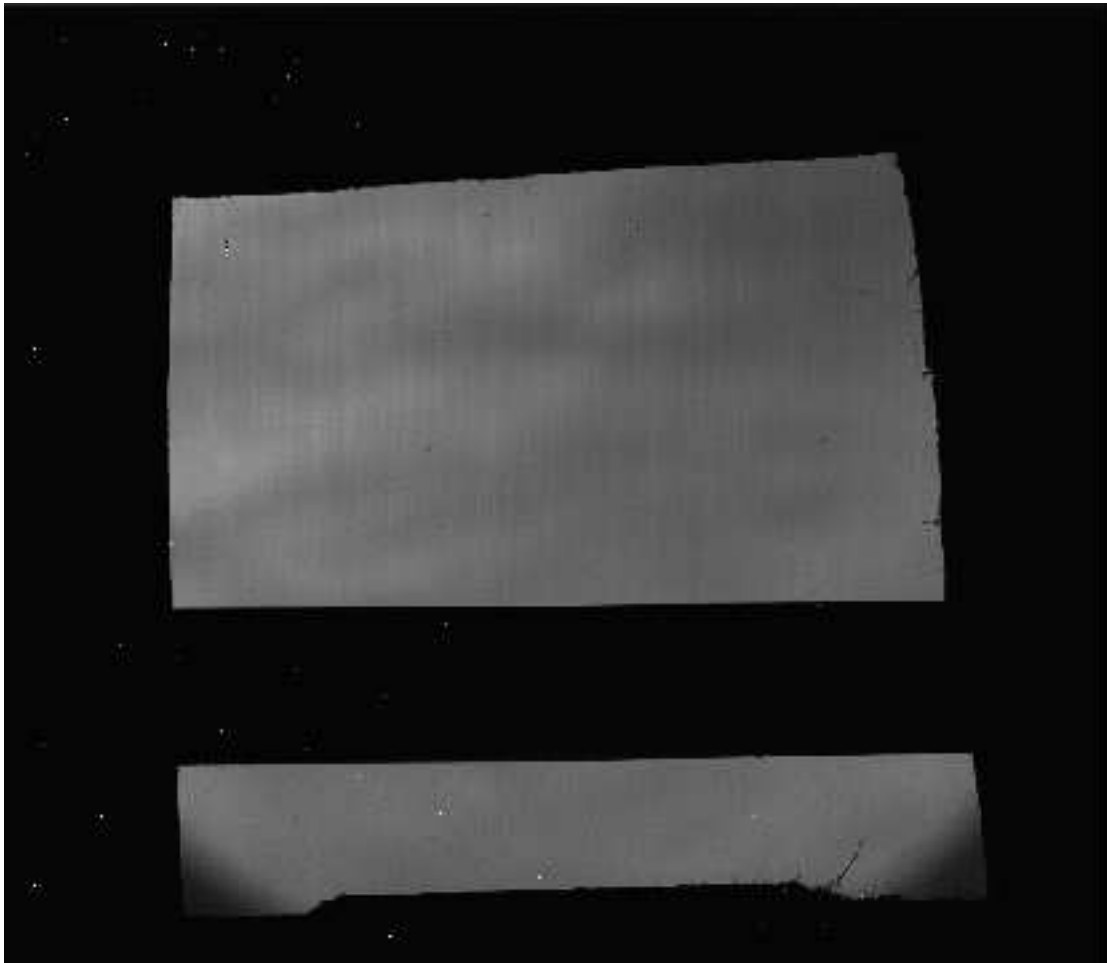
Figure F.5: This image of a sharp edge on a SB226/InSb Hybrid was used to evaluate its MTF. This approach did not work as effectively as the chrome reticle, but yielded usable results.

the array, and several images were taken at various filter wheel positions. The best of these images, taken with only visible wavelengths, is shown here:

Various other images were taken at infrared wavelengths, but the sharpness of these edges was not as good.

F.3 Analysis

The upper edge of the plastic strip was used, in the neighborhood of row 641 from columns 450 to 650. An average dark value and average light value were computed above and below the edge. Then a centroid was computed on the derivative across the edge, to estimate its position at each column. Since the plastic strip had some tilt and curvature to it, its profile was approximated with a third order polynomial curve fit. The normalized intensities of the pixels near the edge were paired with their deviation from the edge position.

These data were compared to the model at various scaling factors, employing (incorrectly) a Gaussian point spread function. The scaling factor that best approximated the model was found to be 0.52, yielding an overall system MTF of 0.518 at Nyquist.

This measurement was very close to the NGST specification (0.53), but unfortunately did not meet it.

It was a promising result, however. Several other mechanisms arguably exist that would bias this measurement lower, such as the quality of the edge. (Mechanisms that would bias it higher are hard to imagine.) At longer wavelengths, it was noticed that the black plastic allowed some light to pass through it. The quality of the edge applied to the array is at best a sharp edge, but likely not perfect, and is letting in some fraction of light in the transition zone.

This MTF measurement was made using an SB226-based multiplexer with a pixel pitch of 27 microns. NGST is allowing pixel pitch ranging from 18-25 microns. A finer pitched sensor with identical detector material should have improved spatial frequency response in cycles per millimeter, since the rect portion is now higher bandwidth. Such a sensor will improve spectrograph resolution, all other things being equal. On the other hand, the Nyquist is now higher and the MTF at this higher Nyquist will certainly be lower, since the diffusion component of the detector is now wider relative to pixel size. Cosmic hit
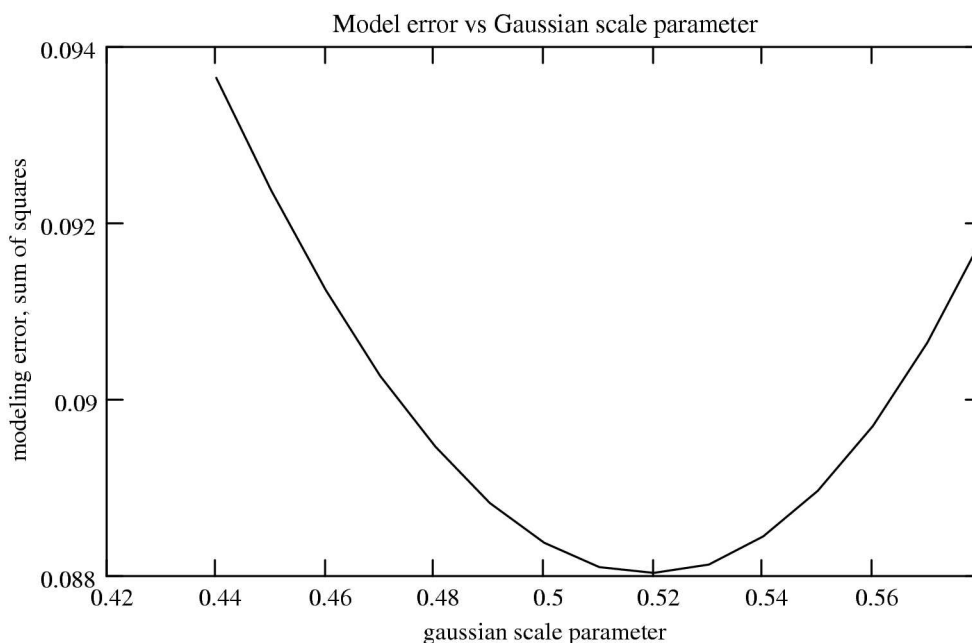
Figure F.6: This plot shows total squared model error as a function of the Gaussian shape parameter. Using Gaussian diffusion was inappropriate for this per-pixel depleted detector, but at the relatively sharp diffusion MTF involved, the difference at the Nyquist was very small.

susceptibility in pixels per hit is now degraded. Rauscher's MTF paper hints at the trade-offs here and indicates that the importance of even having an independent MTF spec was questionable. The MTF ties in to other specified system parameters. The spread of cosmic events is claimed to be the most important parameter.

The MTF - crosstalk connection is not a strong one, mathematically. See Chapter 5 of this dissertation for a detailed discussion of this. A detector substrate with a point spread of a pixel sized rect, rather than a Gaus, would exhibit an overall MTF of $0.64^2 = 0.41$ (falling sadly short of the MTF spec) and still contain cosmic hits entirely within 4 pixels, exceeding the cosmic ray pixels per hit spec by one full pixel. Of course, one would be hard pressed to find such a magical detector. The point is that the mathematical connection between

crosstalk and MTF is not mathematically firm, it is based on a simple exponential crosstalk model, and the connection between MTF, pixel spacing, and overall system performance is still an area for hot debate.

The incorrect use of the Gaussian blur may have changed the measurement slightly, but most probably not by much. Since the theoretical diffusion profile shown in Figure 4.11 (derived after the competition deadline) has better MTF for the same diffusion variance, it seems possible that a gain in MTF could have been obtained with the more accurate model. However, both curves are approximately parabolic in the center where most of the energy is, and the shape of this center is most closely tied with the MTF estimator — the MTF from diffusion is approximately 0.52 divided by 0.64 = 0.81, and there is little difference in the diffusion profiles in Figure 4.11 at that MTF.

F.4   Conclusions

It was not conclusively proven that the 226-InSb detector met or did not meet the JWST MTF spec. A re-evaluation with the diffusion model in Equation 4-25 seems academic at this point. In terms of imaging characteristics, however, the result appears to be quite sufficient — the telescope will dominate overall system MTF and the cosmic ray susceptibility aspects of the NGST MTF specification are questionable.

F.5   Multichannel noise measurements in two systems

During the JWST near infrared detector competition, the Independent Detector Testing Lab (IDTL) at the Space Telescope Science Institute was unable to confirm the low noise readings obtained at the University of Rochester's NIR lab. Analysis of their data indicated a cross-channel noise source. Using the cross-channel correlation techniques expressed in
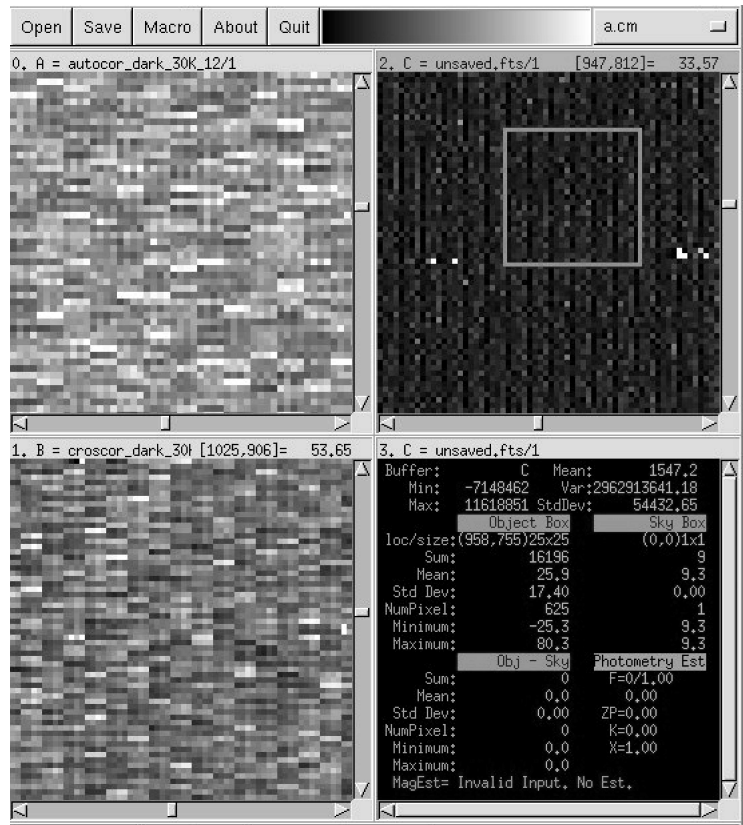
Figure F.7: This screenshot shows equally scaled autocorrelation, cross-correlation, and residual noise images in a multichannel system with dominant system noise. The darker image is the residual (autocorrelation minus the cross-correlation), and represents the device noise.

Equations C-10 and C-11, the IDTL data showed a low residual noise for the device in agreement with the NIR lab observations.

Autocorrelation and cross-correlation images were built up from the squares of successive "deltas" using "up-the-ramp" data collected from an imaging device operated under dark conditions. Figure F.7 is from a (Leach-electronics based) system at the Space Telescope Science Institute's Independent Detector Testing Laboratory that exhibited a large amount of interference relative to the device noise. The cross-correlation image is almost
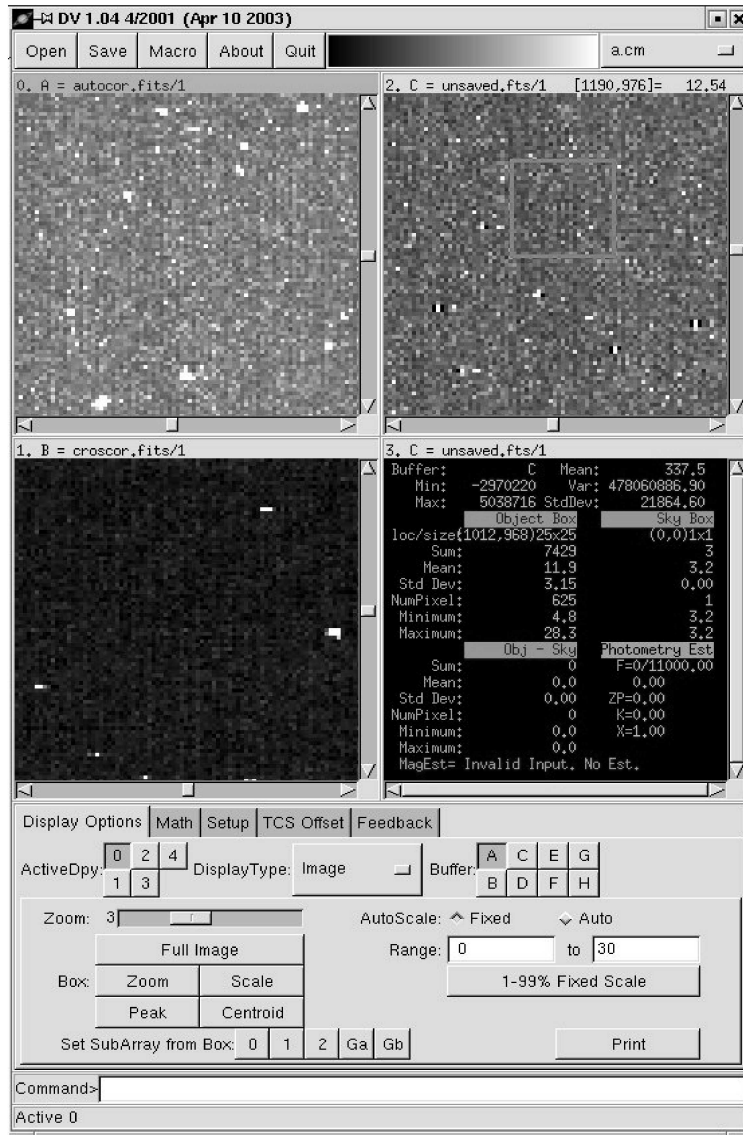
Figure F.8: Autocorrelation, cross-correlation, and residual noise images from the same device, operated in a low noise system. The cross-correlation image represents the system noise, and is small compared to the residual device noise.

as bright as the total image, but the difference image is quite dark, indicating a low residual device noise. Figure F.8 is from the University of Rochester's "silver box" system. The cross-correlated component is quite dark relative to the autocorrelation image. The residual noise of the same device in both systems resulted in very similar values.

Appendix G

Array Controller System Overview

One focus of this dissertation has been investigating the hybridized array as a small system. This appendix gives an overview of the system used for controlling, testing, and operating arrays — the system in which such arrays are themselves a component. Appendices H and I continue this topic in more detail. The array control system was a central figure in this research, and a variety of controllers were investigated during its course. This control system is itself a component in an even larger system shown in Figure G.1.

G.1 Agile Systems

Research systems such as camera controllers are subject to uncertain and changing requirements and require adaptability. Flexibility is a key quality of such systems. New devices and discoveries bring new requirements for test and operation, and systems that handle new and changing requirements gracefully will fare better in this environment. Most of this flexibility is realized in the software. Modern software development has formulated a development methodology called "Agile Software Development" [92] that succeeds in the face of such turmoil where other development processes typically fail. Agile development has several key practices:
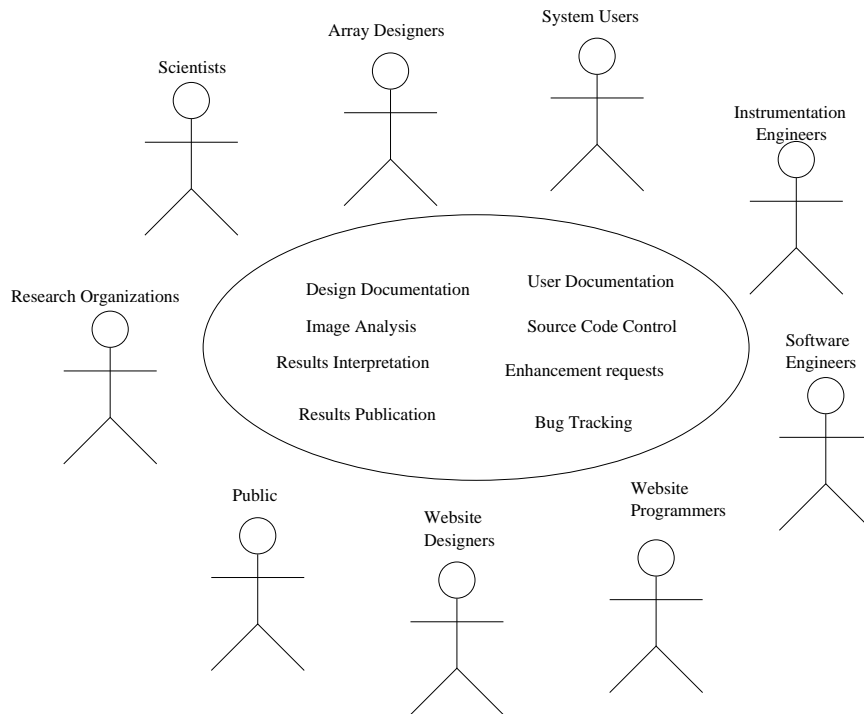
Figure G.1: Many different people connect in different roles to the images produced by an astronomical camera.

Continuous Customer Involvement

The user is constantly involved in system development. The developers and users work as a team, strive to understand the issues facing each other, and constantly communicate to maintain and refine this mutual understanding.

Simple Design

Simplicity is a key practice in Agile development. There should be as little software as possible to do the job. The team strives to keep the system as simple and clean as possible, removing duplication and refraining from solving problems that are not of immediate concern.

Short Iterations / Continuous integration

Software is developed and released in short cycles, usually two weeks or so. The team selects a small set of activities for the cycle, based on the needs of the users. As developers produce new software, it is integrated into the rest of the system. This keeps the programmers working together, and the feedback loop between the system users and the system programmers tight.

Test Driven Development

The system should be able to automatically verify that its components operate properly with a suite of unit tests. These tests also clarify the design itself, and so should be written first. Tests also provide a "safety net" so if changes to the design introduce bugs, the bugs are detected very early. This empowers developers to maintain simple design with less fear of introducing inadvertent bugs.

G.2   Python: Connecting Imager and Researcher

A search for a good language for controller software resulted in the choice of Python. Python [93] is "an interpreted, object-oriented, high-level programming language with dynamic semantics" developed by Guido Van Rossum. Python can be operated in a command-line mode, and this was a useful feature of the FORTH system that was being replaced. As time passed, it was realized that Python was not only a good choice, it was an excellent choice. Python has proved superb for Agile system development. It works very well as a "systems glue" language, and is suited for a wide variety of tasks, small to large, from hardware interfacing to user interfacing and web interfacing.

Python is a "very high level" language, and expresses solutions to problems in short and extremely readable programs. There is evidence that one line of Python code is equivalent to 10 lines of Java or C++. Python is highly portable. It is a strongly-typed language, but typing is "latent," meaning type checks occur at runtime. Type declarations are not needed — one reason why Python excels at rapid application development.

Although Python is not yet included in most undergraduate computer science curricula, it is quite popular and continues to become more so with 25-30% growth per year — and inclusion in CS coursework is increasing[94]. Python is learned very quickly, and is well-supported with many modules.[95, 96, 97] It interfaces to hardware and other languages quite easily, and has found wide support in the scientific[98] and astronomical community[99, 100, 101, 102, 103]. The Scientific Python community[104] actively develops many tools for scientists to use. 2D plotting packages such as matplotlib[105] and 3D visualization libraries like VTK[106] and VPython[107] are available for Python as well. VTK is used in the Atamai viewer[108] for 3D medical imagery produced by tomographic imaging systems. VPython has been incorporated in a college-level physics curriculum[109].

The Space Telescope Science Institute has recognized the advantages of Python. It is now the preferred language for all new STScI software development. Python is used in the Hubble data processing pipeline.

Although the topic of global connectivity and large scale collaboration is not elaborated upon much in this work, Python plays a significant role in the development of large web services.[110, 111, 112] The GNU "mailman" mailing list server[113], Zope web application framework[114] and accompanying Zope Content Management Framework (CMF,) and the Plone content management system[115] are all large collaborative web technologies built with Python. The Google[116] search engine is written in Python, as is the Bit-Torrent file distribution system. Consider the number of astronomical imagers in operation

232

at any one time, the amount of data that each can produce, the variety of objects that these imagers can be called upon to observe, and the variety of interests that various scientists and researchers have in the data. Web connectivity is extremely important to astronomers who wish to build systems that are able to access and share large amounts of data. In this context, the Python language remains a superb technological choice.

G.3   System support

A software system benefits from several support mechanisms — an issue tracker that allows users to request changes and report problems, a source control system so that changes to the software may be tracked incrementally, and documentation so that users can find out more about the system.

Source Code Control System

The source code, both Python and clocking, can be found in a subversion repository at:

http://astro.pas.rochester.edu/svn/pydsp.

The source code in a subversion or cvs repository may also be browsed via "viewcvs", also written in Python.

A good amount of insight to the design and capabilities of the system can be obtained by reading the source code. Several automated tests are included, and these tests are suggested as a place to start for both learning about, debugging, and enhancing the system. Ideally, all functionality of the system has an accompanying automated test. Ideally, the test is written first.

Documentation Wiki

The system documentation is kept in a Plone/Zope/Zwiki site. As stated above, Plone and Zope are written in Python. Zwiki is a Zope "Product" and is written in Python as well. The web address is currently:

http://itchy.pas.rochester.edu:8080.

It may migrate to a more central URL. Recent versions of design files and other resources may be found in the wiki if they are not to be found in the source code control system. (The word "wiki" is Hawaiian for "quick", and it is a simple way of keeping a team communicating.)

Issue Tracker

The wiki contains an issue tracker. An issue tracker allows users to enter requests for enhancements, and to report unexpected or improper behavior. Wiki subscribers will be informed by email of the new issue and also of changes in status, or comments added to the issue. A user may opt to only subscribe to particular pages in the wiki. The issue serves as a point of communication and a record of why what was changed when. Although nothing is more effective than a face-to-face conversation, it is good to keep track of goals and plans written down in a shared central location, and periodically review issues that have not been resolved yet.

Appendix H

Software

This system draws upon previously existing electronics and software. The camera controllers produced by Robert Leach (SDSU) were investigated. The Leach controllers are the defacto standard in this domain, and were investigated in great depth before it was decided not to use them. The electronics package and much of the lower level software that was selected was originally designed by Greg Burley for the Observatories of the Carnegie Institute of Washington (OCIW) to operate a CCD mosaic. OCIW offers the design for free to any who are interested. [117] The original OCIW design was modified in various ways to improve performance and flexibility, and to run the Raytheon SB226 and similar multiplexers.

The host software is a Python rewrite of the "dspsys" system developed at the University of Rochester for the NIR lab infrared array detector testing. The original dspsys silver box system was instrumental in much IR detector research, notably the development and test of InSb detectors for SIRTF. [118, 79, 80, 81, 86] Its noise performance has proven difficult to match. Dspsys, written in FORTH, was initially modified to communicate with the new electronics directly. The first P-I-N images were taken with this system.

A Linux PCI device driver very similar to the one in use by OCIW, and DSP clock programs (written in a mixture of C and assembly) glue the Python user interface to the electronics.

H.1 Embedded Software

The embedded software, a.k.a. the clocking program, operates the cameras. Typical clocking programs are written in assembly code. Given the complexity of the parallel architecture of the processor used, it was felt that assembly code was best avoided if possible. Programming such a processor requires intimate knowledge of the concurrency aspects of the processor, a digital signal processor (DSP) in this case.

DSP Processor

The Leach, University of Rochester, and OCIW electronics all have a Motorola 56xxx DSP as the processor responsible for running the array. University of Rochester and Leach both used the 56002, an older DSP, for clocking the array. The Burley electronics use a more recent processor, the 56303. More recent Leach controllers use this device as well.

This DSP has all of the features of the 56002, plus several enhanced features. One of its enhancements is speed; it is capable of running up to 100 million instructions per second.

DSP boot process

The DSP board contains a boot EPROM that can download and execute a file in Motorola's "S-record" format. Special bit patterns on the data transmitted to the DSP board force it to reset and start executing this boot EPROM. Reset will clear the voltages in all clock and bias drivers.

Clock Program implementation

As mentioned, clock programs have traditionally been written in assembly language. The new system uses C as much as possible. Originally, assembly was a requirement, as the

code needed to be efficient and predictable. This is still true in some areas of the clock program. C is much more maintainable for the bulk of the code, however. Only areas like the per-pixel code in the clocking loop has been implemented in assembler.

PCI device driver

The driver is a loadable kernel module (LKM.) An excellent reference for Linux device drivers by Rubini and Corbet [119] was found to be extremely helpful for driver development. The first device driver written here "did too much." (It took responsibility for Fowler averaging, used memory mapping, etc.) In the face of changing requirements, the mistake of this design became apparent: the device driver would require frequent modification, and driver development is difficult. A new device driver, only responsible for emptying the PCI hardware FIFO into system memory, was developed. The user process simply reads the stream of bytes from the driver using a standard read call directly from Python. All image processing and memory mapping has been removed from this new driver.

Interfacing to the device driver

The first (overly complex) device driver was connected to a Python extension module written in C. When the device driver was simplified, the C extension module was eliminated as well. All communication to the device driver is now accomplished directly from Python. One file, `ociw.py` handles the lowest level communication. The s-record download, originally in C, was also converted to Python and now resides in `sload.py`.
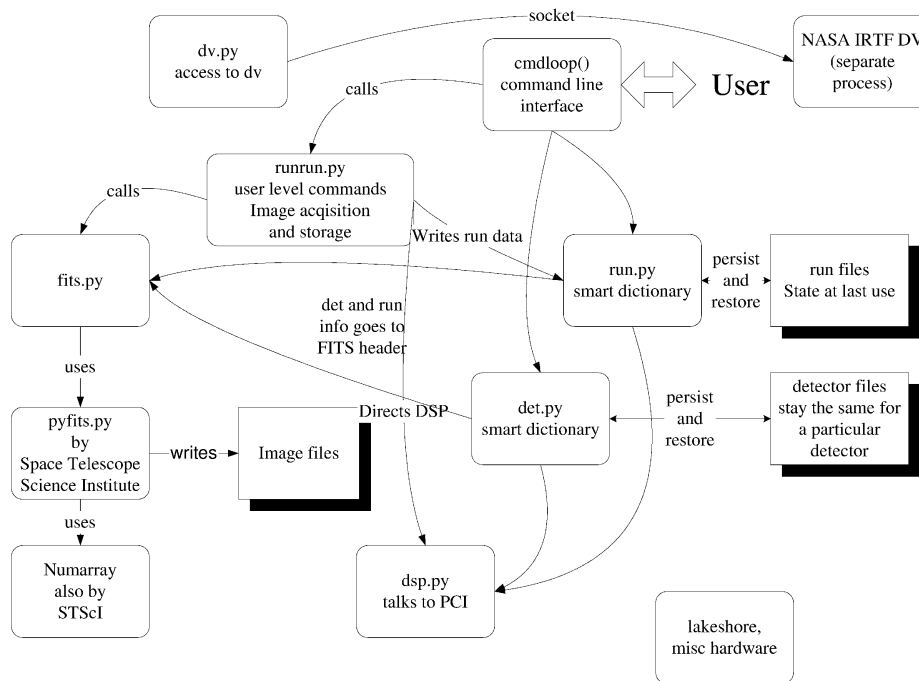
Figure H.1: The host software, called 'pydsp' is a simple collection of Python modules. The 'py-FITS' and 'numarray packages' from STScI, and the 'dv' FITS viewer were employed for handling the FITS data.

H.2   User Interface Software

The user is mainly concerned with operating the array under specific conditions, acquiring data, and analyzing the results. It is helpful to have a user interface that allows easy access to the required functionality, as well as tolerance for user error.

"Pydsp" Host Computer Python Software

Figure H.1 shows the main components in the architecture of pydsp, the Python based user interface software. Python, like FORTH, has its own command line interpreter. In FORTH, a single word at the command line can invoke execution of code. In Python, an executable

object's name must be followed by a pair of parentheses to invoke execution, otherwise a string describing the object is printed. A simple Python command loop was implemented to allow simple words to execute code. This loop prompts the user and then interprets and executes the user's input. It was written to emulate commonly used dspsys commands and new ones were added as well.

The "break" command exits the loop, returning back to the Python command prompt. Typing "cloop()" in Python brings the command loop back up again.

The Space Telescope Science Institute (STScI) has developed several modules for Python, and offers them without cost. Their "pyFITS" module, which requires their "numarray" package, is used by pydsp to save image data in the standard FITS image format. (Python acquisition and analysis scripts using pyFITS and Numarray were used for many of the results presented in this dissertation.)

The "DV" FITS image analysis package [120] was used to view images. Socket-based communication from pydsp triggers DV to automatically load images after acquisition. DV offers several analysis tools for quick evaluation of acquired images.

In the pydsp system, FITS images are stored in an "object" subdirectory of a "night" subdirectory of the main FITS data directory. At a telescope, each observing session is stored in its own "night." As the telescope moves from object to object, new directories are created for each object. Images of the same object are stored together in object directories. In the laboratory, the night directory is typically changed for each new detector, and within that directory, object directories store the images from the various tests that are run. Two commands, "night" and "object", allow the user to create new night and object directories.

Commands to take an image and place it in the current object directory are provided. In astronomy, images of interest often have a "background" image subtracted from them to remove system artifacts, so commands were made to distinguish a "source" image from a "background" image. Either can be set as the default. A distinction is made between a

239

"scan" which takes a temporary image and a "run" which allocates a unique new file name that is not to be overwritten. Commands to add comments to the FITS header were also implemented. Sample-up-the-ramp mode is also supported.

At system startup, an initializing state of the system is searched for. A variable from the OS environment directs pydsp to where a file entitled "lastrun.run" may be. The state of the system can be persisted to this file (or another file) with a "savesetup" command. The "lastrun.run" file directs pydsp to several other files and directories. Given a detector name from "lastrun.run", pydsp looks for a matching "*detname*.map" file that maps names of clock rails and biases to their appropriate DAC numbers. After this file is found and loaded, a "*detname*.bias" file maps these names to their proper voltages.

The names of the bias and clock voltages are added to the pydsp vocabulary when these detector files are loaded. Once in the vocabulary, entering the name of the voltage returns its present value in millivolts and entering a number with the name causes the voltage to be set to that value. Voltages are saved in the FITS image headers, keyed by their name. These words, and several others, are keys in a python "smart dictionary" with overloaded "get" and "set" operations. If setting or getting the value involves an extra operation (such as communication with the DSP) the additional code is invoked automatically by the dictionary access. Acquisition scripts using this mechanism are easily written in Python, and executed using Python's "execfile" capability.

The system has several threads and is capable of concurrency. Currently, three threads are present. One is the hardware thread, which handles serialization of access to the embedded program. The graphical user interface runs in another thread. The text console runs in a third thread. Temperature control is handled as a background process in the hardware thread.

Appendix I

Electronics

The electronics system described here can operate long-integration high-resolution multi-channel imagers for use in low-light applications such as ground and space based astronomy. It allows precise control of the voltages and waveforms applied to the imager, and digitizes the video with low noise and high resolution. It is specifically tailored to control and test hybridized FPAs such as those produced by Rockwell and Raytheon.

I.1   History

The Silver Box

The University of Rochester's Near Infrared Astronomy team developed a "silver box" - a suite of completely custom circuit boards for analog control and acquisition, operated from a Linux host. The host box contains three DSP cards, (1 control and 2 data acquisition) and two custom 16 digitizer boards.

This system has several problems, however. Voltages are adjusted with 20-turn potentiometers which are unstable and can not be adjusted automatically. The system lacks sufficient memory to store an entire image of modern arrays. Much of the system is obsolete and cannot be purchased today. The host computer, containing the converters, could not be located a long distance from the silver box.

The overall design of the system, however, was sensible and well thought out. Many systems based on the University of Rochester "silver box" / dspsys combination are still in use today.

The Leach Electronics

Robert Leach of San Diego State University designs popular array controllers that are commercially available. The latest systems consist of a control unit and a PCI interface board with a DSP on it. These are connected by a fiber optic link. The control unit, packaged in a gold (anodized) box, is a backplane-connected suite of cards, typically a DSP controller card, clock generator card, and one or more video acquisition boards. A DSP based "utility' card is optional. Java-based software is the interface to the user.

One of these controllers was purchased and many months were spent on it before setting it aside. After a thorough investigation of the system, including a trip to San Diego to talk with Leach directly, issues were still not getting resolved. Many parts of the system seemed needlessly complex, and the software was difficult to understand. In addition, the programmable logic on the boards was considered proprietary and was unavailable. Leach's systems have many good points however. They are compact and easily used in an application setting. The fiber optic link allows the control unit to be placed a long distance from the user, and helps avoid grounding problems. They have a large and helpful user community.

Developing Technology, OCIW Magellan and Guider

Before attempting to run the Leach system, construction of another system had been in progress at RIT. This system was being developed for the Observatories of the Carnegie Institute of Washington (OCIW) by a designer named Greg Burley. Burley had previously

investigated and dismissed Leach's systems, and was designing and prototyping a system of his own design to run 8K by 8K CCD mosaics. This system wasn't complete, but was becoming operational. OCIW provided blank boards for the full set to RIT, and the DSP and PCI board had been assembled and were being testing when the Leach electronics arrived. Similar to Leach and University of Rochester, Burley's system had a controller box that was located near the sensor, a computer with interface electronics in it that the user interface program ran on, and a communication link between them. His controller box had a power supply board that ran off a single 48 volt supply, a DSP board, a level shifter board for generating clocks, and a video board for generating biases and digitizing the video. The PCI card had no processor on it, just a FIFO, some programmable logic, and the PCI interface chip. Months of constant communication with Greg Burley led to the conclusion that he was a seasoned and sensible designer. In addition, this system was "open source." All of the design details were made freely available to the scientific community, in the hopes that it would be built upon. This approach had great appeal.

Custom approach, from scratch

Prior to embarking upon the Burley electronics, some thought was put into designing such a system from scratch. An approach similar to Burley's design, show in Figure I.1 was envisioned. The main difference is that the processor in this proposed system would have been on the PCI card. The clocking patterns would have been written to a "brainless" controller over a high-speed serial link. This approach was appealing in that it kept the processor (feared to be a noise source) away from the sensitive analog electronics. Burley's design indicated that this was not necessary. University of Rochester and Leach both kept their supplies in separated enclosures.
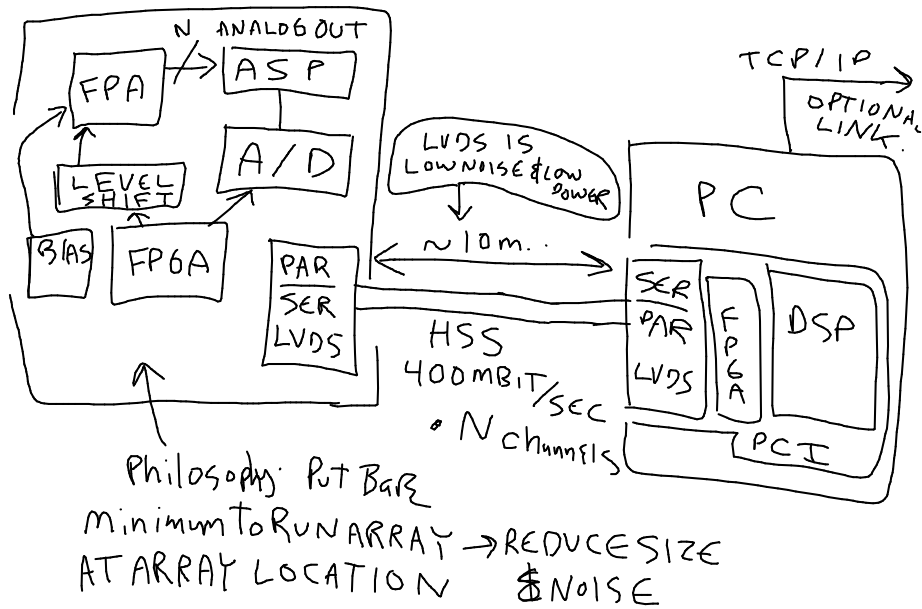
243

Figure I.1: This early sketch of a proposed controller system (Feb 2000) was so close to an open-source design that Greg Burley was developing at the time that it seemed most sensible to build upon his development effort.

Custom approach, using purchased components

An approach considered was using purchased computer cards for generating the sequences, generating the bias voltages and clock rails, and digitizing the video. Such cards are available from many vendors, among them Spectrum, Transtech, Mirotech, Data Translation, Hunt Engineering, and Pulse Instruments. Such an approach is quite attractive, since the engineering and debugging of the circuitry is done by a third party. However, if the system needs to be duplicated some time in the future, it is sometimes discovered that the desired boards are not manufactured anymore. Still, this is an attractive option, and is likely to be useful for at least part of a system. The NIR system used purchased components for their clocking and data boards, as well as the generation of special biases and digitization of some diagnostic voltages. This remains an option for enhancement as well.

I.2 Technical Description

Design Goal

It was desired to increase system capability beyond NIR lab's "silver box" system while reducing system complexity and maintenance cost. The increased capability would benefit the user, and the reduced complexity would benefit the engineer and programmer responsible for maintaining and enhancing the system.

Only one processor (in addition to the host computer) a Motorola DSP56303, controls the electronics box. It handles both writing the clocking patterns and reading the A/D converters. This design choice has pros and cons. A single processor is easier to deal with, especially when there are concurrency issues. On the other hand, doing concurrent tasks on a single processor can have its own impact, both in complexity and performance limitations. The major concurrency issue considered was that of clocking the array versus reading the pixels back. Previous designs put these tasks in separate processors. It was felt that the clocking of the array and the reading of pixels were more synchronous than independent tasks, and it was simply a matter of having sufficient processor power and bus bandwidth to do both.

Basic capabilities

- LVDS, RS485, or fiber optic communication links available.

- Data rates to 2M pixels per second. 10x Faster rates should be achievable

- Minimum system: Four slot backplane, 2 video channels

- Four slot four channel systems built for U/R

- Ten slot, eight channel systems have been built at OCIW.

- 16 bit A/D converters for video.

- 13 bit D/A converters for clock rails and bias voltages.

- 12 bit aux A/D converters for monitoring.

- 22 clocks per system. 16 biases per video card.

- Clocks and biases controllable to 2 millivolt resolution over a +/- 8.192 volt range.

- Four slot system: 10" by 5" by 4", including the power supply card.

- Total component cost under $3000.

Development, in review:

Development of the system was incremental and iterative. It was used for actual data collection early and often. It was used first at RIT driven by the DSP debugger. The PCI card and device driver were then integrated into the FORTH based system at University of Rochester's NIR lab, still using the original clocking and converter cards. This expanded the capabilities of the "silver box" electronics system from 512 by 512 images to handle the goal of 2K by 2K. In addition, the individual images acquired during "Fowler-sampling" or "sampling up the ramp" were made available. Access speed to the image data improved as well. At RIT, a new system with the modified OCIW electronics was operated for several months using the FORTH "dspsys" for the user interface software. The "pydsp" Python software replaced the FORTH software when it was capable.

I.3 System Boards

A boxed backplane of four cards, arranged from noisiest (power supply, then DSP) to most noise sensitive (clocking card, then digitizer) attaches via a "header board" to the dewar and

246

device, and via a high-speed serial communication link to a PCI card in the host computer. The DSP generates the clocking sequence patterns. The clocking card receives the sequence patterns, and level-shifts the digital pattern to the voltages required by the array. The array outputs are digitized by the video board and sent back to the host PC.

Backplane

A modified four-slot backplane allows improved connection to external devices, with additional points for wiring control signals.

Current Sense Header board

OCIW provides design details for a header board and preamp tailored to their dewar and CCD mosaic. A board more appropriate for the Rochester detectors and laboratory environments was designed and constructed from scratch.

This header board, a small 4.25" by 3.5" circuit board, fits between the backplane and the camera end of the electronics box. It interfaces the array control electronics to the device, providing "RC" filtering for 16 clocks and 16 biases, and preamplification for four returning video signals. The boards used here were configured with a gain of 25 and a programmable +/- 1.2 volt offset. The video signals are then passed to the video card. Additional diagnostic circuitry was also added to sense the voltages and currents in the clock and bias lines and buffer those signals to "monitor" outputs without incurring risk of static discharge damage to the device. Analog multiplexers allow 16 signals to share the same monitor output. The voltage monitor is unity gain. The current monitor senses the drop across the resistor in the RC filter with an instrumentation amplifier with a gain of 10 millivolts per microamp.

DSP Card and Clock Program

The DSP56303 processor clock rate is software programmable. 100 MIPS is the maximum speed of the DSP. Programs used here were run at 50 - 80 MIPS. A field programmable gate array (FPGA) on the DSP card latches 20-bit clocking patterns. The special addressing modes added to the sequence logic to simplify the clocking program allow bits to be set, cleared, and toggled independently. 16 of these bits drive the clocking card. Three of the four remaining bits go to the video card — one bit for conversion timing and two for analog switching. The last bit can be used for diagnostic output. Oscilloscope synchronization was provided with this last bit, and a shutter was operated with one of the video bits. Additional digital outputs from the DSP are available and some have been used for stepper motor control.

A timer module (one of three) in the DSP is used for integration time control, simplifying timing software and providing millisecond resolution with high stability.

The clock programs use C with inlined assembly language. The C compiler (for the Motorola 56300 family) was obtained free from Motorola. Wine (Windows compatibility software for Linux) allows the (Windows) C compiler to run on the Linux host PC.

Clocking Card

The clocking card level-shifts 16 bits of the sequence pattern and outputs 20 control signals to the array. Four octal 13 bit D/A converters provide 32 programmable voltage levels for clock rails. In OCIW's design, some voltages and sequence bits are shared among outputs. Jumpers were added to a new clocking card design to allow either OCIW's original configuration or 16 completely independent clocks.

OCIW Two Channel Video Card

The OCIW two-channel video card's design supports correlated double sampling circuitry for CCD control. This circuitry was modified to multiplex two pairs of video inputs into the pair of 16 bit Analogic A/D converters, allowing 4 output multiplexers like the SB226 to be operated.

Digitization at 16 bits with a range at the converter of +/- 5 volts and a header board gain of 25 gave 6.1 microvolt resolution of the array's output voltage. The video card design also provides 8 programmable biases, but a layout error on the (OCIW prototype) boards used hindered their implementation; unused clock lines were used for biases in the first systems.

Four Channel Video Card

A four channel video card using LT1608 converters was designed and constructed. The LT1608 devices are much less expensive than the Analogic devices, and much smaller as well. The number of biases on the video card was increased from 8 to 16, although only 12 of these voltages are brought to the backplane.

PCI Card

The PCI card in the host PC, shown in Figure I.2, is very simple. An AMCC S5920 PCI interface chip, an Altera Max 7128 FPGA, and a Cypress CY4255 8K by 18 bit FIFO compose the core of the card. Low Voltage Differential Signaling (LVDS) was used for the communication link. A fiber-optic communication link is also available in the design, but was not implemented here. The small size of the FIFO has proved sufficient at data rates of 400K pixels/sec. FIFO overflow has never been observed at these rates, and no special precautions have been taken regarding what else is running on the host computer.
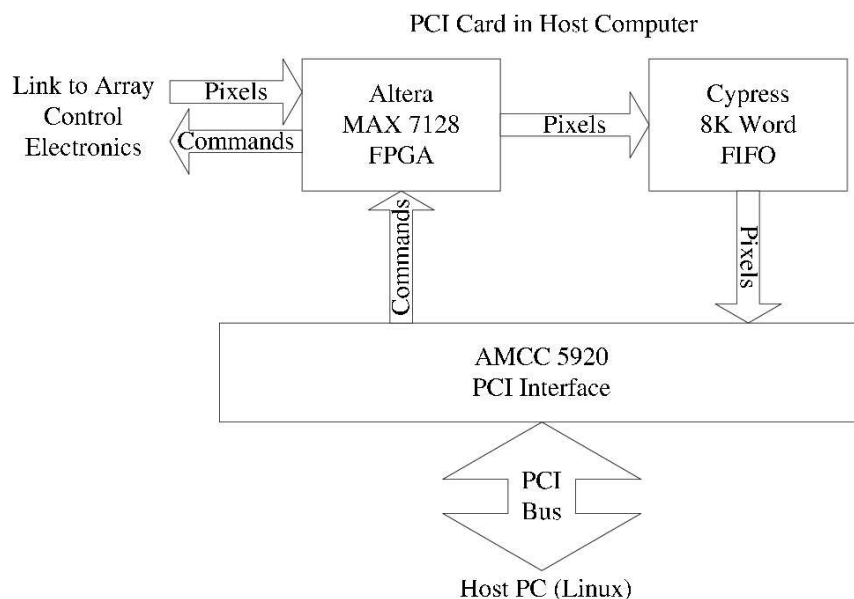
Figure I.2: The PCI card was a very simple design. An FPGA serialized and deserialized the communication with the DSP board, and a FIFO buffered the incoming pixels between interrupt service routines.

Operation at 2M pixels/sec was reliable virtually all of the time, but FIFO overflows were noticed on rare occasions. No investigation into the source of these overflows was done since that data rate was not required.

OCIW's original PCI hardware only allowed for an interrupt when there was a single pixel in the FIFO. Reading the FIFO would thus entail reading a single pixel, checking the FIFO status, and looping until no more pixels remained. Although this approach would maximize allowable latency, it would leave little time for other processes in the host; the processor would be re-interrupted almost immediately after exiting the ISR and spend excessive time context switching while pixels were arriving. Checking FIFO status every pixel limits the maximum data rate that pixels can be copied from the PCI card. The FIFO provides a signal it can assert when it is filled to some level, with a default level of half full, and a modification to the board allowed this line to serve as the interrupt source. This

250

change increased the amount of time the processor was allowed to execute other processes as the FIFO filled, and eliminated the need to check FIFO status for every pixel, but allowed only 4K pixels (10 millisecond interrupt latency) before overflow.

Two special hardware features of the PCI chip were also employed, allowing faster access to the FIFO. The serial EPROM for the PCI chip needed a programming change to enable these special features. One feature was the ability to "prefetch" a block of data. A specially defined "region" in the PCI chip, when read by the host, tells the PCI chip to assume that sequential access of the entire block will be performed. The interface chip then fetches as many additional reads as it can hold in a small FIFO of its own. If a DMA operation or higher priority interrupt blocks the FIFO interrupt service routine (ISR), the PCI chip will continue to unload the FIFO. A 4K word read region was defined with all read accesses mapped to the FIFO. When 4K pixels are known to be in the FIFO, they can be read from this region. The PCI chip also provides bus width translation. In this mode, the PCI chip accesses the FIFO in two 16 bit reads and presents the same data on the PCI side as a single 32 bit read. This mode was employed as well, cutting the number of PCI reads in half.

Suggestions for Increased Data Rates

To date, machines at RIT and U/R have read large numbers of multiply-sampled megapixel images, while running other applications, without any buffer overflow or pixel loss. Acquisition rates have only been in the 400K pixels per second range, however. It is anticipated that higher rates may be required in the future. Some of the enhancements just described were made in anticipation of higher data rates. Some more are offered:

Since the PCI card operates at an independent clock frequency from the PCI bus, it is expected that further improvements to read rate can be made by speeding this clock up, and

perhaps running it at the PCI clock rate. The PCI chip operated initially from a 10 MHz master oscillator, but its data sheet indicates that it can be run faster. The maximum speed of the PCI bus in 32 bit mode is 132 megabytes per second, or 66 megapixels per second. An improved circuit should easily exceed 15 million pixels per second. At such speeds, interrupt latency becomes a concern. Increasing the FIFO size will help if this is needed. A 64K word pin-compatible FIFO is available from Cypress and would increase latency tolerance. A revised PCI card with a pair of FIFOs side by side could present pixels to the PCI chip without bus width translation overhead. The data rate of the serial link would also have to be increased above the 50-80 megabits per second used here. (LVDS can operate at 400 megabits per second.) The most recent versions of the DSP and PCI cards have "hackable" footprints for a high speed flat panel LVDS link that should be able to serialize and deserialize pixel data at near-PCI bus data rates.

Appendix J

Multiplexer and Array Test Procedures

New devices are generally only slightly different from previous devices — so although some test procedures for previous devices may be inappropriate for new devices, most are probably appropriate. The procedures that follow have been applied on many devices. As with most things, it helps to consider if the procedure being followed makes sense for the current situation.

The SB226 mux is used in many of the following procedures as an illustrative example.

J.1 Plugging in a new device

Power up the controller disconnected first and verify with an oscilloscope and voltmeter that all signals are acting as expected. If the controller has limiting circuits available, make sure they are configured properly. Double-check all connections from the controller to the device socket.

When the device is first "brought to life," perform additional sanity checking. Verify again that voltages are reasonable. Measure currents as well. Unconnected signals will draw very little or no current. Shorts will draw more than expected.

Most devices have means of configuring the operation of the unit cell. This configuration is generally concerned with the voltages on the unit cell's output FET. The gate of this

FET swings through the detection range of the device, from reset to unbiased. The drain is connected to the unit cell supply rail. The source of the FET supplies the buffered output to the next stage of amplification. Its voltage should closely parallel the node voltage. The current flowing from the source to the drain is controlled by a programmable current source. A source follower will work perfectly if it drives a perfect current source and its drain to source voltage is kept constant. The unit cell supply rail may even be included in the output amplifier's feedback loop to achieve a specific drain-source drop. Even if the drain is not kept constant, a FET's gate-source voltage is relatively independent of the drain voltage.

J.2   Settle Time (signal path bias currents):

After the gate and drain voltages for the unit cell output FET have been selected, the unit cell drain current should be considered. Many devices have an adjustable operating point for the unit cell's current. Operation at higher current results in faster settling, but at the cost of increased power dissipation. For devices that need to operate at low power, this current should be carefully set by monitoring the settling time. When the column shift register is clocked to select the next pixel, a transition occurs on the output(s) of the array, and time is required for this transition to settle out before the new pixel may be digitized properly. If this time is not allowed to pass, some of the previous pixel's value will be reflected in the new pixel. Although the transition is not exactly an exponential decay, it can be approximated as one. Many time constants (5-10) are allowed to pass before sampling the output voltage. Since 16 bit conversion is frequently used, it can be argued that approximately 11 time constants are required for proper settling.

Most of this settling is due to the output impedance of the unit cell FET and the capacitance of the column bus. The column bus needs to operate at a sufficient bias current

to overcome the capacitive load, but not such a large bias current that power dissipation is excessive. Many multiplexers employ current mirrors to set this bias current. A control current is fed into the input of the current mirror, which sets up a gate-source voltage that is duplicated on the mirror FETs. The settling time of the column bus may be controlled by setting this control current.

A hot pixel or optical artifact that rapidly transitions from dark to light and from light to dark needs to be set up in the column direction. (For N-output interleaved multiplexers such as the SB226, the transition is easy to obtain. Clocking ahead one electrical column clocks each output ahead by N pixels, so an edge does not need to be optically sharp.) As this transition is repetitively clocked, the output voltage is observed on an oscilloscope. This acquisition is repeated. Current is increased until the settling shape is appropriate.

For large transitions, the asymmetry of the unit cell output drive should be considered. On column bus transitions where the unit cell output FET shuts off, the current mirror is the sole drive behind the transition. (On the SB226, negative-going transitions tend to turn the unit cell output FET on, and positive-going transitions tend to turn the output FET off. Thus, the positive going transitions are strongly influenced by the setting of the current mirror, and may show slew rate limiting. A settle time constant on the order of a microsecond is appropriate for the SB226 multiplexer.)

The current in each main output driver FET is also a consideration, and should be adjusted as well. The capacitive load on the output FET is more controllable, however — it is typically dominated by the cable capacitance.

J.3   Signal Path Gain

The signal path gain can be observed after the column bias current and output bias have been set. A straightforward way to do this is by keeping the array in reset and varying the

reset voltage. This applies a range of known voltages to the detector node. The corresponding output voltages are observed. Vreset must be an independent bias for this technique to work, and this is the case on most multiplexers. If the reset voltage is not independent and the multiplexer has been bonded to a detector, another method is suggested: Illuminate the detector slightly, so that the detector conducts and depletes. Now, the detector node is a controllable voltage source, effectively "shorted" to the detector common. Vary detector common and observe the output voltage.

(Technically, sweeping the reset voltage is not a valid gain test for the SB226 — the reset voltage and the drain of the unit cell output FET are tied together to simplify its design, and sweeping both together does not yield the proper operating conditions. If the current mirror supplying the unit cell is perfect, this test will show a gain of unity for the unit cell source follower regardless of the quality of the unit cell output FET. The FET remains at the same operating point throughout the sweep. Gate-source voltage changes slightly with increasing drain-source voltage at the same current, and unity gain is not actually attainable. Practically, it does not seem significant. At low drain currents, the effect is small, and experiment has also shown the unit cell output FET gain is very close to unity on other multiplexers. Papers such as [121] present this as a valid method for measuring the gain.)

J.4   Charge Dump

Several unit cell signals capacitively couple in to the detector nodes. One is the row enable line. Another is the reset enable line. A third is the unit cell supply itself. The reset voltage may also couple. For very low dark current devices, which means most astronomical detector arrays, it is easy to characterize the coupling of these signals into the detector nodes.

The row enable FET, as shown in Figure 2.2, is effectively a switch. Once it is "closed", there is no variation in the row enable FET resistance. Variation of the row enable line after the switch is fully closed will produce a change in output voltage indicative of capacitive coupling from this line into the unit cell.

A reset FET is also a switch. Once the reset FET has been turned off, coupling of the reset gate into the detector node can be measured by varying the reset off voltage while observing the array output.

Similarly, Vdduc can be varied and its influence on the detector node can be observed. Assuming that V_{GS} is constant, a change in supply voltage will reflect this coupling at the array output.

Charge dump effects are useful to know so that the pixels in a diffusion-mode detector may be properly biased. Infrared detectors have much lower bandgaps than visible detectors, and these charge dump effects may be quite significant compared to their well depth.

The detector substrate will typically have a very large coupling into the detector node voltage as well, but it is rarely switched.

J.5 Nodal Capacitance

Well capacity is a fundamental measurement of a detector array. The wells are effectively small capacitors. Their voltage changes as charge accumulates. The capacitance is impossible to measure directly with a meter. High capacitance detector nodes are actually less desirable. They require more charge to produce the same voltage. If multiplexer noise is significant, then signal to noise ratio is better for lower capacitance detector nodes.

Good detector nodes typically have tens of femto-Farads of capacitance, resulting in several microvolts of signal per electron.

J.5.1 Noise Variance versus Signal

The "Noise squared versus signal method" [65] uses Poisson noise to measure the conversion factor in an imaging array. The mean and variance are identical in the Poisson process. By measuring the mean and variance of some process assumed to be Poisson, a unique conversion factor that makes the mean and variance identical may be computed.

The difference of two otherwise identical images should yield a residual zero mean white noise image. Multiple samples can be used to reduce the read noise. Noise is not Poisson distributed in Fowler averaged images (unless a shutter is employed) so compensation using Equation E-63 is necessary in this case. A more typical approach is to observe the slope of the noise variance with respect to the signal and assume that the read noise is a constant.

J.5.2 Measuring Inter-pixel Capacitance

Possible capacitive coupling of pixels to neighbors must be considered to measure nodal capacitance accurately. This is an easy measurement. Simply take the set of noise images obtained for the noise variance test. Compute the average horizontal and vertical noise correlation by multiplying the noise images with themselves shifted by one pixel (vertically an horizontally). Compare the mean square of this product to the mean square noise. If the first term is measurably non-zero, and even a tiny fraction of the mean square noise, it should be included in the overall noise calculation. These correlation terms can be included in the noise slope versus signal method as well.

This works because the net area under the autocorrelation is equal to the energy of the white noise in the detector nodes. For small amounts of inter-pixel coupling, only the four direct vertical and horizontal neighbors are significant and the total Poisson noise is the mean square noise plus twice the mean square horizontal and vertical correlations.

J.6 Read Noise and Dark Current

Read noise is simple to measure if the dark current can be neglected. A pair of images is taken, and their difference is examined. Low frequency variations in signal between the images frequently exist, due to variations in temperature and bias, and this is typically not considered to be noise. The intercept of "noise squared versus signal" can also serve as a read noise estimator.

Dark current can be measured in dark images, varying integration times and temperatures. It typically varies exponentially with temperature. The dark current of some arrays is extremely low however, so direct measurement has several difficulties. First, integration times long enough to accumulate any dark current are long enough to accumulate a large number of cosmic events (muons). Rejection of muon hits is then required for measurement. Temperature sensitivity is another issue. An active temperature controller only stable to 0.1 degrees Kelvin in conjunction with a device whose output voltage can vary by as much as 1 to 10 e- per milli-Kelvin may result in thermal variations that quickly mask the dark current.

Measuring noise that dark current produces is a practical alternative. Dark current should obey Poisson statistics, and the noise produced by the dark current is the fundamental concern in most cases, so measuring noise increase over time serves well when direct measures of dark current fail.

It is tempting to try to beat down the read noise with Fowler sampling, however one must be careful here. Dark current noise accumulates during the pedestals and signals, so the variance in a Fowler image does not properly reflect the Poisson noise attributable to dark current when the pedestal and signal times are a significant fraction of the total time. Consideration of the expression in Equation E-63 is required here.

J.7   Spectral Sensitivity:

The spectral sensitivity of an astronomical detector is a parameter of particular importance. Inefficient detectors require more time on a telescope to achieve the same results, and telescope time is expensive. Thus, it is desirable to know how what percentage of photons are actually captured by a detector at any given frequency.

Spectral response measurement requires a stable light source, a way to vary the spectral content of it, and a calibrated detector. The calibrated detector is placed in the position that the array will occupy, and the optical flux is measured with the first filter in the path. This measurement is repeated for each wavelength. Then, the calibrated detector is removed and the array being tested is put in its place. The filters are again placed in the optical path, and images are taken with the array. With knowledge of the electrons per analog to digital converter unit of the system and of the geometry of the array, the quantum efficiency is calculated.

Two variations of measuring relative quantum efficiency (RQE) are presented here: The first method measures the brightness of a source, a quantity that is independent of the distance from the source. Knowing the source brightness at all particular wavelengths of interest, the system stop's aperture diameter, and the distance from that aperture to the detector, the photon arrival rate per unit area may be calculated at the detector. This method allows the entire detector to be characterized, but is more complicated.

The second method measures the photon arrival rate per unit area at the system stop from a source that is limited in diameter. If the geometry of the source, system stop, and detector is such that all photons leaving the source and passing through the system stop are guaranteed to hit the detector then the total photons per second is known from the product of the arrival rate per unit area at the stop and the stop's diameter. This method assumes that the detector has uniform sensitivity, but it is a simpler experiment to perform.

For either of these methods, the path to the device under test is frequently different from the path to the calibrated detector. Calibrated detectors are usually calibrated warm, and may not be easily operable at cryogenic temperatures. The optical elements inside the dewar may operate differently at cryogenic temperatures as well, so knowing the attenuation of the optical path to the device is somewhat tricky.

Accurate measure of nodal capacitance is also required to accurately measure quantum efficiency. Pain and Hancock [74] observe that typical detector nodal capacitance varies with saturation level, and when noise is measured at higher signal strengths, the noise appears in the differential capacitance while the signal appears on the integrated capacitance, producing variations in measurement with applied bias. One simple solution for this effect is to only use low photon fluxes. Pain and Hancock describe an alternative.

J.8 DQE

Detective quantum efficiency (DQE) is a more meaningful specification than RQE. Wideband detectors may have gain for higher energy photons and yield good RQE without good information capture. After the RQE is known, the theoretical noise may be compared to the observed noise as an indicator of how well the detector is really capturing the available information.

J.9 MTF

Spatial frequency response, also called modulation transfer function (MTF,) can be measured in various ways, but they are all fundamentally similar. An image of known and broadband spatial frequency response (such as a spot, a line, an edge, or a fixed noise pat-

tern) is focused on the array, and the signal this stimulus yields is compared to the original. Any of these approaches is acceptable. An edge is an easy image to produce.

J.10   Image Persistence

After a saturating image is taken, a ghost image frequently appears in a subsequent image. This so called "latent" image appears to be due to traps in the semiconductor that become populated when the pixel wells are full. During the integration time of a subsequent exposure, the traps decay and appear as signal in that frame. There are typically several different types of traps, all having some sort sensitivity to exposure, (possibly non-linear) and a time constant of exponential decay.

J.11   Undiscovered Tests

Research into new devices asks more questions than it answers — A list of tests is never complete! These new questions will undoubtedly spur the proposal of theories to explain the unexplained. These new theories will suggest the implementation of new experiments to perform so that the theories can be moved in one direction or the other. This is where this dissertation ends, but where it really starts as well... the scientist and the engineer, working together with the research system — and the next mystery to solve.

Bibliography

[1] J. Janesick, "Charge-coupled CMOS and hybrid detector arrays," in *Focal Plane Arrays for Space Telescopes*, T. J. Grycewicz and C. McCreight, eds., **5167**, pp. 1–18, Aug. 2003.

[2] J. Janesick, "Lux transfer: Complementary metal oxide semiconductors versus charge-coupled devices," *Optical Engineering* **41 (6)**, pp. 1203–1216, June 2002.

[3] P. Magnan, "Detection of visible photons in ccd and cmos - a comparative view," *Nuclear Instruments and methods in Physics Reseach A* **504**, pp. 199–212, 2003.

[4] A. M. Fowler and I. Gatley, "Demostration of an Algorithm for Read-Noise Reduction in Infrared Arrays," *The Astrophysical Journal* **353**, pp. L33–L34, 1990.

[5] W. J. Forrest and J. L. Pipher, "Evaluation of a 32x32 InSb CCD for use in Astronomy," in *Infrared Detector Technology Workshop*, pp. 16.1–16.69, Aug. 1983.

[6] W. J. Forrest, A. Moneti, C. E. Woodward, and J. L. Pipher, "The New Near-Infrared Camera at the University of Rochester," *Publications of the Astronomical Society of the Pacific* **97**, pp. 183–198, Feb. 1985.

[7] P. E. Allen and D. R. Holberg, *CMOS Analog Circuit Design*, Holt, Rinehart and Winston, NY, 1987.

[8] B. Backer, Z. Ninkov, and C. Massimilano, "Characterization of a cid-38 charge injection device," in *Proc SPIE, Solid State Sensor Arrays and CCD Cameras*, C. N. Anagnostopoulos, M. M. Blouke, and M. P. Lesser, eds., **2654**, pp. 11–19, Mar 1996.

[9] G. Lungu, G. Lubberts, Z. Ninkov, and L. F. Fuller, "Design, fabrication, and characterization of a family of active pixel CID imagers," in *Proc. SPIE, Sensors and Camera Systems for Scientific/Industrial Applications*, M. M. Blouke and G. M. Williams, eds., **3649**, pp. 67–73, Apr. 1999.

[10] L. Struder and et al., "Xeus wide-field imager: first experiments with the X-ray active pixel sensor DEPFET," in *X-Ray and Gamma-Ray Instrumentation for Astronomy XIII*, K. A. Flanagan and O. H. Siegmund, eds., **5165**, pp. 10–18, Aug. 2003.

[11] J. C. Pickel, A. H. Kalma, G. R. Hopkinson, and C. J. Marshall, "Radiation Effects on Photonic Imagers — A Historical Perspective," *IEEE Transactions on Nuclear Science* **50 (3)**, pp. 671–688, June 2003.

[12] Z. Ninkov, C. Tang, B. Backer, R. L. Easton, and J. Carbone, "Charge injection devices for use in astronomy," in *Proc SPIE, Instrumentation in Astronomy VIII*, D. L. Crawford and E. R. Craine, eds., **2198**, pp. 868–876, 1994.

[13] Z. Ninkov, C. Tang, and R. L. Easton, "Evaluation of a charge injection device array," in *Proc SPIE, Charge-Coupled Devices and Solid State Optical Sensors IV*, M. M. Blouke, ed., **2172**, pp. 180–186, 1994.

[14] W. E. Miller, H. D. Hendricks, and R. D. Thom, "Monolithic InSb imaging arrays with charge-coupled device /CCD/ readout," in *Recent advances in TV sensors and systems; Proceedings of the Seminar, San Diego, Calif., August 27, 28, 1979. (A80-*

44626 19-35) Bellingham, Wash., Society of Photo-Optical Instrumentation Engineers, 1979, p. 173-178., pp. 173–178, 1979.

[15] J. Sarathy, G. A. Gasparian, M. J. Lange, M. J. Cohen, G. H. Olsen, D. Kim, P. Studenkov, and S. R. Forrest, "Monolithic active pixel InGaAs focal plane arrays for near-infrared imaging," in *Proc. SPIE Vol. 2999, p. 225-234, Photodetectors: Materials and Devices II, Gail J. Brown; Manijeh Razeghi; Eds.*, pp. 225–234, Apr. 1997.

[16] J. D. Offenberg, D. J. Fixsen, B. J. Rauscher, W. J. Forrest, R. J. Hanisch, J. C. Mather, M. E. McKelvey, R. E. McMurray, M. A. Nieto-Santisteban, J. L. Pipher, R. Sengupta, and H. S. Stockman, "Validation of Up-the-Ramp Sampling with Cosmic-Ray Rejection on Infrared Detectors," *Publications of the Astronomy Society of the Pacific* **113**, pp. 240–254, Feb. 2001.

[17] J. D. Offenberg, D. J. Fixsen, R. Sengupta, M. A. Nieto-Santisteban, H. S. Stockman, and R. J. Hanisch, "Cosmic Ray Rejection and the Next Generation Space Telescope," in *Bulletin of the American Astronomical Society*, **31**, pp. 884–+, May 1999.

[18] J. Janesick, *Scientific Charge-Coupled Devices*, SPIE Press, Bellingham, WA, 2001.

[19] B. G. Streetman, *Solid State Electronic Devices*, Prentice-Hall , Englewood Cliffs, NJ, 1980.

[20] S. M. Sze, *Semiconductor Devices Physics and Technology*, Wiley, New York, 1985.

[21] G. H. Rieke, *Detection of Light from the Ultraviolet to the Submillimeter*, Cambridge University Press, Cambridge, 1994.

[22] A. Papoulis, *The Fourier Integral and its Applications*, McGraw-Hill, New York, 1962.

[23] R. Bracewell, *The Fourier Transform and its Applications*, McGraw-Hill, New York, 1965.

[24] A. Papoulis, *Systems and Transforms with Applications in Optics*, McGraw-Hill, New York, 1968.

[25] C. D. McGillem and G. R. Cooper, *Continuous and Discrete Signal and System Analysis*, Holt, Rinehart and Winston, NY, 1974.

[26] J. D. Gaskill, *Linear Systems, Fourier Transforms, and Optics*, p. 47. John Wiley and Sons, New York, 1978.

[27] A. V. Oppenheim and A. S. Willsky, *Signals and Systems*, Prentice-Hall, Englewood Cliffs, NJ, 2nd ed., 1997.

[28] E. Hecht, *Optics*, Addison Wesley, Reading, MA, 4th ed., 2002.

[29] M. Born and E. Wolf, *Principles of Optics*, Pergamon, New York, 1965.

[30] N. S. Jayant and P. Noll, *Digital Coding of Waveforms - Principles and Applications to Speech and Video*, Prentice-Hall, Englewood Cliffs, NJ, 1984.

[31] J. D. Gaskill, *Linear Systems, Fourier Transforms, and Optics*, John Wiley and Sons, New York, 1978.

[32] R. N. Bracewell, *Two-Dimensional Imaging*, Prentice-Hall, Englewood Cliffs, NJ, 1995.

[33] D. E. Dudgeon and R. M. Mesereau, *Multidimensional Digital Signal Processing*, Signal Processing Series, Alan V. Oppenheim, series editor, Prentice-Hall, Englewood Cliffs, NJ, 1984.

[34] A. Papoulis, *Probability, Random Variables, and Stochastic Processes*, McGraw-Hill, New York, 2nd ed., 1984.

[35] G. R. Cooper and C. D. McGillem, *Probabilistic Methods of Signal and System Analysis*, Holt, Rinehart and Winston, NY, 2nd ed., 1986.

[36] R. E. Blahut, *Principles and Practice of Information Theory*, Addison-Wesley, Reading, MA, 1987.

[37] J. M. Mendel, *Lessons in Estimation Theory for Signal Processing, Communications, and Control*, Prentice Hall PTR, Englewood Cliffs, NJ, 1995.

[38] D. Kavaldjiev and Z. Ninkov, "Subpixel Sensitivity Map for a Charge Coupled Device sensor," *Optical Engineering* **37**, pp. 948–954, Mar. 1998.

[39] D. Kavaldjiev and Z. Ninkov, "Experimental measurement of the variation in sensitivity within a single pixel of a CCD," in *Proc. SPIE, Solid State Sensor Arrays: Development and Applications*, M. M. Blouke, ed., **3019**, pp. 42–49, Apr. 1997.

[40] A. Piterman and Z. Ninkov, "Measurements of the subpixel sensitivity for a backside-illuminated ccd," in *Proc. SPIE, Sensors and Camera Systems for Scientific, Industrial, and Digital Photography Applications*, M. M. Blouke and N. Sampat, eds., **3965**, pp. 289–297, 2000.

[41] A. Piterman and Z. Ninkov, "Effect of nonuniform ccd pixel sensitivity variations on measurement accuracy," in *Proc. SPIE, Sensors and Camera Systems for Scientific,*

Industrial, and Digital Photography Applications II, M. M. Blouke, N. Sampat, and J. Canosa, eds., **4306**, pp. 280–288, 2001.

[42] G. Boreman, *MTF in Optical and Electro-Optical Systems*, SPIE PRESS, 2001.

[43] B. J. Rauscher, "A note on NGST Detector Modulation Transfer Function Guidelines," *www.ngst.nasa.gov/doclist/bytitle.html* **Document 662**, 2000.

[44] R. N. Bracewell, *Two-Dimensional Imaging*, p. 149. Prentice-Hall, Englewood Cliffs, NJ, 1995.

[45] M. H. Crowell and E. F. Labuda, "The Silicon Diode Array Camera Tube," *Bell Systems Technical Journal* **48**, pp. 1481–1528, 1969.

[46] H. Holloway, "Collection Efficiency and Crosstalk in Closely Spaced Photodiode Arrays," *Journal of Applied Physics* **60**, pp. 1091–1096, 1986.

[47] H. Holloway, "Theory of Lateral-Collection Photodiodes," *Journal of Applied Physics* **49**, pp. 4264–4269, 1978.

[48] S. H. Klapper, P. Singer, and J. Rossbeck, "Lateral Diode Program Analysis." Unpublished Raytheon interdepartmental memo, 1978.

[49] P. Love and A. Hoffman, "Mtf model for backside illuminated p-on-n insb." Unpublished Raytheon mathcad document, 1999.

[50] D. T. Cheung, "MTF Modeling of Backside-Illuminated PV Detector Arrays," *Infrared Physics* **21**, pp. 301–310, 1981.

[51] M. Davis, M. Greiner, J. Sanders, and J. Wimmers, "Resolution Issues in InSb Focal Plane array system design," in *Proc SPIE, Conf on IR Detectors and Focal Plane arrays V*, **3379**, pp. 288–299, 1998.

[52] W. J. Forrest and Z. Ninkov, "Cross talk in InSb arrays." Unpublished mathcad document.

[53] V. I. Blynskii, A. Y. Kulikov, S. Y. Rakhley, and V. I. Osinskii, "Photoelectric Crosstalk between Silicon Photoelements," *Physica Status Solidii* **121**, pp. 227–233, 1990.

[54] L. C. Shen and J. A. Kong, *Applied Electromagentism*, pp. 326–330. Brooks / Cole Engineering Division, Monterey, CA, 1983.

[55] M. A. Plonus, *Applied Electromagnetics*, McGraw-Hill, USA, 1978.

[56] J. D. Gaskill, *Linear Systems, Fourier Transforms, and Optics*, pp. 339–345. John Wiley and Sons, New York, 1978.

[57] I. Brouk, Y. Nemirovsky, S. Lachowicz, E. A. Gluszak, S. Hinckley, and K. Eshraghian, "Characterization of crosstalk between CMOS photodiodes," *Solid State Electronics* **46**, pp. 53–59, 2001.

[58] I. Shcherback, B. Belotserkovsky, A. Belenky, and O. Yadid-Pecht, "A Unique Submicron Scanning System use for CMOS APS crosstalk characterization," in *Proc. SPIE, Sensors and Camera Systems for Scientific, Industrial, and Digital Photography Applications IV*, **5017**, pp. 136–142, Jan. 2003.

[59] C. McCreight, M. Greenhouse, D. Figer, R. Martineau, M. Jurotich, and B. Seery, "NGST ISIM Technology Development Requirements and Goals for NGST Detectors," *www.ngst.nasa.gov/doclist/bytitle.html* **Document 641**, 2001.

[60] W. Shockley and W. T. Read, Jr., "Statisics of the Recombinations of Holes and Electrons," *Phys. Rev.* **87**, pp. 835–842, 1952.

[61] S. Kavadias, K. Misiakos, and D. Loukas, "Calculation of Pixel Detector Capacitances through Three Dimensional Numerical Solution of the Laplace Equation," *IEEE Transactions on Nuclear Science* **40 (2)**, pp. 397–401, April 1994.

[62] Caccia, M. and Borghi, S. and Campagnolo, R. and Battaglia, M. and Kucewicz, W. and Palka, H. and Zalewska, A. and Domanski, K, and Marczewski, J, "Characterisation of Hybrid Pixel Detectors with capacitive charge division," *5th international Linear Collider Workshop*, 2001.

[63] Battaglia, M. and Borghi, S. and Caccia, M. and Campagnolo, R. and Kucewicz, W. and Palka, H. and Zalewska, "Hybrid Pixel Detector Development for the Linear Collider Vertex Detector," *9th Internationa Workshop on Vertex Detectors*, 2001.

[64] A. C. Moore, Z. Ninkov, W. J. Forrest, C. McMurtry, G. S. Burley, and L. Avery, "Operation and test of Hybridized Silicon p-i-n Arrays using Open-source Array Control Hardware and Software," in *Proc. SPIE, Sensors and Camera Systems for Scientific, Industrial, and Digital Photography Applications IV*, M. M. Blouke, N. Sampat, and R. J. Motta, eds., **5017**, pp. 240–253, Jan. 2003.

[65] L. Mortara and A. Fowler, "Evaluations of CCD: Performance for Astronomical Use," in *Proc. SPIE, Solid State Imagers for Astronomy*, **290**, pp. 28–33, 1981.

[66] A. C. Moore, Z. Ninkov, and W. J. Forrest, "Interpixel capacitance in nondestructive focal plane arrays," in *Proc. SPIE, Focal Plane Arrays for Space Telescopes*, T. J. Grycewicz and C. McCreight, eds., **5167**, pp. 204–217, Aug. 2003.

[67] R. B. Blackman and J. W. Tukey, *The Measurement of Power Spectra*, Dover, New York, 1958.

[68] E. C. Doerner, "Wiener spectrum analysis of photographic granularity," *J. Opt Soc. Am A* **52**, pp. 669–672, 1962.

[69] R. Shaw, "The equivalent quantum efficiency of the photographic process," *J. Phot. Sci.* **11**, pp. 199–204, 1963.

[70] M. Rabbani, R. Shaw, and R. Van Metter, "Detective Quantum Efficiency of imaging systems with amplifying and scattering mechanisms," *J. Opt Soc. Am A* **4 (5)**, pp. 895–901, May 1987.

[71] M. Rabbani and R. Van Metter, "Analysis of signal and noise propogation for several imaging mechanisms," *J. Opt Soc. Am A* **6 (8)**, pp. 1156–1164, Aug 1989.

[72] J. Yao and I. A. Cunningham, "Parallel Cascades: New ways to describe noise transfer in medical imaging systems," *Journal of Medical Physics* **6 (8)**, pp. 2020–2038, Oct 2001.

[73] K. Ennico, M. McKelvey, C. McCreight, R. McMurray, R. Johnson, A. W. Hoffman, P. Love, and N. Lum, "Large Format Si:As IBC Array Performance for NGST and Future IR Space Telescope Applications," in *Proc. SPIE, IR Space Telescopes and Instruments*, J. C. Mather, ed., **4850**, pp. 890–901, 2002.

[74] B. Pain and B. Hancock, "Accurate Estimation of Conversion Gain and Quantum Efficiency in CMOS Imagers," in *Proc. SPIE, Sensors and Camera Systems for Scientific, Industrial, and Digital Photography Applications IV*, M. M. Blouke, N. Sampat, and R. J. Motta, eds., **5017**, pp. 94–103, Jan. 2003.

[75] P. Hickson, "A Visible Imager for NGST," *www.ngst.nasa.gov/doclist/bytitle.html* **Document 518**, 1999.

[76] R. Alexander, "NGST Visible Imager Detector Testing Report," *www.ngst.nasa.gov-/doclist/bytitle.html* **Document 937**, 2001.

[77] P. Hickson, "Canadian Visible Imager for NGST Final Report," *www.ngst.nasa.gov-/doclist/bytitle.html* **Document 936**, 2001.

[78] R. Alexander, "Potential CSA Contributions to NGST; Science Instruments and Observatory and Ground Systems," *www.ngst.nasa.gov/doclist/bytitle.html* **Document 542**, 1999.

[79] J. Wu, W. J. Forrest, J. L. Pipher, N. Lum, and A. Hoffman, "Development of infrared focal plane arrays for space," *Review of Scientific Instruments* **68**, pp. 3566–3578, Sept. 1997.

[80] J. L. Pipher, W. J. Forrest, and J. Wu, "InSb arrays for SIRTF," in *Proc. SPIE, Infrared Detectors and Instrumentation for Astronomy,*, A. M. Fowler, ed., **2475**, pp. 428–434, June 1995.

[81] A. W. Hoffman, K. J. Ando, A. D. Estrada, J. D. Garnett, N. A. Lum, P. J. Love, J. P. Rosbeck, K. P. Sparkman, A. M. Fowler, J. L. Pipher, and W. J. Forrest, "Near IR arrays for ground-based and space-based astronomy," in *Proc. SPIE, Infrared Astronomical Instrumentation,*, A. M. Fowler, ed., **3354**, pp. 24–29, Aug. 1998.

[82] G. Ottaviani, L. Reggiani, C. Canali, F. Nava, and A. A. Quaranta, "Hole drift velocity in silicon," *Physical Review B Solid State* **12(8)**, pp. 3318–3329, 1975.

[83] C. Jacoboni, C. Canali, G. Ottaviani, and A. A. Quaranta, "A review of some charge transport properties of silicon," *Solid State Electronics.* **20(2)**, pp. 77–89, 1977.

[84] C. Canali, F. Nava, and L. Reggiani, "Hot electron transport in semiconductors," *Topics in Applied Physics* **58**, pp. 107–110, Springer-Verlag, (Berlin), 1985.

274

[85] G. Persky and D. Bartelink, "Diffusion of electrons in silicon transverse to a high electic field," *Applied Physics Letters* **16**, pp. 191–194, 1970.

[86] G. G. Fazio, J. L. Hora, S. P. Willner, J. R. Stauffer, M. L. Ashby, Z. Wang, E. V. Tollestrup, J. L. Pipher, W. J. Forrest, C. R. McCreight, S. H. Moseley, W. F. Hoffmann, P. Eisenhardt, and E. L. Wright, "Infrared array camera (IRAC) for the Space Infrared Telescope Facility (SIRTF)," in *Proc. SPIE, Infrared Astronomical Instrumentation,*, A. M. Fowler, ed., **3354**, pp. 1024–1031, Aug. 1998.

[87] R. Fastow and A. Strum, "Monte Carlo Simulations of the Cross Talk in InSb Matrices," *Proc SPIE Infrared Detectors State of the Art II* **2274**, pp. 136–146, 1994.

[88] G. R. Cooper and C. D. McGillem, *Probabilistic Methods of Signal and System Analysis*, pp. 122–127. Holt, Reinhart, and Winston, 1986.

[89] A. M. Fowler and I. Gatley, "Noise reduction strategy for hybrid IR focal-plane arrays," in *Proc. SPIE, Infrared Sensors: Detectors, Electronics, and Signal Processing,*, T. S. Jayadev, ed., **1541**, pp. 127–133, Nov. 1991.

[90] J. D. Garnett and W. J. Forrest, "Multiply sampled read-limited and background-limited noise performance," in *Proc. SPIE, Infrared Detectors and Instrumentation,*, A. M. Fowler, ed., **1946**, pp. 395–404, Oct. 1993.

[91] J. M. Mendel, *Lessons in Estimation Theory for Signal Processing, Communications, and Control*, pp. 121–146. Prentice Hall PTR, Englewood Cliffs, NJ, 1995.

[92] R. C. Martin, *Agile Software Development*, Prentice Hall, Upper Saddle River, NJ, 2003.

[93] python.org, "www.python.org." web site.

[94] G. V. Wilson, "Software Engineering with Python for Scientists and Engineers." Proposal, submitted and approved by PSF, 2004.

[95] M. L. Hetland, *Practical Python*, Apress, Berkeley, CA, 2002.

[96] M. Lutz, *Programming Python*, O'Reilly, Sebastapol, CA, 2nd ed., 2001.

[97] D. M. Beazley, *Python Essential Reference*, New Riders, Indianapolis, IA, 2nd ed., 2001.

[98] H. P. Langtangen, *Python Scripting for Computational Science*, Springer-Verlag, Berlin Heidelberg, 2004.

[99] P. Barrett and W. Bridgman, "PyFITS, a FITS module for Python," *Astronomical Data Analysis Software and Systems VIII*, 1998.

[100] R. L. White and P. Greenfield, "Using Python To Modernize Astronomical Software," 1999.

[101] P. Greenfield, J. C. Hsu, and W. Hack, *PyFITS Users Manual*, Space Telescope Science Institute, 2002.

[102] D. M. Beazley, "Scientific Computing with Python," in *Astronomical Data Analysis Software and Systems IX, ASP Conference Proceedings, Vol. 216, edited by Nadine Manset, Christian Veillet, and Dennis Crabtree. Astronomical Society of the Pacific, ISBN 1-58381-047-1, 2000., p.49*, **9**, pp. 49–+, 2000.

[103] P. E. Barrett and W. T. Bridgman, "PyFITS. a Python FITS Module," in *Astronomical Data Analysis Software and Systems IX, ASP Conference Proceedings, Vol. 216, edited by Nadine Manset, Christian Veillet, and Dennis Crabtree. Astronomical Society of the Pacific, ISBN 1-58381-047-1, 2000., p.67*, **9**, pp. 67–+, 2000.

[104] "http://www.scipy.org." Scientific Python web site.

[105] "http://matplotlib.sourceforge.net." matplotlib 2D plotting library web site.

[106] "http://www.vtk.org." The Visualization Toolkit web site.

[107] "http://www.vpython.org." The VPython web site.

[108] "http://www.atamai.com." Atamai Interactive Visualization web site.

[109] R. Chabay and B. Sherwood, *Matter and Interactions*, Wiley, New York, 2002.

[110] G. K. Thiruvathukal, T. W. Christopher, and J. P. Shafee, *Web Programming in Python*, Prentiss-Hall PTR, Upper Saddle River, NJ, 2002.

[111] S. Holden, *Python Web Programming*, New Riders, Indianapolis, IA, 2002.

[112] "http://www.twistedmatrix.com." The twisted networking framework web site.

[113] "http://www.list.org." Mailman, The GNU Mailing List Manager web site.

[114] "http://www.zope.org." The Z Object Publishing Environment.

[115] "http://www.plone.org." The Plone Content Management System web site.

[116] "http://www.google.com." Google web site.

[117] G. Burley, "www.ociw.edu/~burley/ccd/base.html." Observatories of the Carnegie Institute of Washington web site, 2002.

[118] W. J. Forrest, H. Chen, J. D. Garnett, S. L. Solomon, and J. L. Pipher, "Near-infrared arrays for SIRTF, the Space Infrared Telescope Facility," in *Proc. SPIE, Infrared Detectors and Instrumentation,*, A. M. Fowler, ed., **1946**, pp. 18–24, Oct. 1993.

[119] A. Rubini and J. Corbet, *Linux Device Drivers*, O'Reilly, Sebastapol, CA, 2nd ed., 2001.

[120] T. Denault and K. M. Hawarden-Ogata, "irtf.ifa.hawaii.edu." web site.

[121] C. McMurtry, W. J. Forrest, A. C. Moore, and J. L.Pipher, "Next Generation Space Telescope: NIR InSb Array Development," in *IR Space Telescopes and Instruments*, J. Mather, ed., **4850**, pp. 847–857, Aug. 2002.